MICROBIAL SYNTHESIS OF METAL OXIDE, METAL SULFIDE AND METAL NANOPARTICLES

THESIS SUBMITTED TO

UNIVERSITY OF PUNE

FOR THE DEGREE OF

DOCTOR OF PHILOSOPHY

IN

BIOTECHNOLOGY

ATUL A. BHARDE

BIOCHEMICAL SCIENCES DIVISION
NATIONAL CHEMICAL LABORATORY
PUNE 411 008
INDIA

FEBRUARY 2007

The role of infinitely small is infinitely large

—— **Luis Pasteur**

Dedicated to Aai, Baba & those who struggled for the advancement of Science

CERTIFICATE

This is to certify that the work discussed in the thesis entitled **“MICROBIAL SYNTHESIS OF METAL OXIDE, METAL SULFIDE AND METAL NANOPARTICLES”** by **ATUL BHARDE**, submitted for the degree of *Doctor of Philosophy in Biotechnology* was carried out under my supervision at the Biochemical Sciences and the Materials Chemistry Divisions of the National Chemical Laboratory, Pune, India. Such materials as have been obtained by other sources have been duly acknowledged in this thesis. To the best of my knowledge, the present work or any part thereof has not been submitted to any other University for the award of any other degree or diploma.

Date: **Dr. (Mrs.) Asmita Prabhune**
Place: Pune (Research Guide)

CERTIFICATE

This is to certify that the work discussed in the thesis entitled **"MICROBIAL SYNTHESIS OF METAL OXIDE, METAL SULFIDE AND METAL NANOPARTICLES"** by **ATUL BHARDE**, submitted for the degree of *Doctor of Philosophy in Biotechnology* was carried out under my joint supervision at the Biochemical Sciences and the Materials Chemistry Divisions of the National Chemical Laboratory, Pune, India. Such materials as have been obtained by other sources have been duly acknowledged in this thesis. To the best of my knowledge, the present work or any part thereof has not been submitted to any other University for the award of any other degree or diploma.

Date: **Dr. Murali Sastry**

Place: Pune (Research Co-Guide)

DECLARATION

I hereby declare that the work described in this thesis entitled **“MICROBIAL SYNTHESIS OF METAL OXIDE, METAL SULFIDE AND METAL NANOPARTICLES”** submitted for the degree of *Doctor of Philosophy in Biotechnology* has been carried out by me at the Biochemical Sciences and the Materials Chemistry Divisions of the National Chemical Laboratory, Pune, India under the joint supervision of Dr. (Mrs.) Asmita Prabhune and Dr. Murali Sastry. Such materials as have been obtained by other sources have been duly acknowledged in this thesis. The work is original and has not been submitted in part or full by me for award of any other degree or diploma in any other University.

Date:

Place: Pune

Atul Bharde

(Research Student)

Acknowledgements

I extend my sincere gratitude and appreciation towards many people who made the research work described in this thesis possible. First and foremost reverent and hearty thanks to my research supervisor Dr. Murali Sastry for introducing me to the wonderful world of nanoscience and nanotechnology. I am also thankful to him for his constant support, valuable suggestions, encouragement, advices and ever lasting enthusiasm he has shown in my research work. I will be always thankful to him for teaching me many lessons of life directly or indirectly apart from research. It is my privilege to have been associated with a person like him.

I would like to take this opportunity to express my deep gratitude towards my research guide Dr. Asmita Prabhune, without her support I could not have completed this thesis. I am really thankful to her for always being besides me during the time of crisis and giving me a complete freedom to work in the interdisciplinary field of nanoscience. She has really tried hard to support me many times out of her ways. Her constant guidance, cooperation and support has always kept me going ahead.

I express my heart-felt gratitude to Dr. BLV Prasad for valuable scientific discussions, critical suggestions during the course of my thesis. His friendly nature has always made me feel ease with him and I could always ask for any kind of help through out my Ph.D. tenure. My special thanks to Dr. Satish Ogale for his elderly support, valuable suggestions. I am also thankful to him for the measurements of Mossbauer spectroscopy and the analysis of spectra. Thanks are due for Dr. Absar Ahmad for providing all fungal cultures whenever I asked for my experiments. He was very kind and patient during our discussions and it was a nice experience to work with him. The constant motivation and support from Mrs. Suguna Adhyanthaya and Dr. Pankaj Poddar is also gratefully acknowledged.

This thesis would have been not possible without help and sincere efforts without our collaborators Dr. Yogesh Shouche, Dr. T. Enoki and Dr. Mala Rao. I thank Mr. Rasesh Parekh and Dr. Yogesh Shouche for all the molecular biology work that has been presented in this thesis. Dr. Shouche and Mr. Rasesh provided a great support during all the genetic analysis and valuable discussions for shaping this thesis in its present form. I don't imagine any better collaboration than what I had with them. My special thanks to Rasesh for his constant support and brotherly affection during this course of time. I am grateful to Dr. T. Enoki of Tokyo Institute of Technology, Japan for performing all the magnetic measurements, which constitute an important aspect of this thesis. Contribution from Dr. Milan Sanyal is greatly acknowledged for discussions on magnetism.

I extend my sincere thanks to Ms. Renu Pasricha, who has always been there to perform transmission electron microscopy measurements. I am really appreciative to her for being my 'eyes' during the course of my doctoral research. Apart from a scientist she was a good friend and I would never be able to pay back the love and affection showered upon by her. Thanks are due for all the people in the Center for Materials Characterization, NCL who have assisted me in the course of this work. My sincere thanks to Dr. S. R. Sainkar, Dr. M. Bhadbhade, Mrs. R. Pasricha, Mr. A. B. Gaikwad, Dr. Patil and Dr. A. B. Mandale for making all the specialized facilities available during my *research work. I would also like to acknowledge Minakshi, Manasi and Sanjay for their assistance with AFM measurements.*

My acknowledgements would be incomplete without the special mention of my lab seniors who taught me lab culture and handling of laboratory equipments. Dr. Debabrata,Rautaray, Dr. Sumant Phadatare, Dr. Saikat Mandal, Dr. Anita Swami Dr. Shivshankar were always there to help me in personal and professional problems. Special thanks to Dr. Selvakannan, who was always ready to help me in crucial moments of my thesis writing. I am also thankful to him for the analysis of FTIR spectra.

My heartfelt thanks to my fellow labmates, Hrushikesh, Ambarish, Akhilesh, Tanushree, Amit, Vipul, Sourabh, Minakshi, Prathap, Deepti, Sanjay, Imran, Anil, Priyanka, Virginia, Umesh, Sudarshan, Baisakhi and Ramya for being there to help me during my doctoral work and bearing with me in good and bad times during my wonderful days of Ph.D. My special thanks go to Sourabh for his affectionate and appreciative remarks on my research work. He is also duly acknowledged along with Manasi, Virginia and Deepti for correcting thesis chapters on short notice.

I would like to acknowledge all my friends for always helping me in some or other ways during the period of my graduate research. I am thankful to my college friends Ashish, Tambe, Vikas, Tushar, Rajendra, Ravindra, Manish and Anita for always supporting me during ups and downs in the period of my Ph.D. research. My other NCL friends Anish, Arohi, Shekhar, Nitin, Shailesh, Girish were of great help during tea-time discussions and experimental work.

During the course of my work I had pleasure of getting a helping hand with several project students, Lionel, Dina, Mugdha, and Gauri. There assistance during the presented work is gratefully acknowledged.

I am also thankful to all of my school, college and university teachers who have shown me a way to my future life. Because of there sincere efforts, guidance, blessings and the excitement of research they aroused in me I could traveled all the way to here.

I am grateful to Dr. S. Sivaram, Director NCL, and Dr. S. Pal, Head, Physical Chemistry Division, NCL for giving me an opportunity to work in this institute and making the facilities available for carrying out research. My thanks to the staff of Physical Chemistry division for their help. A special word of gratefulness to Mr. Deepak and Mr. Punekar who have gone out of way to help me with several official matters. I acknowledge the Council of Scientific and Industrial Research (CSIR), Government of India for providing me with the necessary funding and fellowship to pursue research at NCL.

Finally I would like to thanks my parents, because of all there efforts I am successfully standing here. I am thankful to my brother for all his help and moral support. Special thanks go to my beloved grandparents and all my family members for their blessings and well wishes that led me to the completion of my doctoral research work.

— ***Atul Bharde***

Contents

Chapter 1: Introduction

Chapter 2: Characterization Techniques

Chapter 3: Bacteria and Fungi Mediated Biosynthesis of Magnetic Iron Oxide Nanoparticles

Chapter 4: Bacterial Synthesis of Metal Sulfide Nanoparticles

Chapter 5: Bacterial Synthesis of Anisotropic Metal Nanoparticles

Chapter 6: Biological Synthesis of Anisotropic Metal Nanoparticles Using Bacterial Metabolites

Chapter 7: Conclusions

Chapter I

Introduction

This chapter is an introduction to the research work presented in this thesis and gives a brief overview of the biosynthesis of inorganic materials occurring naturally followed by their recent application in deliberate synthesis of nanomaterials by living organisms. Further, an account of biomimetic synthesis of nanomaterials has been described and a brief discussion on the various reported strategies used for the synthesis of nanoparticles as diverse as oxides, sulfides and metals has been illustrated. Finally, some interesting properties of nanoparticles synthesized by biological methods illustrated in this thesis are described.

1.1 Introduction

The end of twentieth century witnessed a major scientific and technological development, the consequences of which are only now beginning to become apparent. Three factors – a better understanding of the properties of matter at the atomic level, progress based on the molecular approach to the way living organisms operate, and the rise of information processing – have led to the increasing unification of different disciplines of science (physics, chemistry, biology) on the nanometer scale, forming what we now know as the nanosciences. Nanotechnology is an emerging field of research and technology dealing with the fabrication and engineering of materials, structures, and systems with nano-scale size at least in one dimension [1]. The origin of this movement is often traced to the end of 1959, the date of the founding speech by Richard Feynman 'There is plenty of room at the bottom' [2], made at the annual meeting of the American Physical Society at California Institute of Technology. The term "nanotechnology" was first coined in 1974 by Norio Taniguchi, then a professor of Tokyo Science University [3]. The essence of nanoscience and nanotechnology is the ability to understand, fabricate and engineer materials, devices and systems in the nanometer regime. The concepts and ideas derived from chemistry, physics, engineering and biology are merged together to design a novel material with desired properties. The properties and functionalities of the materials building blocks may be different as their size grows from the nano-regime to the micro regime and finally to bulk structures [1b]. Nanotechnology is considered as an enabling technology by which existing materials, virtually all man-made materials and systems, can acquire different properties rendering them suitable for numerous novel applications varying from structural and functional to advanced in-vivo biomedical applications [4]. Structural arrangement of atoms and the length scale of the materials are the two parameters, which when tailored properly at the nanometer scale could lead to the variation in properties of materials compared to its bulk structure [5]. Figure 1.1 shows a picture illustrating the comparison between various naturally occurring objects and man-made materials at different length scales.

In order to realize practical devices with nanomaterials utilizing their unique properties, nanoparticles with different sizes, shapes and compositions need to be synthesized. Incidentally, significant achievements have been accomplished in this regard and nanoparticles with myriad size and shapes over a wide range of compositions can be synthesized today. For the synthesis of nanoparticles researchers routinely practice either "top-down or "bottom-up" approach.

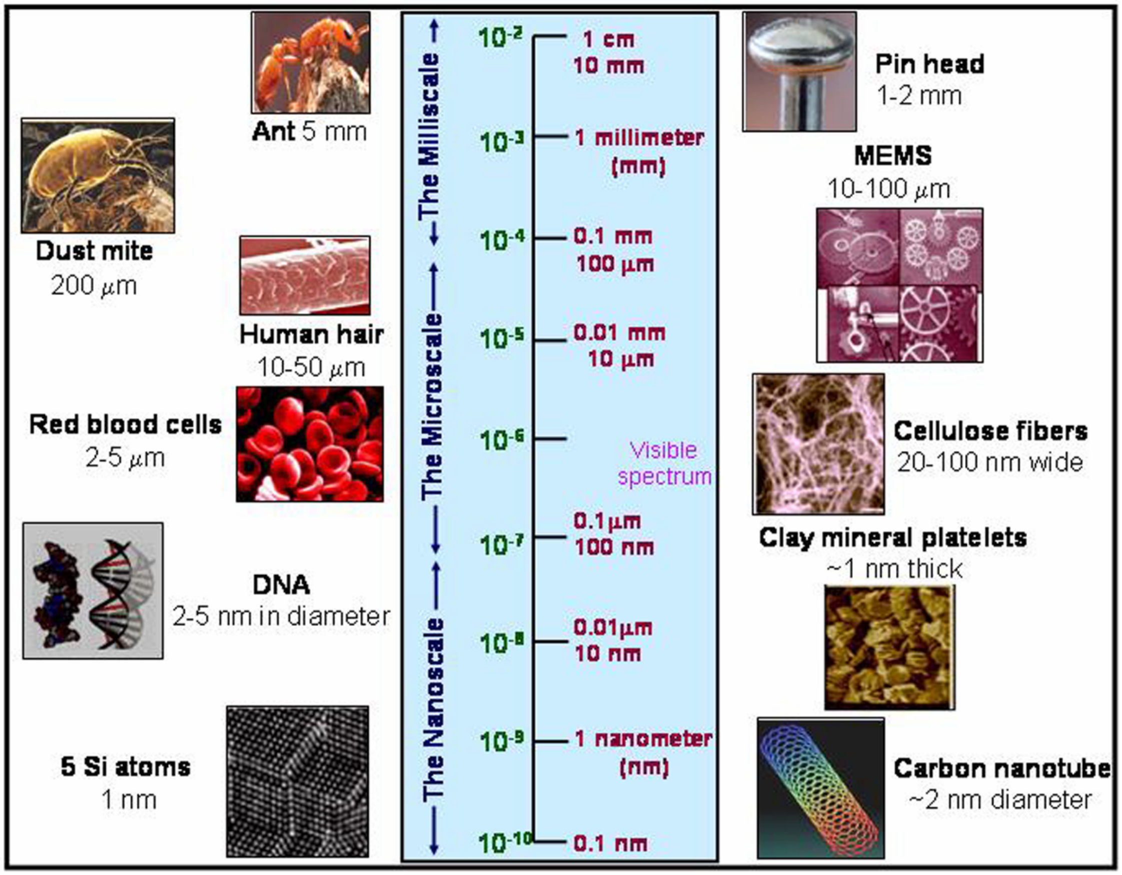

Figure 1.1 *A picture representing the relative sizes of various natural and human made objects. (courtesy- www.sustainpack.com/images).*

Figure 1.2 illustrates different structures synthesized at various length scales by top down and bottom up approaches. In the top-down approach nanoparticles are synthesized by physically slicing or by abrasion of bulk material till the desired size is achieved. This approach was practiced by Neanderthal man almost 300,000 years ago in Paleolithic period, when human race first learnt to fabricate tools [6]. In the course of evolution human being has mastered in this art by being able to realize the structure of sub-micron level using different sophisticated techniques such as laser induced chemical etching, ball milling etc [1,4].

The bottom-up approaches mainly involve chemical and biological methods to make nanostructures and nanoparticles. These processes involve controlled condensation of solute molecules that are formed during a chemical reaction. The restriction of the condensation or growth leads to the formation of particles of desired size and shape [7a]. However, unlike chemical synthesis of molecules with desired structure, the synthesis of nanomaterials with uniform size and shape is difficult. Thus, large scale synthesis of nanomaterials with specific composition, uniform size and shape still remains an arduous task.

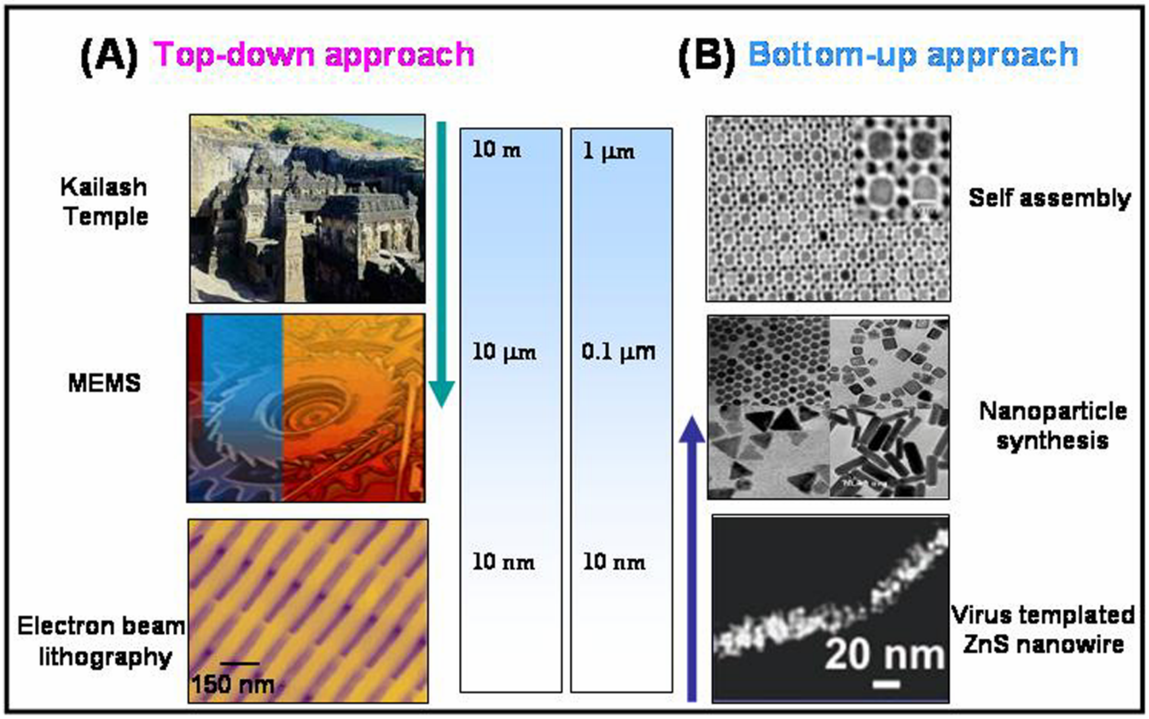

Figure 1.2 *Examples that depict the fabrication of materials at different length scales by 'Top-down' (A) and 'Bottom-up' (B) approaches. (Courtesy ref. no.[7b]). Images shown in the Top-down approach are-Kailash temple in Ellora caves, India, Micro electro mechanical structure (MEMS) and an array of Si nanostrips synthesized by electron beam lithography. Images shown in the Bottom-up approach are self assembly of iron oxide nanocrystals, Gold nanoparticles of various shapes (spheres, cubes, rods and prisms) and ZnS nanowire synthesized on virus template.*

In attempts to fabricate miniaturized devices, it has been realized that the reduction in the size of a material leads to changes in properties such as electrical conductivity, color, mechanical strength, magnetic behavior and melting point etc, those that are considered substantial in nature against their bulk counterpart [8]. Increasing knowledge about the unique properties of nanomaterials has lead to renewed interest in them for potential applications. Gold nanoparticles have been used since ancient times to impart red color to glass – a fine example is the famous Lycurgus cup that dates back to

4th century AD [9]. Although described in Roman times, the production of gold – ruby glass was not rediscovered until the seventeenth century when sizable red glass vessels were first made by adding 'Purple of Cassius', a precipitate of colloidal gold and stannic hydroxide, added to the base glass [9]. In the present days the application of nanomaterials extends to wide-ranging areas such as catalysis [10], biosensing [11], drug delivery [12], diagnostics [13], solar cell [14], optoelectronics [15], cell labeling and imaging [16], photonic band gap materials [17], single electron transistors [18], non-linear optical devices [19], and surface enhanced Raman spectroscopy [20] etc. to list a few.

An interesting aspect of nanomaterials is the number of various factors that could influence their observable properties only to make them applicable in the various aspects of our day-to-day life. The change in observable properties of nanomaterials such as color, optical and electronic behavior, and magnetic response is due to the fact that as the size approaches atomic dimensions, energy level bands are slowly transformed into quantized discrete energy levels. Since the changes in the electronic structure occur in the nanometer region, it gives an insight as to how the properties evolve from the molecular or atomic level to the bulk. Further, the reduction in size would confine the electronic motion, which will affect the physical and chemical properties of the material [21]. The change in physical properties of nanomaterials is also because of their dimensions being comparable to the de Brogilie wavelength of the charge carriers and their high surface to volume ratio [22].

One of the readily discernible properties in case of certain metal nanoparticles is their color. The color of metal nanoparticles originates from the surface plasmons i.e. coherent and collective oscillations of the surface electrons [21, 23]. The excitation of the surface plasmons by the electromagnetic field at an incident wavelength where the strong resonance occurs results in strong light scattering and the appearance of intense surface plasmon resonance bands and an enhancement of local electromagnetic fields [24]. The quantum size effects are studied well in case of semiconductor nanoparticles and the energy level spacing for the spherical nanoparticles is predicted to be inversely proportional to the square of the nanoparticle radius [25]. Thus with decreasing size the effective band-gap energy of semiconducting nanoparticle increases effecting the blue shift in observed absorption and emission spectra. Beside the optical properties, an advantageous result of the size of the nanoparticles is the large surface to volume ratio of the corresponding material compared to their bulk counter parts. Greater availability of the surface area facilitates in a number of applications such as catalysis [26], drug delivery [27] and energy storage [28].

Recorded methods for the synthesis of nanoparticles existed much before the 17th century, when ancient Hindus used powdered gold nanoparticles known as '*Suvarna bhasma*' in Ayurvedic medicine for the treatment of rheumatoid arthritis [29]. However, the method used by Hindus was cumbersome and employed a 'Top-down approach'. Therefore, Michel Faraday is considered as the first to chemically synthesize gold nanoparticles, in solution from aqueous chloroauric acid and phosphorous dispersed in CS_2 [30]. In recent times, formulation of inorganic nanoparticles with a range of compositions, sizes and shapes has been demonstrated by various physical, chemical and biological means. Some of the very successful physical methods for the synthesis of nanoparticles include photoirradiation [31], radiolysis [32], ultrasonication [33], spray pyrolysis, solvated metal atom dispersion [34], chemical vaporization [35], and electrochemical methods [36]. However, physical methods have had limited success and therefore chemical methods for the synthesis of inorganic nanoparticles are widely accepted and most commonly practiced. Inorganic nanoparticles such as metal oxides, metal and semiconducting nanoparticles can be synthesized chemically by reduction or oxidation of metal ions, or by the precipitation of the necessary precursor ions in the solution phase. The control of size, shape, stability and the assembly of nanoparticles can be achieved by incorporating different capping agents, solvents and templates. Various capping agents ranging from simple ions, to polymers to biomolecules are routinely used for the capping and stabilization of nanoparticles [37]. As a solvent, either water or non-aqueous organic solvents are used for the synthesis of nanoparticles depending on the ultimate application of nanoparticles. On the other hand, biological methods utilize nature's most efficient machines i.e. living cells for the synthesis of nanoparticles. Biological methods also involve the use of biomolecules as templates or scaffolds for synthesis and assembly of nanoparticles. Schematic in Figure 1.3 shows various strategies used for the synthesis of nanoparticles.

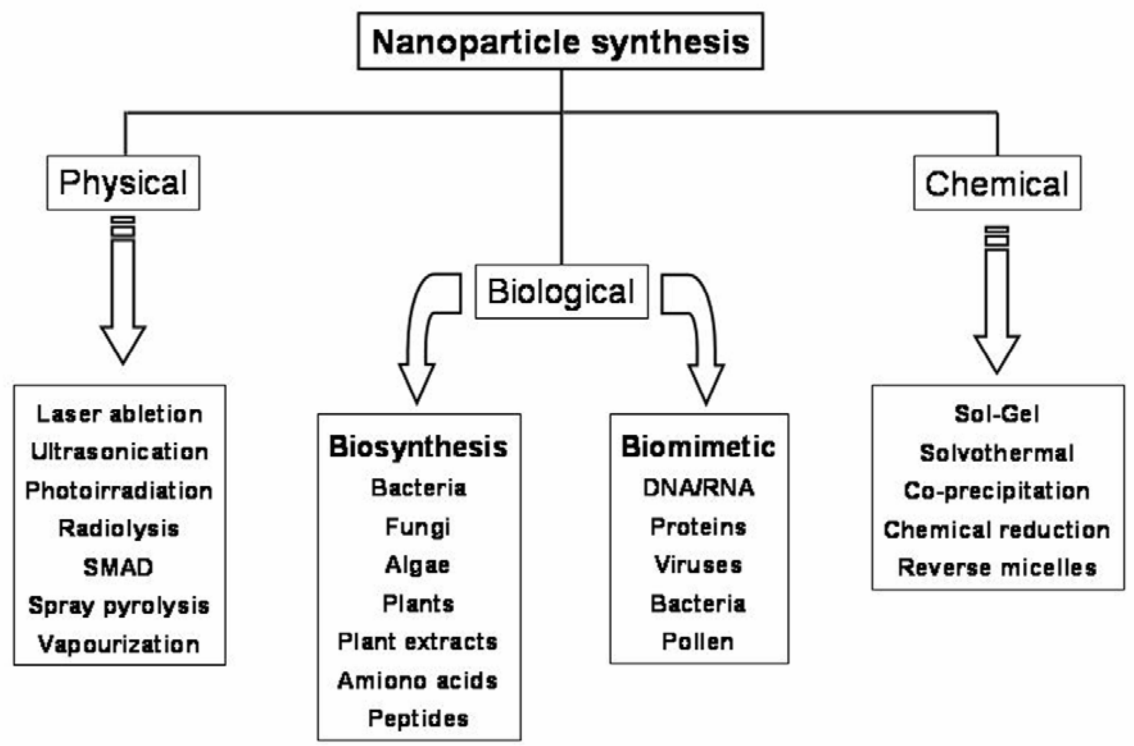

Figure 1.3 *Outline of the various approaches such as physical, chemical and biological for the synthesis of nanoparticles.*

Many soft and rigid templates such as micelles [38], polymer materials [39], DNA [40], and mesoporous materials [41] have been employed to facilitate control over the formation of desired shape, size and assembly of nanoparticles. Evidently the synthesis of nanoparticles has become important and the scope for new synthetic methods for nanomaterials preparation has been ever demanding with innovative contribution. Though the synthesis protocols have been largely dominated by physical and chemical methodologies, more recently the advantageous use of biological means for nanoparticles synthesis is gaining importance. In the following section of the chapter, various biological methods for the synthesis of nanoparticles have been described followed by a brief view of chemical synthesis protocols and the properties of material at nanometer length scale. The ever expanding horizons of nanotechnology will always demand new protocols for the synthesis of nanoparticles with different composition and dimensions. In spite of being successful in the synthesis of a range of inorganic nanostructures with myriad shapes and sizes, conventional chemistry based nanoparticle synthesis processes are often hazardous to the environment and human health. Therefore it is necessity to develop environmental friendly green chemistry based methods for the synthesis of nanoparticles. In the present thesis, an attempt has been made to describe new, green chemistry based biological protocols for the synthesis of nanoparticles such as metals, metal oxides and metal sulfides.

1.2 Biological means for the synthesis of nanoparticles

Nature has devised ingenious and elegant ways of creating the most efficient miniaturized functional materials. With evolution, living organisms have inventively succeeded in giving rise to a variety of inorganic structures. Nature knows how to build extremely specialized materials, which are constructed and indeed engineered to exert specific biological functions with maximum efficacy. The term ‘nano’ is not new for biological systems as biological reactions occur at nanoscale time range in nanomolar concentrations and involve nanometer sized biological molecules. From the nano-world of rusty proteins and magnetic compasses in bacteria to the macroscopic structures of oyster shells, corals, ivory, bone and enamel, biology has evolved a new type of chemistry that brings together the synthesis and construction of hard and soft matter for the design of functionalized inorganic-organic materials. Therefore a growing number of interdisciplinary research themes have emerged at the frontier between biology and materials science. Living organisms exhibit many remarkable examples of such integrated materials systems. Scientists and engineers have long been inspired by the beautiful structural and functional intricacy of the materials formed within living organisms. Biological methods for synthesis of nanoparticles employ use of living organisms, molecules of biological origin such as peptides and biological templates such as DNA. Out of these, biomineralization of inorganic materials has been explored in great detail in certain living organisms.

1.2.1 Biosynthesis of nanomaterials by living organisms

Living organisms, especially micro-organisms have a remarkable ability to form exquisite inorganic structures often in nanodimensions. This ability of living creatures has lured material scientists towards these biological systems to learn and improve the skills for the precise fabrication of nanomaterials at ambient conditions. There exist several examples in biological systems demonstrating not only the efficient synthesis of macroscopic materials like bones and teeth with precise positioning [42] but also in making functional structures in mesoscopic and nanometer dimensions. Generally synthesis of inorganic nanomaterials by living creatures has been classified in two categories such as – biologically controlled synthesis and biologically induced synthesis [43]. Biologically controlled synthesis of inorganic materials can often be considered as biomineralization as it is known to occur naturally in few specific organisms. Biogenic nanomaterials commonly have attributes which distinguish them from their inorganic counterparts. Large variety of inorganic nanomaterials synthesized by different living organisms is listed in Table 1.1.

The vast array of organisms are now known to synthesize inorganic materials and more than 60 different biogenic minerals have been identified to date [43], most of them are calcium carbonates, calcium phosphates, silicates, iron oxides and iron sulfides [44]. Unicellular organisms such as bacteria and algae also are capable of synthesizing inorganic nanomaterials, both intra- and extracellularly. Biologically controlled synthesis of inorganic materials has been studied in great detail. However it is only recently realized that biologically induced or deliberate synthesis of nanomaterials can be an outcome of biotechnological applications such as remediation of toxic metals occurring by reduction of metal ions or by formation of insoluble complexes with the metal ion in the form of nanoparticles [45].

During biologically controlled synthesis of inorganic materials, inorganic phases grow within or on organic matrix or vesicles inside the cell, allowing the organism to exert a strict control over the composition, grain size, habit, and intracellular or surface location of the produced minerals [43, 46]. Examples of such synthesis include silica biosynthesis in diatoms [47], sponges [48] and radiolarians [49], calcareous structures in coccoliths [50], gypsum in S-layer bacteria [51] and the nanocrystals of magnetite and greigite in magnetotactic bacteria [52]. Figure 1.4 shows images of some of the above mentioned exquisite structures obtained by biologically controlled synthesis of nanomaterials. The confinement of mineralization of silica and calcium carbonate leading to various exotic porous shells or aligned structures has been explained to be directed by the geometric patterning of the vesicles in the cells [53]. Biosilicification in diatoms and sponges has been facilitated by small peptides – silafins [54] and silicatein [55] respectively at the molecular level. However, few other peptides such as frustulins [56] and pleurolins [57] have been identified to play a crucial role in the formation of biosilica.

Table 1.1 Biosynthesis of various nanomaterials by various organisms

Biogenic nano/meso structures		Formula	Organism	Location
Carbonates	Calcite, aragonite, vaterite, amorphous $CaCO_3$, Mg-calcite, Siderite etc.	$CaCO_3$, (Mg,Ca) CO_3, $CaCO._nH_2O$, Fe_2CO_3	Marine organisms, Aves, Plants, Mammals	Shell, Exoskeleton, Teeth, Bones, Leaves, Cell surface
Phosphates	Hydroxylapetite, dahllite, amorphus ferric phosphate, Francolite	$Ca(PO_4)$, $Ca(PO_4)_6OH_2$ $Fe(PO_4)$	Vertibrates, Fish, Mammals, Molluscs, Chordates, Annelids	Bone, Teeth, Scales, gills,cell surface
Oxalates	Whewellite, Weddelite	$CaC_2O_4.H_2O$ $CaC_2O_4.2H_2O$	Plants, Fungi, Mammals	Leaves, Hyphae, Gall bladder
Halides	Fluorite, Amorphus fluorite	CaF_2	Molluscs, gastropods, Echinoderms	Teeth
Oxides	Iron oxides, silica, titania, zirconia	Fe_3O_4, FeOOH, SiO_2, TiO_2, ZrO_2	Bacteria, Mammals, Sponges, Diatoms, Radiolarians, Fungi, Plants	Magnetosomes, Extracellular environment, Cell wall, Ferritin, Leaves, Spicules
Sulfates	Gypsum, celestite, barite	$CaSO_4.2H_2O$, $SrSO_4$, $BaSO_4$	Jellyfish, Protozoa, Fungi	Statoconia, Intracellular, Extracellular
Sulfides	Iron sulfide, cadmium, zinc and lead sulfide	FeS_2, Fe_3S_4, CdS, ZnS, PbS	Bacteria, Yeast, Fungi, Plants	Magnetosomes, Intracellular, Extracellular
Metals	Gold, Silver, Selenium	Au, Ag, Se	Bacteria, Fungi, Plants	Extracellular, Intracellular

Silafins and silicateins isolated from diatoms cell wall and sponge spicules are demonstrated to induce *in vitro* formation of silica by hydrolyzing silicic acid or tetra ethoxy orthosilane (TEOS) [54, 55]. $CaCO_3$ is one of the most abundant biominerals formed by living organisms. $CaCO_3$ based biomaterials such as nacre of mollusc shell

[58] and coccoliths [50] have complex structures of nano to submicron length scales. Calcite crystals mineralized by holococcoliths are generally extracellular and of simple rhombohedral or prismatic forms, whereas, in heterococcoliths the morphologies are quite complex and species specific occurring intracellularly. Biological molecules like proteins are found to be associated with the surface of $CaCO_3$ biominerals [58].

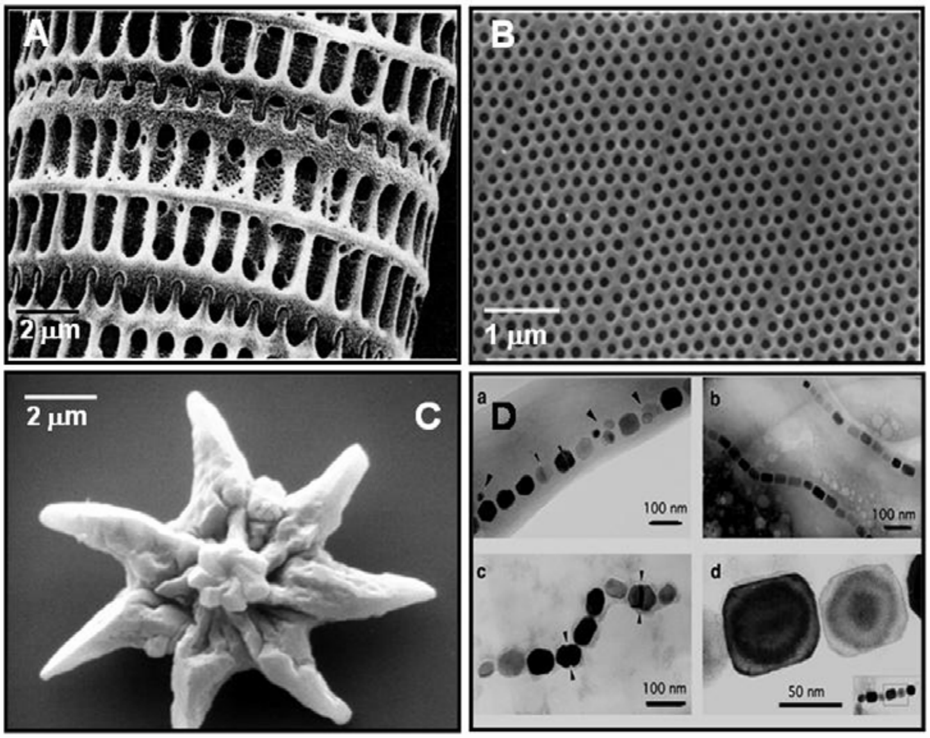

Figure 1.4 *Images of various inorganic nano materials obtained by biologically controlled synthesis. (A) diatomic silica (B) siliceous exoskeleton of radiolarian (C) calcareous structures in coccolith and (D) magnetite nanocrystals from magnetotactic bacteria. Image courtesy reference [43]*

The mineral-associated proteins like macromolecules are responsible for initiating and stabilizing non-equilibrium crystal polymorphs and morphologies through interactions between anionic moieties and cations in solution or at mineral surfaces. Little is known regarding the molecular mechanism responsible for the transport of Ca^{2+} ions and HCO^{3-} or CO^{3-} ions required for the mineralization of $CaCO_3$. Calcite minerals have been shown to be associated with polyanions and acidic proteins and polysaccarides [59].

Magnetite, a ferrimagnetic oxide of iron is synthesized in the nanocrystalline form by many living organisms. Magnetotactic bacteria and iron reducing bacteria are naturally known to precipitate magnetite nanocrystals [43]. Besides bacteria, unicellular algae- Euglena [60], dinoflagellates, as well as higher animals such as salmon [61], butterfly [62], army ants [63], pigeons [64], and even human brain [65] mineralize magnetite nanoparticles. Synthesis of magnetite has been thoroughly investigated in magnetotactic bacteria and to some extent in iron reducing bacteria. The magnetotactic bacteria are a heterogeneous group of fastidious prokaryotes that display a myriad of cellular morphologies including coccoid, rod shaped, vibriod, helical and even multicellular [66]. Magnetotactic bacteria synthesize magnetite or greigite nanocrystals arranged in the linear fashion surrounded by phospholipid membrane bound vesicles known as magnetosomes [67]. Magnetite and greigite crystals are typically 35 to 120 nm long and are within the permanent single domain size range for both minerals and is large enough to align them in the Earth's magnetic filed of 50 μT, overcoming the thermal forces [68]. In most of the cases the accumulated iron content in magnetotactic bacteria is observed to be in the range of 3-10 % of dry bacterial biomass [68]. The magnetite crystals synthesized by magnetotactic bacteria have high chemical purity, narrow size distribution, specific arrangement within cell and species specific crystal morphology. The crystal morphologies found in magnetotactic bacteria have been classified as cubooctahedral, pseudohexagonal, elongated prismatic and tooth, arrowhead or bullet-shaped all having the cubic face centered lattice of magnetite [68].

The molecular mechanism of magnetite synthesis in magnetotactic bacteria is a complex, multistep process, which includes magnetosome vesicle formation, iron transport and magnetite crystallization. Biochemical and genetic analysis of magnetite crystallization has been studied in detailed in *Magnetospirillum magneticum* AMB-1 by Matsunaga and coworkers [69]. The first event in the magnetite formation is the formation of magnetosome vesicles. Invagination of cytoplasmic membrane is initiated by magnetosome membrane specific GTPase (also called as Mms 16, one of the proteins associated with bacterial magnetic particles) to form the intracellular vesicle. The second process of magnetite formation is iron transport into magnetosome vesicle. This step is facilitated by iron chelating siderophores and iron reductases. The ferric iron is reduced on the cell surface, taken into the cytoplasm and transported into the magnetosome vesicle. Mag A protein encoded by mag-1 gene is thought to be responsible for ferrous ion transport in magnetosome. Finally in the last step ferrous ions are oxidized, dehydrated and precipitated to produce magnetite. However, the last step of magnetite precipitation still remains unclear.

Another group of bacteria known as iron reducing bacteria has been found to produce magnetite crystals extracellularly [70]. Iron reducing bacteria generally precipitate ultra-fine magnetite granules under strictly anaerobic conditions. However, unlike magnetotactic bacteria, iron reducing bacteria synthesize magnetite for energy generation to support metabolism and growth. Magnetite is synthesized by coupling the oxidation of organic mater to the reduction of ferric iron during bacterial metabolism [71]. Generally, most of the iron reducing bacteria utilize poorly crystalline ferrihydrite as an electron acceptor which in turn is reduced to magnetite.

Similar to the biosynthesis of silica, magnetite and calcium carbonates, biomineralization of MnO_2 and gypsum has shown to occur on the S-layer of photosynthetic bacteria [72] and the occurrence of zinc-iron sulfide within the body of hydrothermal vent worms *Alvinella pompejana* [73]. Marine sulfate reducing bacterial biofilms of the family *Desulfobacterioceae* are known to synthesize micron sized spherical aggregates of sphalerite nanocrystals of ZnS, which are 2-5 nm in diameter [74]. However, very little is known about the biological mechanism of sphalerite formation. More recently, Reith and co-workers have shown extracellular biomineralization of gold ions into elemental form by the bacterial biofilms of Ralstonia [75]. In this report, bacterioform gold nanoparticles in the form of aggregates of ~ 100 nm have been demonstrated to be associated with exopolymers synthesized by bacteria.

Although, there are numerous reports on naturally occurring biological synthesis of inorganic materials by living organisms, recently, micro-organisms have been induced to synthesize different inorganic materials such as simple metallic nanoparticles to more complex sulfide and oxide nanoparticles. This route of biological synthesis of nanoparticles has been realized only recently, when micro-organisms were used for the bioremediation of toxic metal ions. During the deliberate or biologically induced synthesis of inorganic materials, organisms modify its ambient microenvironment and create conditions suitable for extracellular precipitation of minerals. Deliberate synthesis of inorganic nanoparticles is possible because of the specific resistant mechanism exerted by micro-organisms against the high metal ion concentration. At higher concentration of metal ions micro-organisms can cope with the toxic effect of metal ions by one of the defense mechanisms such as effluxing of metal ions by efflux pumps, alteration in the solubility of metal ions, alteration in redox state, extracellular compelxation and extracellular precipitation of metal ions etc [76].

Lately, material scientists have looked upon the detoxification of metal ions occurring by their reduction or complexation by micro-organisms for the synthesis of nanoparticles. Thus micro-organisms can be considered as living, eco-friendly nanofactories. Though biologically controlled mineralization or the synthesis of inorganic nanomaterials exerts tight control over the size, shape and composition of nanoparticles it is restricted to the synthesis of limited number of nanoparticles with different composition. On the other hand deliberate or induced biological synthesis of inorganic nanomaterials has wide range of composition. Various nanomaterials from simple metals, to more complex systems such as metal sulfides and metal oxides can be synthesized by the deliberate synthesis of nanomaterials using micro-organisms [45]. Novel methods for the synthesis of inorganic nanomaterials can be designed by using deliberate synthesis of inorganic nanomaterials by micro-organisms.

Beveridge and co-workers have demonstrated the synthesis of gold nanoparticles on the cell surface of the bacterium *Bacillus subtilis* by incubation with gold ions [77]. The deposition of gold nanoparticles was believed to occur by stoichiometric interaction between soluble metal ions and the reactive chemical groups of bacterial cell surface followed by their nucleation into elemental form leading to further accumulation of metal in non-stoichiometric amount. Klaus and co-workers have demonstrated the biosynthesis of silver nanoparticles using the bacterium *Pseudomonas stutzeri* AG 259 isolated from silver mine. It has been demonstrated that the bacterium intracellularly synthesizes silver nanoparticles with distinct size and morphology within the periplasmic space when cultured in the presence of silver ions [78]. The metallic silver synthesized by the bacterium was reported to be about 5 % of total bacterial dry mass. Further, it has been demonstrated that, silver nanoparticles after isolation and film formation on aluminium substrate followed by heat treatment could make materials with typical cermet properties [79]. These materials with interesting optical properties prepared by convenient low-cost method have been proposed to have technical application as coating for effective photothermal conversion of solar energy. Similarly Nair and Pradeep have demonstrated the formation of gold, silver and gold-silver alloy by exposing gold and silver ions to *Lactobacillus* strains isolated from buttermilk [80]. The extent of metal deposition by *Lactobacillus* was found to be ~ 35 % of bacterial dry mass. Yong *et al* have demonstrated the synthesis of palladium nanoparticles ~ 20 nm in size using a bacterium *Desulfovibrio desulfuricans* [81]. It was argued that Pd^{2+} bioreduction is an enzymatically accelerated process in which activation energy for nucleation in biological environment could be lowered by reducing the interfacial energy. The target ions form crystal nuclei, interacting initially with the localized surface binding sites, and reduction probably occurs via H^+ using the reducing power of hydrogenase activity. It was assumed that Pd^{2+} crosses the outer membrane of the bacterial cell and is probably reduced by a periplasmic hydrogenase enzyme. The biogenic Pd nanoparticles could be used for catalysis applications as efficiently as chemically synthesized Pd nanoparticles [81].

In an attempt to make biosynthesis of metallic nanoparticles competent with chemical synthetic route, Sastry and co-workers have shown the synthesis of fairly monodisperse nanoparticles of gold using a thermophilic actinomycete *Thermomonospora* sp. [82]. Biosynthesis of selenium nanospheres have been demonstrated by Oremland and co-worker using selenium respiring, haloalkaliphilic bacteria *Bacillus selenitireducens* [83]. Recently Lengke and co-workers have demonstrated the synthesis of gold nanoparticles with different morphologies using filamentous cyanobacteria *Plectonema boryanum* UTEX 485 [84]. Lengke and co-workers have also demonstrated extracellular and intracellular biosynthesis of platinum nanoparticles by exposing the same bacterium to platinum ions [85]. Reductive precipitation of gold nanoparticles has been shown to occur in dissimilarity iron reducing bacteria and archaea by Lovley *et al* [86]. They have postulated the presence of an enzyme Au (III) reductase in anaerobic Fe (III) reducing bacteria that carry out the reductive precipitation of gold nanoparticles.

Besides metal nanoparticles, bacteria and yeast have been shown to synthesize semiconductor sulfide nanoparticles. Nanocrystalline quantum dots of CdS have been synthesized intracellularly using two different yeasts species *Candida glabrata* and *Schizosaccharomyces pombe* by Dameron and co-workers [87]. Recently, biosynthesis of nanocrystalline CdS and subsequent fabrication of diode using biogenic CdS have been shown to occur in the yeast *S. pombe* [88]. Kowshik and co-workers have demonstrated intracellular biosynthesis of PbS nanocrystallites using the yeast *Torulopsis* sp. by reacting with aqueous lead ions [89]. Bacterial species have long been explored for the synthesis of inorganic sulfides. Sulphate reducing bacteria use inorganic sulfate for cellular respiration and generates energy for bacterial growth and metabolism. In doing so inorganic sulfates act as a terminal electron acceptor and are converted into respective sulfides. A bacterial species *Klebsiella planticola* Cd-1 has been shown to synthesize CdS nanoparticles in high quantity under anaerobic conditions [90]. An enzyme thisulfate reductase produced by bacterial cells has been shown to be responsible for the synthesis of CdS. Also biosynthesis of CdS has been shown to occur by *Klebsiella pneumoniae* [91]. In this case an enzyme cysteine desulfydrase converts cysteine into H_2S, which in turn reacts with Cd^+ ions to form CdS. Recently Belcher and co-workers have shown biosynthesis of nanocrystalline CdS using *E. coli* [92].

In an attempt to pursue newer "green chemistry" based biological methods, Sastry and co-workers have demonstrated that other than prokaryotic organisms, such as bacteria, eukaryotic organisms like fungi can play an efficient role as living nanofactories for the synthesis of different inorganic nanoparticles. In their pioneering work gold nanoparticles have been synthesized using two different fungi *Verticillium* sp. [93] and *Fusarium oxysporum* [94] respectively. Similarly, exposing the biomass of *Verticillium* sp. [95] and *F. oxysporum* [96] to aqueous silver ions resulted in the formation of silver nanoparticles. While the bioreduction of metal nanoparticles in case of *Verticillium* sp. was observed to be intracellular, exposure of gold and silver ions to *F. oxysporum* biomass resulted in extracellular synthesis of respective metal nanoparticles. Extracellular biosynthesis of metal nanoparticles can be advantageous from large scale synthesis point of view, since nanoparticles can be readily isolated and purified from the reaction solution. Later, it was demonstrated that gold-silver alloy nanoparticles with varying concentrations can be extracellularly synthesized by *F. oxysporum* [97]. Further, Sastry and co-workers have comprehended their preliminary results for the synthesis of more complex inorganic nanoparticles like metal sulfides and metal oxides using *F. oxysporum*. Semiconductor nanoparticles of CdS were successfully obtained after exposure of aqueous $CdSO_4$ solution to the biomass of *F. oxysporum* [98]. Synthesis of oxide nanoparticles like silica, titania and zirconia was shown to occur from respective anionic metal salts using the fungus *F. oxysporum* [99]. Specific proteins induced in the presence of anionic metal ion precursors were found to be responsible for the hydrolysis of respective metal ion complexes resulting in the synthesis of respective oxide nanoparticles.

From the above discussion it is realized that the deliberate synthesis of inorganic nanoparticles through biological route is largely focused on the use of micro-organisms only. However it is observed that even plants are capable of biomineralization of many inorganic materials. The most commonly available biominerals in plants are $CaCO_3$, CaC_2O_4 (calcium oxalate), and silica [100] are usually synthesized by the plant species of cactaceae family. In certain species of cactaceae family silica is found to be present in the form of opal or quartz [101]. Silica is also observed to be present in grasses [102]. Botanically originated ~ 4 nm magnetite nanocrystals were isolated from the disrupted cells of grass plant growing in iron-rich soil [103]. Most of magnetite nanocrystals were reported to be cubo-octahedral shaped with small percentage of prismatic morphologies. Magnetite nanocrystals synthesized by botanical route were an order of magnitude much smaller than their bacterial counterpart. Botanical magnetite nanocrystals are self-organized, in ordered micrometer sized agglomerates [103] distinct from the linear chain like arrangement of magnetite in magnetotactic bacteria. A number of plant species are known to accumulate and subsequently reduce gold ions within their tissues in large percentage. *Equisatum* (horsetail) has been shown to accumulate elemental gold within its biomass by the secretion of free cyanide within their tissue, which helps in keeping the elemental gold in solution form [104].

It would be interesting therefore, to explore plants as a means for the synthesis of metal nanoparticles analogous to the use of micro-organisms for their synthesis. In fact, Jose-Yakaman and co-workers have demonstrated the synthesis of gold and silver nanoparticles within the different parts of live alfalfa plant after the exposure to the respective metal ion solution [105]. In an endeavor to expand the successful demonstration of the synthesis of metal nanoparticles based on the foundation of above-mentioned observations, Sastry and co-workers have developed a novel, botanical route for the synthesis of metallic nanoparticles. Aqueous extracts from plants like geranium (*Pelargonium graveolens*), and neem (*Azadirachta Indica*) have been used for the synthesis of gold, silver and gold-silver bimetallic nanoparticles [106]. Plant based methods for the synthesis of metallic nanoparticles can also be used for the shape directed synthesis of prism shaped gold nanoparticles. High percentage of prism shaped gold nanoparticles could be synthesized using lemon grass (*Cymbopogan flexuosus*) leaf extract [107 a]. It has been further demonstrated that the edge length and the optical properties of gold nanotriangles can be tuned by varying the concentration of leaf extract used for the reduction of gold ions [107 b]. Synthesis of triangular gold nanoparticles has also been demonstrated by using *Aloe vera* plant extract [108 a]. Liu and co-worker have also demonstrated the synthesis of high percentage of single-crystalline triangular gold nanoparticles using the extract of the brown sea weed *Sargassum* sp. [108 b].

1.2.2 Biological synthesis of nanoparticles: biological macromolecules and biomimetics

The previous section of this chapter described the synthesis of inorganic nanoparticles by means of living organisms. In an attempt to learn nature’s elegant architectural skills and precision offered during the fabrication of inorganic materials, biological processes offer a lot. Synthesis of inorganic nanomaterials can be effected by using different biomolecules. One of the fundamental process involved in the regulation of mineral deposition in biological organisms is the organic matrix composed of proteins or other biological macromolecules that controls the nucleation and growth of inorganic structures. Realization of this fact has led many materials scientists to explore proteins identified from biomineralizing organisms as ‘enzymes’ for materials synthesis *in vitro*. In such systematic attempts a limited success has been achieved in synthesizing inorganic nanoparticles with specific compositions, sizes and shapes. Since, proteins are known to initiate, catalyze and fabricate nano/micro structures, attempts have been made to synthesize various nanostructures using the proteins isolated from biominerals, with which they are associated. Some well studied examples include silica formation by silicateins [109 a], silaffins [109 b] and silica precipitating peptides [109 c]. Silicatein-α, a major filamentous protein associated with the spicules of demosponge *Tethya aurantia* has been explored for the synthesis of titania and gallium oxide nanocrystallites [110].

Mehra and coworkers have demonstrated the synthesis of semiconductor quantum dot nanoparticles using phytochelatin peptides [111]. Aizenberg and coworkers have successfully synthesized complex and varying morphological crystal forms of calcite nanocrystals using acidic proteins isolated from abalone nacre [112].

Recently, a new biological approach for design of inorganic nanomaterials has been developed, wherein small peptide molecules with high specificity towards particular inorganic moiety is designed by combinatorial phage display library. Though the method is rather cumbersome, it is extremely successful in synthesizing certain inorganic nanoparticles due to the ability to identify a specific atomic composition, crystallographic orientation, or morphology of an inorganic entity [113]. Highly stable gold nanoparticles with desirable chemical properties in aqueous media have been synthesized using gold binding peptide [114]. Similarly synthesis of anisotropic structures of silver and their patterning has been demonstrated using silver binding peptides identified by combinatorial phage display library [115]. Recently, directed synthesis of magnetic and semiconductor nanowires has been shown to occur using peptides isolated by phage display, and selected by evolutionary screening process [116]. Similar strategy has been adopted for the synthesis of iron oxide nanoparticles by iron oxide binding peptides isolated from bacterial peptide display technology [117].

Material scientists are trying to learn from nature to develop new synthetic materials with sophisticated properties. Attempts to adopt/utilize the constructional principles of natural materials have acquired the term biomimetics: the art of mimicking biology [118]. Inspirations from natural, bioinorganic structures have leid the foundations of this very science, in which materials scientists are trying to fabricate nanostructures with the precision of nature's flawless architectural skills that far exceed present anthropogenic capacities. Most of the work in this direction has been facilitated by the systematic use of biological structures that act as templates for the synthesis of nanomaterials with complex morphologies. The reproducible formation of nanoparticle arrays in large scale with predefined lattice spacing and symmetries is very important for the development of future nanoelectronics. Biomolecular templating can be very helpful in this regard, as the self assembly of molecules into molecular arrays is an intrinsic property of many biological molecules. Bacterial cell surface [118], viruses [119], DNA

[120], proteins [121] and small peptides [122] and even pollen grains [123] have been used for the synthesis of nanostructures with variety of compositions, size and shapes.

Biological polymers are used as frameworks for the formation of inorganic structures such as calcium carbonates, hydroxyapetite, iron oxide and silica [124]. Douglas and co-workers have successfully employed S- layer of *Deionococcus radiodurans* for the synthesis of ordered arrays of oxides and magnetic nanoparticles [125]. Further, Sleytr and co-workers have demonstrated the use of bacterial S-layer in the formation of supramolecular structures of metals and semiconductor nanoparticles [125]. In this study ordered array of gold nanoparticles with uniform size of 4 nm has been synthesized by the templating action of bacterial S-layer with square lattice symmetry. DNA has also been used for the synthesis of nanowires of metals [126] and semiconductors [127]. Mann and coworkers have demonstrated the formation of superparamagnetic, monodisperse iron oxide nanoparticles such as magnetite and maghaemite and semiconductor nanocrystallites such as CdS using iron storage protein-Ferritin [128 a,b]. Additionally, extending their work, Mann and coworkers have synthesized CoPt nanoparticles and films with promising potential in ultra-high density data storage [128 c]. In recent contribution, an enzyme lumatin synthase has been used to synthesize iron oxide nanoparticles with an average diameter of 8 nm [128 d]. DNA, the carrier of genetic information in all living organism is also a versatile material for designing nanometer-scale structures. DNA can be used as an ideal template for the synthesis of nanoparticles due to some key features such as: inherent nanoscale dimensions, high specificity exerted towards inorganic materials and structural flexibility to build a programmable assembly [129]. Due to the above-mentioned indigenous properties, DNA has been indeed used for the synthesis of conductive metallic wires [126] Also, nanowires of the semiconducting quantum dot nanocrystallites have been synthesized using double stranded DNA [130 a]. Furthermore, DNA has been used as a template for the synthesis of nanowires of wide band-gap semiconductor, zinc oxide [130 b]. Fabrication of ordered nanomaterials superstructure has been demonstrated using DNA as designer templates [130 a].

Virus particles are another type of biological structure that can be applied as a biotemplate for synthesis of nanomaterials. Tobacco mosaic virus (TMV) has been demonstrated to synthesize semiconductor nanocrystalline CdS and ZnS nanoparticles with mean diameter of 5 nm and 30 nm respectively [119]. The TMV particles have also been subjected to the synthesis of uniform film of magnetite composed of fine nanoparticles with 2 nm diameter [131 a]. Furthermore cowpea chorotic mottle virus and cowpea mosaic virus have been used as nucleation cages for the mineralization of inorganic materials [131 b]. Besides viruses, protein-protein interactions have been used for organization and the assembly of nanoparticles. Streptavidin-biotin interaction has been used for uniform organization of gold nanoparticles separated by a minimum distance of 4 nm [132]. In a novel biomimetic approach for the fabrication of nanomaterials, Mann and coworkers have demonstrated the use of pollen grains as a biological template for the synthesis of silver and $CaCO_3$ nanoparticles [123].

Thus, in addition to supplying useful materials in their own right, the living world provides endless inspiration for the design of synthetic materials with sophisticated structure and function. Therefore, biological inspirations towards the development of novel experimental procedures for the reproducible synthesis of nanomaterials of controlled size, chemical composition and shape are becoming an integral part of nanotechnology. The strength of biological synthesis methods for designing nanomaterials can be realized by various types of nanomaterials synthesized by different living organisms as discussed above. Though, biological means of nanoparticles synthesis is in its infancy and far from the ease offered by chemical synthesis protocols, growing research in this direction would render biological synthesis methodologies as competent as chemical methods of nanomaterials synthesis. Also, nanomaterials formed by biological systems ranging from biological molecules to biological cells are extremely fine examples of organic-inorganic hybrid materials with unique properties.

1.3 Physical and chemical means for nanoparticles synthesis

1.3.1 Physical synthesis methods

(1) Evaporation methods: Physical vapor deposition (PVD), sputtering and chemical vapor deposition (CVD) are the commonly used methods to form thin films of inorganic nanomaterials [133]. PVD involves condensation from the vapor phase. The PVD process is composed of three main steps: (a) generating a vapor phase by evaporation or sublimation of the material, (b) transporting the material from the source to the substrate, and (c) formation of the particle and/or film by nucleation and growth. Different techniques have been used to evaporate the source such as electron beam, thermal energy, sputtering, cathodic arc plasma, and pulsed laser. Si nanowire, GeO_2 nanowire, Ga_2O_3 nanowire, ZnO nanorod, GaO nanobelt and nanosheet, SnO2 nanowire, nanoribbon, nanotube, etc., have been synthesized using PVD. In CVD, the carrier gases containing the elements of the desired compound flow over the surface to be coated. This surface is heated to a suitable temperature to allow decomposition of the carrier gas and to allow the mobility of the deposited atoms or molecules on the surface. The CVD process consists of three steps: (a) mass transport of reactants to the growth surface through a boundary layer by diffusion, (b) chemical reactions on the growth surface, and (c) removal of the gas-phase reaction byproducts from the growth surface. In sputtering a discharge of non reactive ions such as argon is created which fall on the target and break the surface atoms, which are collected on the surface to be coated.

***(2) Solvated metal atom deposition (SMAD)*: ** Most metals vaporize as atoms, which are highly reactive as a result of the input of the heat of vaporization and the lack of steric interactions. The basic strategy in this process is to co–deposit the metal atoms with a large excess of reactant, thereby promoting reaction between the metal atom and the substrate and suppressing recombination to the bulk metal. In SMAD, a bulk metal is evaporated under vacuum and the vapors of the metal are co-condensed with vapors of organic solvents like acetone to form nanoparticles in solution using a physical method [134]. Evaporation of metal is achieved by electrically heating a metal wire under vacuum. The resulting solution would consist only of colloids and solvent with no byproducts of gold salt. Polar protic or aprotic solvents yield generally stable colloids but those with nonpolar organic solvents and water yielded large gold particles that undergo irreversible precipitation. SiO_2, Co-Mn and Pt-Sn alloys, metallic nanoparticles like Au etc have been synthesized using SMAD.

(3) Laser ablation: When intense laser pulses are focused on a metal target, metal atoms present in the exposed region will be desorbed. In a Laser ablation experiment, a bulk metal is immersed in a solvent containing surfactant. During the laser irradiation, the metal atoms will vaporize and are immediately solvated by the surfactant molecules to form nanoparticles in solution [135]. The intensity of the laser pulse and time of exposure are two parameters, which control the size of the nanoparticles formed during laser ablation. Metal nanoparticles such as gold, silver and platinum nanoparticles are prepared by this way with good control over size.

(4) Photolytic and radiolytic methods: These methods involve the reduction of metal salts by radiolytically produced reducing agents such as solvated electrons and free radicals and the photolysis of metal complexes in the presence of some donor ligands [136]. Radiolysis of aqueous solutions of metal ions gives solvated electrons that may directly react with the metal ions or with other dissolved materials to produce secondary radicals, which then reduce the metal ions to form nanoparticles. Alcohols are known to form radicals when they are irradiated with UV light. Radicals thus generated by this way can reduce the metal ions to form nanoparticles when UV light is irradiated on mixture of aqueous metal ions and alcohols metallic nanoparticles like gold and silver has been synthesized by this method.

1.3.2 Chemical synthesis methods

(1) Sol-gel method: The sol-gel method is based on inorganic polymerization reactions. The sol-gel process includes four different steps: hydrolysis, polycondensation, drying, and thermal decomposition [137]. Precursors of the metal or nonmetal alkoxides hydrolyze with water or alcohols according to the hydrolysis process

$$\mathrm{M(OR)}_x + m\mathrm{H_2O} \rightarrow \mathrm{M(OR)}_{x-m}\mathrm{(OH)}_m + m\mathrm{ROH}$$

where if m is up to x, the reaction is total hydrolysis, followed by either a water condensation or alcohol condensation. In addition to water and alcohol, an acid or a base can also help to hydrolyze the precursor. In the case of an acid, a reaction takes place between alkoxide and the acid.

$$\text{-M-OR} + \text{AOH} \rightarrow \text{-M-O-A} + \text{ROH}$$

After the solution has been condensed to a gel, the solvent must be removed. Higher temperature calcination is needed to decompose the organic precursor. The size of the sol particles depends on the solution composition, pH, and temperature. By controlling these factors, one can tune the size of the particles. This method has been used to synthesize metal oxide nanostructures, such as TiO_2, UO_2, TnO_2, ZrO_2, CeO_2, SnO2, SiO_2, CuO, SnO_2, ZnO, Al_2O_3, Sc_2O_3, $ZnTiO_3$, $SrTiO_3$, $BaZrO_3$, $CaSnO_3$, and other nanostructures.

(2) Chemical precipitation: During the synthesis of inorganic nanoparticles by chemical precipitation method, the kinetics of nucleation and particle growth in homogeneous solutions can be adjusted by the controlled release of anions and cations. Careful control of precipitation kinetics can result in monodisperse nanoparticles. Once the solution reaches a critical supersaturation of the species forming particles, only one burst of nuclei occurs. Thus, it is essential to control the factors that determine the precipitation process, such as the pH and the concentration of the reactants and ions. Organic molecules are used to control the release of the reagents and ions in the solution during the precipitation process. The particle size is influenced by the reactant concentration, pH, and temperature. By engineering these factors, nanoparticles with narrow size distributions, such as $Zr(OH)_4$, Ba-TiO_3, $YBaCu_3Oy$, CdS, HgTe, and CdTe, have been produced. Although the method of using precipitation to prepare nanoparticles is very straightforward and simple, very complicated nanostructures can also be constructed using this method such as CdS/HgS/CdS, CdS/$(HgS)_2$/CdS and HgTe/CdS quantum well systems and other core/shell structures [137].

(3) Hydrothermal synthesis: Hydrothermal synthesis is a common method to synthesize zeolite/molecular sieve crystals [133, 137]. This method exploits the solubility of almost all inorganic substances in water at elevated temperatures and pressures and subsequent crystallization of the dissolved material from the fluid. Water at elevated temperatures plays an essential role in the precursor material transformation because the vapor pressure is much higher and the structure of water at elevated temperatures is different from that at room temperature. The properties of the reactants, including their solubility and reactivity, also change at high temperatures. The changes mentioned above provide more parameters to produce different high-quality nanoparticles and nanotubes, which are not possible at low temperatures. During the synthesis of nanocrystals, parameters such as water pressure, temperature, reaction time, and the respective precursor- product system can be tuned to maintain a high simultaneous nucleation rate and good size distribution. Different types of oxides and sulfides nanoparticles such as TiO_2, $LaCrO_3$, ZrO_2, $BaTiO_3$, $SrTiO_3$, $Y_2Si_2O_7$, Sb_2S_3, CrN, α-SnS_2, PbS, Ni2P, and SnS_2 nanotubes, Bi_2S_3 nanorods, and SiC nanowires have been successfully synthesized in this way. The solvent is not limited to water but also includes other polar or nonpolar solvents, such as benzene, and the process is more appropriately called solvothermal synthesis in different solvents.

(4) Micelles or microemulsion based synthesis: In this method, the synthesis of nanoparticles can be achieved by confining the reaction volume in a restricted place. When the surfactant concentration exceeds the critical micelle concentration (cmc) in water, micelles are formed as aggregates of surfactant molecules. In normal micelles, the hydrophobic hydrocarbon chains of the surfactants are oriented toward the interior of the micelle, and the hydrophilic groups of the surfactants are in contact with the surrounding aqueous medium. On the other hand, reverse micelles are formed in nonaqueous medium where the hydrophilic headgroups are directed toward the core of the micelles and the hydrophobic groups are directed outward. A microemulsion is a dispersion of fine liquid droplets of an organic solution in an aqueous solution. Such a microemulsion system can be used for the synthesis of nanoparticles. The chemical reactions can take place either at either at the interfaces between the organic droplets and aqueous solution, when reactants are introduced separately into two immiscible solutions or inside the organic droplets when all the reactants are dissolved into the organic droplets. This method is particularly useful for the synthesis of semiconductor, oxide and metal nanoparticles such as CdSe, CdTe, CdS, ZnS, ZrO_2, TiO_2, SiO_2, Fe_2O_3, Pt, Au, Cu etc respectively [133, 137].

1.4 Some interesting properties of inorganic nanoparticles

As the size of the material approaches to nanometer regime, changes in physical and chemical properties are observed that can be explored for various applications. Nanoparticles exhibit many interesting properties, which are unusual in the sense that they are not observed in their bulk counterpart.

1.4.1 Optical properties

When the size of metal and semiconductor nanoparticles is reduced to a certain limit they exhibit remarkable optical properties. The color variations arising from changes in the composition, size, and shape of nanoparticles, surrounding medium and very high absorption cross-section promoted these materials as inorganic chromophores from visible to near infrared region. Due to this reason they find applications as sensors and imaging agents [138]. These effects in metal nanoparticles are due to the phenomena called surface plasmon resonance, the frequency at which conduction band electrons oscillate in response to the alternating electric field of incident electromagnetic radiation [21]. However, only gold, silver and copper nanoparticles possess plasmon resonances in the visible spectrum, which give rise to such intense colors. A nanoparticle is a complicated many electron system, where the confinement of electronic motion due to the reduction in size leads to fascinating new effects, potentially tunable with particle size and shape.

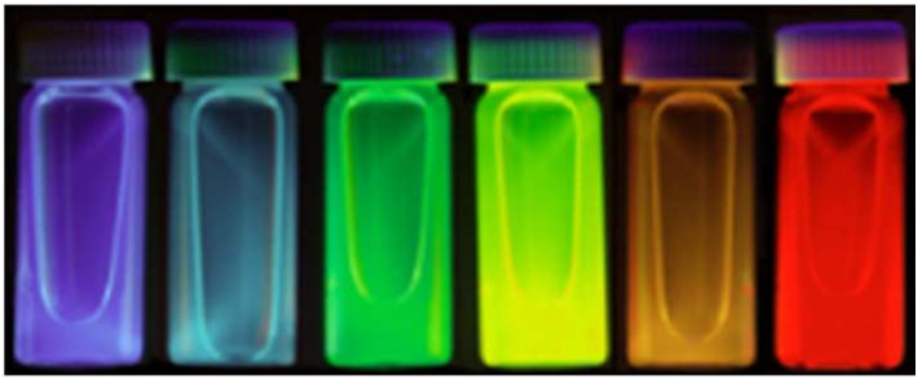

Figure 1.5 A photograph of CdSe semiconductor quantum dot nanocrystallites solutions irradiated with UV light. CdSe quantum dots were dispersed in hexane and each glass vial represents the solution of CdSe nanocrystallites with different size (increasing order of size from left to right). Image courtesy M. G. Bawendi research group home page http://web.mit.edu/chemistry/nanocluste

Optical properties of semiconductor nanoparticles are also very sensitive to its size and shape. In a bulk semiconductor, excitation involves the formation of an electron and hole (the charge carriers), which are separated by Bohr radius, which in on the nanometer length scale. The Bohr radius along with the high dielectric constant of the material makes the band-gap energy relatively small. When the size of semiconductor nanoparticles are reduced to and becomes smaller or equal to its Bohr radius, the space in which charge carriers is reduced confining the motion of exciton resulting in increaser in the band gap energy of semiconductor nanoparticles [25]. Figure 1.5 represents a photograph of CdSe semiconductor quantum dot nanocrystallites solutions irradiated with UV-light. The emission of light with the wavelength corresponding to particular color is a strong function of the size of nanoparticles. Therefore semiconductor nanoparticles composed of same material such as CdSe with different sizes emit different colors when excited with UV light. Equally important, the energy of the band gap absorption (and thus the nanoparticle color) and that of the emission increases and become sensitive to the size and shape of the particles. Thus, the optical and other physical and chemical properties of semiconductor nanoparticles become sensitive to the size and shape of the particles.

1.4.2 Electronic properties

Metal or semiconductor nanoparticles when embedded between metal – insulator – metal junction, or between the tip of STM and an electrode, show a differential capacitance or charging at low temperatures even at zero bias. This effect is called coulomb blockade or coulomb staircase effect. It was realized that this behavior caused by the extremely small capacitance of the metal nanoparticles. These particles can store charge by addition or removal of electrons. Due to its low capacitance, nanometer sized metallic particles are extremely sensitive to neighboring charges [139 a] and therefore, could be useful as sensor materials. The conductance measurements carried out on thin films of nanoparticle in the presence of organic vapors, showed changes in electrical conductivity rapidly and reversibly. Gas adsorption on the surface of a nanoparticle causes swelling, which leads to an increase in the spacing between the metal cores. Electron hopping from one nanoparticle to other is responsible for the conduction and due to its dependence on the distance between metal cores, the absorption of insulating organic vapor leads to a strong decrease in electrical conductivity. This behavior has been exploited technologically as a new concept for vapor sensors [139 b].

1.4.3 Magnetic properties

The magnetic properties of nanoparticles differ from those of bulk in two ways. The large surface to volume ratio results in a different local environment for the surface atoms in their magnetic coupling or exchange interaction with neighboring atoms, leading to the mixed volume and surface magnetic characteristics. Unlike bulk ferromagnetic materials, which usually form multiple magnetic domains, several small ferromagnetic particles could consist of only a single magnetic domain. In the case of a single particle being a single domain, superparamagnetism occurs, in which the magnetizations of the particles are randomly distributed and they are aligned only under an applied magnetic field, and the alignment disappears once the external field is withdrawn since, thermal energy barrier overtakes the intrinsic magnetization resulting in the rapid spin fluctuations [140]. In superparamagnetism, the ferromagnetic transition of a given sample is broadened due to the thermal fluctuation of the total moment on each particles of the sample, attributed to their single domain nature. This situation arises usually when the size of the particle is lower than certain critical value. This property could have important implications and for example, in ultra-compact information storage where the size of the domain determines the limit of storage density [141].

1.5 Outline of the thesis

The work presented in this thesis describes novel biological protocols for the synthesis of metal oxides, metal sulfides and metallic nanoparticles in an attempt to extend the biological means for nanoparticles synthesis. Many exciting results are observed during the course of experiments, which are described in details. An attempt has been made to synthesize magnetic iron oxide nanoparticles under aerobic conditions using micro-organisms, which are not shown to synthesize inorganic materials previously. Further, quantum dot semiconductor metal sulfide nanocrystallites have been synthesized by engineering of assimilatory sulfate reduction pathway of the bacterium *P. aeruginosa.* Moreover, anisotropic metal nanoparticles such as gold and silver have been synthesized using the bacterium or bacterial metabolites. The thesis is composed of seven chapters and the chapter wise description of these studies is described as follows:

The **first chapter** is an introduction to the thesis and provides a brief and general introduction to nanotechnology, with a detailed account of various strategies of biological methods practiced for the synthesis of nanoparticles. Finally this chapter discusses in brief various existing physical and chemical methodologies for the synthesis of nanoparticles and some important properties of nanoparticles.

The second chapter describes different techniques of the characterization of nanoparticles synthesized by the methods described in this thesis. Physical principles of various instrumentation techniques such as, UV-visible Spectroscopy, Photoluminescence spectroscopy (Florescence spectroscopy), Fourier Transform Infrared Spectroscopy (FTIR), X-ray diffraction (XRD), Transmission Electron Microscopy (TEM), Scanning Electron Microscopy (SEM), Atomic force microscopy, Magnetic measurements techniques, Mossbauer spectroscopy, Thermo gravimetric Analysis (TGA) etc. has been described. Further, various techniques such as Sodium dodecyl sulfate polyacrylamide gel electrophoresis for proteins and agarose gel electrophoresis for DNA, Polymerase chain reaction, DNA sequencing, thin layer chromatography etc. studied to understand the biological mechanism of nanoparticles formation has been described.

The **third chapter** discusses the synthesis of magnetic oxides of iron namely magnetite and maghaemite. The employment of different microbial systems, namely bacterial and fungal has been studied for the synthesis of magnetite (Fe_3O_4). The remarkable fact about this biosynthetic process is the formation of magnetite under aerobic conditions. Serendipitous discovery of a bacterial species which was identified later as *Actinobacter spp.* was explored for the synthesis of magnetite from ferry/ferro cyanide solution. Bacterially synthesized magnetite showed superparamagnetic behavior at room temperature. Ionic stress imparted by ferry/ferro cyanide resulted in the induction of two new proteins by the bacterium, which may be responsible for the synthesis and stability of the magnetite nanoparticles. We believe that the bacterial cyanase or cyanide dihydratase is induced in the presence of ferri/ferrocyanide that is responsible for the hydrolysis of the metal complex. UV-vis spectroscopic analysis of the reaction progress indicates that the ferri/ferrocyanide is degraded within 72-96 h with subsequent formation of magnetite nanoparticles. Two different fungi *Verticillium sp.* and *F. oxysporum* are also employed for the synthesized of magnetic nanoparticles from ferry/ferrocyanide. Similar to bacterial magnetite, fungal magnetite was also found to be superparamagnetic in nature. Cyanide hydratase secreted by the fungi is responsible for the hydrolysis of ferry/ferrocyanide mixture and subsequently magnetite was formed. Another aspect of this chapter is biosynthesis of maghaemite (γ-Fe_2O_3) nanoparticles by *Actinobacter* spp. Maghaemite nanoparticles with overall dimensions of 5-7nm were obtained which showed superparamagnetic behavior. A detailed mechanistic aspect of the formation of maghaemite nanoparticles has been investigated. The pivotal role of ferrisiderophore reductase in the formation of maghaemite nanoparticles has been shown in this chapter. The reaction appears to progress via reduction of ferric iron to the ferrous form which is then reoxydized and subsequently converted into iron oxyhydroxide. The last step is dehydration that converts iron oxyhydroxide into maghaemite. Analysis of particle bound proteins indicated the presence of four different proteins with molecular weights of 15, 16 19, 20 kDa. Extracellular protein profile of bacterial culture supernatant in the presence and absence of iron salts indicated the presence of new protein with the molecular weight of 55 kDa.

The **fourth chapter** describes bacterial synthesis of semiconductor and magnetic metal sulfides. Quantum dots like CdS, ZnS and PbS have been successfully synthesized by the bacterium *Pseudomonas aeruginosa* strain isolated from marine water. These sulfide nanoparticles show size quantization effect since all the nanoparticles synthesized were well in the quantum size regime. All the sulfide nanoparticles showed fluorescence emission in the visible region of the electromagnetic spectrum. The biochemical and molecular mechanism of the synthesis of these sulfide nanoparticles was investigated in detail. Two enzymes of assimilatory sulfate reductase metabolism appear to be responsible for the reduction of sulfate into sulfides. Incorporation of these two genes into *E.coli* cells indeed confirmed the requirement of these two enzymes for the synthesis of sulfide nanoparticles. This chapter also describes the synthesis of mixed phase iron sulfide by the bacterium *Actinobacter spp.* Detailed characterization of these iron sulfide nanoparticles showed the presence of two phases, namely greigite (Fe_3S_4) and pyrite (FeS_2). Bacterially synthesized greigite nanoparticles behave as a soft magnet and exhibit superparamagnetism at low temperature. We believe that Actinobacterial sulfate reductases are responsible for the conversion of iron sulfate into iron sulfide. PCR amplification of one of the two genes which are likely to be responsible for sulfate reduction reaction in *Actinobacter spp*. has been successfully carried out. Presence of chromate ions in the reaction medium did not yield any iron sulfide nanoparticles indicating that PAPS reductase is involved in the conversion of sulfate into sulfide. There are five different proteins associated with iron sulfide nanoparticles with respective molecular weights of 15, 16 19, 20 and 27 kDa. The First four proteins are similar in molecular weight with the particle associated proteins of maghaemite nanoparticles discussed above. This chapter also describes the synthesis of silver sulfide nanoparticles from *Actinobacter spp*. when silver sulfate was used as a precursor.

The **fifth chapter** describes the synthesis of anisotropic gold and silver nanoparticle by *Actinobacter* spp. Mechanistic aspects of gold ion reduction and phenomenon of shape control is also demonstrated. Bioreduction of gold ions with *Actinobacter* spp. yielded triangular nanoparticles with the edge length varying from 50 nm to 2 μm while thickness of these nanotriangles was found to be around 20 nm. The edge length of Au nanotriangles can be controlled by varying the reaction conditions. This chapter also describes the synthesis of irregular, plate-like silver nanoparticles by *Actinobacter* spp.

The **sixth chapter** illustrates the preparation of Au and Ag nanoparticles by different bacterial metabolites, such as the pigments, siderophores and enzymes. Interestingly, the siderophore-pyoverdin isolated from *P.aeruginosa* resulted in the formation of triangular Au nanoparticles with the controllable edge length as a function of siderophore concentration. The edge length of triangular gold particles was found to vary between 250 nm to 5 μm and the thickness was measured to be around 15-20 nm. Pyoverdin was also capable of reducing silver ions forming silver nanoparticles. However, shape of silver nanoparticles so produced was found to be irregular. Interestingly, reduction of gold ions with the bacterial pigment pyocyanin resulted in nearly monodisperse gold nanoparticles. Reduction of silver ions with pyocyanin resulted in the formation of long wire-like nanostructures of silver. Surprisingly, reduction of silver ions by pyocyanin was faster than that of reduction of gold ions and was completed within hour. This chapter also describes bacterial enzyme mediated synthesis of anisotropic and uniform sized gold nanoparticles. Rate of the synthesis of gold nanoparticles was drastically affected by the presence or absence of atmospheric oxygen.

The **seventh chapter** summarizes the biological methods used for the synthesis of nanoparticles as diverse as oxides, sulfides and metals. Also the scope for the possible future work in this area has been described briefly.

1.6 References

[1] (a) Schmid, G. *Nanoparticles from Theory to Applications*, **2004**, Wiley-VCH, Weinheim (b) http://www.nano.gov.

[2] (a) Feynman, R. P. *Eng. Sci*. **1960**, *23*, 22. (b) The text of Feynman’s speech- http://www.its.caltech.edu/~feynman/plenty.html

[3] Taniguchi, N. On the Basic Concept of 'Nano-Technology'. In: *Proceedings of the international conference on production engineering. Tokyo, Part II,* Japan Society of Precision Engineering, 1974: 18-23: Tokyo: JSPE.

[4] Timp, G. Nanotechnology, 2004, Springer, New Jersy.

[5] Heath, J. R., *Science*, **1995**, *270*, 1315.

[6] http://en.wikipedia.org/wiki/Neanderthal

[7] (a) Whitesides, G. M. *Small*, **2005**, *1*, 172. (b) http://www.cnms.ornl.gov/ nanosci/nanosci.shtm (c) http://www. www.kol.to (d) http:// www.sandia.gov (e) www.answers.com/topic/electron-beam-lithography (f) Redl, F.X., Chao, K. S., Murrey, C. B., O’Brien,S. *Nature*, **2003**, *423*, 968.

[8] Thomas, J. M. *Pure Appl. Chem.* **1988**, *60*, 1517.

[9] Wagner, F. E., *et al. Nature*, **2000**, *407*, 691.

[10] Roucoux, A., Schulz, J., Patin, H. *Chem. Rev.* **2002**, *102*, 3757.

[11] Niemeyer, C. M., *Angew. Chem. Int. Ed.* **2001**, *40*, 4128.

[12] Langer, R., *Sci. Am.* **2003**, *288*, 50.

[13] Rosi, N. L., Mirkin, C. A. *Chem. Rev.* **2005**, *105*, 1547.

[14] Hagfeldt, A., Graetzel, M. *Acc. Chem. Res.* **2000**, *33*, 269.

[15] Jackson, J. B., Westcott, S. L., Hirsch, L. R., West, J. L., Halas, N. *J. Appl. Phys. Lett.*2003, 82, 257.

[16] (a) Parak, W. J., Pellegrino, T., Plank, C. *Nanotechnology* **2005**, *16*, R9. (b) Chan, W. C. W.; Nie, S. M. *Science* **1998**, *281*, 2016.

[17] Moran, C. E., Steele, J. M., Halas, N. J. *Nano Lett*. **2004**, *4*, 1497.

[18] Simon, U. In *Nanoparticles: From Theory to Application*, Schmid, G., Ed. Wiley-VCH, Weinheim, 2004.

[19] Maier, S. A. *Adv. Mater.* **2001**, *13*, 1501.

[20] Li, X. *Langmuir* **2004**, *20*, 1298.

[21] Link, S. El-Sayed, M. A. *Annu. Rev. Phys. Chem.* **2003**, *54*, 331.

[22] (a) Raimondi, F., Scherer, G. G., Kötz, R., Wokaun, A. *Angew. Chem. Int. Ed.* **2005**, *44*, 2190. (b) Zhang, J. H. *Acc.Chem. Res.* **1997,** *30*, 423.

[23] (a) Kreibieg, U., Vollmer, M. *Optical properties of metal clusters*; Springer: Berlin and New York, 1995. (b) Mulvany, P. *Langmuir* **1996**, *12*, 788.

[24] Hutter, E., Fendler, J. H. *Adv. Mater.* **2004**, *16*, 1685.

[25] (a) Alivisatos, A. P. *Science* **1996**, *271*, 933. (b) El-Sayed, M. A. *Acc. Chem. Res.* **2004**, *37*, 326.

[26] Lewis, L. N. *Chem. Rev.* **1993**, 93, 2693.

[27] (a) Shukla, S., *et al. Chem. Mater.* **2005**, *17*, 5000. (b) Joshi, H. M., Bhumkar, D. R., Joshi, K., Pokharkar, V., Sastry, M. *Langmuir*, **2006**, *22*, 300.

[28] Hagfeldt, A., Graetzel, M. *Acc. Chem. Res.* **2000**, *33*, 269.

[29] Swami Sivananda, *Practice of Ayurveda,* **2006**, Divine life Soc. Publishers.

[30] Faraday, M. *Philos. Trans. R. Soc. London* **1857**, *147*, 145.

[31] (a) Chen, T., Chen, S., Sheu, S., Yeh, C. *J. Phys. Chem. B* **2002**, *106*, 9717. (b) Ershov, B. G., Henglein, A. *J. Phys. Chem.* **1993**, *97*, 3434.

[32] (A) Henglein, A. *Langmuir* **1999,** *15,* 6738. (B) A. Henglein, J. Phys. Chem. B **2000**, *104*, 1206.

[33] Grieser, F., Ashokkumar, M. Sonochemical synthesis of inorganic and organic colloids. *In Colloids and Colloid Assemblies*, Ed. Caruso, F. 2003, Wiley-VCH, Weinheim.

[34] (a) Wegner, K. ;Walker, B. ;Tsantilis, S. ;Pratsinis, S. E. *Chem. Eng. Sci* 2002, *57*, 1753. (b) Vitulli, G., et al. *Chem. Mater.* **2002**,*14*, 1183. (c) Davis, S. C.; Klabunde, K. J. *Chem.Rev.* **1982**, *82*, 153.

[35] Swihart, M. T. *Curr. Opin. Colloid Interface Sci.* **2003**, *8*, 127.

[36] Rodriguez-Sanchez, M. L., Rodrigues, M. J., Blanco, M. C., Rivas, J., Lopez-Quintela, M. A. *J. Phys. Chem. B* **2005**, *109*, 1183.

[37] (a) Tan, Y., Dai, X.,Y. Li, , Zhu, D. *J. Mater. Chem.* **2003**, *13*, 1069. (b) Jiang, X., *et al*. Langmuir, 2001, 17, 3795.(c) Naka, K., Yaguchi, M., Chujo, Y. *Chem. Mater.* **1999**, *11*, 849. (d) Warner, M. G., Reed, S. M., Hutchison, J. E. *Chem. Mater.* **2000**, *12*, 3316.

[38] (a) Capek, I. *Advances in Colloid and Interface Science* **2004**, *110*, 49. (b) Busbee, B. D., Obare, S. O., Murphy, C. J. Adv. Mater. 2003, 15, 414.

[39] (a) Zhang, M., Drechsler, M., Muller, A. H. E., *Chem. Mater.* **2004**, *16*, 537. (b) Minko, S., Kiriy, A., Gorodyska, G., Stamm, M. *J. Am.Chem. Soc.* **2002**, *124*, 10192.

[40] (a) Braun, E., Eichen, Y., Sivan, U., Ben-Yoseph, G. *Nature* **1998**, *391*, 775. (b) Richter, J., et al. Adv. Mater, **2000**, *12*, 507.

[41] Ongaro, A., *et al*. *Chem. Mater.* **2005**, *17*, 1959.

[42] (a) Mann, S., Weiner, S., *J. Structur. Biol.* **1999**, *126*, 179. (b) Roschger, P., J. *Structur. Biol.* **2001**, *136*, 126.

[43] Mann, S. *Biomineralization: Principles and Concepts in Bioinorganic Materials Chemistry* 2001, Oxford University Press, Oxford.

[44] (a) Lowenstam, H. A. *Science*, **1981**, *211*, 1126. (b) Bommel, K. J. C. V.; Friggeri, A., Shinkai, S. *Angew. Chem. Int. Ed.* **2003**, *42*, 980. (c) Bauerlein, E. *Angew. Chem. Int. Ed.* **2003**, *42*, 614.

[45] Sastry, M., Ahmed,A., Khan, M. I., Kumar, R. *In Nanobiotechnology:Concepts, Applications and Perspectives (ed .Nimeyer and Mirkin)* **2004,** 126.

[46] Yongxin, P., Chenglong, D., Quingsong, L., Nikolai, P., Rixiang, Z. *Chinese Sci. Bullt.* **2004**, *49*, 2563.

[47] (a) Mann, S., *Nature*, **1993**, *365*, 499. (b) Kroger, N., Deutzmann, R., Sumper, M. Science 1999, 286, 1129. (c) Kroger, N., Deutzmann, R., Bersdorf, C., Sumper, M. *Proc. Natl. Acad. Sci. USA*, 2000, **97**, 14133. (d) Kroger, N., Bersdorf, C., Sumper, M. *EMBO, J.* **1994**, *13*, 4676. (e) Kroger, N., Lorenz, S., Sumper, M. *Science*, **2002**, *296*, 584.

[48] (a) Shimizu, K., Cha, J., Stucky, G. D., Morse, D. E. *Proc. Natl. Acad. Sci.USA*, 1998, 95, 6234. (b) Morse, D. E. *Trends. Biotechnol.* **1999**, *17*, 230.

[49] Oliver, S., Kupermann, A., Coombs, N., Lough, A. and Ozin, G. A., *Nature*, 1995, *378*, 47.

[50] (a) Young, J. R., Didymus, J. M., Bown, P. R., Prins, B., Mann, S. *Nature* **1992**, *356*, 516. (b) Young, J. R.; Davis, S. A.; Bown, P. R.; Mann, S. *J. Struct. Biol.* **1999**, *126***,** 195.

[51] Sleytr, U. B., Messner, P., Pum, D., Sara, M. *Angew. Chem. Int. Ed.* **1999**, 38, 1034.

[52] (a) Blackmore, R. P. Science, 1975, 190, 377. (b) Bazilinsky, D. A., Frankel, R. B., Janasch, C. W. 1988, *Nature*, **334**, 518.

[53] (a) Pohnert, G., *Angew. Chem. Int. Ed*. **2002**, *41*, 3167. (b) Mann, S. Angew. Chem. Int. Ed. **2000**, *39*, 3392.

[54] Sumper, M., Kroger, N. *J. Mater. Chem*. **2004**, *14*, 2059.

[55] Cha, J. N., *et al. Proc. Natl. Acad. Sci.USA*, **1999**, 96, 361.

[56] Kroger, N., Bergsdorf, C., Sumper, M. *Eur. J. Biochem.* **1996**, *239*, 259.

[57] Kroger, N., Lehmann, G., Rachel, R., Sumper, M. *Eur. J. Biochem.* **1997**, *250*, 99.

[58] (a) Gao, H., Ji, B., Jager, I. L., Arzt, E., Fratzl, P. *Proc. Natl. Acad. Sci. USA* **2003**, *100*, 5597. (b) Addadi, L., Weiner, S. *Nature* 1997, *389*, 912. (c) Mann, S. *Nature* **1993**, *365*, 499.

[59] (a) Bauerlein, E *Angew. Chem. Int. Ed.* **2003**, *42*, 614. (b) Gotliv, B., Adadi, L., Weiner, S. ChemBioChem **2003**, *4*, 522.

[60] Torres de Araujo, F. F.; Pires, M. A.; Frankel, R. B.; Bicudo, C. E. M. *Biophys. J.* **1986**, *50*, 375.

[61] Mann, S., Sparks, N. H., Walker, M. M., Kirschvink, J. L. *J. Exp. Biol.* **1988**,*140*, 35.

[62] Etherage, J. A., Perez, S. M., Taylor, O. R., Jander, R. *Proc. Natl. Acad. Sci. USA* **1999**, *96*, 13885.

[63] Acosta-Avalos, D., Wajnberg, E., Oliveira, P. S., Leal, I., Farina, M., Esquivel, D. M. *J. Exp. Biol.* **1999**, *202*, 2687.

[64] Hanzlik, M., Heunemann, C., Holtkamp-Rötzler, E., Winklhofer, M., Petersen, N., Fleissner, G. *Biometal*, **2000**, *13*, 325.

[65] (a) Kirschvink, J. L., Kobayashi-Kirschvink, A., Woodford, B. J. *Proc. Natl. Acad. Sci USA* **1992**, *89*, 7683. (b) Dobson, J., Grassi, P. P. *Brain Res. Bull.* **1996**, *39*, 225.

[66] (a) Bazylinski, D., A., Garratt-Reed, A., Frankel, R., B. *Microscopy Res. Tech*. **1994**, 27, 389. (b) Spring, S., Schleifer, K., H. *Appl. Microbiol*. **1995**, *18*, 147.

[67] (a) Blackmore, R., P. *Annu. Rev. Microbiol*. **1982,** *36*, 217.(b) Bazylinski, D. A.; Frankel, R.,B., Jannasch, H., W. *Nature*, **1988**, *334*, 518.

[68] Bazilinsky, D. A., Frankel, R. B. *Nat. Rev. Microbiol.* **2004**, *2*, 217.

[69] (a) Matsunaga, T., Okamura, Y. *Trends. Microbiol.* **2003**, *11*, 536. (b) Matsunaga, T.,Sakaguch, T. *J. Biosci. Bioengg.* **2000**, *90*, 1. (c) Astushi, A., Web, J., Matsunaga, T. *J. Biol. Chem.* **2003**, *278*, 8745.

[70] (a) Lovley, D., R., Stolz, J., F., Nord Jr, G., L., Phyllips, E., J., P. *Nature*, **1987**, *330*, 252. (b) Glasauer, S., Langley, S., Beveridge, T., J. *Science*, **2002**, *295*, 117.

[71] Lovley, D., R. *Annu. Rev. Microbiol*. **1993,** *47*, 263.

[72] Bauerlein, E *Angew. Chem. Int. Ed.* **2003**, *42*, 614.

[73] Zbinden M.; Martinez I.; Guyot F.; Cambon-Bonavita M-A.; Gaill F. *Eur. J. Mineral.* **2001**, *13*, 653.

[74] Labrenz, M., *et al.* Science, **2000**, *290*, 1744.

[75] Reith, F., Rogers, S., L., McPhail, D. C., Webb, D. *Science*, **2006**, *313*, 233.

[76] (a) Beveridge, T. J., *et al. Adv. Microb. Physiol.* **1997**, 38, 178. (b) Silver, S. *Gene* **1996**, *179*, 9. (c) Rouch, D.A., Lee, B. T., Morby, A. T. *J. Ind. Micro.* **1995**, *14*, 132.

[77] (a) Southam, G., Beveridge, T. J. *Geochim. Cosmochim. Acta*, **1996**, *60*, 4369. (b) Beveridge, T. J., Murray, R. G. E. *J. Bacteriol*., **1980**, *141*, 876. c) Fortin, D., Beveridge, T. J. in *Biomineralization: From Biology to Biotechnology and Medical Applications* (ed. Baeuerien, E.), Wiley-VCH, Weinheim, 2000, 7.

[78] (a) Klaus, T., Joerger, R., Olsson, E., Granqvist, C. G., *Proc. Natl. Acad. Sci. USA*, **1999**, *96*, 13611. (b) Klaus-Joerger, T., Joerger, R., Olsson, E., Granqvist, C. G. *Trends Biotechnol*. **2001**, *19*, 15.

[79] Joerger, R., Klaus, T., Granqvist, C. G., *Adv. Mater*. **2000**, *12*, 407.

[80] Nair, B., Pradeep, T. *Cryst. Growth Des.* **2002**, *2*, 293.

[81] Yong, P., *et al*, *Biotech. Bioengg.* **2002**, *80*, 369.

[82] Ahmad, A.; Senapati, S.; Khan, M. I.; Kumar, R.; Sastry, M. *Langmuir* **2003,** *19,* 3550.

[83] Oremland, R. S., et al. *Appl. Environ. Microbiol.* **2004**, *70*, 52.

[84] Lengke, M., F., Fleet, M., E., Southam, G. *Langmuir*, **2006**, 22, 2780.

[85] Lengke, M., F., Fleet, M., E., Southam, G. *Langmuir* **2006**, 22, 7318.

[86] Kashifi, K., Torr, J., M., Nevin, K., P., Lovley, D., R. *Appl Environ MIcrobiol* **2001**, *67*, 3275.

[87] Dameron, C., T. *et al*, *Nature*, **1989**, *338*, 596.

[88] Kowshik, M. *et al*, *Biotechnol. Bioengg*. **2002**, *78*, 583.

[89] Kowshik, M., Vogel, W., Urban, J., Kulkarni, S., K., Paknikar, K., M. *Adv. Mater*. **2002**, *14*, 815.

[90] Holmes, J., D., *et al*, *Microbiol*. **1997**, *143*, 2521.

[91] Sweeney, R., Y., *et al*. *Chem. Biol*. **2004**, *11*, 1553.

[93] Mukherjee, P., *et al*. *Angew. Chem. Int. Ed*. **2001**, *40*, 3585.

[94] Mukherjee, P., *et al*. *Chem Bio Chem,* **2002***, 3,* 461.

[95] Mukherjee, P., *et al*. *Nano Lett.* **2001***, 1,* 515.

[96] Ahmad, A., *et al*. *Coll. Surf.B.* **2003***, 28,* 313.

[97] Senapati, S., Ahmad, A., Khan, M. I., Sastry, M., Kumar, R. *Small*, **2005**, *1*, 517.

[98] Ahmad, A., *et al, J. Am. Chem. Soc.* **2002**, *124*, 12 108.

[99] (a) Bansal, V., *et al, J. Mater. Chem.***2005**, 15, 2583. (b) Bansal, V., *et al, J. Mater. Chem.*2004, 14, 3303.

[100] (a) Arnott, H.J. *Three systems of biomineralization in plants with comments on the associated organic matrix.* In (ed. Nancollas, G. H.), 1982, Springer Verlag, Berlin, 199. (b) Monje, P.V., Baran, E.J., 2004a. *Plant biomineralization.* In (ed. Hemantaranjan, H.), Advances in Plant Physiology, vol. 7. Scientific Publishers, Jodhpur, 403.

[101] Monje, P.V., Baran, E.J. *J. Plant Physiol.* **2000**, *157*, 457.

[102] Harrison, C., C. *Phytochemistry* **1996**, *41*, 37.

[103] Gajdardziska-Josifovska M., McClean R.G., Schofield M.A., Sommer C.V., Kean W.F. *Eur. J. Mineral.* **2001**, *13*, 863.

[104] Cannon, H. L.; Shacklette, H. T.; Bastron, H. 1968: Metal absorption by *Equisetum* (horsetail). *United States Geological Survey Bulletin 1278-A:* A1-A21.

[105] (a) Gardea-Torresdey, J. L., *et al. Nano Lett.* **2002, 2,** 397. (b) Gardea-Torresdey, J. L., *et al. Langmuir*. 2003, 19, 1357.

[106] (a) Shankar, S. S., Ahmad, A., Pasricha, R., Sastry, M. *J. Mater. Chem.* **2003**, *13*, 1822. (b) Shankar, S. S., Ahmad, A., Sastry, M. *Biotechnol. Prog.*, **2003**, *19*, 1627. (c) Shankar, S. S., Rai, A., Ahmad, A., Sastry, M. *Appl. Nanoscience* **2004**, *1*, 69. (d) Shankar, S. S., Rai, A., Ahmad, A., Sastry, M. *J. Colloid Interface Sci.* **2004**, *275*, 496.

[107] (a) Shiv Shankar, S., Rai, A., Ankamwar, B., Singh, A., Ahmad, A., Sastry, M. *Nat. Mater.* **2004**, *3*, 482. (b) Shankar, S. S., Rai, A., Ahmad, A., Sastry, M. *Chem. Mater.* **2005**, *17*, 566.

[108] (a) Chandran, S. P., Chaudhari, M., Pasricha , R., Ahmad, A., Sastry, M. *Biotechnol.*

Prog. 2005, 22, 577. (b) Liu, B., Xie, J., Lee, J. Y., Ting, Y. P., Paul Chen, J. *J. Phys. Chem. B.* **2005**, *109*, 15256.

[109] (a) Cha, J. N., Stucky, G. D., Morse, D. E., Deming, T. J. Nature, 2000, 403, 289. (b) Kroger, N., Deutzman, R., Sumper, M. *Science*, **1999**, *286*, 1129. (c) Belton, D., Paine, G., Patwardhan, S. V., Perry, C. C. *J. Mater. Chem.* **2004**, *14*, 2231.

[110] (a) Sumeral, J. L., *et al. Chem. Mater*. **2003**, *15*, 4804. (b) Kisailus, D., Choi, J. H., Weiver, J. C., Yang, W., Morse, D. E. *Adv. Mater*. **2005**, *17*, 314.

[111] (a) Bae, W., O., Abdullah, R., Henderson, D., V., Mehra, R., K. *Bichem. Biophys. Res. Commun.* **1997**, *237*, 16. (b) Bae, W., Mehra, R., K. J. *Inorg. Biochem*. **1998**, *69*, 33. (c) Bae, W., O., Abdullah, R., Mehra, R., K. *Chemosphere* **1998**, *37*, 363. (d) Neail-Reese, R., Mehra, R. K., Bart-Tarbet, E., Winge, D. R. *J. Biol. Chem.* **1988**, *263*, 4186

[112] Aizenberg, J., Lambert, G., Addadi, L., Weiner, S. *Adv. Mat* **1996**, *8*, 222.

[113] (a) Naik, R. R., Broat, L. L. Ckarson, S. J., Stone, M. O. *J. Nanosci. Nanotech*. **2002**, *2*, 95. (b) Whaley, S. R., English, D. L., Hu, E. L., Barbara, P. F., Belcher, A. M. *Nature*, **2000**, *405*, 665.

[114] Slockik, J. M., Stone, M. O., Naik. R. R. Small, 2005, 1, 1048.

[115] Naik, R. R., Stringer, S. J., Agarwal, G., Jones, S. E., Stone, M. O. *Nat. Mater*. **2002**, *1*, 169.

[116] Mao, C., *et al. Science,* **2004**, *303*, 213.

[117] Douglas, T., et al. *Adv. Mater*. **2002**, *14*, 415.

[118] Ball, P. *Made To Measure: New Materials for the 21st Century*, 1997, Princeton University Press, New Jersey.

[119] (a) Shenton, W.; Douglas, T.; Young, M.; Stubbs, G.; Mann, S. *Adv. Mater.* **1999**, *11*, 253. (b) Dujardin, E.; Peet, C.; Stubbs, G.; Culver, J. N.; Mann, S. *Nano Lett.* **2003**, *3*, 413. (c) Ongaro, A., et al. Chem. Mater. 2005, 17, 1959.

[120] Braun, E.; Eichen, Y.; Sivan, U.; Ben-Yoseph, G. *Nature* **1998**, *391*, 775.

[121] Hall, S. R., Shenton, W., Engelhardt, H., Mann, S. ChemPhysCHem 2003, 3, 184.

[122] (a) Bhattachargee, R. R., et al. *J. Nanosci. Nanotechnol.* **2005**, *5*, 1141. (b) Naik, R. R., et al. *Adv. Funct. Mater.* **2005**, *14*, 25.

[123] Hall, S. R., Bolger, H., Mann, S. Chem.Commun. 2003, 2784.

[124] Bauerlein, E., Behrens, P., Matthias, E. *in Handbook of Biomineralization vol. 2.*

[125] Sleytr, U. B., Egelser, E., Pum, D., Schuster, B. *In Nanobiotechnology:Concepts, Applications and Perspectives (ed .Nimeyer and Mirkin)* **2004**, 77.

[126] (a) Storhoff, J. J., Mirkin, C. A. Chem. Rev. 1999, 99, 1849. (b) Mertig, M., et al. *Nano Lett.* **2002**, *2*, 841.

[127] Larisa, L., et al. *Adv. Mater.* **2005**, *17*, 1854.

[128] (a) Maldrum, F. C.,Wade, V. J., Nimmo, D. L., Heywood, B. R., Mann, S. *Nature*, **1991**, *349*, 684. (b) Wong, K. K. W., Mann, S. **Adv. Mater. 1996**, *8*, 928.
(C) Mayes, E. L., Mann, S. *In Nanobiotechnology:Concepts Applications and Perspectives (ed .Nimeyer and Mirkin)* **2004**, 278. Wiley-VCH, Weinheim.
(d) Shenton, W., Mann, S., Coelfen, H., Bacher, A., Fisher, M. *Angew. Chem. Int. Ed.***2001**, *40*, 442.

[129] (a) Mertig, M., Pompe, W. *In Nanobiotechnology:Concepts Applications and Perspectives (ed .Nimeyer and Mirkin)* **2004**, 256 Wiley-VCH, Weinheim.

[130] (a) Braun, P. V., *In Nanocomposite science and Technology (ed. Pulickel A., Schadler, L. S., Braun, P. V.)* 2004, Wiley-VCH, Weinheim. (b) Adam D Lazareck *et al* 2006 *Nanotechnology* **17** 2661.

[131] (a) Fowler, C. E., Shenton, W., Stubbs, G., Mann, S. *Adv. Mater.* **2001**, *13*, 126.
(b) Douglas, T., Young, M. *Nature*, **1998**, *393*, 152.

[132] Niemeyer, C. *Angew. Chem. Int, Ed.* **2001**, *40*, 4128.

[133] (a) Cao, G. Nanostructures and Nanomaterials: Synthesis, Properties and Applications. 2004, Imperial College Press, London. (b) Wolf, E. *Nanophysics and Nanotechnology*, Wiley-VCH, Weinheim, **2004.**

[134] Lin, S. T., Franklin, M. T., Klabunde, K. J. *Langmuir*, **1986**, *2*, 259.

[135] (a) Becker, M. F., et al. *Nanostruct. Mater.* **1998**, *10*, 853. (b) Mafune, F., Kohno, J., Takeda, Y., Kondow, T. *J. Phys. Chem. B*, **2003**, *107*, 4218.

[136] Gachard, E., et al. *New J. Chem.* **1998**, 1257

[137] Burda,C., Chen, X., Narayanan, R., El-Sayed, M. A. Chem. Rev. 2005, 105, 1025.

[138] Rosi, N. L., Mirkin, C. A. *Chem. Rev.* **2005**, *105*, 1547.

[139] (a) Andres, R. P., *Science* **1996**, *272*, 1323. (b) Chen, S., *et al. Science*, **1998**, *280*, 2098.

[140] (a) Skomski, R. J. Phys.: Condens. Matter. 2003, 15, R 841. (b) Lesley-Pelecky, D. L., Rieke, R.D. *Chem. Mater*. **1996**, *8*, 1770.

[141] Auschalorn, D. D.; Di Vincenzo, D. P. Smyth, J. F. *Science*, **1992**, *258*, 414.

Chapter II

Characterization Techniques

The different experimental techniques used for the characterization of nanoparticles synthesized using various biological methods described in present work are discussed in this chapter. Furthermore, different techniques used to study the biological mechanism responsible for nanoparticles synthesis are discussed.

2.1 Introduction

Synthesis of metal oxides, metal sulfides and metallic nanoparticles using different environmentally benign biological protocols is the theme of this thesis. The work described in this thesis also emphasizes on the biological mechanism underlying the synthesis of different metal oxides, metal sulfides and metallic nanoparticles. Nanoparticles synthesized by different biological means are characterized using different spectroscopic techniques such as UV-vis spectroscopy, FTIR spectroscopy, Fluorescent spectroscopy etc. Microscopic techniques such as Transmission electron microscopy, Scanning electron microscopy, Atomic force microscopy and other standard materials characterization techniques such as Energy dispersive X-ray analysis (EDAX), X-ray diffraction (XRD), and Thermogravimetric analysis (TGA) have been used. Magnetic nanoparticles have been characterized using Superconducting quantum interference device (SQUID), Mossbauer spectroscopy etc. Different molecular biology techniques such as Polymerase chain reaction (PCR), DNA sequencing, Gel electrophoresis of proteins and DNA etc. has been used to study the biochemistry of nanoparticles formation by bacteria and fungi.

2.2 UV-vis spectroscopy

Absorption spectroscopy in the visible region has long been an important tool to the analyst [1]. Color transitions arise due to molecular and structural changes in the substances being examined, leading to corresponding changes in the ability to absorb light in the visible region of the electromagnetic spectrum. Appearance of color arises from the property of the colored material to absorb selectively within the visible region of the electromagnetic spectrum. Absorption of energy leads to a transition of electron from ground state to excited state. The intensity of light passing through a sample is given by the relation:

$$I = I_0 \exp(-\alpha\, k\, x)$$

Where I = intensity of transmitted light; I_0 = intensity of incident light; α = molar absorption coefficient; k = constant; x = path length.

The combined Beer-Lambert law is used for quantification of exact concentration of unknown species in a mixture using UV-vis spectroscopy. This can be done by drawing a graph of intensities of absorption for different concentrations of the sample and comparing with a standard graph [1].

The Beer-Lambert law is:

$$A = \varepsilon \, c \, l$$

Where ε = proportionality constant known as the absorptivity.

Noble metal nanoparticles absorb strongly in the visible region due to surface plasmon resonance, which was discussed briefly in the previous chapter. Hence the UV–Visible absorption spectroscopy is a primary characterization tool to study the metal nanoparticles formation [2]. On the other hand semiconductor nanoparticles absorbs in the UV region of the electromagnetic spectrum due to single electronic excitation. All the UV–Visible absorption spectra presented in the thesis were carried out on Jasco V-570 dual beam spectrophotometer and HP diode array spectrophotometer operated at a resolution of 2nm [3].

In a dual beam spectrophotometer, light from either the visible or ultraviolet source enters the grating monochromator before it reaches the filter. Broad band filters contained in a filter wheel are automatically indexed into position at the required wavelengths to reduce the amount of stray light and unwanted orders from the diffraction grating. The light from the source is alternatively split into one of two beams by a rotating mirror called a chopper; one beam is passed through the sample and the other through the reference. The detector alternately sees the beam from the sample and then the reference. Its output which ideally would be an oscillating square-wave gives the ratio of I to Io directly i.e. the reference correction is made automatically. Array-detector spectrophotometers allow rapid recording of absorption spectra. Dispersing the source light after it passes through a sample allows the use of an array detector to simultaneously record the transmitted light power at multiple wavelengths. These spectrometers use photodiode arrays as the detector. The light source is a continuum source such as a tungsten lamp. All wavelengths pass through the sample. The light is dispersed by a diffraction grating after the sample and the separated wavelengths fall on different pixels of the array detector. The resolution depends on the grating, spectrometer design, and pixel size, and is usually fixed for a given instrument. These instruments use only a single light beam, so a reference spectrum is recorded and stored in memory to produce transmittance or absorbance spectra after recording the sample spectrum.

2.3 Fourier Transform Infrared Spectroscopy

The atoms in a molecule do not remain in a fixed relative position and vibrate about some mean position. Due to this vibrational motion, if there is a periodic alternation in the dipole moment then such mode of vibration is infrared (IR) active. The IR region of the electromagnetic spectrum is 100 μm – 1 μm wavelength. The vibrating molecule absorbs energy only from radiation with which it can coherently interact, i.e. the radiation of its own oscillation frequency. The appearance or non-appearance of certain vibrational frequencies gives valuable information about the structure of a particular molecule. Each functional group have specific range of vibrational frequencies and are very sensitive to the chemical environment and the neighbouring, thus provide valuable information regarding the presence of certain functional groups in the specific sample for their further characterization and identification. The frequency of vibration is given by the relation:

$$V = \frac{1}{2\pi}\sqrt{\frac{k}{\mu}}$$

where, k is force constant and μ is a reduced mass [4]. Silicon is the most commonly used substrate for IR measurements, for variety of reasons. It is chemically very stable and generally not very reactive even at high temperatures. It is excellent for optical studies of deposited films in the visible region using reflection techniques. It does not have strong lattice absorption bands in the useful regions of the infrared and thus can be used for transmission studies in this region. To correct for the lattice absorption bands in silicon, a reference silicon sample is used as a reference. FTIR measurements of the films of nanoparticles in the present study were carried out in the diffuse reflectance mode at a resolution of 4 cm^{-1} on a Perkin-Elmer FTIR Spectrum One spectrophotometer.

2.4 Fluorescent spectroscopy

Fluorescence spectroscopy or photoluminiscent spectroscopy or spectrofluorimetry is a type of electromagnetic spectroscopy used for analyzing fluorescent spectra [5]. It involves using a beam of light, usually ultraviolet light, that excites the electrons in molecules of certain compounds and causes them to emit light of a lower energy, typically, but not necessarily, visible light. Molecules have various states referred to as energy levels. Fluorescence spectroscopy is primarily concerned with electronic states and vibrational states. Generally, the species being examined will have a ground electronic state (a low energy state) of interest, and an excited electronic state of higher energy. Each of these electronic states has various vibrational states.Photons of light are small "packets" of energy, each with an energy proportional to its frequency; photons of high frequency light have higher energy than those of low frequency light. These can be absorbed by molecules, with the molecule gaining the energy of the photon, or emitted by molecules, with the photon carrying some of the energy of the molecule away. In fluorescence spectroscopy, the species is first excited, by absorbing a photon of light, from its ground electronic state to one of the various vibrational states in the excited electronic state. Collisions with other molecules cause the excited molecule to lose vibrational energy until it reaches the lowest vibrational state of the excited electronic state.The molecule then drops down to one of the various vibrational levels of the ground electronic state again, emitting a photon in the process. As molecules may drop down into any of the vibrational levels of this ground state, the photons will have different energies, and thus frequencies. Therefore, by analysing the different frequencies of light emitted in fluorescent spectroscopy, the structure of these different vibrational levels can be determined.

2.5 Transmission electron microscopy

A beam of accelerated electrons can interact with an object in a conventional transmission electron microscope in one of two ways [6]. Usually elastic scattering takes place, whereby the electrons change their path in the specimen without a loss of energy. Inelastic scattering can also occur, resulting in a loss of energy due to an interaction of the impinging electrons with the orbital electrons surrounding the nucleus of each atom in the object. Those electrons, which are not or hardly scattered, contribute positively to the image. Those that are considerably deflected are prevented from doing so by apertures in the optical path. As a result differences in light intensity (contrast) are created in the final image, which relate to areas in the object with different scattering potentials. This fact can be deduced from the following formula of Rutherford, which describes the deflection potential of an atom

$$K = \frac{-e.eZ}{r^2}$$

K is deflection potential, e= electron charge, z= positive charge and r =distance from electron to nucleus. As the atomic number increases, their scattering efficiency will also increase. Hence heavy metals can form images with good contrast. The imaging system consists of an objective lens and one or more projector lenses. The chief lens in transmission microscopes is the objective. It determines the degree of resolution in the image. It forms the initial enlarged image of the illuminated portion of the specimen in a plane that is suitable for further enlargement by the projector lens. The projector lens, as it implies, serves to project the final magnified image on the screen or photographic emulsion. The great depth of focus provides the high magnification of the sample. All the TEM images presented in the thesis were recorded on a JEOL model 1200 EX instrument at an accelerating voltage of 120 kV. Samples for TEM have been made by drop coating the sample on the carbon coated copper grids and allowing the solvent to evaporate.

2.6 Scanning electron microscopy

The scanning electron microscope is able to provide images of threedimensional objects because in its normal mode of operation it records not the electrons passing thorough the specimen (as in TEM) but the secondary electrons that are released from the sample by the electron beam impinging on it [7]. The images created without light waves are rendered black and white. The electron beam travels downward through a series of magnetic lenses designed to focus the electrons to a very fine spot. Near the bottom, a set of scanning coils moves the focused beam back and forth across the specimen, row by row. As the electron beam hits each spot on the sample, secondary electrons are generated from its surface. A detector counts these electrons and sends the signals to an amplifier. The final image is built up from the number of electrons emitted from each spot on the sample. Detectors collect the secondary or backscattered electrons, and convert them to a signal that is sent to a viewing screen to produce an image. When the electron beam strikes the sample some of the electrons will interact with the nucleus of the atom. The negatively-charged electron will be attracted to the positive nucleus but if the angle is just right instead of being captured by the gravitational pull of the nucleus it will circle the nucleus and come back out of the sample without slowing down. These electrons are called backscattered electrons because they come back out of the sample. Because they are moving so fast, they travel in straight lines. In order to form an image with backscattered electrons, a detector is placed in their way. When they hit the detector a signal is produced which is used to form the image. Also beam electrons interact with the electrons present in the atom rather than the nucleus. Since all electrons are negatively charged, the beam electrons will repel the electrons present in the sample. This interaction causes the beam electrons to slow down as it repels the specimen electrons, the repulsion may be so great that the specimen electrons are pushed out of the atom, and exit the surface of the sample, these are called secondary electrons. Unlike the backscattered electrons, the secondary electrons are moving very slowly when they leave the sample. Since they are moving so slowly, and are negatively charged, they can be attracted to a detector, which has a positive charge on it. This attraction force allows you to pull in electrons from a wide area and from around corners. The ability to pull in electrons from around corners is what gives secondary electron images a 3-dimensional look. SEM images presented in the thesis were carried out on a Leica stereoscan – 440 instrument. Samples are usually made either by drop coating or supported on silicon wafers.

2.7 Atomic force microscopy (AFM)

The atomic force microscope (AFM) is a very high-resolution type of scanning probe microscope, with demonstrated resolution of fractions of an Angstrom, more than 1000 times better than the optical diffraction limit [8]. The AFM was invented by Binnig, Quate and Gerber in 1986, and is one of the foremost tools for imaging, measuring and manipulating matter at the nanoscale. The AFM consists of a microscale cantilever with a sharp tip (probe) at its end used to scan the specimen surface. The cantilever is typically silicon or silicon nitride with a tip radius of curvature on the order of nanometers. When the tip is brought into proximity of a sample surface, forces between the tip and the sample lead to a deflection of the cantilever according to Hooke's law. The force between the cantiliver tip and the sample surface is very small, usually less than 10^{-9} N. Depending on the situation, forces that are measured in AFM include mechanical contact force, Van der Waals forces, capillary forces, chemical bonding, electrostatic forces, magnetic forces, Casimir forces, solvation forces etc. Typically, the deflection is measured using a laser spot reflected from the top of the cantilever into an array of photodiodes. Other methods that are used include optical interferometry, capacitive sensing or piezoresistive AFM probes. These probes are fabricated with piezoresistive elements that act as a strain gage. Using a Wheatstone bridge, strain in the AFM probe due to deflection can be measured, but this method is not as sensitive as laser deflection or interferometry.If the tip were scanned at a constant height, there would be a risk that the tip would collide with the surface, causing damage. Hence, in most cases a feedback mechanism is employed to adjust the tip-to-sample distance to maintain a constant force between the tip and the sample. Traditionally, the sample is mounted on a piezoelectric tube, that can move the sample in the z direction for maintaining a constant force, and the x and y directions for scanning the sample. Alternately a 'tripod' configuration of three piezo crystals may be employed, with each responsible for scanning in the x,y and z directions. This eliminates some of the distortion effects seen with a tube scanner. The resulting map of the area $s = f(x,y)$ represents the topography of the sample.The AFM can be operated in a number of modes, depending on the application. In general, possible imaging modes are divided into static (also called Contact) modes and a variety of dynamic modes. The primary modes of operation are static (contact) mode and dynamic mode. In the static mode operation, the static tip deflection is used as a feedback signal. Because the measurement of a static signal is prone to noise and drift, low stiffness cantilevers are used to boost the deflection signal. However, close to the surface of the sample, attractive forces can be quite strong, causing the tip to 'snap-in' to the surface. Thus static mode AFM is almost always done in contact where the overall force is repulsive. Consequently, this technique is typically called 'contact mode'. In contact mode, the force between the tip and the surface is kept constant during scanning by maintaining a constant deflection.In the dynamic mode, the cantilever is externally oscillated at or close to its resonance frequency. The oscillation amplitude, phase and resonance frequency are modified by tip-sample interaction forces; these changes in oscillation with respect to the external reference oscillation provide information about the sample's characteristics. Schemes for dynamic mode operation include frequency modulation and the more common amplitude modulation. In frequency modulation, changes in the oscillation frequency provide information about tip-sample interactions.

Frequency can be measured with very high sensitivity and thus the frequency modulation mode allows for the use of very stiff cantilevers. Stiff cantilevers provide stability very close to the surface and, as a result, this technique was the first AFM technique to provide true atomic resolution in ultra-high vacuum conditions. In amplitude modulation, changes in the oscillation amplitude or phase provide the feedback signal for imaging. In amplitude modulation, changes in the phase of oscillation can be used to discriminate between different types of materials on the surface. Amplitude modulation can be operated either in the non-contact or in the intermittent contact regime. In ambient conditions, most samples develop a liquid meniscus layer. Because of this, keeping the probe tip close enough to the sample for short-range forces to become detectable while preventing the tip from sticking to the surface presents a major hurdle for the non-contact dynamic mode in ambient conditions. Dynamic contact mode (also called intermittent contact or tapping mode) was developed to bypass this problem. In dynamic contact mode, the cantilever is oscillated such that it comes in contact with the sample with each cycle, and then enough restoring force is provided by the cantilever spring to detach the tip from the sample.Amplitude modulation has also been used in the non-contact regime to image with atomic resolution by using very stiff cantilevers and small amplitudes in an ultra-high vacuum environment.

2.8 X-ray diffraction (XRD)

X-ray diffraction has been the single most important technique for determining the structure of materials characterized by long-range order [9]. The work presented in the thesis, emphasizes on the synthesis of metal oxides, metal sulfides and metallic nanoparticles. Their crystalline nature and crystal type could be identified from their XRD patterns. When the diffraction pattern is recorded, it shows concentric rings of scattering peaks corresponding to the various interplanar spacing in the crystal lattice. The positions and the intensities of the peaks are used for identifying the underlying structure of the material. X-rays are electromagnetic radiation with typical photon energies in the range of 100 eV - 100 keV. For diffraction applications, only short wavelength x-rays in the range of a few angstroms to 0.1 angstrom (1 keV - 120 keV) are used. Because the wavelength of x-rays is comparable to the size of atoms, they are ideally suited for probing the structural arrangement of atoms and molecules in a wide range of materials. The energetic x-rays can penetrate deep into the materials and provide information about the bulk structure. X-rays are produced generally by either x-ray tubes or synchrotron radiation. In a x-ray tube, which is the primary x-ray source used in laboratory x-ray instruments, x-rays are generated when a focused electron beam accelerated across a high voltage field bombards a stationary or rotating solid target. As electrons collide with atoms in the target and slow down, a continuous spectrum of x-rays are emitted, which are termed Bremsstrahlung radiation. The high-energy electrons also eject the core electrons in atoms through the ionization process. When an electron from higher energy orbital fills the shell, a x-ray photon with energy characteristic of the target material is emitted. Common targets used in x-ray tubes include Cu and Mo, which emit 8 keV and 14 keV x-rays with corresponding wavelengths of 1.54 Å and 0.8 Å, respectively [10].

X-rays primarily interact with electrons in atoms. When x-ray photons collide with electrons, some photons from the incident beam will be deflected away from the direction where they original travel. If the wavelength of these scattered x-rays did not change, the process is called elastic scattering in that only momentum has been transferred in the scattering process. These are the x-rays that are measured in diffraction experiments, as the scattered x-rays carry information about the electron distribution in materials. Diffracted waves from different atoms can interfere with each other and the resultant intensity distribution is strongly modulated by this interaction. If the atoms are arranged in a periodic fashion, as in crystals, the diffracted waves will consist of sharp interference maxima with the same symmetry as in the distribution of atoms. Measuring the diffraction pattern therefore allows us to deduce the distribution of atoms in a material. When certain geometric requirements are met, X-rays scattered from a crystalline solid can constructively interfere, producing a diffracted beam. In 1912, W. L. Bragg recognized the following relationship among several factors.

$$n\lambda = 2d\sin\theta$$

The above equation is called Bragg equation, where n denotes the order of diffraction, λ represents the wavelength, d is the interplanar spacing and θ signifies the scattering angle. The distance between similar atomic planes in a crystal, which, is called the *d* spacing and measured in angstroms. The angle of diffraction is called as the theta angle and measured in degrees. For practical reasons the diffractometer measures an angle twice that of the theta angle. All the XRD data presented in this thesis were carried out on a Philips PW 1830 instrument operating at a voltage of 40 kV and a current of 30 mA with Cu kα radiation. The XRD samples were made by drop coating the aqueous solution of nanoparticles on a glass substrate.

2.9 Energy dispersive analysis of X-rays (EDAX)

Energy Dispersive analysis of X-rays (EDAX) is a chemical microanalysis technique. The technique utilizes X-rays that are emitted from the sample during bombardment by the electron beam to characterize the elemental composition of the analyzed volume. Features or phases as small as about 1 μm can be analyzed using EDAX [11]. When the sample is bombarded by the electron beam of the SEM, electrons are ejected from the atoms comprising the sample's surface. A resulting electron vacancy is filled by an electron from a higher shell, and an X-ray is emitted to balance the energy difference between the two electrons. The EDAX X-ray detector measures the number of emitted X-rays versus their energy. The energy of the X-ray is characteristic of the element from which the X-ray was emitted. A spectrum of the energy versus relative counts of the detected X-rays is obtained and evaluated for qualitative and quantitative determinations of the elements present in the sampled volume. In this thesis we have used EDAX measurements in ordered to determine the chemical composition of various nanoparticles synthesized using biological methods.

2.10 Thermogravimetric analysis (TGA)

Thermal analysis includes a group of techniques in which a physical property of a substance is measured as a function of temperature while the substance is subjected to a controlled temperature program. Thermogravimetry provides a quantitative measurement of any weight change associated with a transition [3]. For TGA, the sample is continuously weighed as it is heated to elevated temperatures. Samples are placed in a crucible or shallow dish that is attached to an automatic recording balance. The automatic null-type balance incorporates a sensing element, which detects a deviation of the balance beam from its null position. One transducer is a pair of photocells, a slotted flag connected to the balance arm, and a lamp. Once an initial balance has been established, any changes in sample weight cause the balance to rotate. This moves the flag so that the light falling on each photocell is no longer equal. The resulting nonzero signal is amplified and fed back as a current to a taut-band torque motor to restore the balance to equilibrium. This current is proportional to the weight change and is recorded on the y-axis of the recorder. The sample container is mounted inside quartz or pyrex housing which is located inside the furnace. Furnace temperature is continuously monitored by a thermocouple whose signal is applied to the x-axis of the recorder. Linear heating rates from 5° C to 10° C are generally employed. All TGA measurements of the nanoparticle samples in the form of purified powders were recorded on a Seiko instruments model TG / DTA 32 instrument at a heating rate of 100 C per minute.

2.11 Superconducting quantum interference device (SQUID)

A superconducting quantum interference device (SQUID) is used to measure extremely weak magnetic signals, they are currently the most sensitive such devices known, with noise levels as low as 3 $\mathrm{fT\cdot Hz}^{-½}$. While a typical fridge magnet is ~0.01 tesla (10^{-2} T) [12]. Using a device called a Josephson junction, a SQUID can detect a change of energy as much as 100 billion times weaker than the electromagnetic energy that moves a compass needle. A Josephson junction is made up of two superconductors, separated by an insulating layer so thin that electrons can pass through. A SQUID consists of tiny loops of superconductors employing Josephson junctions to achieve superposition: each electron moves simultaneously in both directions. Because the current is moving in two opposite directions, the electrons have the ability to perform as qubits (that theoretically could be used to enable quantum computing). SQUIDs have been used for a variety of testing purposes that demand extreme sensitivity, including engineering, medical, and geological equipment. Because they measure changes in a magnetic field with such sensitivity, they do not have to come in contact with a system that they are testing. SQUIDs are usually made of either a lead alloy (with 10% gold or indium) and/or niobium, often consisting of the tunnel barrier sandwiched between a base electrode of niobium and the top electrode of lead alloy. A radio frequency (RF) SQUID is made up of one Josephson junction, which is mounted on a superconducting ring. An oscillating current is applied to an external circuit, whose voltage changes as an effect of the interaction between it and the ring. The magnetic flux is then measured. A direct current (DC) SQUID, which is much more sensitive, consists of two Josephson junctions employed in parallel so that electrons tunneling through the junctions demonstrate quantum interference, dependent upon the strength of the magnetic field within a loop. DC SQUIDs demonstrate resistance in response to even tiny variations in a magnetic field, which is the capacity that enables detection of such minute changes. One of the device's most promising uses is in magnetoencephalography (MEG), the process of measuring magnetic fields to enable brain imaging. Physical processes, such as muscular or neural activity, in humans (and other animals) create magnetic fields as small as a thousand billionth of a tesla [13].

2.12 Mossbauer spectroscopy

Mossbauer spectroscopy is a spectroscopic technique based on the Mossbauer effect. The Mossbauer effect, a physical phenomenon discovered by Rudolf Mossbauer in 1957, refers to the resonant and recoil-free emission and absorption of gamma rays by atoms bound in a solid form [14]. gamma rays are produced by nuclear transitions: from an unstable high-energy state, to a stable low-energy state. The energy of the emitted gamma ray corresponds to the energy of the nuclear transition, minus an amount of energy that is lost as recoil to the emitting atom. If the lost "recoil energy" is small compared with the energy linewidth of the nuclear transition, then the gamma ray energy still corresponds to the energy of the nuclear transition, and the gamma ray can be absorbed by a second atom of the same type as the first. This emission and subsequent absorption is called resonance. Additional recoil energy is also lost during absorption, so in order for resonance to occur the recoil energy must actually be less than half the linewidth for the corresponding nuclear transition. In its most common form, Mossbauer Absorption Spectroscopy, a solid sample is exposed to a beam of gamma radiation, and a detector measures the intensity of the beam that is transmitted through the sample, which will change depending on how many gamma rays are absorbed by the sample. The atoms in the source emitting the gamma rays are the same as the atoms in the sample absorbing them. It is thanks to the Mössbauer effect that a significant fraction of the gamma rays emitted by the atoms in the source do not lose any energy due to recoil and thus have almost the right energy to be absorbed by the target atoms. The gamma-ray energy is varied by accelerating the gamma-ray source through a range of velocities with a linear motor. The relative motion between the source and sample results in an energy shift due to the Doppler effect. In the resulting spectra, gamma-ray intensity is plotted as a function of the source velocity. At velocities corresponding to the resonant energy levels of the sample, some of the gamma-rays are absorbed, resulting in a drop in the measured intensity and a corresponding dip in the spectrum. The number, positions, and intensities of the dips (also called peaks) provide information about the chemical environment of the absorbing nuclei and can be used to characterize the sample.In order for Mössbauer absorption of gamma-rays to occur, the gamma-ray must be of the appropriate energy for the nuclear transitions of the atoms being probed, which is almost always achieved by having the same atoms of the same isotope in both the source and the target. Also, the gamma-ray energy should be relatively low, otherwise the system will have a low recoil-free fraction resulting in a poor signal-to-noise ratio. Only a handful of elemental isotopes exist for which these criteria are met, so Mössbauer spectroscopy can only be applied to a relatively small group of atoms including: ^{57}Fe, ^{129}I, ^{119}Sn, and ^{121}Sb. Of these, ^{57}Fe is by far the most common element studied using the technique. In the current thesis we have used Mossbauer spectroscopy to differentiate between biogenic magnetite and maghaemite.

2.13 Polymerase Chain Reaction (PCR)

Polymerase chain reaction (PCR) is a biochemistry and molecular biology technique invented by Kary Mullis in 1983 for enzymatically replicating DNA without using a living organism [15]. Like amplification using living organisms, the technique allows a small amount of DNA to be amplified exponentially. As PCR is an *in vitro* technique, it can be performed without restrictions on the form of DNA, and it can be extensively modified to perform a wide array of genetic manipulations. PCR is commonly used in medical and biological research labs for a variety of tasks, such as the detection of hereditary diseases, the identification of genetic fingerprints, the diagnosis of infectious diseases, the cloning of genes, paternity testing, and DNA computing. Beginning with a single molecule of the genetic material DNA, the PCR can generate 100 billion similar molecules in very short time. PCR is used to amplify specific regions of a DNA strand. This can be a single gene, just a part of a gene, or a non-coded sequence. PCR typically amplifies only short DNA fragments, usually up to 10 kilo base pairs (kb).

Certain methods can copy fragments up to 25 kb in size. PCR, as currently practiced, requires several basic components. These components are:

- *DNA template,* which contains the region of the DNA fragment to be amplified
- Two *primers,* which determine the beginning and end of the region to be amplified (see following section on primers)
- *Taq polymerase* (or another durable polymerase), a DNA polymerase which copies the region to be amplified
- *Deoxynucleotide triphosphates,* (dNTPs) from which the DNA polymerase builds the new DNA
- *Buffer solution,* which provides a suitable chemical environment for the DNA Polymerase
- *Divalent cation,* magnesium or manganese ions or *Monovalent cation,* potassium ions

The PCR process is carried out in a thermal cycler. This is a machine that heats and cools the reaction tubes within it to the precise temperature required for each step of the reaction. The lid of the thermal cycler is heated to prevent condensation on the inside of the reaction tube caps. Alternatively, a layer of oil may be placed on the reaction mixture to prevent evaporation. Typical reaction volumes range from 15-100 µl. The PCR process usually consists of a series of twenty to thirty-five cycles. Each cycle consists of three steps.

1. The double-stranded DNA has to be heated to 94-96 °C usually for 1-2 minutes in order to separate the strands. This step is called *denaturing*; it breaks apart the hydrogen bonds that connect the two DNA strands. Prior to the first cycle, the DNA is often denatured for an extended time to ensure that both the template DNA and the primers have completely separated and are now single-strand only.
2. After separating the DNA strands, the temperature is lowered for 2 minutes so the primers can attach themselves to the single DNA strands. This step is called annealing. The temperature of this stage depends on the primers and is usually 5 $^{\circ}$C below their melting temperature (45-65 °C). A wrong temperature during the annealing step can result in primers not binding to the template DNA at all, or binding at random.
3. Finally, the DNA polymerase has to copy the DNA strands. It starts at the annealed primer and works its way along the DNA strand. This step is called elongation. The

elongation temperature depends on the DNA polymerase. Taq polymerase elongates optimally at a temperature of 72 °C. The time for this step depends both on the DNA polymerase itself and on the length of the DNA fragment to be amplified.

2.14 DNA sequencing

DNA sequencing is the process of determining the nucleotide order of a given DNA fragment, called the DNA sequence. For thirty years a huge fraction of DNA sequencing has been achieved using the chain termination method [16], developed by Frederick Sanger in 1975. This technique uses sequence-specific termination of an *in vitro* DNA synthesis reaction using modified nucleotide substrates. 'Next generation' sequencing technologies, such as Pyrosequencing and 454 Sequencing, are recently delivering noticeable amounts.

Chain termination method: In chain terminator sequencing (Sanger sequencing), which is possible because of the availability of clones and/or thermal cycling DNA amplification, extension is initiated at a specific site on the template DNA by using a short oligonucleotide 'primer' complementary to the template at that region. The oligonucleotide primer is extended using a DNA polymerase. Included with the primer and DNA polymerase are the four deoxynucleotide bases (DNA building blocks), along with a low concentration of a chain terminating nucleotide (most commonly a di-deoxynucleotide). Limited incorporation of the chain terminating nucleotide by the DNA polymerase results in a series of related DNA fragments that are terminated only at positions where that particular nucleotide is used. The fragments are then size-separated by electrophoresis in a slab polyacrylamide gel, or more commonly now, in a narrow glass tube (capillary) filled with a viscous polymer. The classical chain termination method or Sanger method first involves preparing the DNA to be sequenced as a single strand. The DNA sample is divided into four separate samples. Each of the four samples has a primer, the four normal deoxynucleotides (dATP, dGTP, dCTP and dTTP), DNA polymerase, and only one of the four dideoxynucleotides (ddATP, ddGTP, ddCTP and ddTTP) added to it. The dideoxynucleotides are added in limited quantities. The primer or the dideoxynucleotides are either radiolabeled or have a fluorescent tag. As the DNA strand is elongated the DNA polymerase catalyses the joining of deoxynucleotides to the corresponding bases. The bases available to the polymerase are a mixture of normal and tagged/terminating nucleotides. So if the appropriate dideoxynucleotide happens to be near the polymerase, it is incorporated into the elongating DNA strand. The tagged/terminating base prevents further elongation because a dideoxynucleotide lacks a crucial 3'-OH group. So a series of DNA fragments are produced with random length and (base-nonspecific, hence the four separate reactions) tags. Unfortunately, only short stretches of DNA can be sequenced in each reaction. The polymerase chain reaction (PCR) technique is limited to 10,000 base-pairs and the maximum length of extension is dictated by the concentration of tagged/terminating nucleotides. The DNA is then denatured and the resulting fragments are separated (with a resolution of just one nucleotide) by gel electrophoresis, from longest to shortest. Each of the four DNA samples is run on one of four individual lanes (lanes A, T, G, C) depending on which dideoxynucleotide was added. Depending on whether the primers or dideoxynucleotides were radiolabeled or fluorescently labeled, the DNA bands can be detected by exposure to X-rays or UV-light and the DNA sequence can be directly read off the gel. In the image on the right, X-ray film was exposed to the dried gel, and the dark bands indicate the positions of the DNA molecules of different lengths. A dark band in a lane indicates a chain termination for that particular DNA subunit and the DNA sequence can be read off as indicated. There can be various problems with sequencing through the Sanger method and the problems of this method are the standard problems one would encounter in PCR. There are two sub-types of chain-termination sequencing. In the original method, the nucleotide order of a particular DNA template can be inferred by performing four parallel extension reactions using one of the four chain-terminating bases in each reaction. The DNA fragments are detected by labelling the primer with a base-nonspecific label, radioactive phosphorus for example, prior to performing the sequencing reaction. The four reactions would then be run out in four adjacent lanes on a slab polyacrylamide gel. The Sanger method can be done using primers that add a non-specific label on the 5' end of the PCR product. Instead of the label being included in the terminating nucleotide, the label is in the primer. The difference between this and the radioactive Sanger method is that the label is at the 5' end instead of the 3' end. Four separate reactions are still required, but the dye labels can be read using an optical system instead of film or phosphor storage screens, so it is faster, cheaper, and easier to automate. This approach is known as 'dye-primer sequencing' [17].

Dye terminator method: An alternative to the labelling of the primer is to label the terminators instead, commonly called 'dye terminator sequencing'. The major advantage of this approach is that the complete sequencing set can be performed in a single reaction, rather than the four needed with the labeled-primer approach. This is accomplished by labelling each of the dideoxynucleotide chain-terminators with a separate fluorescent dye, which fluoresces at a different wavelength. This method is easier and quicker than the dye primer approach, but may produce more uneven data peaks (different heights), due to a template dependent difference in the incorporation of the large dye chain-terminators. This problem has been significantly reduced with the introduction of new enzymes and dyes that minimize incorporation variability. This method is now used for the vast majority of sequencing reactions as it is both simpler and cheaper. The major reason for this is that the primers do not have to be separately labelled although this is less of a concern with frequently used 'universal' primers [18].

2.15 Gel electrophoresis

The term electrophoresis describes the migration of a charged particles under the influence of an electric field. Most of biomolecules such as proteins and nucleic acids possess ionizable functional groups and therefore, exist in solution as electrically charged species either as cations or anions [19]. Under the influence of electric field these charged particles will migrate either to cathod or anode depending the nature of their net electrical charge. The equipment required for electrophoresis consists basically of two items, a power pack and an electrophoresis unit. Electrophoresis units are available for running either vertical or horizontal gel systems. In this thesis, we have used a vertical gel system. Vertical slab gel units are commercially available and routinely used to separate proteins in acrylamide gels. The gel is formed between to glass plates that are clamped together but held apart by plastic spacers. Gel dimensions are typically 12 cm x 14 cm, with a thickness of 0.5 to 1 mm. A plastic comb is placed in the gel solution and is removed after polymerization to provide loading wells for samples. When the apparatus is assembled, the lower electrophoresis tank buffer surrounds the gel plates and affords some cooling of the gel plates. The electrophoresis is carried out in an appropriate buffer, which is essential to maintain a constant state of ionization of the molecules being separated.

Electrophoresis of proteins

Sodium dodecyl sulphate-polyacrylamide gel electrophoresis: SDS-polyacrylamide gel electrophoresis (SDS-PAGE) is the most widely used method for analyzing protein mixtures qualitatively. It is particularly useful for monitoring protein purification and, because the method is based on the separation of proteins according to size, the method can also be used to determine the relative molecular mass of proteins. SDS (CH3-(CH2)10- CH2OSO3 -Na+) is an anionic detergent. The protein samples to be run on SDS-PAGE are firstly boiled for 5 min in sample buffer containing β-mercaptoethanol and SDS. The mercaptoethanol reduces any disulphide bridges present that are holding together the protein tertiary structure, and the SDS binds strongly to, and denatures the protein. Each protein in the protein mixture is therefore fully denatured by this treatment and opens up into a rod-shaped structure with a series of negatively charged SDS molecules along the polypeptide chain. The original negative charge on the molecule is therefore completely swamped by the negatively charged SDS molecules and hence, the polypeptide chains move in an SDS-PAGE according to their relative masses [20]. The protein fraction responsible for the control of mineral morphology was analyzed by 10 % SDS-PAGE carried out at pH 8.2.

Electrophoresis of DNA:

For majority of DNA samples, electrophoretic separation is carried out in agarose gels due to considerably large size of DNA. Separation of DNA in agarose gels is achieved due to resistance to its movement caused by the gel matrix.The largest molecules will have most the difficulty passing through the gel pores, whereas the smallest molecules will be relatively unhindered. Consequently the mobility of DNA molecules during gel electrophoresis will depend on their size. While passing through the pores, a DNA molecule will experience drag, so the longer the molecule, the more it will be retarded by each pore. The gel concentration has to be chosen so as to suit the size range of DNA molecules to be separated. Gels containing 0.3 % agarose will separate double stranded DNA molecules of between 5 and 60 kb size, whereas 2 % gels are used for samples of between 0.1 and 3 kb. DNA molecules in the range of 0.5 % to 10 kb are routinely separated on 0.8 % agarose gels. Since agarose gels separate DNA according to size, the molecular weight of DNA fragment may be determined from its electrophoretic mobility by running a number of standard DNA molecular weight markers. DNA gels are invariably run as horizontal, submarine or submerged gels, so named because such a gel is totally immersed in buffer solution. For the analysis of DNA two buffer systems namely Tris-borate EDTA (TBE) and Tris-acetate EDTA (TAE) depending on the size of DNA molecules to be analyzed. Agarose, dissolved gel buffer by boiling is poured onto a glass or plastic plate, surrounded by a wall of adhesive tape or a plastic frame to provide a gel about 3 mm in depth. Loading wells are formed by placing a plastic well-forming template or comb in the poured gel solution, and removing this gel solution once the gel has set. The gel is placed in the electrophoresis tank, covered with buffer, and samples loaded by directly injecting the samples into the wells. Samples are prepared by dissolving them in a buffer solution that contains sucrose, glycerol or Ficoll, which makes the solution dense and allows it to sink at the bottom of the well.A bye such as bromophenol blue is also included in the sample solvent to make it easier to see the sample that is being loaded and also acts as a marker of the electrophoresis front. General purpose gels are approximately 25 cm long and 12 cm wide, and are run at a voltage gradient of about 1.5 V cm^{-1} overnight. For rapid analysis of DNA that do not need extensive separation, it is common to use minigels that are less than 10 cm long. In this way information can be obtained in 2 to 3h [21].

In present thesis we have used 0.8 % to 1 % agarose gels for the analysis of PCR amplified DNA and genomic DNA respectively using TBE buffer. Further, for the analysis of charge on the surface of metallic nanoparticles synthesized using biological methods 1 % agarose gels are used in TAE buffer.

2. 16 References

[1] Li, M.; Schnablegger, H.; Mann, S. *Nature* **1999**, *402*, 393.

[2] Wang, Z. L. Characterization of nanophase materials, **2000**, Wiley-VCH, Weinheim,

[3] Willard, H. H.; Merritt, L. L.; dean, J. A. Instrumental methods of analysis, 1951, D van Nostrad Publications, Torranto,.

[4] (a) McCrackin, F. L.; Passaglia, E.; Stromberg, R. R.; Steinberg, H. L. *J. Res. Natl. Inst. of Stand. & Tech.* **2001**, *106*, 589. (b) George, W.O.; Mcintyre, P.S. *Infrared Spectroscopy: Analytical Chemistry by open learning*, **1987,** John Wiley, USA.

[5] (a) Rendell, D.; Mowthorpe, D. *Fluorescence and Phosphorescence Spectroscopy*: *Analytical Chemistry by open learning*. **1987**, John Wiley & Sons, USA.

[6] Williams, D. B. Transmission Electron Microscopy, A textbook for Material Science, **1996**, Plenum Press. New York and London.

[7] Everheart, T. E., Hayes, T. L. *Sci. Am*. **1972**, *226*, 55.

[8] Binnig, G., Quarter, C. F., Gerber, C. *Phys. Rev. Lett*. **1986**, *56*, 930.

[9] Cullity, B. D. Elements of X-ray diffraction, **1978**, Addison-Wesley Publishing Co.

[10] Azaroff, L. V. X-Ray diffraction, **1974**, McGraw Hill company.

[11] Lawes, G. *Scanning electron microscopy and X-ray microanalysis: Analytical chemistry by open learning*, 1987, John Wiley & sons.

[12] Gersten, G., Smith, F. W. The Physics and Chemistry of Materials. 2001, Wiley.

[13] http://www. hyperphysics.phy-astr.gsu.edu/hbase/solids/squid.html.

[14] ftp://ftp.wiley.com/public/sco_tech_med/materials

[15] Newton, C. R., Graham, A. *PCR* 2nd ed. **1997**, Bios Scientific, Oxford.

[16] Sanger, F., Nicklen, S., Coulson, A. R. *Proc. Natl. Acad. Sci. USA* **1977**, *74*, 5463.

[17] Brown, T.A. *Genomes*, 2nd ed. **2002**, Garland Science, New York.

[18] Alphey, L. *DNA Sequencing* **1997**, Bios Scientific, Oxford,.

[19] Wilson, K., Walker, J. Practical Biochemistry. 5th ed. **2003**. Cambridge University Press, Cambridge**.**

[20] Walker, J. M. The Proteins Protocols Handbook. **1996**, Humana Press.

[21] Sambook, J., Fritsch, E., Manniatis, T., Molecular cloning: A Laboratory manual, 2nd ed., 1989, Cold Spring Harbor Laboratory press, New York.

Chapter III

Bacteria and fungi mediated biosynthesis of magnetic iron oxide nanoparticles

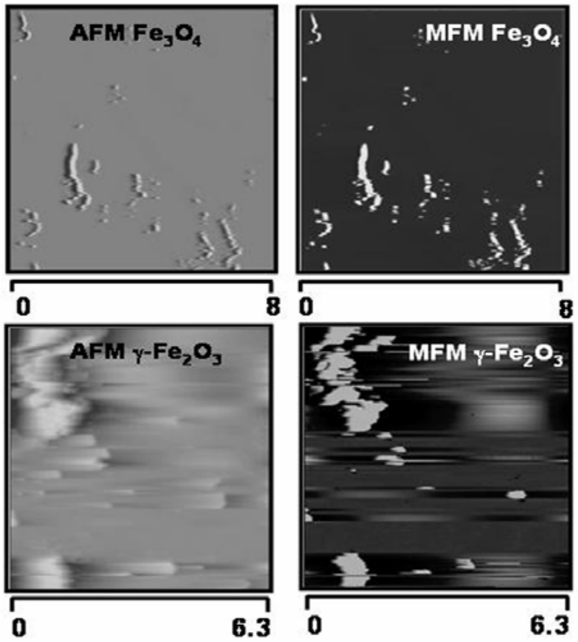

This chapter describes a biological route for the synthesis of magnetic iron oxide nanoparticles mediated by bacteria and fungi. A bacterium, serendipitously isolated from our laboratory, was explored for the synthesis of magnetite and maghaemite nanoparticles. Two fungi, namely, *Fusarium oxysporum* and *Verticillium* sp. were assessed for the biosynthesis of magnetite. In all processes, synthesis of magnetic iron oxide nanoparticles is shown to occur under aerobic conditions, which was not demonstrated in microorganisms until now. Magnetic measurements performed on the iron oxide nanoparticles synthesized by the methods described here show superparamagnetic behavior. Preliminary biochemical analysis of all the reactions showed the induction of new proteins in bacterial cells as well as in fungi. Also, the time required for the synthesis of iron oxide nanoparticles by the methods described here is considerably smaller than existing biosynthetic methods involving magnetotactic bacteria and iron reducing bacteria.

Part of the work presented in this chapter has been published or communicated in the following journals: (1) A. Bharde, A. Wani, Y. Shouche, P. A. Joy, B. L. V. Prasad, M. Sastry *J. Am. Chem. Soc* 2005, *127*, 9326. (2) A. Bharde, D. Rautray, I. Sarkar, M. Seikh, M. Sanyal, A. Ahmad, M. Sastry *small*, 2006, *2*, 135. (3) Bharde, A. A., Parekh, R., Baidakova, M., Shouche, Y., Enoki, T., Hannoyer, B., Ogale, S., Prasad, B.L.V., Sastry M. *Nat. Mater.* (2007).

3.1 Introduction

Oxide nanoparticles occupy an important place among nanomaterials due to their enormous applications ranging from catalysis to electronics to biomedics [1]. Among the vast range of oxide nanoparticles, iron oxide nanoparticles like magnetite and maghaemite are unique due to their technological interest. Magnetic iron oxides are a versatile class of material that enables a wide range of technologies, many of which are contingent with their distinct magnetic properties. Hence, there is a great interest in fabricating iron oxide based magnetic materials. Iron based magnetic oxides have been exploited for magnetic recording and multi-terabit magnetic storage devices [2], ferrofluids [3], as contrast enhancers in magnetic resonance imaging [4] and in other biomedical applications like separation [5], diagnostics [6] and drug delivery [7].

Current chemical protocols in vogue for the synthesis of magnetic iron oxides include sol-gel, forced hydrolysis, sonochemical and electrochemical methods [1]. Some of these methods require harsh experimental conditions of high temperature and pressure and therefore are considered to be energy intensive. Most of chemical synthesis procedures employ specialty chemicals and often yield particles in non-polar organic solutions [8] thereby precluding biomedical applications. Toxic and environmentally harmful chemicals like surfactants are uniformly utilized for size and shape controlled synthesis of iron oxide nanoparticles. There are few reports which describe formulation of magnetic iron oxides in aqueous medium [9]. However, these methods require stringent control over reaction conditions and employ strong alkalis like sodium hydroxide.

In contrast to chemical synthesis methods, biological synthesis of iron based inorganic material is characterized by ambient experimental conditions of temperature, pH and pressure. Iron is the most essential trace element for all the forms of life since it is at the center of most of the biochemical processes that occur inside the living cell [10]. Many unicellular as well as multicellular living forms synthesize iron oxide nanoparticles [11]. Biomineralization of magnetite has been shown to occur in diverse range of organisms like algae, insects, mollusks, fish, birds and even humans [12]. However, biological synthesis of iron oxide by microorganisms has been extensively studied. Considerable amount of magnetite is deposited by magnetotactic and iron reducing bacteria in nature. Magnetotactic bacterium was first discovered by R. P. Blackmore in 1975 as a motile, aquatic life form that swims along geomagnetic field lines of the earth [13]. Magnetite synthesis in magnetotactic bacteria occurs in a unique intracellular structure called magnetosomes. Magnetosome is a lipid bilayer structure, which houses highly ordered magnetite crystals aligned parallel to the cellular axis [14]. The magnetite synthesized by magnetotactic bacteria shows species specific morphology and size variation [14].

Magnetotactic bacteria are a heterogeneous group of fastidious prokaryotes that display a myriad of cellular morphologies including coccoid, rod shaped, vibriod, helical and even multicellular [15]. Magnetite crystals are typically 35-120 nm long, which is a permanent single domain size range for magnetite. In most of the magnetotactic bacteria, the magnetosomes are arranged in single or multiple chains. Magnetic interactions between the magnetosomes in chain cause their magnetic dipole moments to orient parallel to each other along the length of the chain. Thus, the overall magnetic moment is maximized by linear arrangement of magnetosomes enabling cells as tiny, self- propelled magnetic compass needles [16]. Magnetite crystals synthesized inside the magnetosomes shows unusual crystal morphologies [14].

Magnetite formation in magnetotactic bacteria is a complex process which involves numerous discrete steps. The first step in magnetite synthesis appears to be synthesis of magnetosome vesicles. However, it has recently been shown that magnetosome vesicles can exist before magnetite biomineralization [17]. The formation of magnetosome vesicles is followed by iron reduction from Fe (III) to Fe (II) with its subsequent uptake and transport inside the vesicle. Iron uptake in magnetotactic bacteria is believed to occur either by siderophores or by iron reduction [18]. The last step in magnetite formation seems to be the controlled biomineralization of magnetite.

Siderophores are low molecular weight (05-1.5 kDa) ferric iron chelating molecules synthesized by most bacteria under iron limiting conditions [19]. Most magnetotactic bacteria are known to synthesize one or more types of siderophore [18, 20]. Iron is likely to be taken by a cation efflux protein, Mag A in *Magnetospirillum magneticum* AMB-1 in an energy dependent process. Mag A protein was found to be present on cellular as well as magnetosome membrane and function as a H^+/Fe(II) antiporter [16]. Once iron is taken inside the cell, it is thought to be reoxidized into hydrous Fe (III) oxide, which is similar to the mineral ferihydrite by the action of membrane bound iron oxidase. In the final step of magnetite formation, one third of the Fe (III) ions in the hydrous oxide are reduced and finally dehydrated to magnetite [21]. Thus, magnetite formation in magnetotactic bacteria is studied in great depth to understand the biomolecular mechanism underlying the process. Matsunaga *et a*l have given a detailed account of genetic and biochemical basis of magnetite formation in a magnetotactic bacterium *Magnetospirillum magneticum* AMB-1[22].

Another group of bacteria, generally referred to as iron reducing bacteria, is also known to synthesize magnetite nanoparticles. Unlike magnetotactic bacteria, iron reducing bacteria synthesize magnetite extracellularly in the surrounding environment [23]. Iron reducing bacteria generally precipitate ultra-fine magnetite granules under strictly anaerobic conditions. However, unlike magnetotactic bacteria, iron reducing bacteria synthesize magnetite for energy generation. Magnetite is synthesized by coupling the oxidation of organic mater to the reduction of ferric iron during the metabolism of the bacteria [24]. Generally, most of the iron reducing bacteria utilizes poorly crystalline ferrihydrite as an electron acceptor which in turn is reduced to magnetite.

The morphology and size of magnetite synthesized by iron reducing bacteria is quite distinct from that synthesized by magnetotactic bacteria. There is no evidence of association of any cellular material (e.g. lipid bilayer in case of magnetotactic bacteria) with the magnetite that is extracellularly precipitated. However, the association of exopolysaccharides with magnetite has been observed in *S. putrefaciens* [25]. The magnetite particles are usually round and oval in shape and range in size from 10-50 nm [24]. The mechanism of magnetite formation by iron reducing bacteria is much simpler than that of magnetotactic bacteria. *Geobacter* metallireducens GS-15 utilizes ferric iron as a terminal electron acceptor and reduces it to tabular single domain magnetite [26]. Most of the iron reducing bacteria like *Shewanella*, *Geobacter, Desulfovibrio and Thiobacillus* contain a membrane bound Fe (III) reductase that reduces ferric iron. Also, these bacteria are shown to contain several membrane bound *c*-type cytochromes which are involved in the electron transport [27]. Since magnetite formation is an end-product of an energy generating metabolism, on per cell basis, iron reducing bacteria like *Geobacter* generates 5000 times more magnetite than a magnetotactic bacterium [28].

Outline of the present work:

The current chapter describes the biological synthesis of magnetic iron oxide nanoparticles using bacteria and fungi. Until now, biosynthesis of magnetite has been considered the domain of magnetotactic and iron reducing bacteria. In this work, it is shown that extracellular biosynthesis of magnetite at room temperature can occur *under totally aerobic conditions.* The first part of the chapter describes biosynthesis of iron oxides like magnetite (Fe_3O_4) and maghaemite (γ-Fe_2O_3) by using a bacterium *Actinobacter* spp. The magnetic iron oxides so formed show superparamagnetic behavior at room temperature. The second part of the chapter describes biosynthesis of magnetite (Fe_3O_4) nanoparticles using fungi. Magnetite nanocrystals thus formed show ferromagnetic transition at low temperatures. The most unusual and remarkable feature of the biosynthetic protocols that are described here is the use of non-conventional microbes for the synthesis of nanomaterials.

Part I. Biosynthesis of magnetite and maghaemite nanocrystals using *Actinobacter* spp.

3.2 Isolation and identification of *Actinobacter* spp.

A bacterium *Actinobacter spp*. was discovered in a serendipitous manner which was growing in aqueous mixture of potassium ferri/ferrocyanide salts. Typically, *Actinobacter* spp. was isolated from 2:1 molar aqueous solution of $K_3Fe(CN)_6$ and $K_4Fe(CN)_6$ respectively, which was stored over a period of week. The bacterial growth was observed as turbidity showing the presence of some suspended matter in the mixture. That this indeed is a microbial growth could be conclusively shown by streaking a 50μl of ferri/ferrocyanide mixture on Luria agar plate. The bacterium was preserved in solution of 30% (v/v) glycerol and Luria broth (1:1 ratio). The culture was further maintained on Luria agar slant at 4 °C.

For identification, the bacterium was freshly cultured on Luria agar, incubated at room temperature and analyzed with molecular taxonomy method of 16S rRNA sequencing using bioinformatics tools. DNA extraction for 16S rRNA amplification and sequencing was carried out using standard phenol-chloroform extraction procedure [29]. The gene for 16S rRNA was amplified by Polymerase Chain Reaction (PCR) by a set of eubacterial universal bacterial primers [30] and then sequenced from 3′ end. The sequence was initially analyzed at NCBI server using BLAST program. Similarity matrix of BLAST resulted sequence was prepared using Dnadist program in PHYLIP analysis package using Jukes Cantor corrections. The region of 16S rRNA gene used for analysis gives reliable information about phylogenetic affiliation [31]. Around 789 bases from 3′ end of PCR amplified gene was used for phylogenic analysis. The sequence showed maximum similarity (98.2%) with *Actinobacter* strain EC5 (Genbank accession no. AY 337600). The isolate thus could be assigned to the genus *Actinobacter* (GenBank accession no. AY 864333).

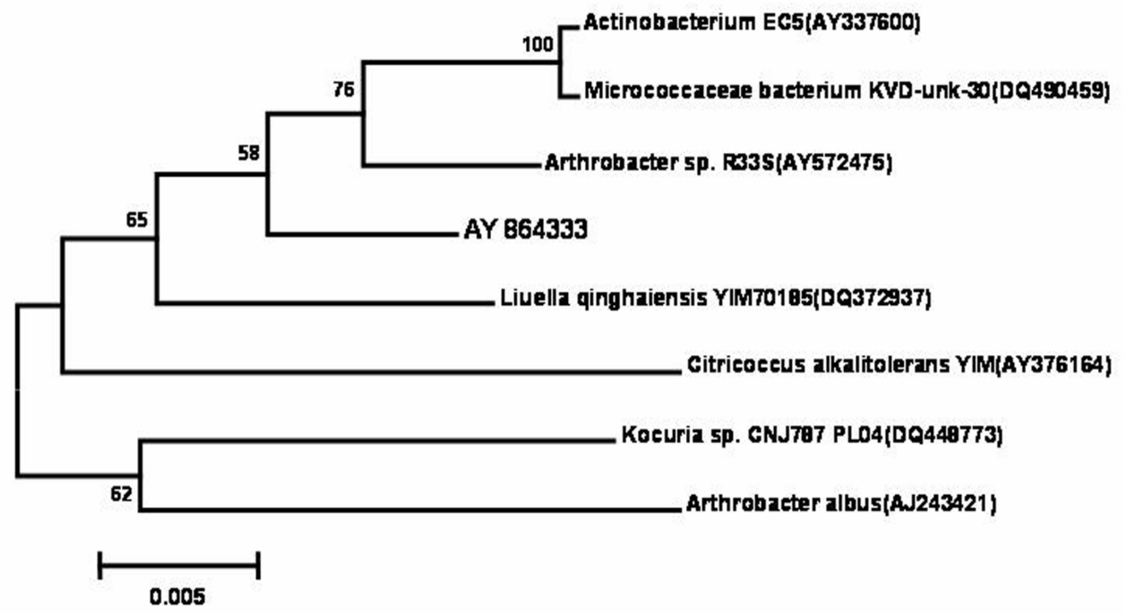

Figure 3.1 *Phylogenetic affiliation based on 16S rRNA gene sequence comparisons over 900 bases showing the relationship between closest cultivable relatives and isolate MB1 NCL. The bar represents distance values calculated in MEGA 3.1 and values at node represent percentage of 1000 bootstrap replicates. Number in parenthesis represents GenBank accession numbers.*

Figure 3.1 represents phylogenetic affiliation of *Actinobacter* spp. with the closest cultivable strains. The analysis was performed by sequencing the first 943 bases of 16 S r- RNA gene. Based on this analysis it is clear that our isolate shows maximum similarity with the group *Actinobacterium* and therefore could be considered as a species of the genus *Actinobacter.*

3.3 Biosynthesis of nanocrystalline magnetite (Fe_3O_4)

This part of the chapter describes the extracellular, aerobic biosynthesis of magnetite nanoparticles using *Actinobacter* spp.

3.3.1 Experimental details

In a typical experiment, seed culture of Gram-positive bacterium *Actinobacter spp.* was prepared in Luria broth (LB) for 24 h as an inoculum. The inoculum was then transferred to 100 ml of LB and incubated at 37 °C for 24 h at 150 rpm till the bacterium entered into the late log phase of the growth cycle. Filter sterilized aqueous mixture of $K_3Fe(CN)_6$ and $K_4Fe(CN)_6$ was then added to the bacterial culture and the flask was incubated for another 72 h on a shaker (150 rpm) at 37 °C. Magnetite synthesized in culture medium was harvested from bacterial biomass by centrifugation at 5000 rpm (2560 X g). The supernatant containing magnetite was then lyophilized and used for further analysis by Transmission electron microcopy (TEM), X-ray diffraction analysis (XRD), Fourier transformed infrared spectroscopy (FTIR), Magnetic force microscopy (MFM), Mossbauer spectroscopy, magnetic measurements etc. The biochemical investigation of magnetite formation was carried out by analysis of protein profile and enzymatic assays.

3.3.2 Transmission electron microscopic analysis

Figure 3.2 shows TEM images of magnetite nanoparticles synthesized after 48 h and 72 h of reaction between ferri/ferrocyanide salts and *Actinobacter* spp., respectively. After 24 h of reaction, a number of quasi-spherical particles were observed with 10- 20 nm size range (Figure 3.2A and B). These nanoparticles appear to be well separated from each other since they are stabilized by the proteins present on the surface. In most of the magnetite nanocrystals, twinning was observed indicating the presence of defects in the crystal structure (Figure 3.2B). When the bacterial culture is incubated further along with the ferri/ferrocyanide mixture, after about 72 h of the reaction the quasi-spherical structure of magnetite nanoparticle is completely lost. Prolonged incubation yielded uniform cubical nanoparticles of edge length of 50-150 nm (Figure 3.2C) suggesting the assembly of spherical nanoparticles into cubic superstructures. High magnification image of the cubes reveal voids that could arise from aggregation of smaller spherical nanoparticles (inset, Figure 3.2C). Even under these conditions of aggregation, the magnetite nanoparticles were extremely stable in solution for weeks suggesting stabilization of the particle surface with bio-organic molecules secreted by *Actinobacter* spp.

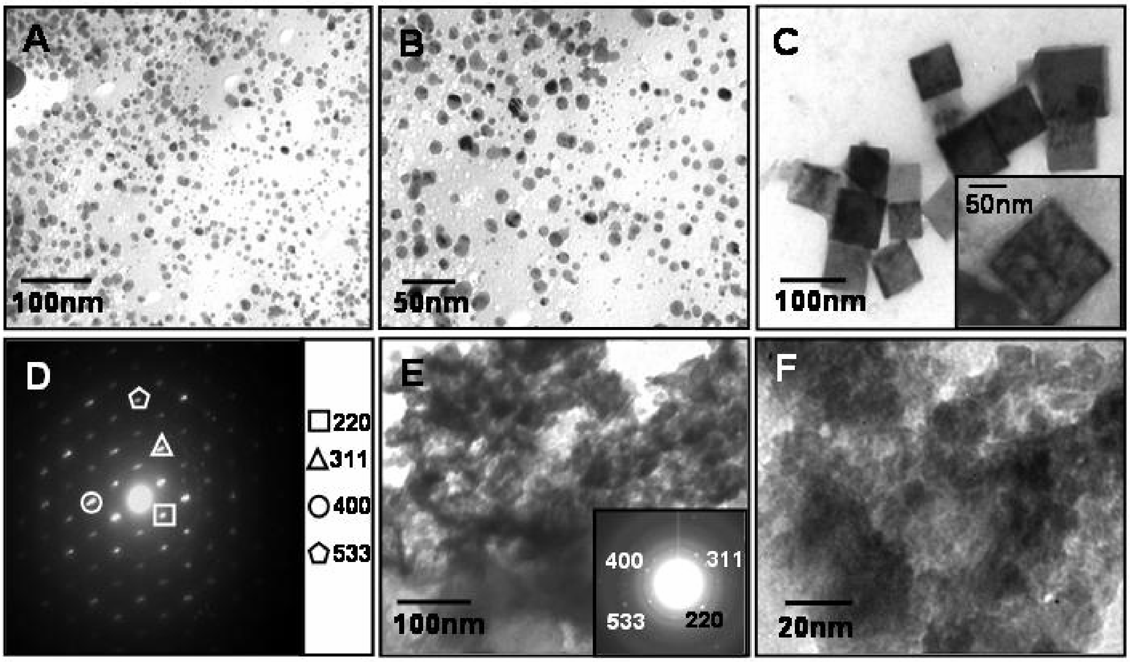

Figure 3.2 *TEM images of as synthesized magnetite nanoparticles synthesized after 24 h (A & B) and 72 h (C) of reaction between Actinobacter spp. and ferri/ferrocyanide mixture. SAED pattern (D) shows that the particles are single crystals and the diffraction spots could be indexed on the basis of the magnetite structure. Calcination of the as-synthesized nanoparticles leads to aggregation with drastic change in overall morphology (E and F). Inset in (E) shows SAED pattern obtained from calcined nanoparticles.*

Selected area diffraction analysis showed the presence of well defined diffraction spots indicating that nanoparticles are crystalline. The diffraction spots could be indexed on the basis of magnetite crystal structure [32].

While the as-synthesized powdered magnetite nanoparticles were calcined at 350 °C for 3 h, the morphology of nanoparticles was drastically altered. The cubic assembly of the magnetite nanoparticles is completely destroyed and the particles are uniformly dispersed over the grid surface. Some amount of sintering of the particles also appears to have occurred with the growth of individual nanocrystallites indicating the formation of aggregates with dimensions around 20 nm (Figure 3.2E and G). This change in the morphology of as-synthesized nanoparticles could be attributed to partial loss of surface capped proteins. Also, in this case the SAED pattern showed the presence of diffraction rings indicating the polycrystalline nature of the particles that show excellent match with magnetite crystal structure [32].

3.3.3 X-ray diffraction analysis

The X-ray diffraction pattern recorded from the solution cast magnetite film on glass surface is shown in Figure 3.3.A number of strong Bragg reflections are observed originating from the sample which could be indexed on the basis of magnetite crystal structure. The high intensity of (220) Bragg reflection indicates preferential orientation of these crystals. Along with magnetite, reflections from the crystal planes marked as "•" were found to show a match with the maghaemite (γ-Fe_2O_3) phase of iron oxide.

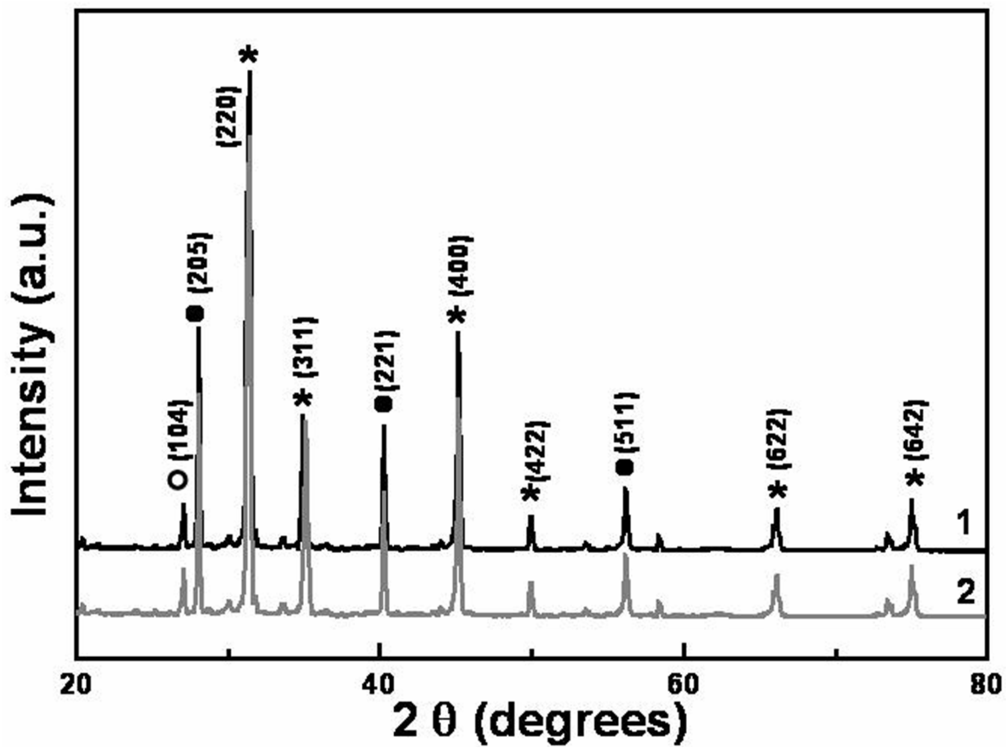

Figure 3.3 *XRD pattern of magnetite nanoparticles synthesized after 72h of reaction between Actinobacter spp. and ferri/ferrocyanide salts. XRD pattern could be indexed on the basis of mixed phases of iron oxide, magnetite being the major phase. Curve 1in black shows XRD pattern of as synthesized sample, while curve 2 in grey shows XRD pattern obtained from the sample that was calcined at 350 °C for 3h.*

All the peaks shown with the symbol "*" denote reflections originating from magnetite nanoparticles while one peak marked as "○" can be assigned to FeO [32].Curve 1 in Figure 3.3 (black curve) shows the XRD pattern recorded from as-synthesized magnetite nanoparticles. XRD pattern recorded for as-synthesized nanoparticles which were calcined at 350 °C for 3 h also shows excellent match with magnetite crystal structure (curve 2 in grey, Figure 3.3). XRD pattern recorded from as synthesized and calcined nanoparticles showed a little variation and could be superimposed. This indicates that the heat treatment does not cause any crystallite growth and there is no change in the overall composition of the maghaemite particles either by way of sintering of the particles or by oxidation. However, a small improvement in the crystallinity of each individual domain cannot be ruled out. This observation is well supported by TEM analysis wherein a partial aggregation of nanoparticle is seen due to calcination which caused an individual crystallite growth. The *d* values and the respective *hkl* planes are as follows: For magnetite marked as "*" 2.86 (220), 2.44 (311), 2.02 (400), 1.64 (422) 1.26 (622), 0.96 (642). For maghaemite (γ-Fe_2O_3) marked as "•": 3.23 (205), 2.20 (113), 1.63 (511) and for FeO marked as "○": 1.51 (104).

3.3.4 FTIR spectral characterization and TGA analysis

Figure 3.4A shows the FTIR spectrum of culture supernatant containing magnetite nanoparticles before (curve 1 Figure 3.4A) and after (curve 2 Figure 3.4A) synthesis. Curve 1 in Figure 3.4A shows the FTIR spectrum of *Actinobacter* spp. ferri/ferrocyanide reaction mixture, recorded immediately after the addition of ferri/ferrocyanide salts to the bacterial suspension. This spectrum does not show any Fe–O vibration bands specific to iron oxide.

Curve 2 in Figure 3.4A depicts the FTIR spectrum of powdered magnetite nanoparticles synthesized after 72 h of reaction between *Actinobacter spp*. and ferri/ferrocyanide salts**.** Spectrum 2 (black curve) shows a number of vibration bands that arise due to the stretching and bending mode of Fe-O bonds in magnetite. A strong vibration band at around 610 cm^{-1} along with a small band at 547 cm^{-1} is due to the Fe-O bending mode while, a broad peak at around 840 cm^{-1} is due to Fe-O stretching vibrations (solid lines in the spectrum) [33]. Along with these vibration bands the spectrum shows the presence of two peaks centered around 1650 and 1560 cm^{-1}. These bands could be assigned to the vibrations due to amide I and II bands that arise most probably due to the presence of proteins (dotted lines spectrum 2, Figure 3.4A). This analysis suggests that there is association of proteins with the surface of magnetite nanoparticles.

Thermogravimetric analysis (TGA) of as-synthesized magnetite nanoparticles was carried out to quantify the bio-organic loading of magnetite nanoparticles. Figure 3.4B shows the TGA profile recorded from carefully weighed powdered magnetite sample. As-synthesized magnetite nanoparticles display a gradual weight loss of c.a. 65% around 500 °C.

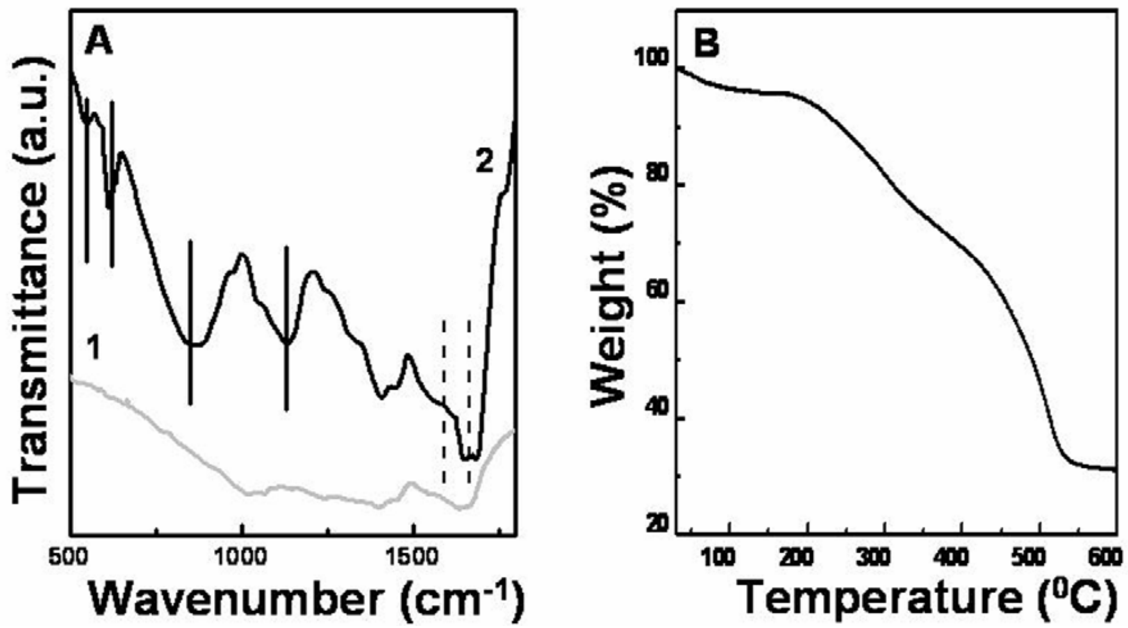

Figure 3.4 *FTIR and TGA analysis of as synthesized magnetite nanoparticles after 72h of the reaction between Actinobacter spp. and ferri/ferrocyanide reaction mixture. FTIR spectral measurement shows the presence of number of Fe-O and amide bond vibrations indicating the presence of proteins along with magnetite nanoparticles (Figure 3.3A, curve 2). Curve 1 in Figure 3.3A shows the FTIR spectra of ferri/ferrocyanide reaction mixture before incubation with Actinobacter spp. TGA analysis (figure 3.3B) indicates a gradual weight loss of ~ 65% which is due to decomposition of biomolecules present along with magnetite nanoparticles.*

A steady weight loss around 200 °C can de attributed to removal of water that is associated with magnetite nanoparticles. A sharp and steady weight loss in the temperature range of 250 °C to 500 °C can be attributed to desorption and decomposition of the surface bound bio-organic molecules present along with the magnetite nanoparticles. After 500 °C the curve shows no further weight loss, indicating that around 35% of inorganic matter, most of which could be magnetite is left by 600 °C.

3.3.5 Magnetic measurements

Magnetic measurements were performed on dried magnetite nanoparticles before and after calcination. Magnetization as a function of the field at different temperatures was recorded by varying the applied field between -50 KOe to 50 KOe. Temperature dependent magnetization of magnetite nanoparticles is studied by ZFC (Zero-field-cooled) and FC (field cooled) modes for as prepared as well as calcined nanoparticles. Figure 3.5A shows the magnetization curves (M-H curves) obtained from as synthesized powdered magnetite nanoparticles at 5 K, 20 K, 150 K and 250 K, respectively. Magnetic particles below a certain size regime exist as single domain particles displaying properties characteristic of superparamagnetism [34]. In these size regimes the thermal energy, above a temperature termed as blocking temperature (T_B), is sufficient enough to make the remanent magnetization overcome the barriers dictated by any of the different anisotropies, making the moments jump between two stable orientations of magnetization. Consequently, above T_B, the M-H curves of the superparamagnets show no hysterisis, while below this temperature the curves open up displaying curves very similar to those observed for ferromagnets.

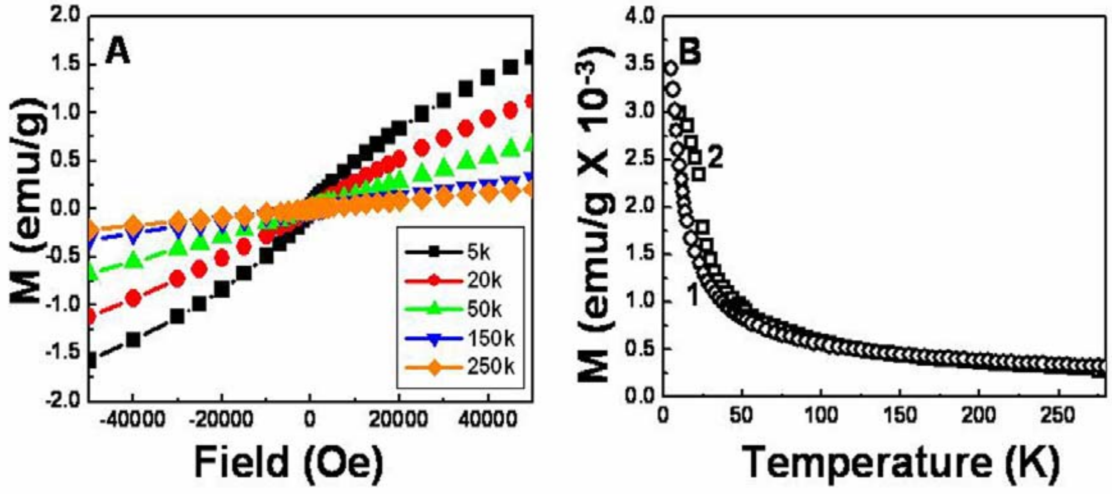

Figure 3.5 *M-H curve of as prepared magnetite samples measured at various temperatures (5K-black, 20K-red, 50K-green, 150K-blue and 250K-orange respectively) indicate the superparamagnetic nature of the particles (Figure 3.5A). ZFC (curve 1) and FC (curve 2) measurements (Figure 3.5B) show that both curves almost superimpose above 60 K.*

Magnetite has a complex spinel structure with one Fe^{2+} ion and two Fe^{3+} ions per formula unit. In each unit cell there are eight molecules of Fe_3O_4 and two distinct types of sites; 64 tetrahedral sites and 32 octahedral sites, which the iron ions can occupy. In these, only 16 of the octahedral sites are occupied and are shared by Fe^{3+} and Fe^{2+} ions and only 8 of the 64 possible tetrahedral sites are occupied by the other trivalent ion. In a very simple way it can be explained that the two trivalent Fe^{3+} ions interact antiferromagnetically in Fe_3O_4 and hence their magnetic moments cancel each other out and the net moment observed, comes from the remaining divalent iron [35]. Magnetite nanoparticles prepared using *Actinobacter spp.* clearly reveal the superparamagnetic nature. Here, as-synthesized nanoparticles showed a weak magnetic signal at room temperature (orange colored curve in Figure 3.5A), which is attributed to the presence of high amount of proteins along with the nanoparticles. However, at low temperature magnetization is greatly enhanced and showed a characteristic superparamagnetic behavior (black and red curve for 5 and 20 K respectively in Figure 3.5A). Figure 3.5B shows the zero field cooled and field cooled (ZFC-FC) measurements performed at an applied external field of 1000 Oe. FC and ZFC curves almost superimpose on each other suggesting the absence of blocking phenomenon in the nanoparticles. This could most probably be due to the considerable size variation in the as synthesized magnetite nanoparticles by *Actinobacter* spp.

Figure 3.6A shows the magnetization curves recorded from magnetite nanoparticles, which were calcined at 350 °C for 3 h. These calcined nanoparticles showed enhanced magnetic response under magnetic field with the signature of superparamagnetic behavior at room temperature (Figure 3.6A brown curve). At low temperature (5 K), a characteristic hysteresis loop was observed with opening of the loop indicating ferrimagnetic behavior of the nanoparticles. The increase in the magnetization signal in calcined sample is attributed to the removal of diamagnetic proteins from the surface of nanoparticles, a result consistent with TGA studies, which indicated that there is heavy loading of bio-organic molecules on magnetite nanoparticles. For magnetic nanoparticles, as the capping molecules become more and more bulky the overall magnetization of the nanoparticles is reduced [36].

The maximum magnetization and the coercivity values calculated for magnetite synthesized by *Actinobacter spp.* shows considerable variation from the reported literature. Maximum magnetization value (σ_s) per unit mass under given experimental conditions for magnetite is found to be ~ 9 emu / g while the coercivity was calculated to be ~ 600 Oe at 5 k. The decrease in the saturation magnetization could be due to either the presence of magnetically dead layer of iron oxide on the nanoparticle surface or due to the very small size of the particles [37]. A small hysteresis loop is observed in the M-H curve that measured at 275 K. However, at lower temperature (below 50 K) the hysteresis loop is sizable with clear opening indicating ferromagnetic transition in the nanoparticles. Also the hysteresis loop is symmetric about the centre, which is a characteristic of superparamagnetic behavior [38].

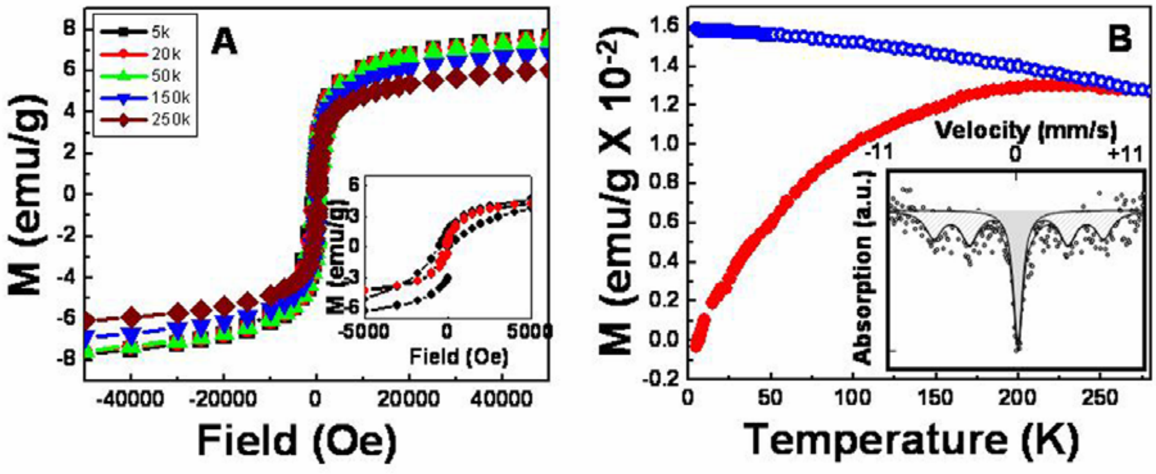

Figure 3.6 (A) *M-H curve of calcined magnetite sample measured at various temperatures (5 K-black, 20 K-green, 50 K-red, 150 K-blue and 250 K-brown respectively). The inset in Figure 3.6A shows clear opening of hysteresis loop at 5 K (black curve) while at room temperature superparamagnetism is restored (red curve). ZFC (red curve) and FC (blue curve) measurement (Figure 3.6B) shows that both curves almost superimpose at 275 K indicating that blocking temperature could be around 275 K. Inset in Figure 3.6B is a Mossbauer spectrum obtained from the calcined magnetite sample.*

In contrast to ZFC-FC behavior of as prepared magnetite nanoparticles, calcined sample exhibited a sharp divergence in ZFC-FC curves (Figure 3.6B). After calcination, the sample showed clear separation in ZFC (red curve, Figure 3.6B) and FC (blue curve, Figure 3.6B) curves with a blocking temperature of around 275 K. This is probably due to the enhanced interaction between the small nanoparticles after the removal of surface capped protein or could be due to the fact that the defects in the nanocrystals are annealed after calcination. To ascertain the crystalline phase of iron oxide as magnetite, Mossbauer spectroscopic analysis was performed on the calcined powder. Inset in Figure 3.6B shows the Mossbauer spectroscopic analysis performed on room temperature. Mossbauer spectrum shows the presence of several sextets resulting from the longer relaxation time or due to the poor statistical fitting of the spectral data points. Mossbauer spectrum clearly shows the superparamagnetic nature of magnetite nanoparticles and the six lined pattern with peak broadening clearly indicates the wide size distribution of magnetite nanoparticles. The corresponding Mossbauer resonance parameters such as isomer shift are (δ) 0.28 mm/s for 64 % of magnetized iron and 0. 21 mm/s for 36 % of relaxed iron component.

Figure 3.7 shows the magnetic force microscopy (MFM) image of the magnetite nanoparticles calcined at 350 °C for 3 h. The surface topographical (height) and magnetic force images (frequency) were recorded on a mica surface, which indicates a detectable contrast in both the images. Figure 3.7A corresponds to the topography of the aggregated nanoparticles while Figure 3.7B shows the magnetic force image. In frequency mode (MFM) the black contrast corresponds to the magnetic domains associated with the aggregated magnetite nanoparticles due to the attractive force between tip and the sample surface. MFM images with a fair contrast can be influenced by the sample topography. However, the shape and size of magnetite nanoparticles is a little different in topographical image and magnetic force image.

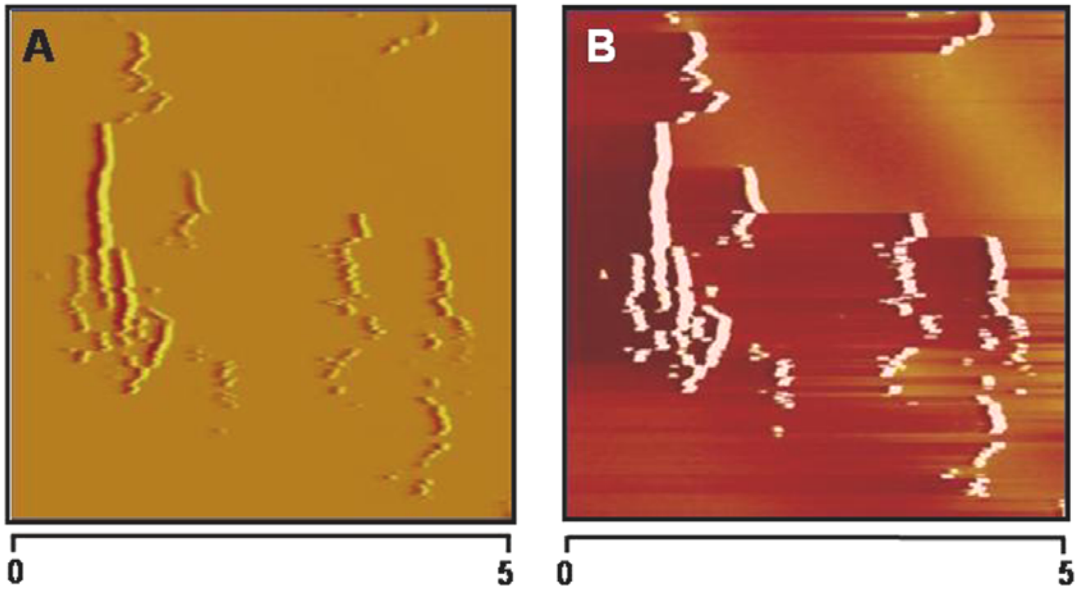

Figure 3.7 *AFM analyses of magnetite nanoparticles indicating the particle topography and magnetic contrast. There is a considerable contrast variation between topographical (height) image (Figure 3.6A) and magnetic (frequency) image (Figure 3.6B) due to the attractive force between tip surface and magnetic domains in the sample. Scale bar in both the images is 5μM and frequency range for magnetic image is 380 Hz.*

MFM images with fair contrast can be influenced by the sample topography. However, the shape and size of magnetite nanoparticles is little different in topographical image and magnetic force image. This indicated that the observed contrast is due to the domain structures present in the sample. In the frequency image discontinuous changes in contrast are observed, which can be possibly due to the distortion of domain structure under the influence of the tip since the stray field of the tip is larger than the coercive field [39].

3.3.6 Biochemical insight into magnetite formation by *Actinobacter* spp.

Magnetite formation in magnetotactic bacteria is extensively studied. There is a fair understanding of the process of magnetite formation at biomolecular level. Iron reducing bacteria like *Geobacter metallireducens* are also investigated for the process of magnetite formation at biomolecular level. The biological basis of magnetite synthesis in iron reducing bacteria lies in the energy production for the bacterial metabolism and growth [27], while magnetotactic bacteria synthesize magnetite for magnetotaxis to sense oxic-anoxic zones [16]. Biomolecular foundation of magnetite synthesis by *Actinobacter* spp. seems to be totally different from magnetotactic bacteria and iron reducing bacteria. *Actinobacter* spp. is a gram positive and aerobic bacterium, which synthesizes magnetite under fully aerobic conditions, contrary to magnetotactic and iron reducing bacteria, which requires strict anaerobic conditions for magnetite biosynthesis.

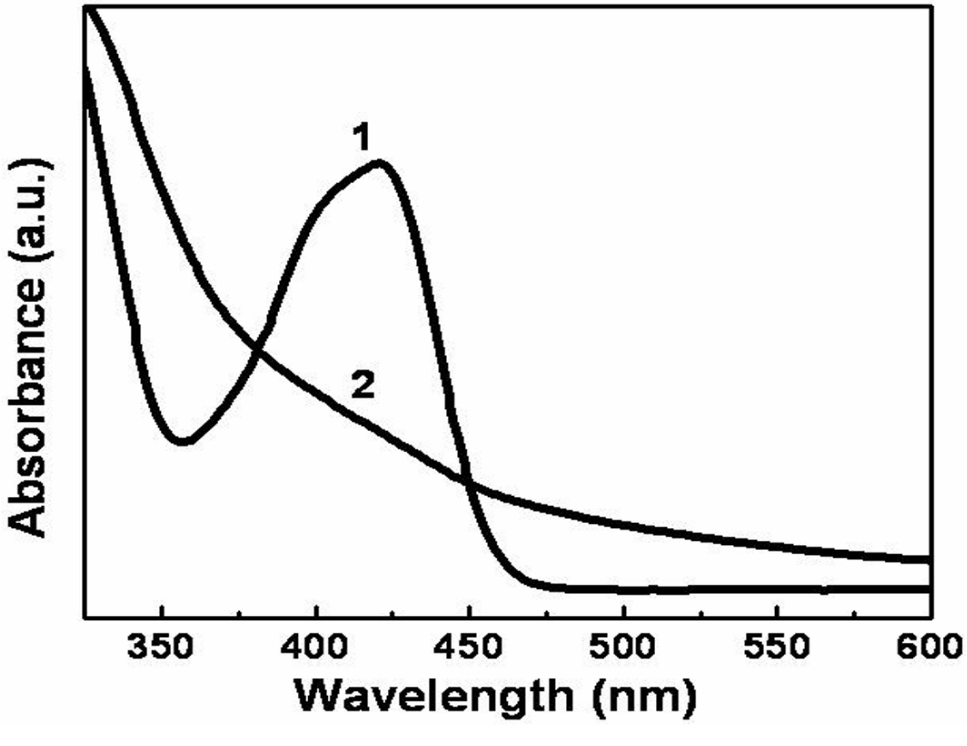

Figure 3.8 *UV-vis spectrum showing the hydrolysis of ferricyanide/ferrocyanide complex by Actinobacter spp. Curve 1 shows the absorption due to ferricyanide/ferrocyanide complex, while curve two shows that absorption at 440nm completely disappears while absorption hump at 325nm is evolved, which is due to iron oxide.*

Magnetite biosynthesis by *Actinobacter* spp. depends on its capacity to grow in the presence of ferricyanide/ferrocyanide reaction mixture. It should be noted that *Actinobacter* spp. was isolated from potassium ferricyanide/ferrocyanide reaction mixture and was able to grow on a Luria agar (LA) plate supplied with potassium ferricyanide/ferrocyanide salts in 2:1 molar ratio respectively. *Actinobacter* spp. could synthesize magnetite when reacted with cyanide complexes of iron and indicates the fact that the bacterium has the ability to hydrolyze iron-cyanide complexes, which is followed by magnetite formation.

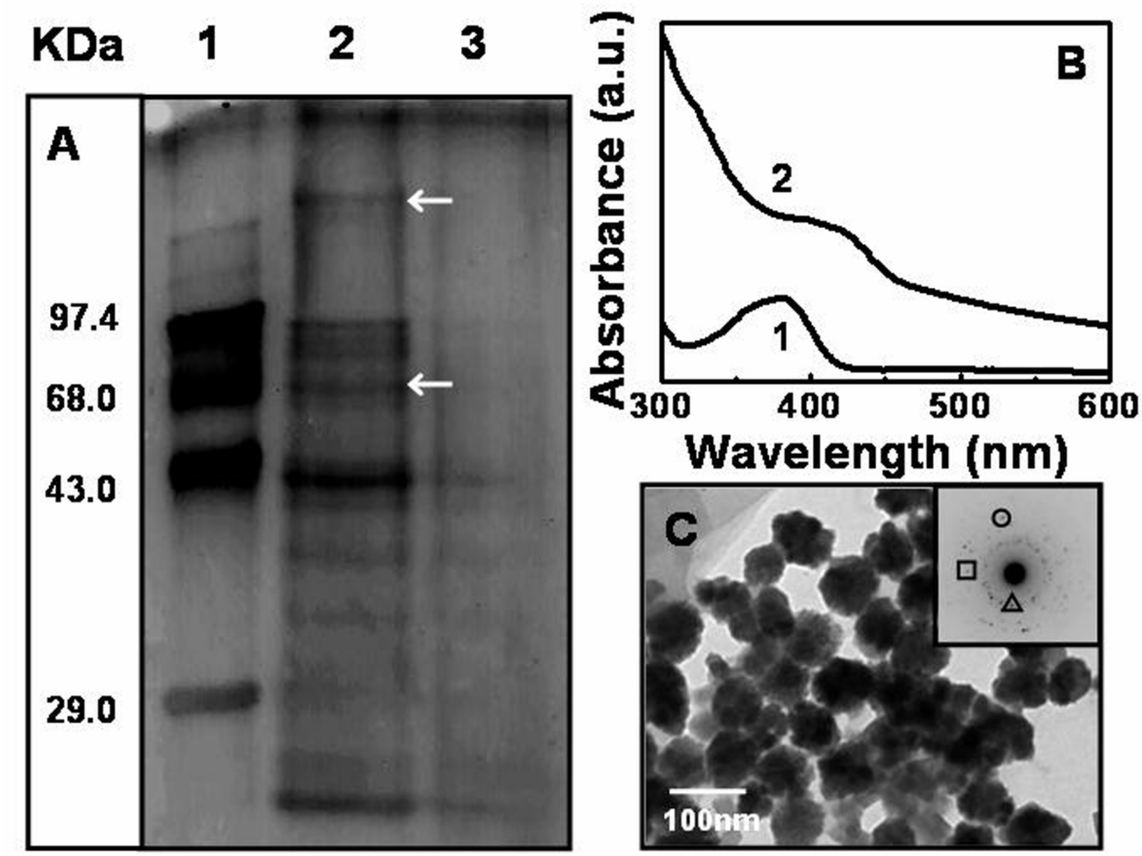

Figure 3.9*(A) SDS-PAGE analysis of extracellular proteins secreted by Actinobacter spp. in the presence (lane2) and absence (lane3) of ferri/ferrocyanide reaction mixture. Lane 1 shows standard molecular weight marker with respective molecular weights. (B) UV-vis spectroscopic assay for ferry/ferrocyanide hydrolysis by inducible proteins with molecular weight of 70 and 100 kDa after elution from gel. A prominent absorbance peak at 440 nm (curve 1) is due to ferri/ferrocyanide salt, which is considerably dampened in the presence of inducible proteins with subsequent evolution of a shoulder peak around 325 nm, due to formation of iron oxide (curve 2). (C) TEM image of magnetite nanoparticles synthesized by reaction between inducible proteins eluted from native polyacrylamide gel and* $K_3Fe(CN)_6$ - $K_4Fe(CN)_6$ *mixture. The inset shows a SAED pattern corresponding to magnetite structure [Δ-(220), □- (311), ○- (400) lattice planes].*

Microorganisms such as bacteria and fungi are known to synthesize various cyanide hydrolyzing enzymes that hydrolyze metal cyanide complexes or free cyanide [40]. Figure 3.8 shows the UV-vis spectroscopic analysis of hydrolytic features of iron cyanide complex before and after reaction with *Actinobacter* spp. In most bacteria, an enzyme called cyanidase or cyanide dihydratase is synthesized in response to metallocyanide complexes, which hydrolyze metal cyanide complexes [41]. For microorganisms and most of the plant, cyanide can serve as a carbon and nitrogen source. We believe that *Actinobacter* spp. can also use cyanide as a source of carbon and nitrogen, since in stationary growth phase bacterium has to rely on alternative energy source to support its metabolic activities. Therefore it extracellularly synthesizes cyanidase, which can hydrolyze iron cyanide complexes.

The process of magnetite formation is extracellular and it is quite possible that iron-cyanide hydrolyzing protein is secreted in the surrounding medium. Once the iron is removed from cyanide complex, it is most probably converted into magnetite by the action of some other protein. Figure 3.9A shows the extracellular protein profile of culture supernatant of bacterium grown in the presence and absence of $K_3Fe(CN)_6$ - $K_4Fe(CN)_6$ mixture. Induction of two new proteins with molecular weight of around 100 kDa and 70 kDa is observed when the bacterium was grown in the presence of ferri/ferrocyanide salt mixture (lane 2, Figure 3.9A). Figure 3.9B shows the UV-vis spectroscopic assay for ferri/ferrocyanide hydrolysis by inducible proteins with molecular weight of 70 and 100 kDa after elution from native polyacrylamide gel. Also, these proteins are not observed in the culture supernatant, when the bacterium was grown in the absence of ferri/ferrocyanide salt. This indicated that the new proteins are synthesized in response to the iron salts. We believe that one of inducible protein is actually cyanidase, an enzyme that catalyzes the hydrolysis of ferri/ferrocyanide salts. Indeed the inducible protein fractions when eluted from native polyacrylamide gel and reacted with iron cyanide complexes 10 mM sodium phosphate buffer (pH 6.4), could hydrolyze and subsequently synthesize magnetite. Curve 1 in Figure 3.9B shows a prominent absorbance at 440 nm, which is due to $K_3Fe(CN)_6$ - $K_4Fe(CN)_6$. After reaction with gel eluted purified proteins, considerable dampening in the intensity of ferry/ferrocyanide absorbance is observed (curve 2). This, along with the concomitant evolution of a shoulder peak around 325 nm (due to formation of iron oxide) suggest that hydrolysis of $K_3Fe(CN)_6$ - $K_4Fe(CN)_6$ salts lead to formation of iron oxide nanoparticles in the presence of two inducible proteins.

Figure 3.9C shows the TEM image of magnetite nanoparticles synthesized by reaction between inducible proteins, eluted from native polyacrylamide gel and $K_3Fe(CN)_6$ - $K_4Fe(CN)_6$ mixture in 10 mM sodium phosphate buffer (pH 6.4) after 12 h incubation. TEM analysis indicates the presence of aggregates of around 50 nm, which are composed of smaller magnetite nanoparticles. That these nanoparticles are indeed magnetite is confirmed by the selected area electron diffraction pattern, which could be indexed on the basis of magnetite crystal structure. These results indicate that magnetite formation by *Actinobacter* spp. is mediated by at least two proteins, one of which is responsible for the hydrolysis of ferri/ferrocyanide salt releasing ionic Fe. Subsequently other protein transforms Fe ions into magnetite. However, other proteins secreted by the bacterium in tandem can also be involved in the synthesis and stabilization of magnetite.

3.3.7 Discussion

This part of the chapter describes the biosynthesis of magnetite by *Actinobacter* spp., which is a gram positive, aerobic bacterium. *Actinobacter* spp. was isolated from $K_3Fe(CN)_6$ - $K_4Fe(CN)_6$ reaction mixture. The bacterium was able to grow in the presence of these iron salts and could even hydrolyze them. It was identified as a species of genus *Actinobacter* by molecular taxonomic method of 16S rRNA sequencing using bioinformatics tools. The most remarkable feature of this extracellular, room temperature biosynthesis method is that magnetite nanocrystals are formed under complete aerobic conditions. The magnetite so formed is characterized by TEM, XRD, FTIR, TGA and magnetic measurements. Biological mechanism of magnetite formation in *Actinobacter* spp. is substantially different from earlier reports of magnetotactic bacteria and iron reducing bacteria, which requires anaerobic conditions for magnetite biosynthesis. Magnetic measurements carried out on as synthesized and calcined magnetite nanoparticles indicated that they are superparamagnetic in nature. Biochemical analysis of the process indicated that there are at least two proteins, which can play an important role in the magnetite biosynthesis. These two proteins with molecular weight of around 70 kDa and 100 kDa are induced in the presence of ferri/ferrocyanide salts. One of the proteins is with the hydrolase activity that hydrolyzes ferri/ferrocyanide complex. We suspect that this enzyme could be a cyanidase, which hydrolyze the iron cyanide complex. We believe that the other protein with a molecular weight c.a. 100 kDa is responsible for the conversion of Fe ions into magnetite. However, these results are preliminary and require further insight.

3.4 Biosynthesis of nanocrystalline maghaemite (γ-Fe_2O_3)

This part of the chapter describes *Actinobacter* spp. mediated biological synthesis of maghaemite nanoparticles. Like magnetite, biosynthesis of maghaemite nanoparticles also occurs at room temperature and under fully aerobic conditions.

3.4.1 Experimental details

In a typical experiment seed culture of *Actinobacter* spp. was grown in the 2ml of LB medium, which was subsequently propagated into 100 ml of the same medium. The flask was then incubated at room temperature (~ 35 °C) on a rotary shaker (150 rpm). After 48 h of the bacterial growth, filter sterilized solution of ferric citrate or ferric chloride was added to the pre-grown *Actinobacter* spp. to the final concentration of 1mM. The flask was then further incubated for another 48-72 h on a rotary shaker (150 rpm) at 37 °C. Maghaemite synthesized in culture medium was harvested from bacterial biomass by centrifugation at 5,000 rpm (2560 X g). Supernatant containing maghaemite was then lyophilized and further analyzed using TEM, MFM, XRD, FTIR, Mossbauer spectroscopy and magnetic measurements etc. as discussed in section 3.3.1.

The biochemical investigation of maghaemite formation was carried out by genetic and protein analysis and by enzyme assays for ferric iron reductase. The extracellular protein profile of the bacterial culture supernatant was checked for the induction of the new protein/s upon iron salt addition. Proteins were analyzed by denaturing polyacrylamide gel electrophoresis (SDS-PAGE) as well as native polyacrylamide gel electrophoresis on 12% gels (12% T and 2.7% C). For the analysis of the proteins bound to the surface of the nanoparticles, Maghaemite and iron sulfide nanoparticles were separated from the culture supernatant. First, the bacterial biomass was removed by centrifugation at 5,000 rpm (2560 *X* g) and the culture supernatant containing nanoparticles was collected. This culture supernatant was again subjected to centrifugation at 15,000 rpm (20579 *X* g) for 30 minutes. After centrifugation, the supernatant was discarded and the black pellet of γ-Fe_2O_3 was washed thrice with 50 mM sodium phosphate buffer (pH 7.4) before dissolving in 100 μl of the same buffer. Proteins were separated from the nanoparticles by treatment with 8M urea and 1% SDS. The solutions were then heated at 60 °C for 10 minutes and then centrifuged at 15,000 rpm for 30 minutes. The supernatant was then extensively dialyzed against 50 mM sodium phosphate buffer (pH 7.4), and then analyzed on SDS-PAGE for the presence of proteins as described above.

Iron reductase activity was measured by the standard method of Dailey [42] with slight modification. The method involves use of ferrous iron chelator, ferrozine [3-(2-pyridyl)-5, 6- bis (4-phenylsulphonic acid)-1,2,4-triazine]. Ferrozine reacts with ferrous iron to form a purple colored chelator with a molar extinction coefficient of 28,000 at 562 nm. The assay mixture in the final volume of 2 ml contained 50 μl of NADH, 100 μl of ferrozine, 50 μl of 5 mM ferric citrate, 200 μl of bacterial culture supernatant in 20mM phosphate buffer (pH-7.2).The reaction was initiated by addition of the culture supernatant containing enzyme and incubated at room temperature for five hours. The spectral measurement was carried out on a JASCO dual beam spectrophotometer (model V-570) operated at a resolution of 1nm. In a control experiment for assay, all the ingredients were kept unaltered, while the bacterial culture supernatant obtained from bacterial growth in absence of iron precursor was added with rest of the ingredients. To elucidate the role of iron reductase in the formation of maghaemite, *Actinobacter* spp. was reacted with ferric ions in the presence of 100 μM of Zn^{2+} ions, which inhibit iron reductase activity [43]. Iron reductase activity in presence of Zn^{2+} ions was assayed as discussed above.

Isolation and sequencing of iron reductase gene from *Actinobacter* spp. was performed by isolating genomic DNA was isolated from *Actinobacter* spp. by standard phenol/chloroform extraction method as described previously [29]. The genes encoding iron reductase was amplified using a polymerase chain reaction with specific primers as fhuf-F (5′ – GAC CCC GAT CTC ACC GCA CT -3′) and fhuf-R (5′ – GAA ACA GCA GTC GCC GCA -3′) designed from S. *Sterpromyces avermitilis* MA-4680 genome (NCBI Genbank no. NC 003155). The PCR conditions used were an initial denaturation at 94 °C for two minutes, followed by 35 cycles of denaturation at 94 °C for one minute, annealing at 60 °C for one minute and extension at 72 °C for 30 seconds and final extension at 72 °C for 10 minutes. From the amplified PCR products, bands with desirable sizes were excised from the gel by QIAquick gel extraction kit according to manufacturer's instructions (Qiagen). The gel eluted PCR products were then sequenced from both the directions using same set of primers on automated DNA analyzer 3730 of Applied Biosystem BigDye terminator chemistry. The sequences so obtained were analyzed at NCBI server using different BLAST programs.

A number of control experiments were carried out to assess the authenticity of iron mineral biosyntheses by *Actinobacter spp*. In the first control experiment, iron precursors were mixed with the culture medium in the absence of *Actinobacter* spp. and the experiment was carried out as described above. In yet another control experiment, a number of other bacteria like *Bacillus subtilis, Aeromonas* spp.*, Micrococus* spp. and *E.coli* were used to check the synthesis of nanoparticles.

3.4.2 Transmission electron microscopic analysis

Figure 3.10 shows the representative TEM images of as synthesized (A-C) and calcined (350 °C, 2 h) maghaemite nanoparticles (D-F). It is clearly seen from low magnification images that particles tend to organize into clusters of roughly 100 nm size (Figure 3.10 A). High magnification image of these clusters show smaller particles with the dimension of around 5-10 nm (Figure 3.10C) that are capped possibly by the proteins secreted by *Actinobacter* spp. Selected area diffraction pattern obtained from one of the images (Figure 3.10A, inset) show well defined diffraction spots indicating the crystalline nature of the nanoparticles and the lattice parameter obtained were consistent with maghaemite crystal structure [44].

After the calcination of as-synthesized sample at 350 °C for 2 h, little change in morphology of nanoparticles was observed. Maghaemite nanoparticles tend to sinter together because of the partial removal of the surface bound proteins resulting in the formation of aggregates with 20-30nm diameter. The aggregation within nanoparticles is also due to the magnetic exchange interaction now much prominent due to the removal of proteins present on the surface of maghaemite nanoparticles. Moreover, the calcination treatment further broadens the size distribution in maghaemite nanoparticles leading to size irregularity

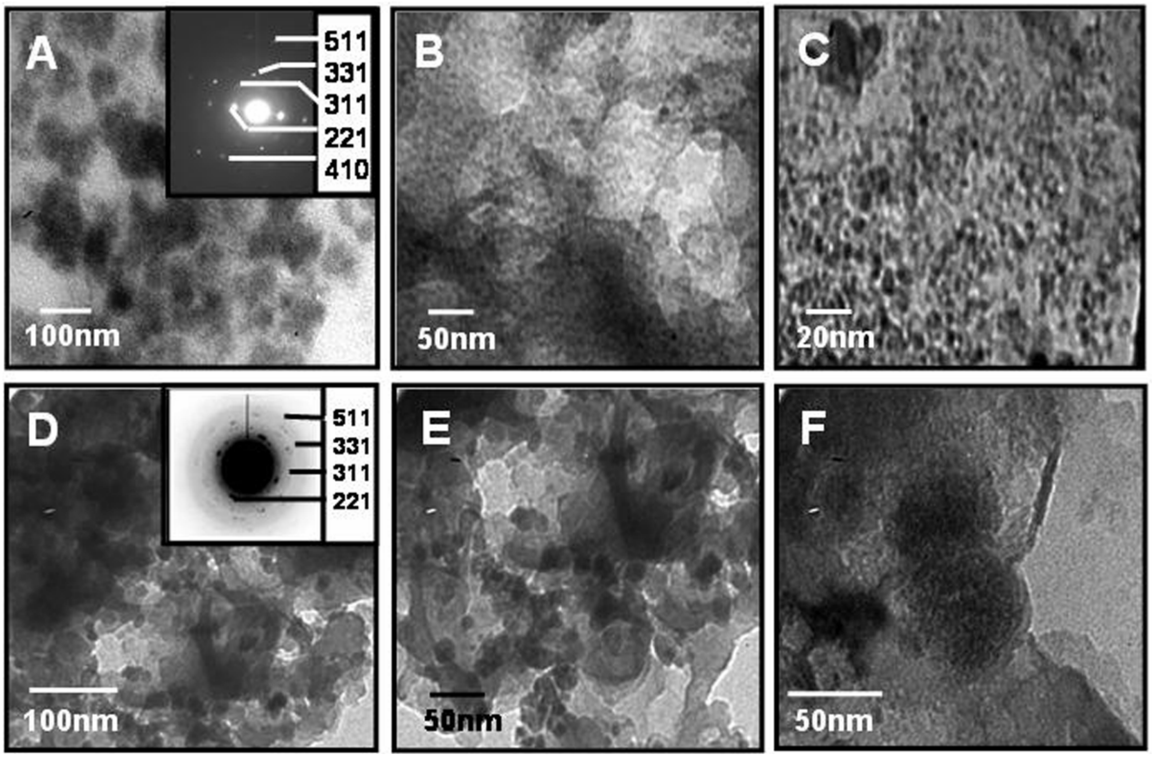

Figure 3.10 *TEM images of as-synthesized maghaemite nanoparticles after 72h of reaction between Actinobacter* spp. *and ferric citrate (A-C). The inset in image A shows SAED pattern obtained from maghaemite nanoparticles. Calcination of as-synthesized nanoparticles leads to aggregation with little change in overall morphology (D - F). The inset in image D shows SAED pattern obtained from calcined nanoparticles.*

Nevertheless some well separated particles were also observed with overall dimension between 10-20 nm along with the aggregates of individual nanoparticles (Figure 3.10D-F) The SAED pattern is much more discernible now which was clearly indexed on the basis of γ-Fe_2O_3 crystal structure (inset in Figure 3.10E).

3.4.3 X-ray diffraction and Mossbauer spectroscopic analysis

Figure 3.11A shows the X-ray diffraction pattern of as synthesized and 350 °C calcined maghaemite (γ-Fe_2O_3) nanoparticles, which were recorded from a solution cast maghaemite film on glass surface. The XRD pattern of as prepared maghaemite nanoparticles shows a number of Bragg reflections originating from the sample (curve 1 in Figure 3.11). Most of the peaks showed excellent match with the reported values of maghaemite crystal structure. Apart from the peaks marked as "○ ", which correspond to maghaemite, a small number of peaks corresponding to other crystal phases of iron oxide, namely γ-FeOOH (goethite) and FeO are also observed. The peak marked as "•" is due to γ-FeOOH, while symbol “*” indicates Bragg reflections due to FeO. Curve 2 in Figure 3.11 shows the XRD pattern recorded from maghaemite nanoparticles, which were calcined at 350^0 C for 2 h.

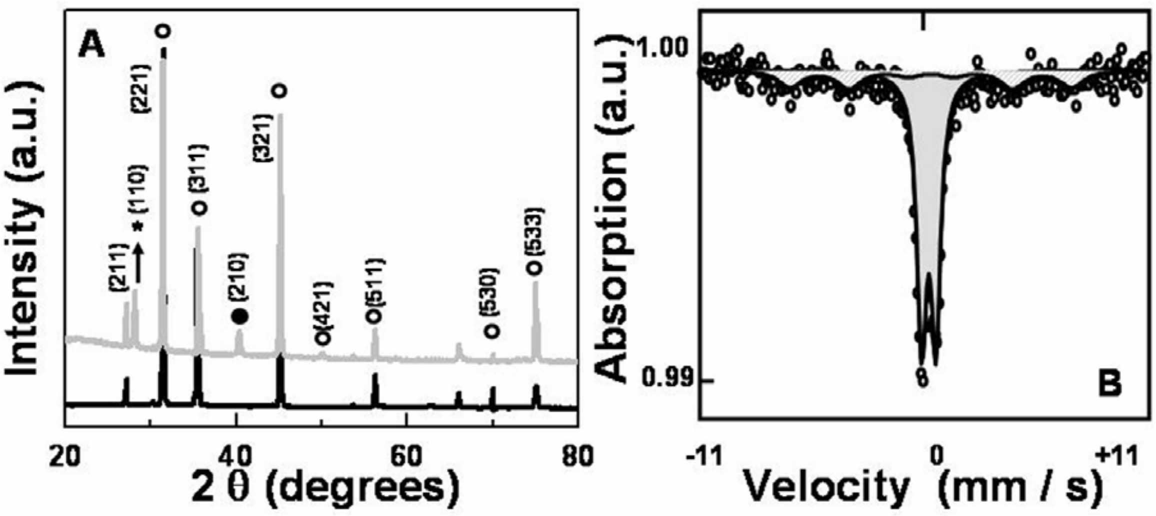

Figure 3.11 *(A) XRD patterns of maghaemite nanoparticles synthesized after 72h of reaction between Actinobacter spp. and ferric citrate. Grey curve represents the XRD pattern of as-synthesized sample while black curve indicates the XRD pattern of maghaemite sample that was calcined at* 350^0*C for 2h. (B) Mossbauer spectroscopic analysis of calcined maghaemite sample.*

There is little variation in the XRD pattern of calcined nanoparticles in comparison with the XRD pattern of as synthesized nanoparticles indicating the fact that heat treatment does not alter the crystallinity of as synthesized nanoparticles. However, small improvement in individual crystal domains due to the partial removal of capped proteins can be expected. The *d* values and the respective *hkl* planes for γ- Fe_2O_3, γ-FeOOH and FeO are as follows: For maghaemite (γ-Fe_2O_3) peaks marked as “○”: 3.42 Å (211), 2.79 Å (221), 2.52 Å (311), 2.24 Å (321), 1.83 Å (421), 1.61 Å (511), 1.45 Å (530), 1.28 Å (533). For γ-FeOOH peaks marked as “•”: 2.95 Å (210) and for FeO peak marked as “*” 1.44 Å (110) [44].

Figure 3.11B shows Mossbauer spectroscopic analysis of calcined maghaemite nanoparticles performed at room temperature. Mossbauer spectroscopic analysis showed a weak sextet peak different that of magnetite, which shows the presence of two sextet peaks. Presence of quadrupole doublet corresponding to the relaxation time arises due to the superparamagnetic nature of maghaemite nanoparticles. The broad lines of the magnetic sextets and the smooth inner slopes suggest the existence of a wide size distribution of the obtained maghaemite nanoparticles [45]. The corresponding hyperfine parameters obtained are as follows- isomer shift (δ) = 0.35 mm/s, quadrupole shift (Δ) = 0.722. Values obtained for isomer shift and quadrupole shift are near to typical values of iron (III) [45].

3.4.4 FTIR spectroscopic analysis

Figure 3.12A shows FTIR spectrum of powdered maghaemite nanoparticles synthesized after 72 h of the reaction between *Actinobacter spp*. ferric citrate**.** The spectrum shows a number of vibration bands that arise due to the stretching and bending mode of Fe-O bonds present in maghaemite.

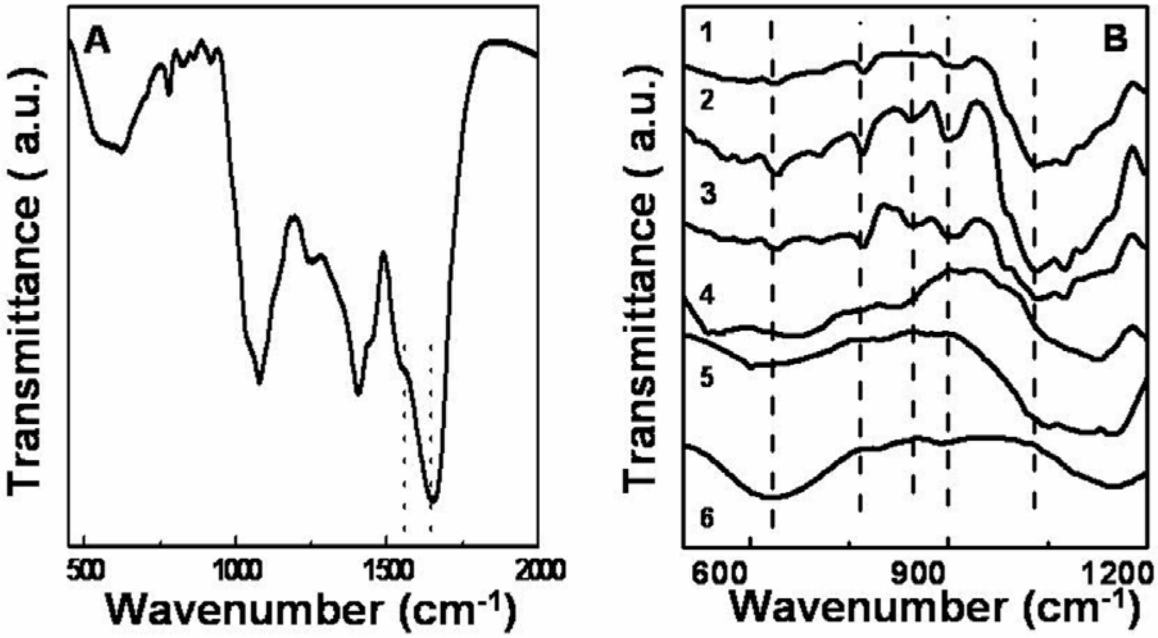

Figure 3.12*(A) FTIR spectrum of as synthesized maghaemite nanoparticles after 72 h of the reaction. A number of Fe-O bond vibrations are observed which correspond to maghaemite. The presence of amide I and amide II bonds in the spectrum suggests the association of proteins along with nanoparticles. (B) FTIR kinetics indicating the progress of reaction at various stages. Curve 1-6 corresponds to the spectral measurements after 12, 24, 36, 48, 60 and 72 h of the reaction .showing that the conversion of ferric citrate into maghaemite occurs via iron oxyhydroxide as an intermediate.*

A strong and broad vibration band at around 620 cm^{-1} along with a small band at 916 cm^{-1} is due to the Fe-O bending vibrations while, a peak at around 840 cm^{-1} is due to Fe-O stretching vibrations (solid lines in the spectrum) [33]. A strong peak around 1030 cm^{-1} is due to the presence of iron oxyhydroxide which can be assigned to γ-FeOOH. Along with these vibration bands, two peaks centered around 1650 and 1560 cm^{-1} could be assigned to the vibrations due to amide I and II bands those arise most probably because of the presence of proteins (dotted lines in the spectrum). This analysis suggests that there is association of proteins on the surface of maghaemite nanoparticles.

Conversion of ferric citrate into maghaemite by *Actinobacter* spp. was studied by FTIR spectroscopy as a function of time. Figure 3.12B shows FTIR analysis of the reaction mixture at various stages of the reaction. It is clearly revealed that the synthesis of γ-Fe_2O_3 occurs through the formation of iron oxyhydroxide as an intermediate stage. After first 12 h of the reaction, a prominent peak at 1030 cm^{-1} is observed indicating the presence of iron oxyhydroxide which can be assigned to γ- FeOOH [44] (curve 1, Figure 3.12B). Along with this peak presence of two small peaks centered around 770 cm^{-1} and 910 cm^{-1} could be ascribed to β-FeOOH [46]. In between 60 to 72 h of the reaction iron oxyhydroxide is almost converted into iron oxide which is indicated by the presence of Fe-O band vibrations at 620 cm^{-1} (curve 6 Figure 3.12B). The small peak at 840 cm^{-1} is due to Fe-O vibrational band, which show shifts towards 810 cm^{-1} after 48 hr (curve 4, 5, 6 Figure 3.12B) of the reaction.

3.4.5 Thermogravimetric Analysis

Thermogravimetric analysis (TGA) of as synthesized maghaemite nanoparticles was carried out to calculate the gross amount of maghaemite in the reaction mixture. Figure 3.13 shows the TGA curve recorded from powdered maghaemite nanoparticles. The curve shows many regions at which, weight loss seems to occur, however only regions corresponding to major weight loss are discussed here. The curve shows overall gradual weight loss in the temperature region between 100 $^\circ$C to 550 $^\circ$C, which is ca. 67 %. The initial, slow loss of weight at 100 $^\circ$C can be due to the removal of water molecules associated with maghaemite powder.

There is a broad region of a gradual weight loss in between 250 $^\circ$C to 550 $^\circ$C which can be assigned to the decomposition and desorption of bioorganic molecules associated with maghaemite nanoparticles. After 550 $^\circ$C no further decrease in weight loss is observed indicating that rest of the material is inorganic maghaemite powder, which is found to be approximately 33% by weight. Association of bio-organic proteinaceous materials with maghaemite nanoparticles is evident by their retention at 500 $^\circ$C.

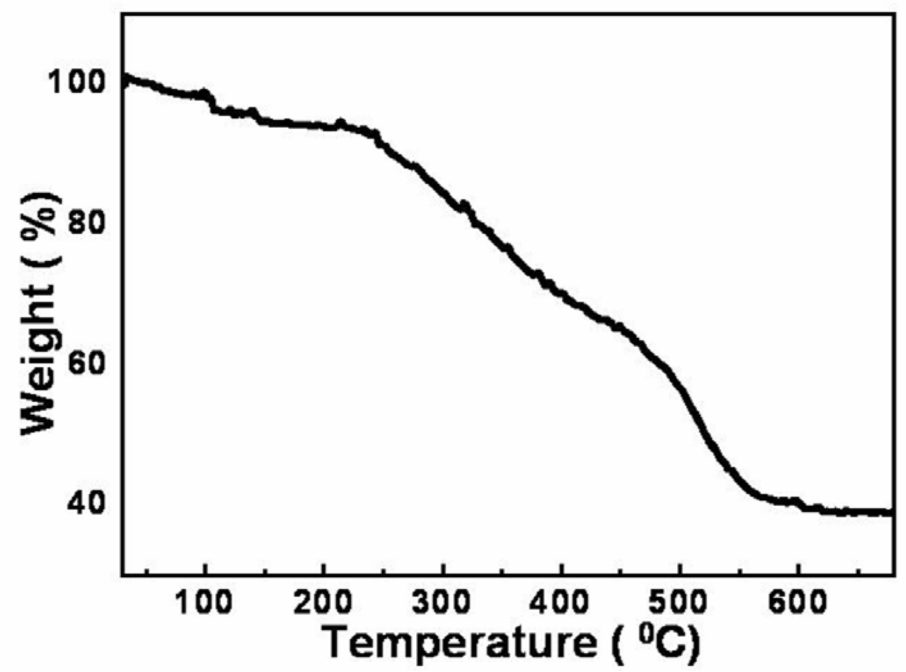

Figure 3.13 *Thermogravimetric analysis of as synthesized, powdered maghaemite nanoparticles. The curve shows a gradual weight loss of ~ 67% which is due to decomposition of biomolecules present along with magnetite nanoparticles by 550 °C. After 550 °C the curve does not show further weight loss.*

Thus, TGA analysis indicates that there is a very high amount of organic material of biological origin associated with maghaemite nanoparticles.

3.4.6 Magnetic measurements

As reported earlier (section 3.3.5), in this case also magnetic measurements were performed on dried maghaemite nanoparticles before and after the calcination. Magnetization as a function of external magnetic field was recorded by varying the applied field between -50 KOe to 50 KOe at different temperatures. Temperature dependence of magnetization in maghaemite nanoparticles is studied by ZFC (Zero-field-cooled) and FC (Field cooled) modes for as-prepared and the calcined nanoparticles at constant applied external field (1000 Oe). Figure 3.14A shows the magnetization curves (M-H curves) obtained from as synthesized powdered maghaemite nanoparticles at range of temperatures like 5 k, 20 k, 150 k and 250 k respectively.

As expected, as-synthesized maghaemite nanoparticles show very weak magnetization at higher temperatures indicating the paramagnetic response (brown curve, corresponding to 275 k, Figure 3.14A) owing to the fact that there is a considerable diamagnetic contribution due to the presence of proteins and other bioorganic components with maghaemite nanoparticles. This observation is quite consistent with the TGA results, which indicated a very high amount of bioorganic molecules associated with maghaemite nanoparticles. However, like magnetite nanoparticles (section 3.3.5) maghaemite nanoparticles shows enhanced magnetization signal at lower temperatures and at 5 k it shows clear superparamagnetic behavior. The enhanced magnetization signal at lower temperature could be due to the fact that magnetic moments in maghaemite overcomes the thermal energy barrier and align themselves in the direction of magnetic field.

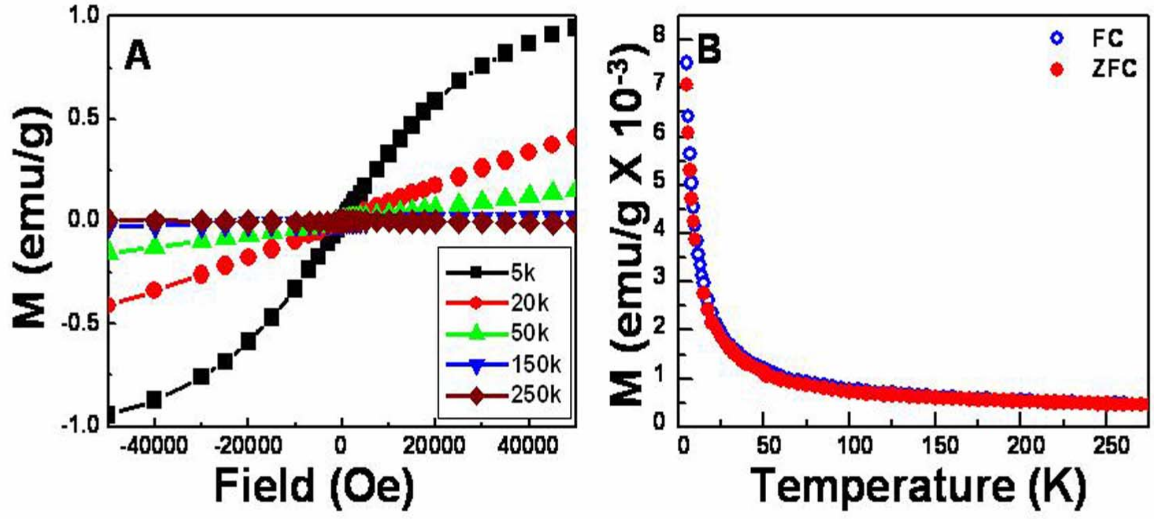

Figure 3.14*(A) M-H curve obtained from as-prepared maghaemite samples at various temperatures (5k-black, 20k-red, 50k-green, 150k-blue and 250k-brown respectively) indicate the superparamagnetic nature of the nanoparticles. (B) The ZFC (red curve) and FC (blue curve) measurements show that both curves almost superimpose indicating the absence of blocking phenomenon.*

Figure 3.14B shows the ZFC-FC measurements performed on as- synthesized maghaemite nanoparticles at an external applied magnetic field of 1000 Oe. ZFC and FC curves almost superimpose each other suggesting that the absence of blocking phenomenon. This could be most probably due to the even lower blocking temperature, which was not achieved by SQUID magnetometer that was used in this study. Absence of blocking phenomenon could arise due to a very small size of the nanoparticles with the considerable size variation [37]. Figure 3.15A shows M-H curves obtained from 350 $^{\circ}$C calcined powdered maghaemite nanoparticles at various temperatures like 5k, 20k, 150k and 250 k respectively (various magnetization curves are indicated by different color coded symbols corresponding to specific temperature as discussed in figure).

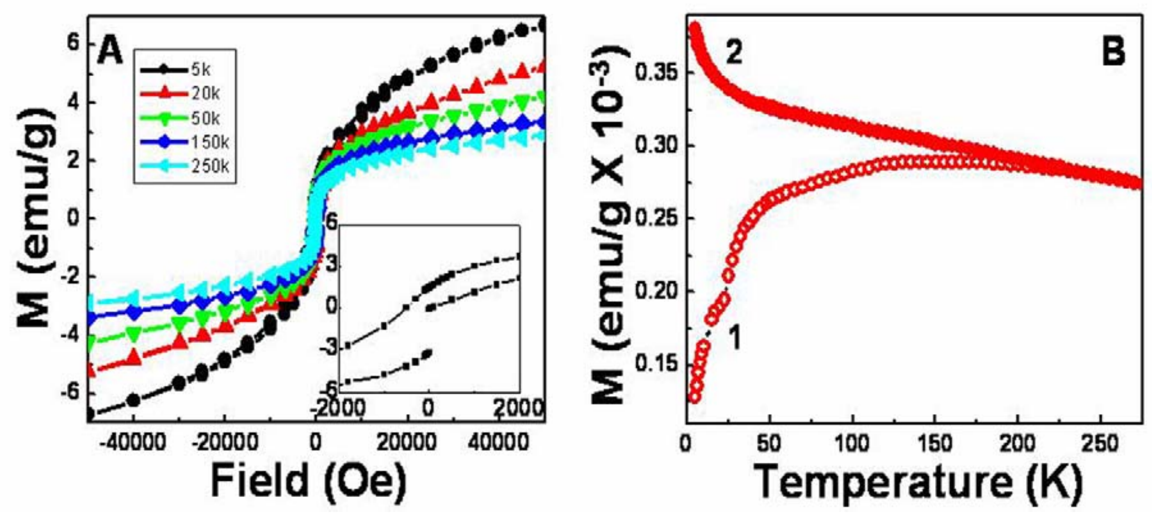

Figure 3.15*(A) M-H curve obtained from the calcined maghaemite nanoparticles measured at various temperatures (5 k-black, 20 k-red, 50 k-green, 150 k-blue and 250 k-cyan respectively) indicate the superparamagnetic nature of the particles at room temperature. The inset in (A) shows the clear opening of hysteresis loop at 5 k. (B) ZFC (curve 1) and FC (curve 2)measurements showing that both curves superimpose at 275 k indicating that the blocking temperature is around 275 k.*

A sharp rise in the induced magnetization is observed at all temperatures in comparison with as-synthesized maghaemite nanoparticles. At room temperature nanoparticles exhibit superparamagnetic behavior (Figure 3.14A, cyan curve). However, at low temperature (5 k) clear opening of hysteresis loop was observed indicating the ferromagnetic behavior of the nanoparticles (inset in Figure 3.15A).

The increase in the magnetization signal of the calcined sample is attributed to the removal of diamagnetic bio-organic molecules with the proteins present on the surface of nanoparticles. This result is quite consistent with TGA studies, which indicated that bio-organic molecules are present in considerable amount along with maghaemite nanoparticles. The value for maximum magnetization per unit mass (σ_s) under given experimental conditions for maghaemite nanoparticles synthesized by *Actinobacter* spp. is found to be around 8.5 emu/g while the coercivity was calculated to be ~ 540 Oe at 5 k. The lower saturation magnetization value reported here for maghaemite nanoparticles is due to the superparamagnetic nature of nanoparticles [37]. M-H curve shows clear opening of hysteresis loop at lower temperature (5 k) indicating the ferromagnetic transition of the nanoparticles. Figure 3.16 shows the magnetic force microscopic image of the maghaemite nanoparticles after calcined at 350 °C for 2 h.

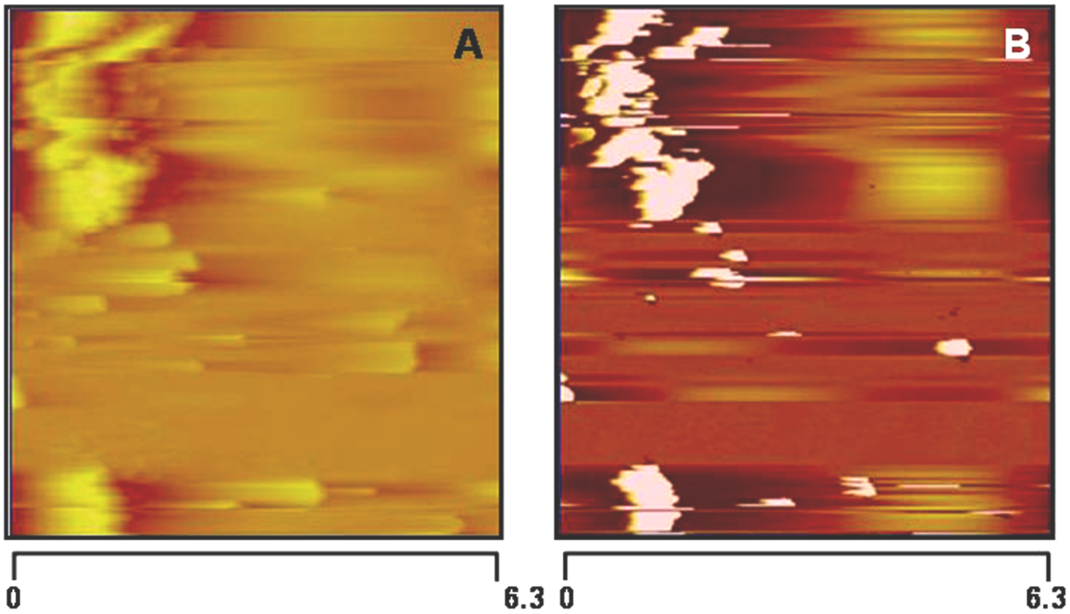

Figure 3.16 *Atomic force microscopy analysis of maghaemite nanoparticles showing the particle topography and magnetic contrast in MFM mode. A significant contrast variation between topographical (height) image (figure 3.16 A) and magnetic (frequency) image (figure 3.16 B) due to the attractive force between tip surface and magnetic domains in the sample can be seen. Scale bar in both the images is 6.3 μM and frequency range for magnetic image is 380 Hz.*

The surface topographical (height) and magnetic force images (frequency) were recorded on a mica surface as indicated above in section 3.3.5. In this case also, topography and height images show a detectable contrast in both images. Figure 3.16 A corresponds to the topography of the aggregated nanoparticles while Figure 3.16B shows the magnetic force image. In frequency image (MFM), black contrast corresponds to the magnetic domains associated with the aggregated maghaemite nanoparticles due to the attractive force between the tip and sample surface. Though the presence of magnetic domain is observed in the frequency image, due to the presence of proteinaceous organic matter with nanoparticles, clarity of the image is considerably affected.

3.4.7 Biochemical analysis of maghaemite formation by *Actinobacter* spp.

Biological synthesis and stabilization of maghaemite nanoparticles by *Actinobacter* spp. seems to be a complex, multistep reaction. Like magnetite, maghaemite biosynthesis occurs under aerobic conditions suggesting that conversion of ferric salts into iron oxides does not result in energy generation as observed in iron reducing bacteria. The very fact that *Actinobacter* spp. was isolated from aqueous iron cyanide complex suggests that the organism could withstand high iron concentration than that is normally required for cellular metabolism (usually ~ 6 μg).

We believe that the bacterium overcomes the toxic effect of excess iron by converting it into iron oxides, in this case maghaemite. The first and key step of the process is the reduction of Fe^{3+} to bio-active Fe^{2+}, followed by the formation of iron oxyhydroxide which then is converted into maghaemite by dehydration. In the first step ferric iron (Fe^{3+}) is reduced extracellularly into ferrous (Fe^{2+}) form by the action of the enzyme ferrisiderophore reductase. This step is very crucial, since inhibition of ferisiderophore reductase activity stops the synthesis of maghaemite nanoparticles. Once reduced, Fe^{2+} is then converted into iron oxyhydroxide either via chemical way or by the action of iron oxidase. In the last step iron oxyhydroxide seems to be transformed to maghaemite by the action of dehydratase enzyme. Extracellular protein profile of *Actinobacter* spp. indicated the induction of a new protein with the molecular weight of around 55 kDa. Four different proteins with the molecular weights of 15, 16, 20 and 23 kDa respectively are found to be associated with the surface of maghaemite nanoparticles.

3.4.7.1 Iron reductase assay and identification of iron reductase gene

Most of the bacteria are known to synthesize iron reductase enzyme for the assimilatory metabolism of iron. *Actinobacter* spp. synthesizes iron reductase extracellularly. We believe that iron reductase of *Actinobacter* spp. is a ferrisiderophore reductase as it scavenges the Fe^{3+} extracellularly. Figure 3.17A shows the assay of iron reductase enzyme that is induced by *Actinobacter* spp. in the presence of excess ferric iron. Ferrisiderophore reductase assay showed the iron reductase activity as indicated by the strong purple colour of assay mixture. A strong absorbance at 560 nm was observed, which indicates the formation of ferrozine-ferrous iron complex (Figure 3.17A). Ferrisiderophore reductase concentration increases in the presence of excess iron salt. However, no ferric reductase activity was observed in the supernatant obtained from bacterial culture grown in the absence of iron salts (curve1, Figure 3.17A). To elucidate the role of iron reductase in the formation of maghaemite, the reaction was carried out in the presence of zinc ions. Synthesis of iron oxide was not observed at all in the presence of zinc ions indicating that iron reductase is required for the synthesis of iron oxide and at the initial stage.

Figure 3.17B shows the PCR analysis of iron reductase gene on 1% agarose gel. When *Actinobacter* spp. genome was analyzed for the presence of iron reductase gene using a set of specifically designed gene primers (see section 3.4.1), a single band of 675 base pairs was obtained corresponding to iron reductase (*fhu* F) gene, The size of *fhu* F gene in the bacterium from which primers for PCR amplification were designed (*Sterpromyces avermitilis* MA-4680 genome, NCBI Genbank no. NC 003155) is around 700 base pairs. The size of PCR amplified fragment is near to the reported value of *fhu* F gene in *Sterpromyces avermitilis* MA-4680 and therefore the amplified gene fragment may be considered as *fhu* F homologue in *Actinobacter* spp.

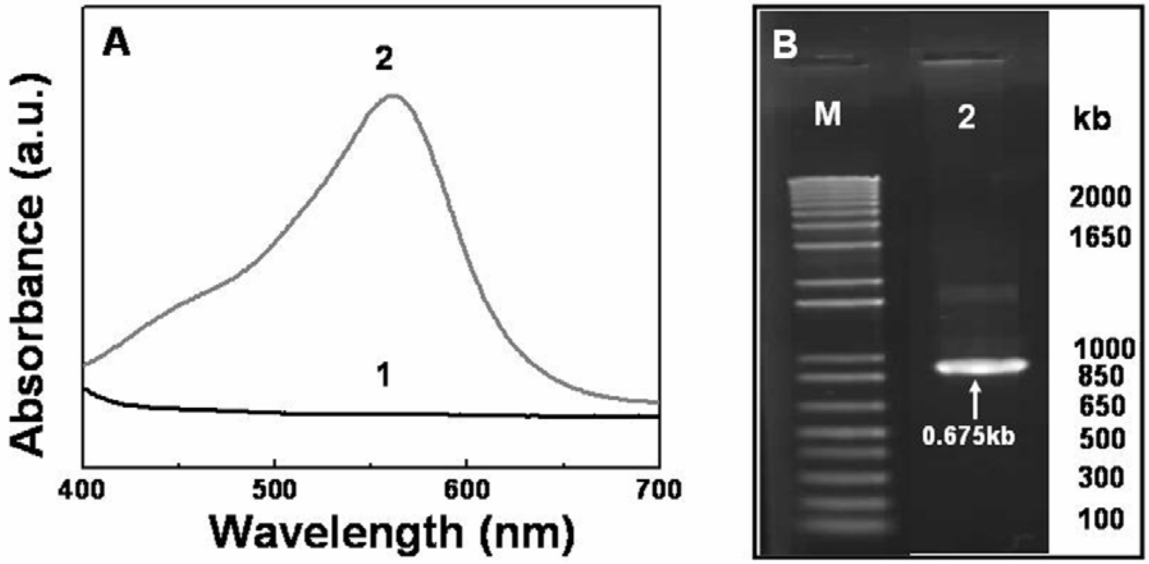

Figure 3.17*(A) Ferrisiderophore reductase assay indicating the presence of ferric iron reductase activity. Iron reductase activity is not observed (curve 1 black) in the culture supernatant of the bacterium grown in the absence of ferric citrate, while induction in the iron reductase activity was observed when bacterium was grown in the presence of ferric citrate (curve 2 in red). (B) Agarose gel picture showing 0.675 kb band for iron reductase gene (lane 2) Lane M shows standard DNA length molecular marker with respective size.*

This result along with iron reductase assay indicates the presence of iron reductase in *Actinobacter* spp. Inability for maghaemite synthesis by the bacterium in the presence of zinc ions, which inhibits iron reductase activity, shows that iron reductase is required for the biosynthesis of maghaemite nanoparticles. However, the exact function of iron reductase during maghaemite nanoparticles is not identified yet, as it not known whether this enzyme specifically synthesized in the presence of excess ferric iron or is a part of regular bacterial metabolism.

3.4.7.2 Analysis of extracellular and surface bound proteins

To study the induction of new protein/s due to iron salt stress, extracellular protein profiles of culture supernatant from the bacterium grown in the presence and absence of ferric citrate were analyzed on polyacrylamide gels in native and denaturing conditions (SDS-PAGE). The denaturing (SDS-PAGE) gel electrophoresis profile (Figure 3.18A) shows the induction of a new protein with molecular weight c.a. 55 kDa in the presence of ferric citrate.

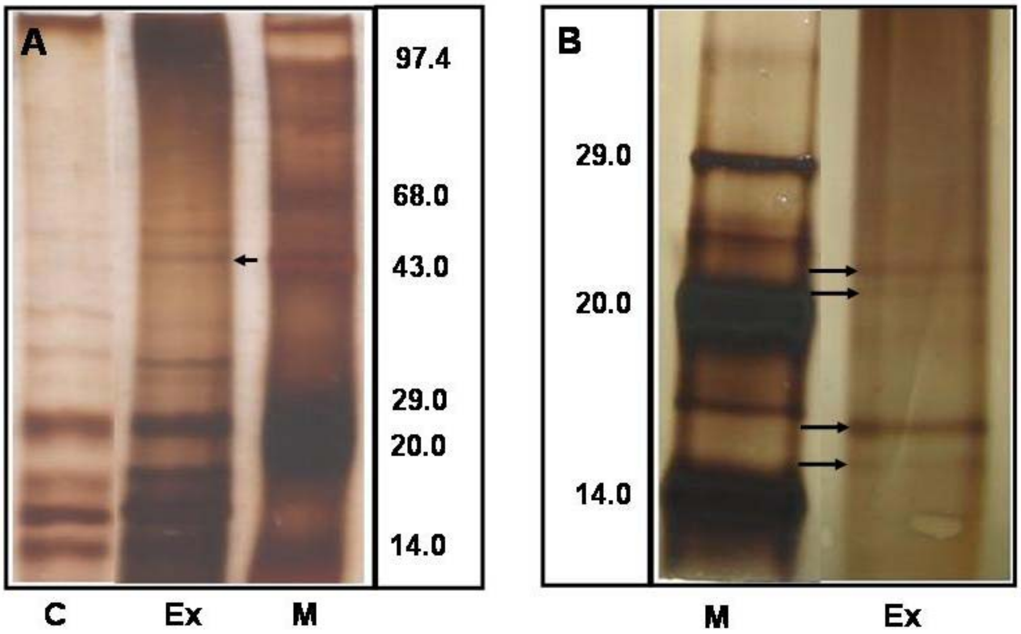

Figure 3.18*(A) SDS-PAGE analysis of extracellular proteins secreted by Actinobacter spp. in the presence (lane Ex) and absence (lane c) of ferric citrate. Induction of a protein with molecular weight of 55 kDa is observed in the presence of iron salt (lane Ex, marked by arrow), which are absent in the culture supernatant of bacterium grown in the absence of iron salt (lane C). Lane M is standard molecular weight marker with respective molecular weights. (B) SDS-PAGE analysis of the proteins bound to the surface of maghaemite nanoparticles. Lane Ex shows the surface bound protein of maghaemite nanoparticles. Lane M is standard molecular weight marker (three bold bands from bottom to top in lane M are of 14 kDa, 20 kDa, and 29 kDa).*

This protein might be playing an important role in the formation of maghaemite nanoparticles. The proteins present on the surface of maghaemite nanoparticles were also analyzed by SDS-PAGE. This analysis revealed the presence of four different surface bound proteins with the respective molecular weights of 15, 16, 20 and 23 kDa (Figure 3.18B). The association of these proteins with the nanoparticles surface indicates that they may be responsible for the stabilization of maghaemite nanoparticles. However, exact function of these proteins is yet to be understood completely. The work described here shows the preliminary results for the biochemical analysis of maghaemite formation by *Actinobacter* spp. Based on these results it can be hypothesized that initially Fe^{3+} ions are reduced extracellularly to Fe^{2+} ions by the action of ferrisiderophore reductase. Immediately after, Fe^{2+} ions are reoxydized to iron oxyhydroxide (ferrihydrite). FTIR kinetics of the reaction progress (Figure 3.12B) revealed the presence of iron oxyhydroxide as an intermediate in the synthesis of maghaemite. This step can be biotic or abiotic. It is possible that ferrous iron can bind to bacterial cell wall, which has anionic organic molecules exposed on its surface. It has been shown that iron show extremely high affinity for polymeric materials present on the bacterial cell wall due to its valence, hydrated radius, hydration energy and electronegativities [47]. Once bound to cell surface, Fe^{2+} can be oxidized to iron oxyhydroxide by the action of membrane bound iron oxidase enzyme. However, it is also possible that Fe^{2+} ions can spontaneously get oxidized into iron oxyhydroxide (ferryhydrite) under aerobic conditions at circumneutral pH. Lastly, the iron oxyhydroxide thus synthesized is dehydrated to maghaemite by the action of bacterial dehydratase enzyme.

3.4.8 Discussion

This part of the chapter describes biosynthesis of nanocrystalline maghaemite (γ-Fe_2O_3) by *Actinobacter* spp. from ferric citrate. Like magnetite, maghaemite formation by *Actinobacter* spp. occurs under aerobic conditions. The biogenic maghaemite nanoparticles are found to be of 5-7 nm in diameter. Magnetic measurements performed on as-synthesized and calcined maghaemite nanoparticles indicated the superparamagnetic behavior with coercivity value 540 Oe at 5 K. MFM measurements performed on maghaemite nanoparticles after calcination clearly showed contrast variation in topographical and magnetic image due to the presence of magnetic domains. Mossbauer analysis was in line with the SQUID measurement indicating that iron oxide nanoparticles are indeed composed of maghaemite phase. Biochemical analysis of maghaemite formation in *Actinobacter* spp. indicated that the maghaemite synthesis is a complex multistep process, which begins with the reduction of ferric iron into ferrous iron by the action of ferrisiderophore reductase. Inhibition of ferrisiderophore reductase activity by the addition of zinc ions completely stops the biosynthesis of maghaemite. Fe^{2+} reduction is followed by the conversion of ferrous ions into iron oxyhydroxide. Conversion of ferric citrate into maghaemite by *Actinobacter* spp. was studied by FTIR spectroscopy as a function of time, which clearly indicated the presence of iron oxyhydroxide. In the last step of the reaction iron oxyhydroxide is dehydrated into maghaemite by the action of bacterial dehydratase.

Part II. Synthesis of nanocrystalline magnetite by eukaryotic microorganism

3.5 Fungi mediated biological synthesis of nanocrystalline magnetite (Fe_3O_4)

This part of the chapter describes biological synthesis of magnetite nanoparticles using eukaryotic microorganisms like fungi. Previous studies from this laboratory illustrated beautifully that, the interaction of metal ions with fungi like *Fusarium oxysporum* and *Verticillium* sp. can lead to the synthesis of metal nanoparticles by enzymatic pathway [48]. We have recognized an important advance in developing this strategy to encompass synthesis of oxide nanoparticles using fungi.

3.5.1 Experimental details

Fungi such as *Fusarium oxysporum* and *Verticillium* sp. were maintained on potato-dextrose-agar (PDA) slants. Stock cultures were maintained by subculturing at monthly intervals. After growing at pH 7 and 27 °C for four days the slants were preserved at 15 °C. From an actively growing stock culture, subcultures of both the fungi were made on fresh slants and after four days of incubation at pH 7 and 27 °C were used as the starting materials for the experiments. Seed inoculums were made from the slants which further are inoculated in 500 ml Erlenmeyer flasks containing 100 ml MGYP medium. After adjusting the pH of the culture medium to 7, the cultures were grown under continuous shaking on a rotary shaker (200 rpm) at 27 °C for 96 hours. After 96 hours of growth, mycelia of the respective fungi were separated from the culture broth by centrifugation (5000 rpm) for 20 minutes at 20 °C and then the mycelia were washed thrice with distilled water under sterile conditions. 20 g (wet weight) of *F. oxysporum* and *Verticillium* sp. each was then resuspended in 100 ml aqueous solutions of $K_3Fe(CN)_6$ and $K_4Fe(CN)_6$ (pH 3.1) in a 2 : 1 molar ratio in 500 ml Erlenmeyer flasks and kept on a shaker (200 rpm) at 27 °C. The reaction was carried out for a period of 120 h. In a control experiment, all the experimental conditions were kept similar, except that 20 g of each fungal biomass was separately exposed to sterilized deionised water instead of iron complex. The bio-transformed products were collected by separating the fungal mycelia from the aqueous extract by filtration under sterile conditions. Filtrate was characterized for the presence of magnetite nanoparticles by TEM, FTIR, XRD and magnetic measurements etc. M vs H curves and χ^{-1} vs temperature plots were obtained for Fe_3O_4 nanoparticles synthesized using *Fusarium oxysporum* and *Verticillium* sp. Magnetization data were collected on frozen colloidal solutions containing magnetite nanoparticles using a vibrating Sample Magnetometer (Oxford Instruments) with superconducting iron magnet generating an external magnetic field of 12 T. FC-ZFC measurements were performed by cooling the samples from 150 K to 2 K in the absence and presence of external magnetic field of 50 Oe respectively.

Biochemical analysis of magnetite formation by *Verticillium* sp. was carried out by analyzing extracellular proteins from *Verticillium* sp. with and without its exposure to the iron precursors. The extracellular extracts thus obtained from *Verticillium* sp. were lyophilized, dialyzed (12 kDa cut off) and their protein profiles were compared by 10 % SDS-PAGE (sodium dodecyl sulphate polyacrylamide gel electrophoresis) carried out at pH 8.2 In a separate experiment, the above two protein profiles were compared by native PAGE and the extra protein bands obtained in the presence of iron precursor ions were eluted from native gel. The hydrolytic activity of these eluted proteins was checked by TEM and SAED analysis. Hydrolysis of ferri/ferrocyanide complex by *Verticillium* sp. was analyzed by UV-vis spectroscopic analysis for the activity of cyanide hydratase.

3.5.2 Transmission electron microscopic analysis

Figure 3.19 shows the TEM images of magnetite nanoparticles synthesized using *F. oxysporum* after the reaction between fungal biomass and aqueous solution of ferri/ferrocyanide salts for 120 h. Representative TEM images recorded at different magnifications of magnetite nanoparticles from the *F. oxysporum* - iron precursor reaction medium after 120 h of reaction are shown in Figure 3.19A and B. The particles formed are irregular in shape presenting an overall quasi-spherical morphology. The particles range in size from 20–50 nm. SAED analysis of the individual particles indicated that they are crystalline; the diffraction pattern could be indexed on the basis of the magnetite (Fe_3O_4) structure (inset in Figure 3.19B).

High magnification of these images indicated that nanoparticles are imbedded in a matrix like structure, which could be a proteinacious material secreted by the fungus. Nanoparticles appear to be well separated from each other, since they are capped by the proteins present on the surface. Figure 3.19C and D shows TEM images of magnetite nanoparticles after calcined at 400 °C for 2 h indicating a little variation in morphology. Nanoparticles appeared to be well separated with little sintering and the overall dimension was found to be around 20-50 nm. However, the crystallinity of nanoparticles dramatically improved due to the heat treatment. This is reflected in the SAED pattern of the calcined nanoparticles, which can be indexed on the basis of magnetite structure quite radially [32].

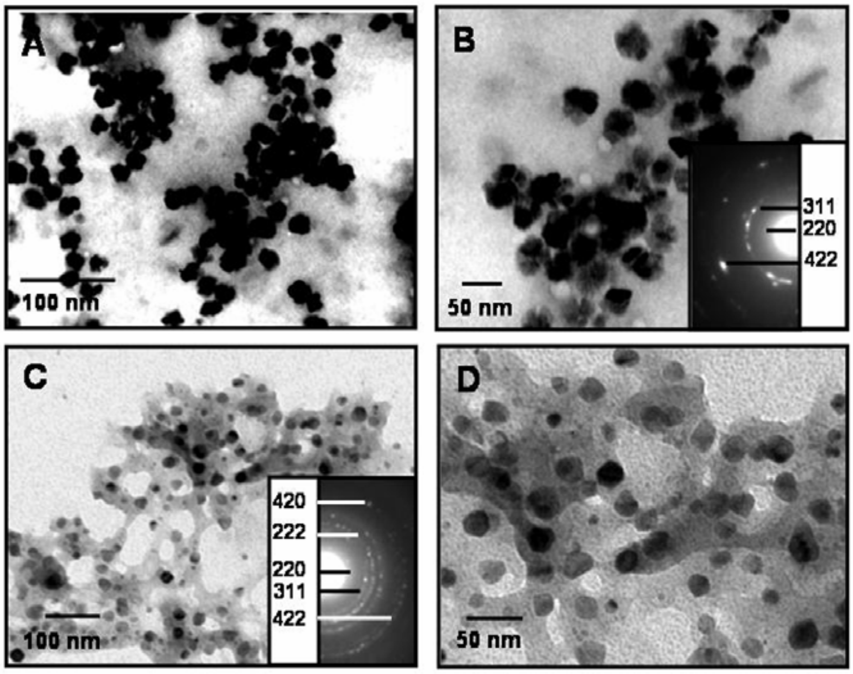

Figure 3.19 *TEM micrographs of iron oxide nanoparticles synthesized by reaction between Fusarium oxysporum and iron cyanide precursors before (A & B) and after calcination at 400 °C for 3 h (C & D) The insets in B and C are SAED patterns recorded from the particles shown in the main images respectively.*

Figure 3.20 shows TEM micrograph of magnetite nanoparticles obtained by the reaction of *Verticillium* sp. and iron cyanide precursors after 120 h. A number of cubo-octahedrally shaped particles ranging in size from 100–400 nm are observed (Figure 3.20

A). Careful analysis of these images indicated that the cubic shape of the nanoparticles is actually an assembly of individual nanoparticles and proteins secreted by *Verticillium* sp. SAED analysis of the particles indicated the spot diffraction pattern that could be indexed on the basis of magnetite crystal structure of iron oxide (inset in Figure 3.20A) [32]. Figure 3.20C and D show the TEM images of magnetite nanoparticles after the calcination at 400 °C for 2 h. Unlike the magnetite nanoparticles synthesized by *F. oxysporum*, the iron oxide nanoparticles synthesized using *Verticillium* sp. undergo a detectable change in overall particle morphology and form large irregularly shaped aggregates (Figure 3.20C & D).

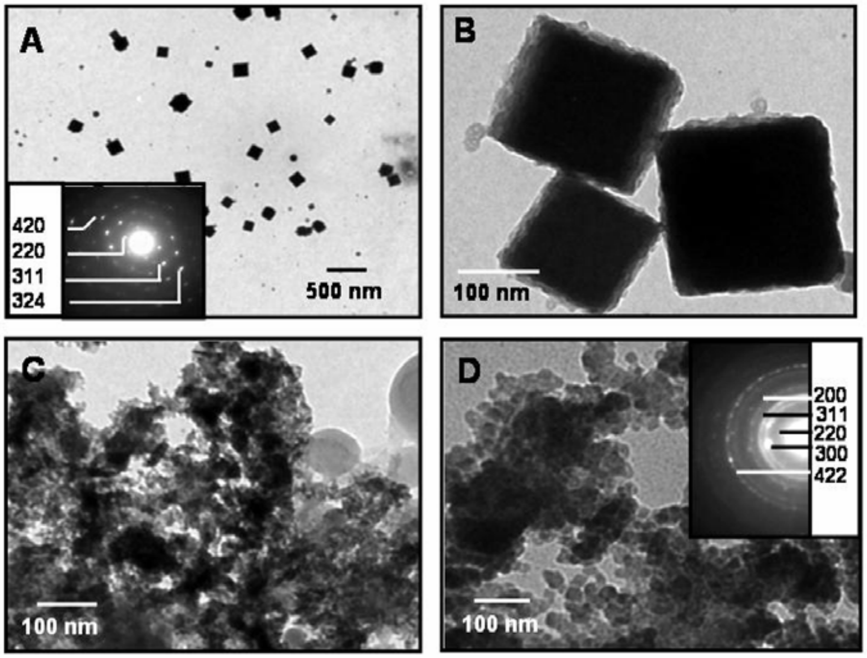

Figure 3.20 *TEM micrographs of iron oxide nanoparticles synthesized by reaction between Verticillium sp. and iron cyanide precursors before (A & B) and after calcination at 400^{o} C for 3 h (C & D) The insets in A and D are SAED patterns recorded from the particles shown in the main images respectively.*

This supports our inference that the cubic structures seen in the as-prepared particles are indeed due to a loosely bound assembly of smaller magnetite particles held together due to the proteins secreted by the fungus. The SAED analysis of iron oxide nanoparticles synthesized using *Verticillium* sp. after the calcination shows that the particles still possess magnetite structure (inset in Figure 3.20D).

3.5.3 X-ray diffraction analysis

Figure 3.21 shows X-ray diffraction pattern of iron oxide nanoparticles synthesized by *F. oxysporum* and *Verticillium* sp. respectively. XRD pattern shows a number of Braggs reflections originated from solution cast film of reaction filtrate. These XRD patters shows excellent match with magnetite structure [32]. All the peaks marked as "o" corresponds to magnetite while peaks marked as "•" could be indexed on the basis of γ-Fe_2O_3 structure of the iron oxide.

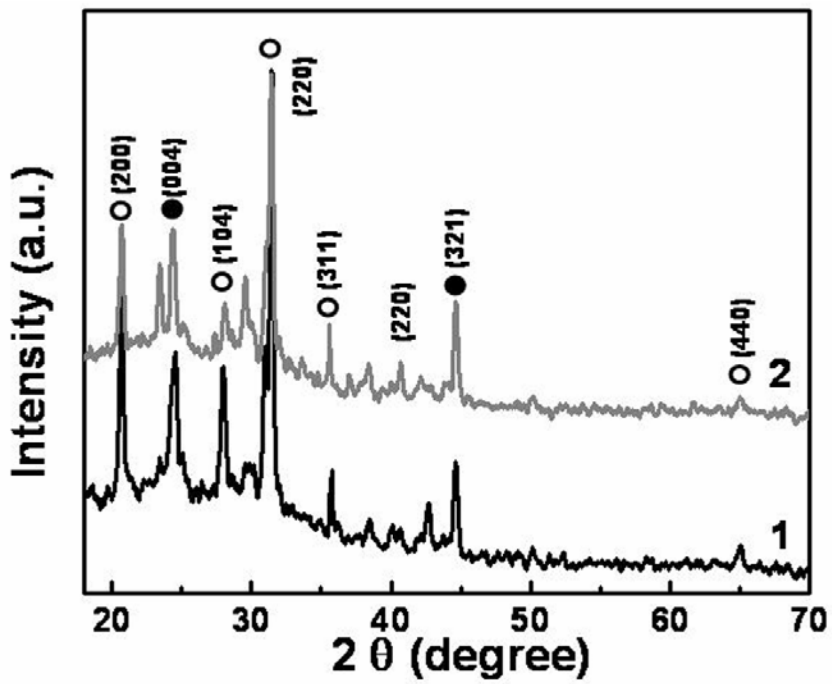

Figure 3.21 *XRD patterns recorded from iron oxide nanoparticles synthesized by the reaction of iron cyanide precursors with F. oxysporum (curve 2 in grey) and Verticillium sp. (curve 1 in black) respectively. The peaks marked with "o" correspond to the* Fe_3O_4 *and "•" to* γ-Fe_2O_3.

The *d* values and the respective *hkl* planes are as fallows: For magnetite marked as "o" 2.86 (220), 2.44 (311), 2.02 (400), 1.64 (422) 1.26 (622), 0.96 (642). For maghaemite (γ-Fe_2O_3) marked as "•" 3.23 (205), 2.20 (113) respectively [32].

3.5.4 FTIR spectral characterization

Figure 3.22 illustreates the FTIR spectra of iron oxide nanoparticles synthesized after 120 h of reaction between *F. oxysporum* and *Verticillium* sp. FTIR analysis of the nanoparticles from *Fusarium oxysporum* - iron precursor reaction medium showed the presence of prominent resonances at ca. 522, 568 and 627 cm^{-1} (curve 1, Figure 3.22) and are attributed to excitation of Fe-O stretching vibration [33]. Two absorption bands centered at 1638 and 1540 cm^{-1} (amide I and II bands respectively; curve 1, Figure 3.22B) attest to the presence of proteins in the quasi-spherical magnetite particles. The FTIR spectrum recorded from iron oxide nanoparticles synthesized using *Verticillium* sp. showed the presence of absorption bands centered around 522 cm^{-1} and 627 cm^{-1} (Figure 3. 22A, curve 2), which are characteristic of Fe-O-Fe vibrational modes. As observed earlier in case of biogenic iron oxide synthesized using *Fusarium oxysporum*, the presence of proteins in the iron oxide nanoparticles synthesized using *Verticillium* sp. is indicated by the amide I and II bands in the FTIR spectrum (curve 3, Figure 3. 22B).

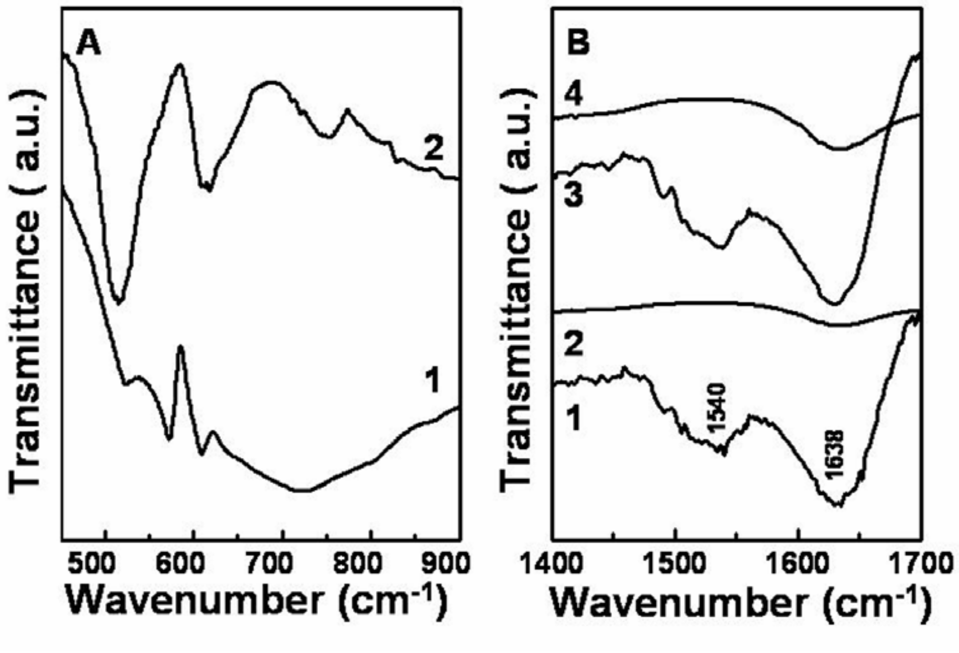

Figure 3.22*(A) FTIR spectra recorded from the powdered iron oxide synthesized by the reaction between iron cyanide complex and fungi F. oxysporum (curve 1) and Verticillium sp. (curve 2) respectively. A number of Fe-O absorption bands are observed which are due to the bending and stretching mode of Fe-O bonds. (B) Presence of amide bands suggests that proteins are associated with the nanoparticles. (curve 1-as synthesized magnetite by F. oxysporum, curve 2- calcined magnetite synthesized by F. oxysporum. curve 3- As synthesized magnetite Verticillium sp, curve 4- calcined magnetite synthesized by Verticillium sp.).*

Calcination treatment of as synthesized iron oxide nanoparticles does not show the presence of amide bands (curve 2 and 4 in Figure 3.22B) indicating the association of proteins along with nanoparticles.

3.5.5 Magnetic measurements

Magnetic measurements were performed on the frozen colloidal solutions containing iron oxide nanoparticles synthesized by both fungi namely, *F. oxysporum* and

Verticillium sp. respectively. Magnetization data from the particles synthesized using the two fungi are shown in Figure 3.23. The magnetization isotherm measurements (M vs H at fixed temperature) were carried out upto ± 5 T at 2 k. There was no observation for the spontaneous magnetization in iron oxide nanoparticles synthesized by both the fungi. However, at low magnetic field M vs H data (Figure 3.23 A) shows sharp rise in the magnetization (M), particularly for magnetite particles synthesized using *Verticillium* sp. This possibly signifies the presence of interparticle dipolar interaction in the ensemble of nanoparticles [49].

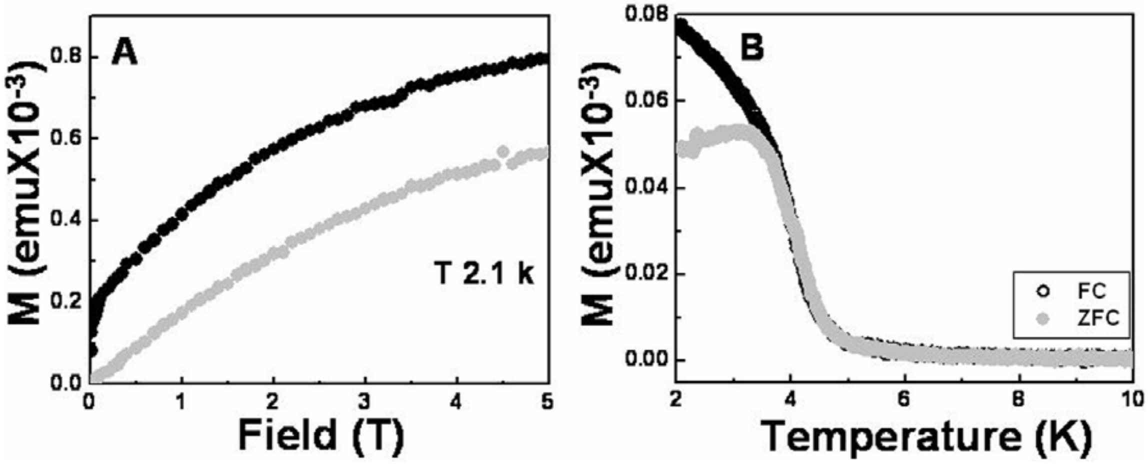

Figure 3.23 *Magnetization data collected on frozen colloidal solution containing magnetite nanoparticles synthesized by F. oxysporum and Verticillium sp. respectively. (A) M-H curve of magnetite nanoparticles showing initial magnetization as a function of applied external field at 2.1 k. Induced magnetization is higher in case of magnetite synthesized by Verticillium sp. (black curve) in comparison with magnetite synthesized by F. oxysporum (grey curve). (B) ZFC-FC plot for magnetite particles synthesized using Verticillium sp. at an external applied magnetic field of 50 Oe. (Black curve – FC plot, red curve-ZFC plot).*

Figure 3.23B shows ZFC-and FC plots for the magnetite sample synthesized by *Verticillium* sp. ZFC-FC plots do not superimpose and show clear branching at a temperature of around 4k. Such behavior has been earlier observed in many ferrofluid systems [50]. On the other hand, the value of branching temperature obtained in our study is quite low compared to the earlier observation for 10 nm magnetite nanoparticles [48]. Thus, from the magnetization data it may be inferred that the correlated magnetic domains are much smaller than the 10 nm magnetite nanoparticles that form larger particles (~ 400 nm) as observed in TEM pictures (Figure 3.20B). For such a small magnetic domains, one expects very low moments for the system.

ZFC-FC plot for iron oxide nanoparticles synthesized using *Fusarium oxysporum* did not show any measurable branching. This may be due to the fact that the measurements were carried out at 0.05 T field, since the reliable data could not be collected with a low field of 0.005 T as used for particles synthesized using *Verticillium* sp. The application of higher fields can cause suppression of blocking phenomenon. The χ^{-1} vs T data for magnetite nanoparticles, synthesized by *F. oxysporum* clearly exhibit a sharp fall below 5 K, however for high temperature region the plot follows the Curie-Weiss law $\chi = C/(T-\theta)$ (dotted line, Figure 3.24 A) yielding a value of $\theta = -32.9$k. Curie-Weiss fit ($\chi^{-1} = (T-\theta)/C-b/(T-\theta_P)$) above the transition temperature θ_P gives the value of 1.0 K (solid line, Figure 3.24A). The corresponding values for particles obtained from *Verticillium* sp. are found to be -68.5 K and 3.0 K respectively (dotted and solid lines, Figure 3.24B respectively). The higher values of θ and θ_P obtained for *Verticillium* sp. implies stronger antiferromagnetic exchange interaction [51].

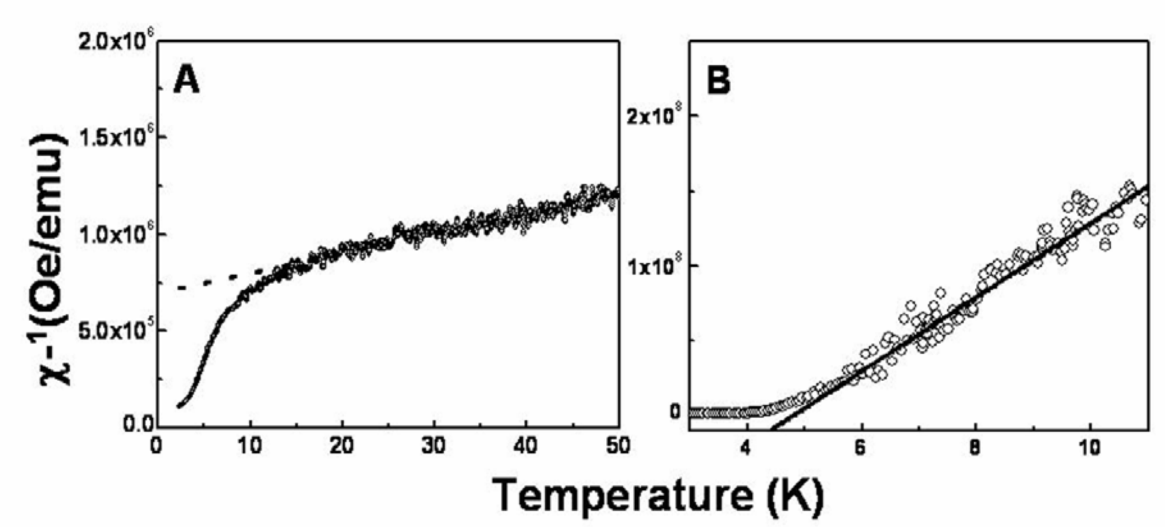

Figure 3.24 *χ^{-1} vs T plots for Fe_3O_4 particles synthesized using fungi Fusarium oxysporum (A) and Verticillium sp. (B) respectively. Doted lines in figure indicate Currie –Weiss law, while solid lines are the fitted data. Note that the plot for the magnetite nanoparticles synthesized by Verticillium* sp. *shows ferromagnetic behavior.*

This result is consistent with the fact that nanoparticles synthesized by this fungus are composed of much smaller particles. Thus, the magnetic measurements indicate the presence of interparticle interaction. M-H curves along with FC-ZFC measurements indicate that iron oxide nanoparticles synthesized by *Verticillium sp.* are superparamagnetic at low temperature with a signature of ferromagnetic transition.

3.5.6 Biochemical analysis

The fact that iron cyanide complexes are not toxic to the fungi indicates that fungi are capable of hydrolyzing these iron complexes subsequently converting them into iron oxides. Many microorganisms including fungi are known to degrade cyanide and metal cyanide complexes [52]. Fungi hydrolyze metal cyanide complex by the action of enzymes like cyanide hydratase or nitrilase, which hydrolyses metal cyanide bond, releasing the free metal moiety. It is also well known that fungi like *F. oxysporum* synthesize low molecular weight ferric iron chelating compound called as siderophores [19]. We believe that the biochemical mechanism of iron oxide formation in both the fungi under consideration is similar. However, there could be structurally different capping proteins, since we observed substantial difference in the morphology of iron oxide nanoparticle synthesized by *F. oxysporum* and *Verticillium sp.* respectively. We have considered magnetite formation by *Verticillium* sp. for biochemical characterization owing to the superior results that we obtained as comparison with *F. oxysporum*.

One of the easier ways to analyze the biochemical mechanism for the extracellular biosynthesis of nanoparticles is to study the protein profile of culture filtrate/supernatant of the fungal biomass incubated with and without precursor salts. To identify the fungal protein(s) responsible for hydrolysis of aqueous precursor complexes into magnetite particles, the extracellular extracts obtained from *Verticillium* sp. with and without its exposure to the iron precursors after 120 h of incubation were analyzed by 12% denaturing polyacrylamide gel electrophoresis (SDS-PAGE).

Exposure of *Verticillium* sp. to the anionic iron complexes resulted in the induction of the proteins with the molecular weights of ca. 13 kDa and 55 kDa (lane Ex, Figure 3.25A), which are absent in the fungal extract profile obtained in the absence of anionic iron complexes (lane C, Figure 3.25A). These two protein profiles, when compared on native PAGE, shows the similar results as observed in SDS-PAGE. When two induced proteins were eluted from the gel and checked for their activity, the formation of iron oxide from its precursors was observed (Figure 3.25B). TEM analysis and SAED pattern of these nanoparticles confirmed that they are magnetite (Figure 3.25B along with inset). We believe that the hydrolysis of iron cyanide complex is mediated by the action of an enzyme cyanide hydratase, which is synthesized by *Verticillium* sp.

extracellularly. The fact that exposure of iron cyanide complex to *Verticillium* sp. results in the induction of two proteins, which have the ability to synthesize iron oxide nanoparticles *in vitro* suggests that one of the inducible protein has cyanide hydratase activity.

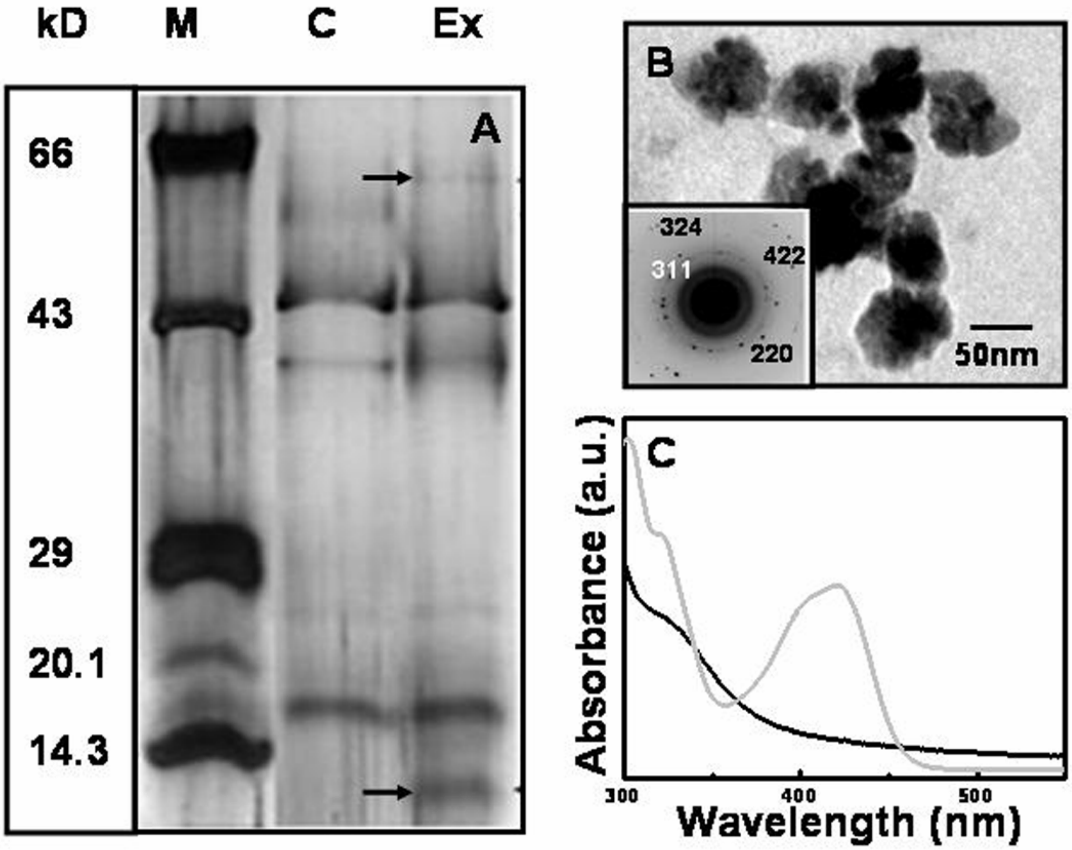

Figure 3.25*(A) Silver stained SDS-PAGE (Sodium dodecyl sulphate- polyacrylamide gel electrophoresis) data showing the extracellular protein profile of Verticillium sp. on 12 % resolving gel. Lanes C and Ex correspond to the extracellular proteins from Verticillium sp. obtained by lyophilization of the fungal filtrate in the absence and presence of iron oxide precursors, respectively. Lane M corresponds to standard protein molecular weight markers with respective molecular weight. (B) TEM micrographs of iron oxide nanoparticles synthesized using two induced proteins fraction obtained from Verticillium sp. and eluted from native PAGE. Inset in image shows the SAED pattern. (C) UV-vis spectroscopic analysis of the hydrolysis of iron cyanide complex by Verticillium sp. Grey curve shows the absorption at 420 nm due to ferricyanide/ferrocyanide complex, while black curve shows the absorption hump at 330 nm, due to the presence of iron oxide.*

It is quite possible that fungus can utilize cyanide as a source of carbon and nitrogen for its own metabolism under the starving conditions as discussed in section 3.3.6. Therefore based on the preliminary results it can be concluded that the exposure of iron cyanide to *Verticillium* sp. results in the induction of two new proteins.

Figure 3.25C shows the UV-vis spectral analysis of degradation of ferri/ferrocyanide reaction mixture and the formation of iron oxide nanoparticles by *Verticillium* sp. It is clearly observed that iron cyanide complex, which shows absorption at 420 nm (Grey curve, Figure 3.25C) is hydrolyzed due to the metal cyanide hydrolyzing enzyme secreted by *Verticillium* sp. Instead, an absorption hump at 330 nm is developed indicating the presence of iron oxide nanoparticles (black curve, Figure 3.25C). One of the proteins has cyanide hydratase activity while other may be involved in the conversion of released Fe ions into magnetite. It should be noted here also that after the incubation of the fungal biomass with iron salts pH of the reaction medium becomes slightly alkaline, which may help in the formation of magnetite. Though preliminary analysis of magnetite biosynthesis suggests that cyanide hydrolyzing enzyme cyanide hydratase is involved in the biosynthesis of magnetite, it further entails detailed investigation of the process.

3.5.7 Discussion

This part of the chapter illustrates the use of eukaryotic microorganisms such as fungi for the synthesis of magnetite nanoparticles from anionic iron cyanide complexes. TEM analysis indicated that magnetite nanoparticles synthesized by using *F. oxysporum* were 20-50 nm in diameter. On the other hand TEM analysis of magnetite synthesized by *Verticillium* sp. indicated cubic superassembly with edge lengths between 100-400 nm, which is destroyed after calcination treatment indicating that is composed of smaller nanoparticles. X-ray analysis of magnetite nanoparticles indicated the presence of mixed phases of iron oxides, magnetite being the dominant one. Magnetic measurements suggest that magnetite nanoparticles synthesized by *Verticillium* sp. and *F. oxysporum* showed superparamagnetic and antiferromagnetic exchange interactions at low temperature. Biochemical analysis of magnetite formation using *Verticillium* sp. indicates that exposure of iron cyanide complex to *Verticillium* sp. induces the synthesis of two new proteins with molecular weights of 55 kDa and 13 kDa. One of these proteins harbored cyanide hydratase activity, which degrades metal cyanide complex as indicated by UV-vis spectroscopic analysis of the reaction mixture. Further in-vitro reaction of inducible proteins and iron precursors resulted in the magnetite formation.

3.6 Conclusions

This chapter describes the biological synthesis of iron oxide nanoparticles by using different microorganisms. A bacterium isolated from our lab, which was latter identified as *Actinobacter* spp. was explored for the biological synthesis of iron oxides like magnetite (Fe_3O_4) and maghaemite (γ- Fe_2O_3). It has been conclusively shown that *Actinobacter* spp. synthesizes different oxides of iron when reacted with the different iron precursors. The reaction with aqueous $K_3Fe(CN)_6$ and $K_4Fe(CN)_6$ mixture in 2:1 M ratio resulted in the synthesis of nanocrystalline magnetite, while exposure to 1mM ferric citrate could yield maghaemite nanoparticles. The TEM analyses of magnetite nanoparticles indicated the overall dimensions of 10-20 nm, whereas maghaemite nanoparticles were found to be 5-7 nm in dimensions. Magnetic measurements performed on both the samples showed superparamagnetic nature of nanoparticles. Biochemical analysis of magnetite nanoparticle synthesis indicated the implication of the enzyme cyanidase, a metal cyanide hydrolyzing enzyme. Extracellular protein analysis showed the presence of two new proteins with molecular weight of 100 kDa and 70 kDa in the culture supernatant of the bacteria exposed to iron cyanide complexes. Maghaemite formation involved iron reduction, followed by hydroxylation and dehydration. Ferrisiderophore reductase synthesized by *Actinobacter* spp. is found to be responsible for Fe^{3+} reduction. Inhibition of its activity blocked the synthesis of maghaemite nanoparticles. Induction of a 55 kDa protein is found to occur extracellularly after the exposure of *Actinobacter* spp. to iron salt. Four different low molecular weight proteins were isolated from the surface of maghaemite nanoparticle with the molecular weights of 15, 16, 20, 23 kDa respectively. Fungi such as *F. oxysporum* and *Verticillium* sp. are also found to yield magnetite nanoparticles when challenged with aqueous solution of $K_3Fe(CN)_6$ and $K_4Fe(CN)_6$. Magnetite nanoparticles 20-40 nm in diameter were synthesized by *F. oxysporum*. On the other hand cubical super assembly of smaller magnetite nanoparticles with edge length of 100-400 nm is resulted using *Verticillium* sp. with superparamagnetic and antiferromagnetic exchange interqctions. Biochemical analysis of magnetite formation in *Verticillium* sp. shows the involvement of the enzyme cyanide hydratase. However involvement of other proteins can not be ruled out at this point of research.

3.7 References

[1] Fernandez-Garcia, M., Martinez-Arias, A., Hanson, J., C., Rodriguez, J., A. *Chem Rev.* **2004**, *104*, 4063.

[2] Speliotis, T., E., *J. Magn. Magn. Mater.* **1999**, *193*, 29.

[3] Raj, K., Moskowitz, R., Casciari, B., *J. Magn. Magn. Mater.* **1995**, *149*, 174.

[4] Bulte, J. W. M., Kraitchman, D. L. *NMR Biomed*. **2004**, *17*, 484**.**

[5] Pankhurst, Q. A., Connolly, J., Jones, S. K., Dobson, J. *J. Phys. D: Appl. Phys.* **2003**, *36*, R167-R181.

[6] Matsunaga, T.,Okamura,Y., Tanaka, T. *J. Mater. Chem.* **2004**, *14***,** 2099.

[7] Shinkai, M. *J. Biosci. Bioeng.* **2002**, *94*, 606.

[8] **(**a) Hyeon, T., Lee, S. S., Park, J., Chung, Y., Na, H. B. *J Am. Chem Soc.* 2001, *123*, 12798. (b) Hyeon, T. *Chem. Commun.* **2003,** 919.

[9] (a) Sahoo, Y., *et al J. Phys. Chem. B,* **2005**, *109*, 3879. (b) Gee, S., H., Hong, Y. K., Erickson, D. W., Park, M. H. *J. Appl. Phys.* **2003**, *93*, 7560.

[10] Nelson, D. M., Cox, M. M. Lehninger's Principals of Biochemistry, 4th ed, 2005.

[11] Bazilinski, D. A., Frakkel, R. B., Garrot-reed, A. J., Mann, S. Iron Biominerals (eds. Frankel, R. B., Blackmore, R. P.) **2000**, 239, Plenum Press, New York.

[12] (a) Toress de Araujo, F. F., Pires, M. A., Frankel, R. B., Bicudo, C. E. M. *Biophys, J.* **1986**, *50*, 376. (b) Maher, B., A. *Proc. R. Soc. Lond. Biol*. **1998**, *265*, 733. (c) Lowenstam, H. A., *Science* **1981**, *211*, 1126. (d) Mann, S., Sparks, N. H. C., Walker, M. M., Kirschvinc, J. L. *J. Exp. Biol.* **1988**, *140*, 35. (e) Wiltschko, R., Wiltschko, W. In *Magnetic orientation in animals*, 1995, Springer, New York. (f) Kirschvinc, J. L., Kobayashi- Kirschvinc, A., Woodford, B., J. *Proc. Natl. Acad, Sci. USA* **1992**, *89*, 7683.

[13] Blackmore, R. P. *Science*, **1975**, *190*, 377.

[14] (a) Blackmore, R. P. *Annu. Rev. Microbiol*. **1982,** *36*, 217.(b) Bazylinski, D. A., Frankel, R. B., Jannasch, H. W. *Nature*, **1988**, *334*, 518. (c) Sakaguchi, T., Burgess, J. G., Matstunaga, T. *Nature*, **1993**, *365*, 47. (d) Schuler, D., Frankel, R. B. *Appl. Microbiol. Biotechnol*. **1999**, *52*, 464. (e) Philse, A. P., Maas, D. *Langmuir* **2002**, *18*, 9977.

[15] (a) Bazylinski, D. A., Garratt-Reed, A., Frankel, R. B. *Microscopy Res. Tech*. **1994**,

27, 389. (b) Spring, S., Schleifer, K. H. *Appl. Microbiol*. **1995**, *18*, 147.

[16] (a) Moskowitz, B. M. *Rev. Geophy*, **1995**, *33*, 123. (b) Bazylinski, D. A., Frankel, R., B. *Nat. Rev. Microbiol*. **2004**, *2*, 217.

[17] Komeili, A., Hojatollah, V., Beveridge, T. J., Newman, D. K. *Proc. Natl. Acad, Sci*., *USA*. **2004**, *101*, 3839.

[18] (a) Calugay, R. P., Miyashita, H., Okamura, Y., Matsunaga, T. *FEMS Microbiol Lett*. 2003, *218*, 371. (b) Naguchi, Y., Fujiwara, T., Yoshimatsu, K., Fukumori, Y. *J. Bacteriol.* 1999, *181*, 2142.

[19] Guerinot, M. L. *Annu. Rev. Microbiol*. **1994**, *48*, 743.

[20] (a) Paoletti, L. C., Blackmore, R. P. *J. Bacteriol.* **1986**, *167*, 73.

[21] Frankel, R. B., Papaefthymiou, G. C., Blackmore, R. P., O'Brien, W. *Biochim. Biophy Acta*, **1983**, *763*, 1947.

[22] (a) Astushi, A., Web, J., Matsunaga, T. *J. Biol. Chem.* **2003**, *278*, 8745. (b) Matsunaga, T., Okamura, Y. *Trends Microbiol.* **2003**, *11*, 536.

[23] (a) Lovley, D. R., Stolz, J. F., Nord Jr, G. L., Phyllips, E. J., P. *Nature*, **1987**, *330*, 252. (b) Glasauer, S., Langley, S., Beveridge, T. J. *Science*, **2002**, *295*, 117.

[24] Lovley, D. R. *Iron Biominerals* (ed. Frankel, R., B., Blackmore, R., P.)**1990**, 151, Plenum press New York.

[25] Dong, H. *et al Chem Geol.* **2000**, 169, 299.

[26] Vali, H. *et al Proc. Natl. Acad, Sci*., *USA* **2004**, *101*, 16121.

[27] Lovley, D. R. *Annu. Rev. Microbiol*. **1993,** *47*, 263.

[28] Frankel, R. B. *Nature,* **1887**, *330***,** 208.

[29] Sambook, J., Fritsch, E., Manniatis, T., *Molecular cloning: A Laboratory manual*, 2nd ed., 1989, Cold Spring Harbor Laboratory press, New York.

[30] Pidiyar, V. J., Jangid, K., Patole, M. S., Shouche, Y. S. *Am J Trop Med Hyg*. **2004**, *70***,** 597.

[31] Lane, D. J. *et al Proc. Natl. Acad, Sci*., *USA* **1885**, *82*, 6955.

[32] The XRD patterns were indexed with reference to the crystal structure of magnetite from *JCPDS-ICDD,* PCPDF WIN version 1.30, 39-1346.

[33] (a) Music, S., Santana, G. P., Smit, G. V., Garg, K. *Croat.Chem. Acta*, **1999**, *72*, 87. (b) Saric, A., Music, S., Nomura, K., Popovik, S. *J. Molec. Sctruct.* **1999**, *480*, 633.

[34] (a) Sorensen, C. M. *Nanoscale materials in chemistry* (ed. Klabunde, K. J.) **2002**, 169, Wiley, New York (b) Leslie-Pelecky, D. L., Rieke, R. D. *Chem. Mater*, **1996***, 8*, 1770.

[35] (a) Culity, B. D. *Introduction to Magnetic Materials*, **1972**, Chapter 6, 184, Addison-Wesley Publishing Reading. (b) http:// www. Uwgb. Edu/dutchs/ PETROLOGY/ Spinel % Structure.HTM.

[36] (a) Plaza, R. C., Gomez-Lopera, S. A., Delgado, A. V. *J. Colloid. Interface Sci.*, **2001**, *240*, 48. (b) Mikhailova, M. *et al Langmuir*, **2004**, *20*, 2472.

[37] Malkinski, L. M., Wang, J. Q., Dai, J. B., Tang, P. B. *J. Appl. Phys. Lett*. **1999**, *75*, 844.

[38] Vassiliou, J. K. *et al J. Appl. Phys.* **1993,** *75*, 5109.

[39] Hoffman, R. *et al J. Magn. Magn. Mater*, **2002**, *250*, 32.

[40] Ebbs, S., *Curr. Opin. Biotechnol.*, **2004**, *15*, 231.

[41] Dursun, A. K., Calik, A., Aksu, Z., *Process Biochem*. **1999**, *34*, 901.

[42] Dailey, H. A., Lascelles, J. *J. Bacteriol*, **1977**, *129*, 815.

[43] Huyer, M, Page, W. J. *J. Bacteriol*, **1989**, *171*, 4031.

[44] The XRD pattern was indexed with the reference to the crystal structure of maghaemite from *JCPDS-ICDD,* PCPDF WIN version 1.30, 39-1346.

[45] Pascal,C., Pascal, J. L., Favier, F., Moubtassim, M. L., Payen, C. *Chem. Mater.* **1999**, *11*, 141.

[46] (a) Shiv Shankar, S., Patil, U. S., Prasad, B.L.V., Sastry, M. *Langmuir*, **2004**, *20*, 1853. (b) Deki, S. *et al*, *J. Mater. Chem*, **1997**, *7*, 1769.

[47] Beveridge, T. J., *Can. J. Microbiol*. **1978**, *24*, 89.

[48] (a) Mukherjee, P. *et al, Angew. Chem. Int ed.* **2001**, 40, 3585. (b) Mukherjee, P. *et al*, *Nano Lett*. **2001**, *1*, 515.

[49] Sankar, S. *et al*, *J. Magn. Magn. Mater.* **2000**, 221, 1.

[50] Poddar, P., Talem-Shafir, T., Fried, T., Markovich, G. *Phys. Rev. B* **2002**, *66*, 60403.

[51] Goya, G. F., Berquo, T. S., Fonseca, F. C., Morales, M., P. *J. Appl. Phys.***2003**, 94, 3520.

[52] Barclay, M., Hart, A., Knowles, C. J., Meeusen, J. C. L., Tet, V. A. *Enzyme Microb Technol*. **1998**, *22*, 223.

Chapter IV

Bacterial synthesis of Metal Sulfide nanoparticles

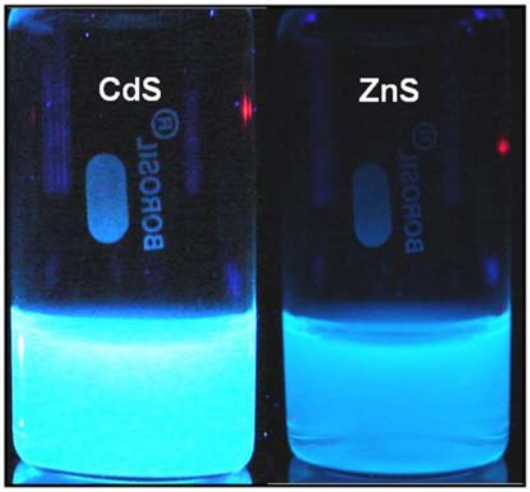

This chapter describes the biosynthesis of metal sulfide nanoparticles using bacteria. Semiconductor sulfide nanoparticles like CdS, ZnS, PbS and Ag_2S are synthesized by two different bacterial species namely *Pseudomonas aeruginosa* and *Actinobacter* spp. Biogenic CdS, ZnS and PbS nanoparticles exhibited size quantization effect and hence can be considered as quantum dots. Moreover, bacterially synthesized CdS, ZnS and PbS quantum dots show excellent fluorescent properties. This chapter also describes the biosynthesis of magnetic iron sulfide–greigite (Fe_3S_4) nanoparticles by *Actinobacter* spp. The molecular mechanism responsible for the synthesis of metal sulfide is studied in detail and two genes underlying the process of sulfate reduction in *P.aeruginosa* were identified, cloned and successfully overexpressed in *E.coli* cells. Exposure of *E. coli* cells overexpressing sulfate reductase genes to cadmium, zinc and lead sulfate solution resulted in the formation of respective metal sulfides. Greigite nanoparticles synthesized using *Actinobacter* spp. exhibited superparamagnetic behavior at low temperatures. One of the genes, known as *cys H* encoding sulfate reductase had been identified in *Actinobacter* spp. Formation of all sulfide nanoparticles proceeds via sulfate reduction by an assimilatory sulfate reduction pathway operating in *P.aeruginosa* and *Actinobacter* spp.

Part of the work presented in this chapter has been communicated in the following journals: (1) Bharde, A. A., Parekh, R., Shouche, Y., Sastry, M. *Nat. Biotechnol.* (2007). (2) Bharde, A. A., Parekh, R., Baidakova, M., Shouche, Y., Enoki, T., Hannoyer, B., Ogale, S., Prasad, B.L.V., Sastry M. *Nat. Mater.* (2007) (3) Bharde, A. A., Sastry, M. *Adv. Mater.* (2007). (4) Bharde, A. A., Sastry, M. *Small* (2007)

4.1 Introduction

The reliance of future technologies on developing scalable and economic methods for the fabrication of one-dimensional (1D) systems has spurred intense and rapid progress in the area of materials synthesis. Semiconductor nanocrystals constitute an important class of nanomaterials due to their unique size dependent chemical and physical properties that render them applicable in the emerging field of nanoelectronics [1]. Therefore developing reliable protocols for the synthesis of nanometer scale semiconductor particles is a problem of great importance. Among nanocrystalline semiconductors, metal sulfides are significant due to their optical, electronic and magnetic properties. Sulfide nanoparticles like CdS, ZnS and PbS are tremendously explored and find applications as fluorescent biological labels [2], optoelectronics such as nonlinear optics, flat panel displays, light emitting diodes, transistor components [3], photocatalysts [4], sensors [5], photoelectric and thermoelectric materials [6], photoimaging and photodetection [7] etc. The interesting properties of semiconductor sulfide nanocrystals are because of electronic quantum confinement and the large number of exposed atoms on the surface [8]. Quantum confinement in luminescent semiconductors enables tuning of the absorption and emission via particle size and shape [9]. Transition metal sulfides are useful as dry lubricants, catalysts and solar cells [10]. There are few reports on the synthesis of nanoparticles of transition metal sulfides like iron and nickel which show magnetic properties [11]. Iron sulfide with structural formulae Fe_3S_4 and Fe_7S_8 are magnetic minerals and called as greigite and pyrrhotite respectively. These magnetic sulfides behave as a soft magnet and are mostly studied from geomagnetic field paleoclimatic magnetism point of view [12].

Numerous protocols have been designed for the synthesis of metal sulfide nanocrystallites over a range of composition, size and shapes [13]. However most of the methods employ non – polar organic solvents or caustic chemicals. Recently, biological methods for the synthesis of metal sulfide nanoparticles are gaining importance since they occur in aqueous medium under ambient experimental conditions of temperature and pressure. Biological methods comprise use of microorganisms, small molecules of biological origin, biological templates and small peptides for the synthesis of various metal sulfide nanoparticles. Also biological molecules have been used for capping of sulfide nanoparticles. Living organisms can exert tight control on the synthesis of materials [14]. Therefore, most of the work till date is centered on the use of micro-organisms for the synthesis of sulfide nanoparticles.

Dameron and co-workers have described the intracellular synthesis of quantum semiconductor crystallites of CdS using two different yeast species, *Candida glabrata* and *Schizosaccharomyces pombe* respectively. Short chelating peptides called as phytochelatins with the general structure $(\gamma - \text{Glu} - \text{Cys})_n - \text{Gly}$ controls the nucleation and growth of CdS nanocrystallites, where n varies from 2 – 6 [15]. Recently synthesis of nanocrystalline CdS and subsequent fabrication of diodes have been shown to occur in the yeast *S. pombe* [16]. Another yeast species, *Torulopsis sp*. has been shown to synthesize semiconductor nanocrystalline PbS [17]. Though CdS and PbS nanocrystallites synthesized by yeasts are in the quantum confinement regime, they are synthesized intracellularly [16-17]. To understand the biochemical mechanism of CdS and PbS nanocrystallite synthesis, it is argued that yeast cells upon exposure to Cd or Pb salts synthesize metal chelating peptide to nullify the stress generated by metal ions. On addition of the metal ions, a metal ion – γ glutamyl complex is initially formed and this is accompanied by an increase in the intracellular sulfide levels. Later this sulfide complexes with Cd or Pb to form CdS or PbS nanocrystals, which accumulate in vacuoles present inside the yeast cells [18]. A previous report from this laboratory describes the biological synthesis of CdS nanoparticles using plant pathogenic fungi *Fusarium oxysporum* [19]. Unlike previous reports, CdS nanoparticles were shown to be synthesized extracellularly and sulfate reductases from the fungus was speculated to be responsible for biosynthesis of CdS nanoparticles. However the process of CdS biosynthesis is considerably slower in comparison to yeasts.

Prokaryotic organisms like bacteria have long been explored for the synthesis of inorganic sulfides. Sulphate reducing bacteria use inorganic sulfates for cellular respiration and generate energy for growth and metabolism. In doing so, inorganic sulfates acts as terminal electron acceptor and are converted into respective sulfide [20]. In nature biofilms of sulfur reducing bacteria form cubic ZnS (sphalerite) from very dilute natural solutions [21]. A bacterial species *Klebsiella planticola* Cd-1 has been shown to synthesize CdS nanoparticles in high quantity under anaerobic conditions [22].

An enzyme thiosulfate reductase produced by bacterial cells has been shown to be responsible for the synthesis of CdS. Also biosynthesis of CdS has been shown to occur by *Klebsiella pneumoniae* [23]. In this case an enzyme cysteine desulfydrase converts cysteine into H_2S, which in turn reacts with Cd^+ ions to form CdS. Recently Belcher and co-workers have shown biosynthesis of nanocrystalline CdS using *E. coli* [24]. However sulphur source used in this study was exogenous and bacterial cells merely act as scavenger for CdS nanoparticles that precipitate intracellularly.

Many biological molecules have been used either for synthesis or capping of CdS nanoparticles. Glutathione, cysteine and thiolates able to form high-affinity metal ligand clusters, and have been shown to promote the formation of CdS and ZnS nanocrystals [25]. Further control over nanocrystal synthesis has been gained by using fatty acids, which have been found to promote the formation of CdSe, CdS and CdTe nanocrystals [26]. Further biological approaches to semiconductor nanocrystal synthesis have been extended to intact biological particles. Viral scaffolds have been used as template for the nucleation and assembly of CdS and PbS crystalline nanowires [27]. Peptides capable of nucleating nanocrystal growth have been identified by combinatorial screens and displayed on the surface of M13 bacteriophage. This genetically engineered phage promoted the synthesis of CdS and ZnS single crystalline nanowires [28]. CdS superlatices were also shown to be directed by using self assembled S – layers from Bacillus *stearothermophilus* NRS2004/3 [29].

Additionally a strain of *Pseudomonas stutzeri* isolated from a silver mine produced nanocrystalline silver sulfide together with silver nanoparticles [30]. Bacterial synthesis of iron sulfide with crystallographic phase Fe_3S_4 (greigite) has been shown to occur in magnetotactic bacteria [31] and sulfate reducing bacteria [32]. Iron sulfide nanoparticles synthesized by magnetotactic bacteria are typically in between 35 – 120 nm and this size range is within the permanent single magnetic domain size. Like magnetite, greigite nanocrystals are synthesized in magnetosomes by magnetotactic bacteria [31]. Along with greigite iron sulfide magnetosome houses cubic and tetragonal FeS – which is thought to be precursors of Fe_3S_4. However greigite nanocrystals found in magnetotactic bacteria are synthesized under natural habitat only and no strain of magnetotactic bacteria has been shown to synthesize greigite in pure cultures in the laboratory. However, strict anaerobic conditions are required for the synthesis of magnetosomes of greigite in natural habitats. Due to the stringent growth requirements and difficulties associated in cultivation of magnetotactic bacteria that harbors greigite magnetosomes, biomolecular mechanism of greigite synthesis is not studied in detail.

Though ample work has been done to understand the basic biomolecular mechanism responsible for the synthesis of inorganic materials, very few reports describe the genetic analysis of material formation in living microorganisms. Here we have shown the biosynthesis of metal sulfide nanoparticles using bacterial species *Pseudomonas aeruginosa* and *Actinobacter* spp.

Outline of the present work

Bacterial synthesis of technologically important metal sulfides like semiconductor quantum dots and magnetic iron sulfide has been illustrated in this chapter. Unlike previous reports, where metal sulfide nanoparticles produced by microorganisms are either intracellular, unstable or require anaerobic conditions, we demonstrate here extracellular, aerobic synthesis of metal sulfide nanoparticles, which are found to be stable for weeks in aqueous solution. Furthermore a detailed biochemical and genetic analysis has been described in this chapter which, we believe is responsible for the formation of metal sulfide nanoparticles or controls the crucial biochemical steps responsible for the process. This chapter also describes identification and cloning of two genes responsible for the synthesis of quantum dot semiconductor crystallites like CdS, ZnS and PbS by *P. aeruginosa*. In addition, overexpression of these two genes in *E. coli* and isolation and purification of overexpressed proteins from *E. coli* has been demonstrated. Second part of this chapter describes the biosynthesis of silver sulfide and iron sulfide using *Actinobacter* spp. Biosynthesis of silver sulfide and iron sulfide is found to be precursor dependent and essentially occurs by reduction of sulfate, which is exogenously provided as a precursor. All the semiconductor nanoparticles synthesized by *P.aeruginosa* are well within the limits of quantum confinement and hence can be considered as quantum dots. These semiconductor nanoparticles show strong fluorescence signal. Iron sulfide nanoparticles synthesized by *Actinobacter* spp. are composed of greigite (Fe_3S_4) and pyrite (FeS_2) and exhibit superparamagnetic behavior.

4.2. Part I: Biosynthesis of CdS, ZnS and PbS semiconductor nanocrystallites using *Pseudomonas aeruginosa*

This part of the chapter describes the biosynthesis and characterization of group II-VI semiconductor sulfide nanoparticles like CdS, ZnS and PbS using a gram negative aerobic bacterium *Pseudomonas aeruginosa*. Further, the biomolecular mechanism for the synthesis of these sulfide nanoparticles has been discussed.

4.2.1 Experimental details

A Gram negative bacterium *Pseudomonas aeruginosa* was isolated from Arabian sea, Goa, India. For cultivation of bacteria in 100 ml batch, the bacterial seed culture was grown overnight in small volume (~2 ml) of Luria broth (LB) medium. This seed culture was then inoculated in 100 ml of LB medium in 500 ml Erlenmeyer flask for propagation. For the biosynthesis of CdS, ZnS and PbS nanoparticles bacterial cells were freshly grown in 100 ml of LB medium in 500 ml Erlenmeyer flask and incubated on a rotary shaker (200 rpm) at 37 °C for ~ 36 h. The bacterial biomass was then harvested from the growth medium by centrifugation at 7000 rpm (5533 X *g*). The supernatant was discarded and the cell pellet was washed twice with saline (0.85 % NaCl, W/V) and finally with deionised water. This is followed by mixing of bacterial biomass with 100 ml of sterilized 10^{-3} M solution of $CdSO_4$, and $ZnSO_4$ each in separate Erlenmeyer flask. For synthesis of PbS nanoparticles, bacterial biomass was mixed with 100 ml sterilized 10^{-3} M solution of $PbCl_2$ and $Ca(SO_4)_2$. In this case $PbCl_2$ acts as a source of lead ions while $Ca(SO_4)_2$ provides sulphate. $PbSO_4$ is very sparingly soluble in water and hence can not be used for the synthesis of PbS nanoparticles. All the flasks were incubated on the rotary shaker at 37° C for 48 h. Next the biomass was separated from each flask by centrifugation at 7000 rpm and the supernatant was collected for further characterization. The supernatants containing sulfide nanoparticles were analyzed by TEM, UV – vis spectroscopy, fluorimetry, and XRD. For the genetic analysis of sulfate reductase genes, genomic DNA of *P.aeruginosa* was isolated and genes for phosphoadenosyl phosphosulfate reductase (PAPS) and sulfite reductase (SIR) were PCR amplified by template specific primers. Primer sequences for PAPS and SIR are *att*B1 forward: 5′-GGGG ACA AGT TTG TAC AAA AAA GCA GGC TTC CTG -3′ *att*B2 reverse: 5′–GTG CCG CGC GGC AGC ATG CTG CCC TTT GCT ACC ATT CCC G -3′ for

PAPS reductase and *att*B1 5′–GGG GAC CAC TTT GTA CAA GAA AGC TGG GTC-3′ *att*B2 reverse: 3′ GGG GAC CAC TTT GTA CAA GAA AGC TGG GTC-5′ respectively. The amplified genes were cloned and overexpressed in *E. coli* BL21-AI™ (F^-, gal, Cm^r) cells using Gateway® Technology according to manufacturer's instructions [33]. Initially PCR products i.e. amplified *cysH* and *cysI* genes were separately cloned in pDONR^{TM}221 plasmid, known as an entry vector. Addition of 5'-terminal *att*B sequences to PCR primers allows synthesis of a PCR product that is an efficient substrate for recombination with a donor vector in the presence of BP CLONASE Enzyme Mix. This reaction produces an Entry Clone of the PCR product [33]. LR recombination reactions were performed between entry clones and a Gateway® destination vector pDEST^{TM}17. Next, the expression clones were transformed in *E. coli* BL21-AI cells and induced with L- arabinose for the expression of recombinant proteins [33]. For overexpression and assay of PAPS and SIR enzymes, *E. coli* BL21-AI cells were grown in the presence of ampicillin (100 μg/ μl) together with 10^{-3} M $CdSO_4$, $ZnSO_4$ and $PbSO_4$ respectively. The clones were induced in the presence of L – arabinose for the expression of recombinant proteins. Control experiments were performed without changing the above mentioned procedure except that non-transformed *E. coli* BL-21 AI cells without pDEST^{TM}17 plasmid containing *cysH* and *cysI* genes for PAPS and SIR respectively were used. Overexpressed proteins were analysed by 10 % SDS-PAGE and visualized by staining the gels with coomassie blue R 250 stain.

4.2.2 Biosynthesis of CdS nanoparticles

4.2.2.1 TEM analysis

Representative TEM images of CdS nanoparticles synthesized using *P. aeruginosa* are shown in Figure 4.1. A dense population of CdS nanoparticles was found to be evenly distributed on the grid area as observed by low magnification images (Figure 4.1 A- C). The size of CdS nanoparticles appears to be nearly uniform. Careful analysis of high magnification image indicates that CdS nanoparticles observed in TEM are clusters of smaller nanoparticles that are loosely assembled together (Figure 4.1 E). These clustered nanoparticles are spherical in shape with size between 4.5 – 6.5 nm. Particle size distribution analysis performed on 100 particles in different micrographs indicated the mean diameter of CdS nanoclusters to be 5.5 nm with a small standard deviation value of 0.59 (inset Figure 4.1E).

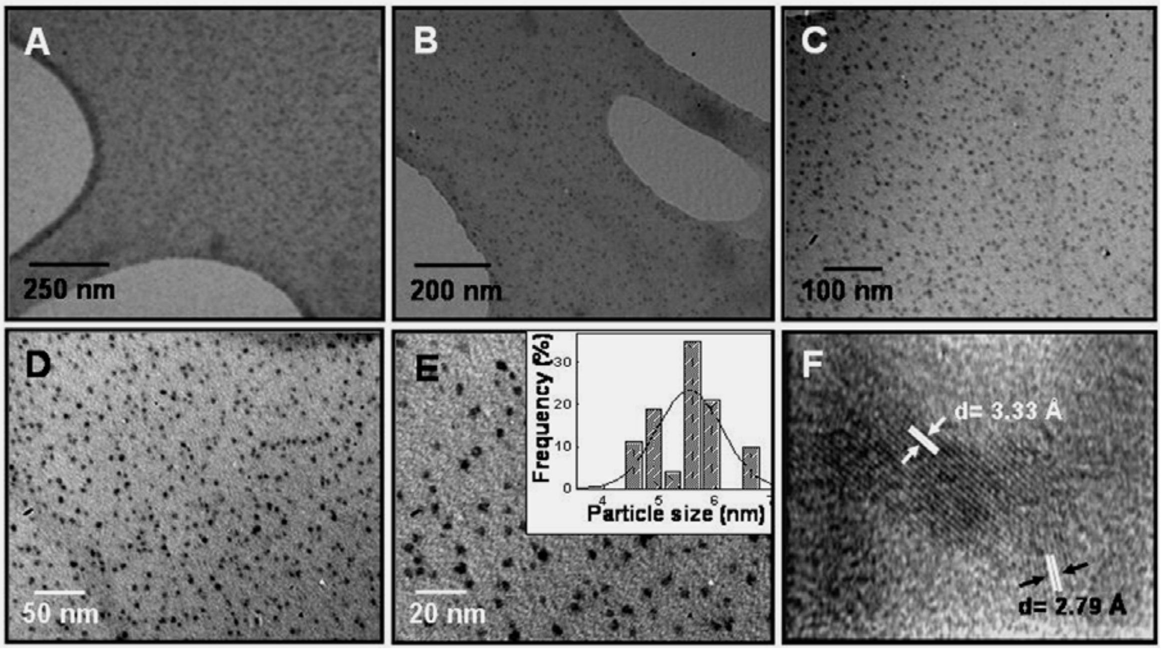

Figure 4.1 TEM images of CdS nanoparticles synthesized using P. aeruginosa. Low magnification images (A – C) show the presence of very high number of CdS nanoparticles. High magnification image (E) shows the loose assembly of smaller particles into bigger clusters. Inset in image E shows particles size distribution analysis. Image F shows a HRTEM image of CdS nanoparticles. The d values correspond to (100) and (111) crystal planes.

Particles smaller than 5 nm were difficult to resolve with the microscope used in this study. A representative HRTEM analysis performed on CdS nanoparticles is shown in the Figure 4.1F. Clearly resolved lattice fringes of CdS nanoparticles are observed in the image indicating the crystalline nature of CdS nanoparticles. The interplanar spacing of 3.33 Å (0.33 nm) and 2.79 Å was assigned to (100) and (111) planes of cubic CdS system respectively. [34].

4.2.2.2 UV – vis spectroscopic analysis

Figure 4.2 shows the UV-vis spectroscopic profile of CdS nanoparticle formation using *P.aeruginosa*. CdS is a direct band gap semiconductor with bang gap energy value of 2.4 eV in the bulk form [35]. Bulk CdS shows a featureless absorption edge around 518 nm. UV-vis spectra recorded as a function of time of reaction between $CdSO_4$ and *P.aeruginosa* is shown in Figure 4.2A. UV-spectroscopic analysis reveals the presence of small absorption peak with absorption maxima around 370 nm, and corresponds to excitonic transitions in CdS nanocrystallites [36a]. Presence of such a sharp absorption peak rather than absorption hump or shoulder indicates the narrow size distribution of nanocrystallites, since large size distribution usually results in wide distribution of the band gaps yielding a broad and featureless absorption edge [36b]. The absorption spectra shown in Figure 4.2A show a large blue shift in comparison with bulk CdS. The absorption of CdS nanoparticles increases with time indicating that $CdSO_4$ is gradually converted to CdS. After around 32 h of reaction all $CdSO_4$ molecules are reduced to CdS by the bacterium. UV-vis spectroscopic analysis suggests the size of CdS nanocrystallites to be in between 2.5 – 3 nm [36a]. This observation is in well agreement with the TEM analysis that shows small clusters of CdS nanoparticles 5 – 6 nm in diameter composed of smaller particles 2.5 to 3 nm in diameter.

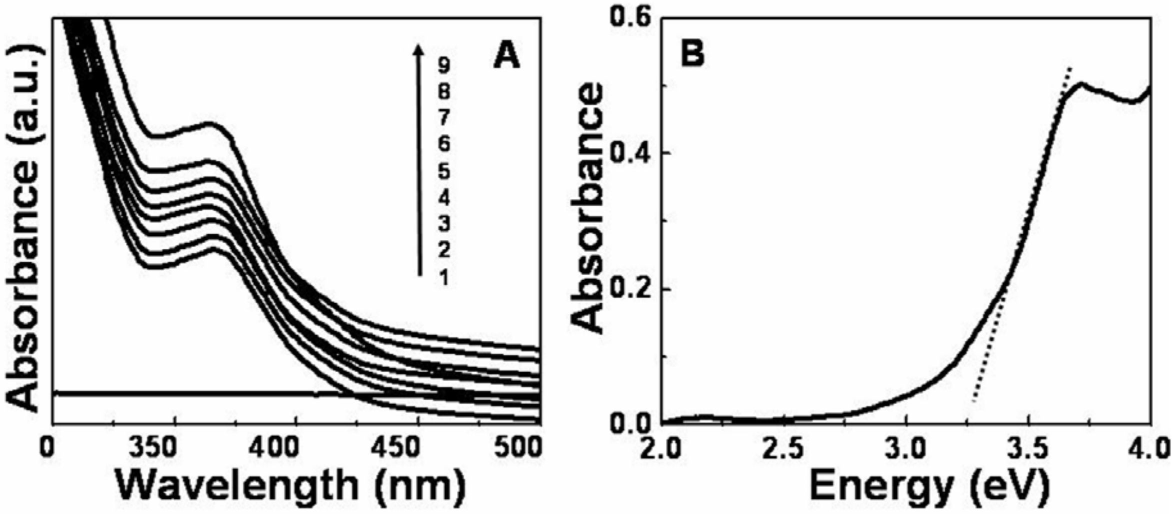

Figure 4.2 *(A) Time dependent UV-vis spectroscopic analysis of CdS nanoparticle formation using P.aeruginosa. Curves 1 to 9 represent exitonic absorption of CdS nanoparticles obtained after every 4 h during the course of reaction. The reaction was carried out for 32 h. (B) Band gap energy curve of CdS nanoparticles obtained by UV-vis spectroscopic analysis performed on CdS nanoparticles after 32 h of reaction. Tangent drawn to the absorption edge (dotted line) corresponds to the band gap energy of CdS nanoparticles.*

A fundamental property of semiconductors is the band gap; the energy separation between the filled valence band and the empty conduction band. As mentioned above bulk CdS has band gap energy of 2.4 eV. All semiconductors show size quantization effects as the size of semiconductor material is reduced [1b, 13a]. Figure 4.2B corresponds to the absorption threshold or band gap energy analysis after 32 h of reaction. The band gap energy value obtained is approximately 3.2 eV, which is considerably higher than the band gap energy of bulk CdS. The increase in band gap energy is due to the reduction in size of CdS and could be a consequence of size quantization effect.

4.2.2.3 Photoluminescence (fluorescence) spectroscopic analysis

CdS nanocrystallites frequently display excellent photoluminescence generally in the visible region of the electromagnetic spectrum depending on the size of CdS nanocrystallites. Figure 4.3 shows the photoluminescence (PL) spectra obtained from the aqueous solution of CdS nanoparticles synthesized using *P.aeruginosa* after 32 h of reaction. The PL spectra were obtained by exciting the aqueous solution of CdS nanoparticles at 300, 320 and 350 nm respectively. PL spectra obtained from excitation at 320 nm and 350 nm are shown in Figure 4.3A

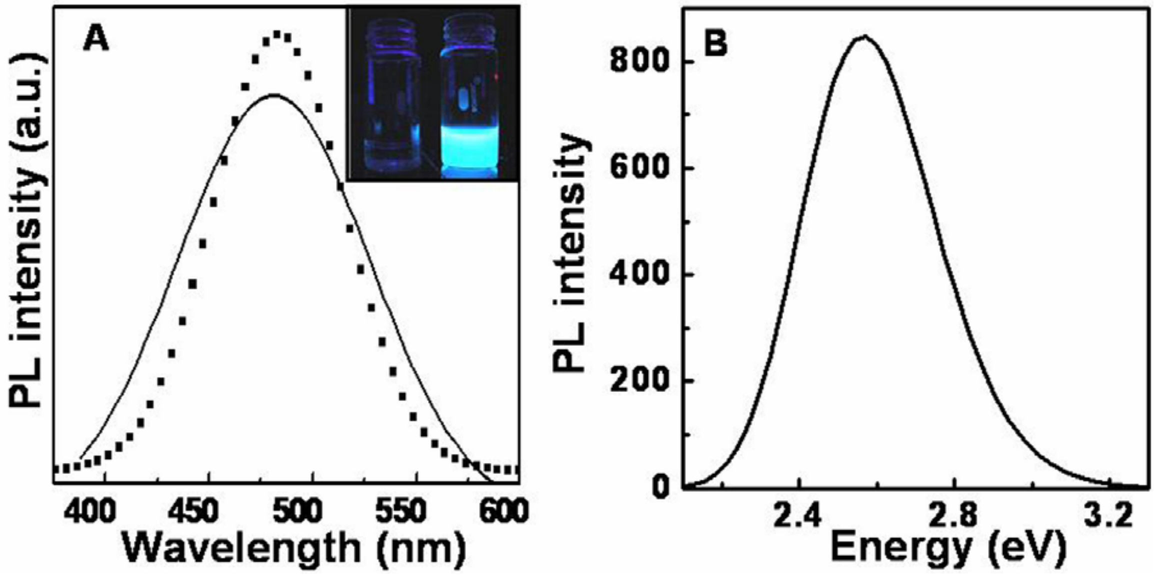

Figure 4.3 *(A) PL spectrum obtained from aqueous solution of biogenic CdS nanoparticles synthesized using P.aeruginosa excited at 320 nm (solid curve) and 350nm (dotted curve). Inset in (A) shows a photograph of biogenic CdS nanoparticle solution after irradiation with UV light of 365 nm showing blue – green light emission. (B) Same spectrum in terms of the energy scale corresponding to emitted light.*

The PL spectrum manifests a strong, sharp and uniform sized curve with emission maxima centered at 485 nm. For all emission spectra, the peak height varies in magnitude and all the spectra have same general features. Since not much difference is observed in the PL spectra obtained from the aqueous solution of CdS nanoparticles exited at various wavelengths, only emission spectra obtained at excitation wavelength of 320 nm (solid curve) and 350 nm (dotted curve) are shown in the Figure 4.3A. The large blue shift observed in the PL band can be attributed to the small size of nanoparticles. The inset in Figure 4.3A shows a photograph of aqueous solution of CdS nanoparticles from which PL measurement was carried on. A strong blue – green emission from the solution is observed when excited at wavelength of 365 nm while, no florescence was obtained from the aqueous solution of 10^{-3} M $CdSO_4$.

Figure 4.3B shows the PL spectrum obtained from aqueous solution of biogenic CdS nanoparticles in terms of energy. Bulk CdS shows a broad peak with very weak photoluminescence (PL) intensity with red emission and photon energy of 0.4 eV much below its absorption threshold. The PL of bulk CdS can be explained as the recombination of charged carriers trapped in the surface states. Therefore PL can be related to the size of CdS nanoparticles, and the PL emission blue-shifts with decreasing particle size [36a]. A sharp and strong peak at 2.5 eV corresponding to 485 nm is observed from biogenic CdS nanoparticles. The large blue shift in the energy of PL spectrum could be assigned to the emission from holes and electron traps frequently located at surface on the particles due to its small size as the density of electron traps increases on the surface due to the large surface area of the particle at smaller size. Therefore the observed blue shift in the PL spectrum can be attributed to the decrease in size of CdS nanoparticle [36b]. Line width of the PL spectra is narrow and regular indicating that no impurity is associated with CdS nanocrystallites.

4.2.2.4 X-ray diffraction (XRD) analysis

Figure 4.4 shows the XRD analysis performed on a solution cast film of biogenic CdS nanoparticles, synthesized by reaction between *P.aeruginosa* and 10^{-3} M $CdSO_4$ on glass substrate. A number of strong Bragg reflections are observed originating from the film surface. The diffraction pattern was indexed on the basis of wurtzite and cubic phase of CdS as observed in Figure 4.4A. CdS nanoparticles in particular size regime exhibit mixed phase structure [37]. The XRD peaks appear to be broadened, however the broadening observed in this case is not very prominent as reported previously [37]. This is most probably due to the fact that the XRD pattern was obtained from solution cast film on glass surface and not from the powder. There is a possibility of aggregation among the nanoparticles due to evaporation while the film was cast. However the broadening of XRD peak is clearly evident from the enlarged view of the spectrum.

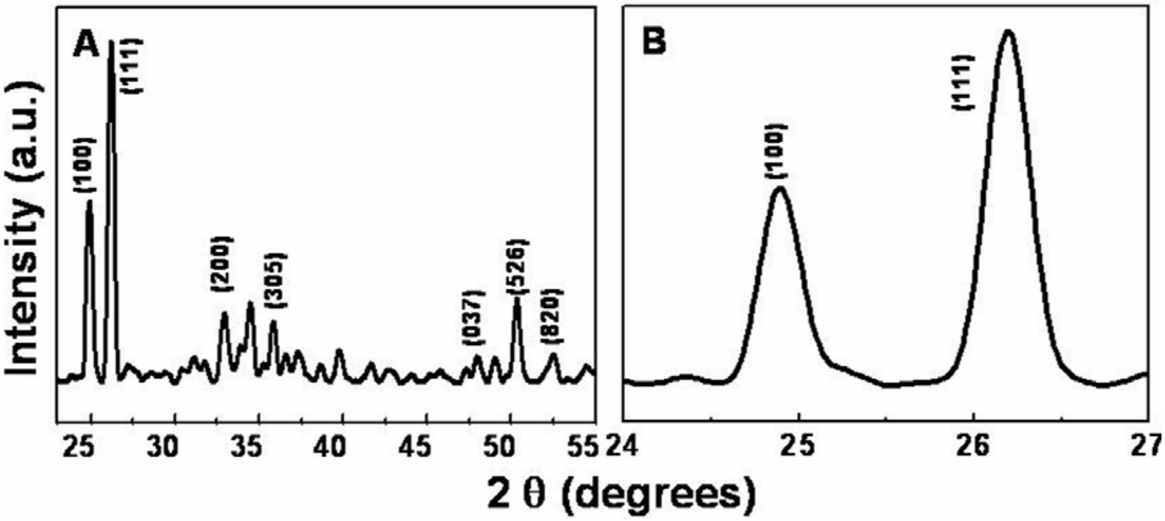

Figure 4.4 *(A) XRD pattern obtained from a solution cast film of aqueous CdS nanoparticles on glass surface. The Bragg reflections arising from the film are indexed with the respective crystal planes. (B) Enlarged view of the XRD pattern in the region of (100) and (111) reflections indicating the peak broadening due to the finite size of CdS nanoparticles.*

Figure 4.4B shows the enlarged view of the XRD spectrum in 2 θ value range in between 24 – 27 degrees. The broadening of XRD peaks in this region is considered since it consist of two most intense Bragg reflections corresponding to (100) and (111) planes. The crystallite size calculated by Debye – Scherrer formula is found to be 6 nm. The XRD pattern obtained from aqueous biogenic CdS is in well agreement with the HRTEM analysis indicating the highly crystalline nature of the nanoparticles. The respective crystal planes with their corresponding *d* values (in Å) are as follows; 3.36 (100), 2.82 (111), 2.46 (200), 2.48 (305), 1.93 (037), 1.79 (526), 1.73 (820) [34].

4.2.3 Biosynthesis of ZnS nanoparticles

4.2.3.1 TEM analysis

Figure 4.5 illustrates the TEM analysis performed on the aqueous reaction mixture of 10^{-3} M $ZnSO_4$ and *P. aeruginosa* after 28 h of reaction. A large population of ZnS nanoparticles was found to be evenly distributed on the surface of the grid as indicated by low magnification images (Figure 4.5 images A, B and C). Biogenic ZnS nanoparticles are nearly uniform in size with narrow size distribution. As observed with CdS, ZnS nanoparticles shown in TEM images could also be resulted by the loose aggregation of smaller particles. Particle size distribution analysis performed on 100 particles selected from different micrographs indicated the mean diameter of ZnS nanoclusters to be 3.5 nm with a small standard deviation value of 0.5. (inset in Figure 4.5E).

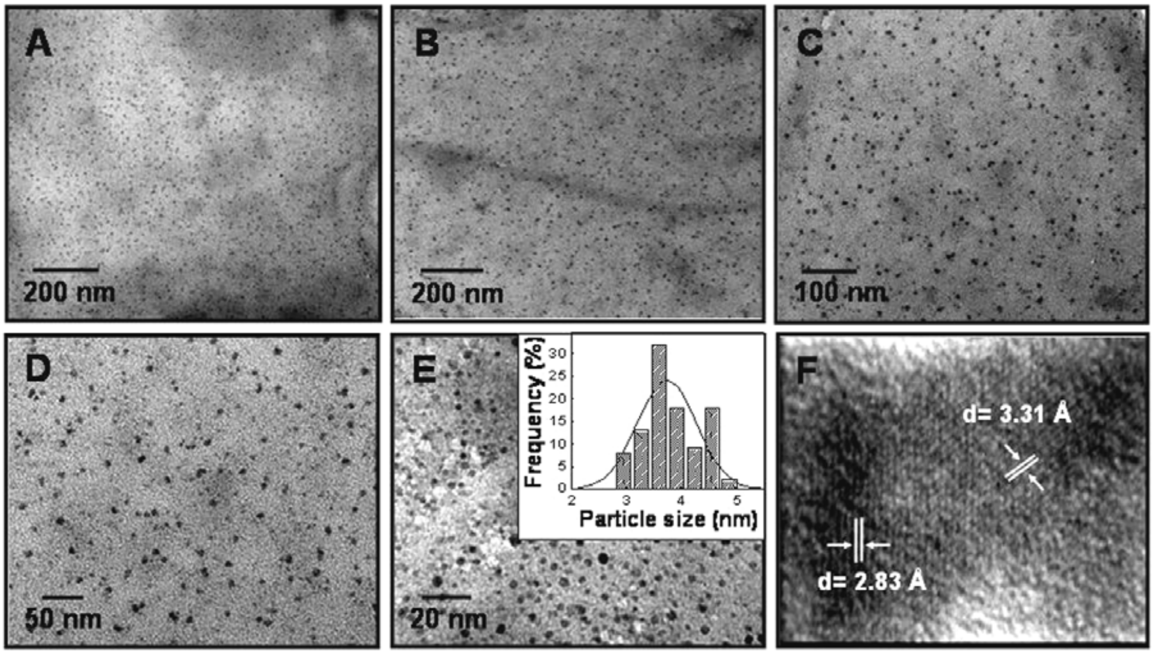

Figure 4.5 *TEM images of ZnS nanoparticles synthesized using P. aeruginosa (A-E). The mean size of ZnS nanocrystallites is 3.5 nm (inset, image E). Image F shows HRTEM analysis of ZnS nanoparticles. The d values correspond to (100) and (101) crystal planes*

Careful analysis of high magnification TEM images reveals the presence of nanoparticles, predominantly with two different sizes. Most of the particles are up to 3.5 nm in diameter while others are in between 4 to 5 nm. HRTEM analysis performed on ZnS nanoparticles clearly indicates the presence of lattice fringes and highly crystalline nature of ZnS nanoparticles (Figure 4.5F). The interplanar spacing of 3.31 Å and 2.83 Å was assigned to (101) and (100) planes of wurtzite ZnS structure respectively. [38].

4.2.3.2 UV – vis spectroscopic analysis

Figure 4.6 shows the UV-vis spectral analysis as a function of time of the reaction mixture containing 10^{-3} M $ZnSO_4$ and *P. aeruginosa*. The progress of reaction, i.e. the formation of ZnS nanoparticles is depicted in Figure 4.6A. ZnS belongs to the family of II–VI semiconductor with direct band gap energy of 3.64 eV at 300 K in bulk form [36a]. Bulk ZnS shows a featureless absorption edge at around 380 nm in the UV-vis spectrum. Figure 4.6A shows time dependent analysis of the formation of ZnS nanocrystallites using *P.aeruginosa*.

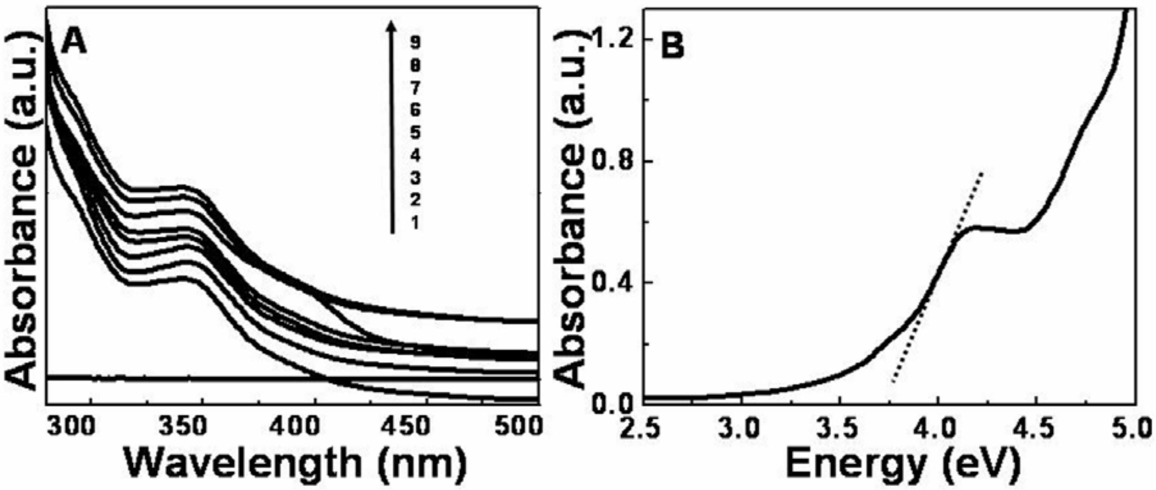

Figure 4.6 *(A) Time dependent UV-vis spectroscopic analysis of the formation of ZnS nanoparticles. The reaction between* 10^{-3} *M* $ZnSO_4$ *and P. aeruginosa was carried out for 28 h. Curves 1 – 9 represent the spectra obtained after every 4 h during the progress of reaction. (B) Band gap energy curve of ZnS nanoparticles obtained by UV-vis spectroscopic analysis performed on ZnS nanoparticles after 28 h of reaction. Tangent drawn to the absorption edge (dotted line) corresponds to the band gap energy of ZnS nanoparticles.*

Formation of ZnS nanoparticles starts immediately after 4 h of reaction as indicated by curve 1 in Figure 4.6A. An absorption hump is developed at 330 nm. This absorption at 330 nm is due to the excitonic transitions in ZnS nanocrystallites [36a]. The absorption hump increases in intensity with time and attains saturation after 28 h of reaction as indicated by curve 8 in Figure 4.6A. No appreciable rise in the absorption is observed further indicating completion of reaction (Curve 9 corresponding to the UV-vis spectrum after 32 h almost superimposes with curve 8, which corresponds to the UV-vis spectrum after 28 h of reaction). According to effective mass model, UV-vis spectrum corresponds to the nanoparticle with 3 – 4 nm diameter [36c]. Along with the absorption hump at 330 nm, another shoulder peak around 300 nm is observed in UV-vis spectra. Appearance of this absorption shoulder together with hump at 330 nm indicates the presence of nanocrystallites with two different sizes. This observation is well supported by TEM analysis which shows the presence of two types of particles corresponding to 2.5 to 3.5 nm of diameter and 4 to 5 nm of diameter respectively.

Figure 4.6B corresponds to the absorption threshold or band gap analysis of ZnS nanoparticles after 28 h of reaction. The band gap energy value obtained for ZnS nanocrystallites is approximately 3.75 eV, which is higher than the band gap energy of bulk ZnS. The increase in band gap energy can be attributed to the reduction in size of ZnS and could be a consequence of a size quantization effect.

4.2.3.3 Photoluminescence spectroscopic analysis

Figure 4.7 shows the photoluminescence (PL) spectra obtained from the aqueous solution of ZnS nanoparticles synthesized using *P.aeruginosa* after 28 h of reaction. The PL spectra were obtained by exciting the aqueous solution of ZnS nanoparticles at 280, nm and 320 nm respectively. As observed with the aqueous CdS nanoparticles synthesized using *P.aeruginosa*, aqueous solution of ZnS nanoparticles also exhibited a sharp emission peak and the wavelength of emitted fluorescence light showed intensity maxima at 440 nm.

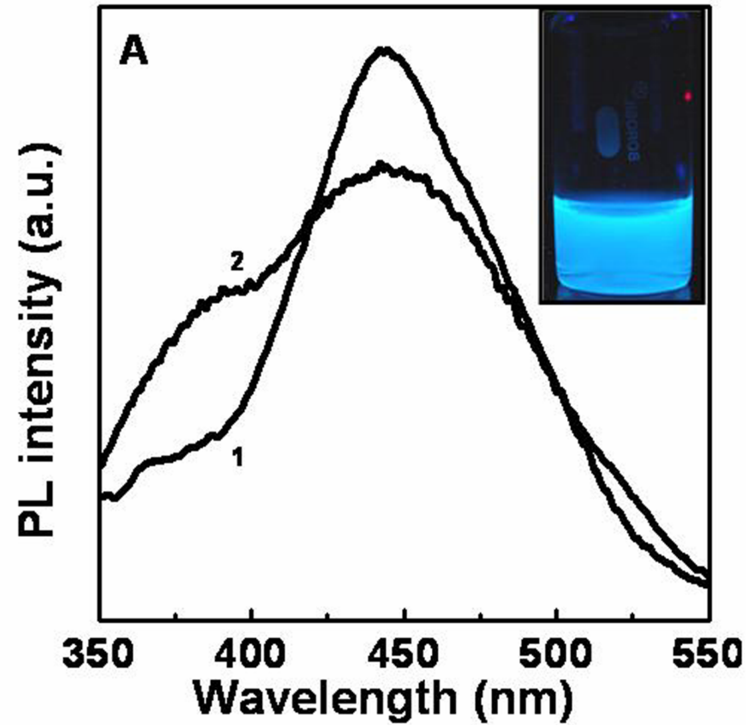

Figure 4.7 *(a) PL spectrum obtained from the aqueous ZnS nanocrystallites at room temperature. Curve 1 indicates the spectrum corresponding to the excitation wavelength of 325 nm while curve 2 corresponds to excitation at 280 nm. The inset shows the photograph of the aqueous solution of ZnS nanocrystallites excited with UV light.*

The curve 1 in Figure 4.7 shows a room temperature PL spectrum obtained from aqueous ZnS nanoparticles excited at 320 nm. The PL spectrum consists of a single, sharp emission peak at 440 nm that could be assigned to surface traps or band-edge emission corresponding to the surface states in the nanocrystallites. The presence of a single peak further suggests that the nanocrystallites are composed of ZnS without detectable quantity of other impurities. The narrow and sharp emission spectrum suggests that the surface of nanocrystallites is fairly flat and regular. Also the lower line width of the emission band indicates regularity in the size of nanocrystallites that gives fluorescence at 440 nm.

The inset in Figure 4.7A shows the photograph of aqueous ZnS nanocrystallites after irradiation with UV light. The blue colored fluorescence emitted by the solution is in well agreement with the PL spectrum that shows the peak maxima, which corresponds to the wavelength of the blue light in the visible region of the electromagnetic spectrum. Curve 2 in Figure 4.7 corresponds to the PL spectrum obtained from the aqueous ZnS nanocrystallites excited at 280 nm. The spectrum shows a broad emission peak with the maximum intensity around 440 nm. The emission spectrum can be resolved in two separate components possibly indicating the presence of nanocrystallites with two different sizes. The low intensity portion of the spectrum with the maximum intensity centered at 390 nm corresponds to the smaller nanocrystallites 2.5 to 3.5 nm in diameter. On the other hand the high intensity component of the spectrum corresponds to the bigger nanocrystallites 4 to 5 nm in diameter. The intensity of the PL decreases with increasing the excitation energy, which means that the line width of the spectrum increases at higher energy of the absorption edge. This can be due to the simultaneous excitation of all nanocrystallites present in the solution resulting in the observed homogeneous profile of luminescence. However, the peak position in both the PL spectra is nearly independent on the excitation energy suggesting that the origin of the emitting state is similar for both spectra.

4.2.3.4 Energy dispersive X-ray analysis (EDAX)

The elemental analysis of nanoparticles can be very informative for the study of the structural or elemental composition. Figure 4.8 corresponds to the EDAX analysis performed on a single ZnS nanoparticle. The EDAX analysis shows the presence of Zn and S indicating that the nanoparticle is is indeed ZnS.

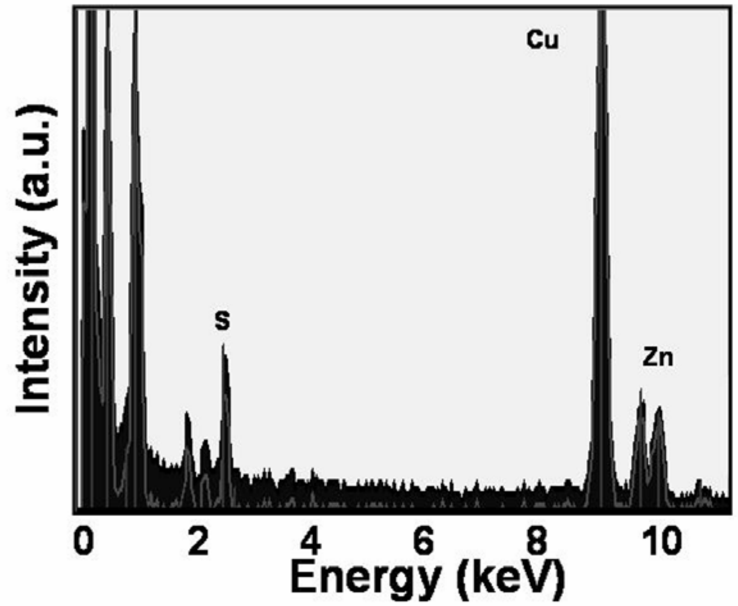

***Figure 4.8** EDAX analysis performed on a single ZnS nanoparticle. Peaks are marked with symbol of the respective element. High intensity peaks below 1 keV originates from C and O present in the sample.*

Along with Zn and S, other elements like C, N and O are also present in the sample. The origin of these elements lies in the biological components, mostly proteins along with ZnS nanoparticles. The peak corresponding to copper arises from the copper grid on which the sample is prepared for the EDAX analysis.

4.2.3.5 X-ray diffraction (XRD) analysis

Figure 4.9 shows the XRD analysis performed on the solution cast film of the biologically synthesized ZnS nanoparticles by reaction between *P.aeruginosa* and 10^{-3} M $ZnSO_4$ on a glass substrate. A number of strong Bragg reflections are observed originating from the film surface. The XRD pattern was indexed on the basis of wurtzite structure of zinc sulfide, though one peak was corresponding to the sphalerite phase of ZnS (indicated by "*" in Figure 4.9A). The XRD pattern shows broadening of peaks indicating the finite size of the nanocrystallites. But the broadening of XRD peaks is not as prominent as observed previously. This could be due to the aggregation of nanoparticles while the film for XRD analysis was prepared by drop coating of the aqueous solution of ZnS nanocrystallites. The peak broadening was prominently observed in the magnified view of the XRD spectrum in the 2 θ region of 27 to 35 degrees. The XRD peaks corresponding to (100), (102), (101) and (106) lattice planes are broadened considerably.

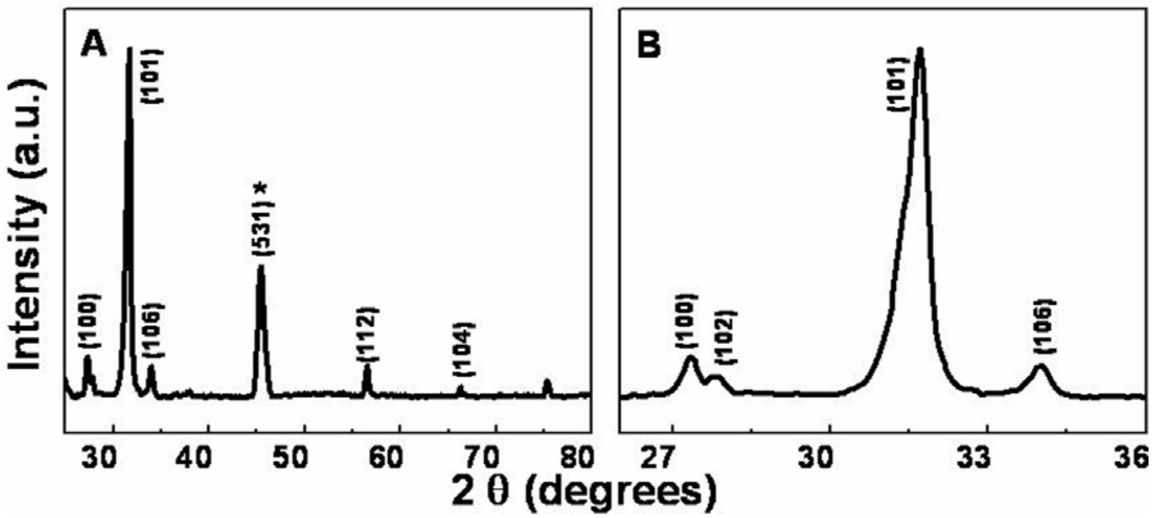

Figure 4.9 *(A) XRD pattern obtained from the solution cast film of aqueous ZnS nanoparticles on glass surface. Bragg reflections arising from the film are indexed with the respective crystal planes. Symbol "*" indicates the XRD peak originating from the sphalerite phase of ZnS. (B) Magnified view of the XRD pattern in the region of (100) and (101) reflections indicating the peak broadening due to the finite size of ZnS nanoparticles.*

The crystallite size calculated by Debye – Scherrer formula is found to be ~ 7 nm. The XRD pattern obtained from aqueous biogenic ZnS is well in agreement with the HRTEM analysis indicating the highly crystalline nature of these nanoparticles. The respective crystal planes with their corresponding *d* values (in Å) are as follows for wurtzite: 3.31 (100), 3.25 (102), 2.92 (101), 2.32 (106), 1.63 (112), 1.41 (104) and for sphalerite: 0.914 (531) [38].

4.2.4 Biosynthesis of PbS nanoparticles

4.2.4.1 TEM analysis

Figure 4.10 illustrates the TEM analysis performed on biogenic PbS nanocrystallites synthesized using *P. aeruginosa*. Nearly spherical nanoparticles with fairly narrow size distribution are observed after 24 h of reaction. The low magnification TEM image shows (Figure 4.10E) small clusters of PbS nanocrystallites, which are composed of even smaller nanoparticles. These clusters of PbS nanoparticles are about 6 to 8 nm in the diameter. The smaller nanoparticles that form the bigger aggregates are about 2 nm in diameter, however, these small nanoparticles could not be resolved with the microscope used in the present study.

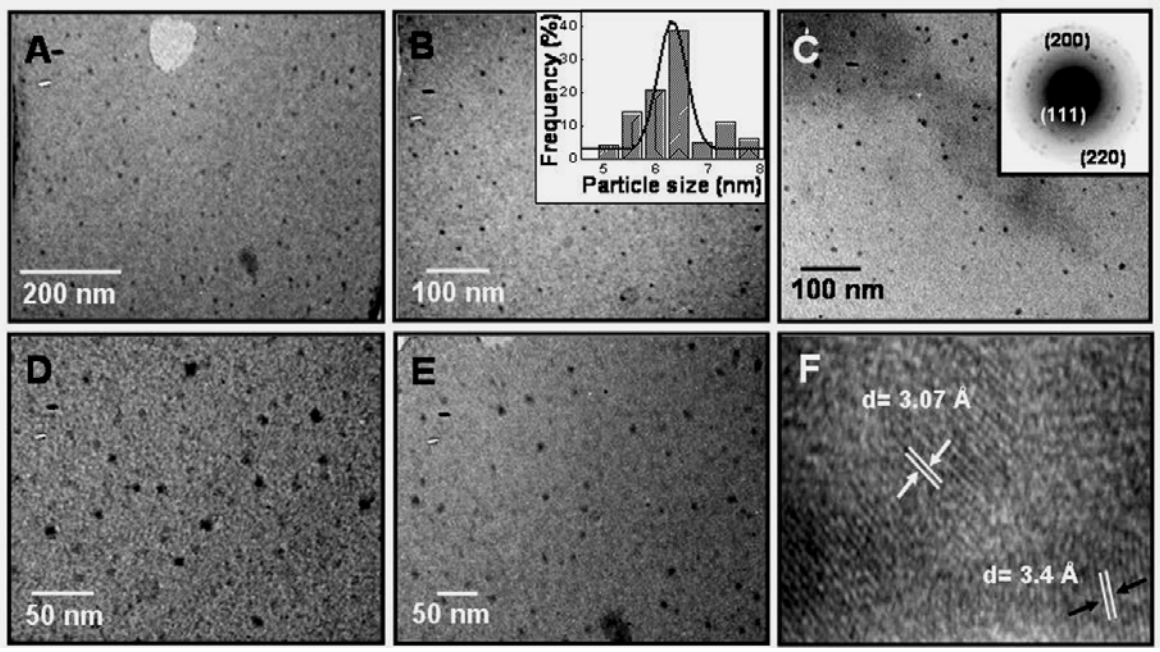

Figure 4.10 *TEM images of PbS nanoparticles synthesized using P. aeruginosa (A-E). Insets in (B) and (C) show the particle size distribution analysis and SAED pattern obtained from PbS nanocrystallites respectively. The HRTEM image shows crystalline nature of PbS nanoparticles (F). The d values3.4 Å and 3.07 Å corresponds to (111) and (200) crystal planes.*

The particle size distribution analysis performed on the nanoparticles shown in the different images shows a mean diameter of PbS nanoparticles to be 6.5 nm with the standard deviation value of 0.28 (inset, Figure 4.10B). The SAED pattern obtained from PbS nanoparticles indicates the crystalline nature of the nanoparticles and the diffraction pattern was indexed on the basis of FCC structure of galena PbS (inset, Figure 4.10C). The crystalline nature of the nanoparticles was further confirmed by HRTEM analysis, which clearly indicates the presence of lattice fringes (Figure 4.10F). The interplanar spacing of 3.4 Å and 3.07 Å was assigned to (111) and (200) respective planes of galena structure of PbS [39].

4.2.4.2 UV-vis spectroscopic analysis

Figure 4.11 shows the UV-vis spectroscopic analysis performed on the aqueous solution of PbS nanocrystallites synthesized by *P.aeruginosa*. PbS belongs to the family of II–VI semiconductor with a small direct band gap energy value of 0.41 eV at 300 K in the bulk form [36a]. Bulk PbS shows the absorption in the infrared (IR) region of the electromagnetic spectrum with the absorption onset at ~3020 nm. Figure 4.11A shows UV-vis spectra of PbS nanocrystallites after 12 h and 24 h of the reaction. Two distinct features are observed in the UV-vis spectrum obtained after 12 h of reaction, which could be assigned to the excitonic transitions in PbS nanocrystallite. A well defined absorption hump is developed at 350 nm that arises due to the presence of PbS nanoparticles. Further, the absorption hump at 350 nm is accompanied with another shoulder peak at higher wavelength region at 310 nm (grey curve, Figure 4.11A).

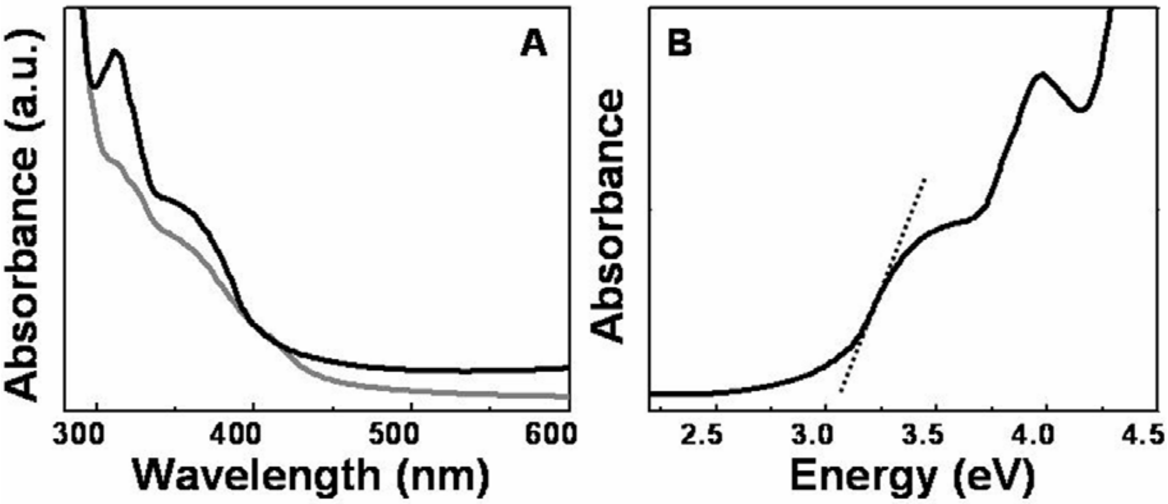

Figure 4.11 (A) The UV-vis spectroscopic analysis performed on the aqueous reaction mixture containing lead salt and P.aeruginosa biomass after 12 h (grey curve) and 24 h (black curve) of the incubation. (B) Absorption threshold or band gap energy curve of PbS nanoparticles obtained by the UV-vis spectroscopic analysis performed on PbS nanoparticles after 24 h of reaction. Tangent drawn to the absorption edge (dotted line) corresponds to band gap energy of PbS nanoparticles.

The remarkable blue shift in the absorption of PbS nanoparticles indicates very small size of nanocrystallites and can be attributed to the quantum confinement of the charge carriers in the nanoparticles [34]. After 24 h of reaction the absorption humps at 350 nm and 310 nm increases with the intensity and becomes sharper. Surprisingly, the absorption hump at 310 nm becomes more prominent and now appears as a sharp peak (black curve, Figure 4.11A). This feature is also observed previously in biologically synthesized PbS nanocrystallites [17]. Presence of two absorption peaks suggests that the overall population of PbS nanoparticles was composed of the particles with two distinct sizes. This observation was consistent with the TEM analysis.

Figure 4.11B corresponds to the absorption threshold or band gap energy analysis of PbS nanoparticles after 32 h of reaction. The band gap energy value obtained is approximately 3.05 eV, corresponding to the larger nanocrystallites among the overall population, while the energy gap value calculated for the smaller nanocrystallites was found to be ~ 3.80 eV. These energy gap values for PbS nanocrystallites are considerably higher than the band gap energy of bulk PbS [36a].

4.2.4.3 Photoluminescence spectroscopic analysis

Figure 4.12 illustrates the PL spectrum obtained from the aqueous solution of PbS nanocrystallites synthesized after 24 h of reaction between lead ions and *P.aeruginosa*. PL spectra were obtained by exciting the aqueous solution of nanocrystallites at 280 nm and 325 nm. The black curve in Figure 4.12 shows the room temperature PL spectrum obtained from the aqueous PbS nanoparticles excited at 330 nm. The PL spectrum consists of a single and sharp emission peak with the emission maxima centered at 460 nm.

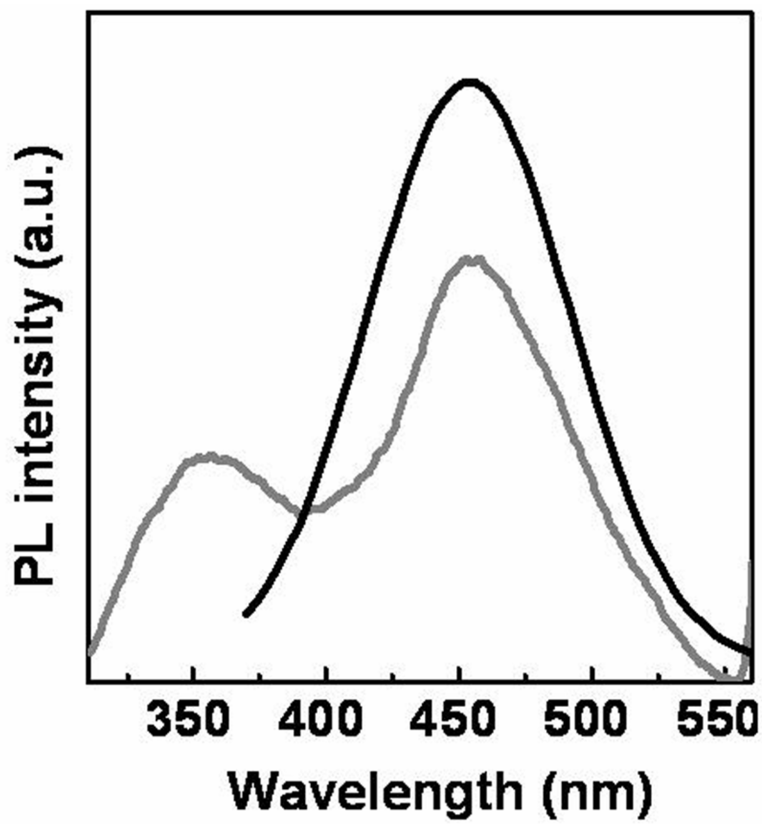

Figure 4.12 *PL spectra obtained from the aqueous solution of biogenic PbS nanocrystallites excited at 280 nm (grey spectrum) and 330 nm (black spectrum). Both spectra were recorded at room temperature.*

The origin of this emission lies in the surface traps or band-edge emission corresponding to the surface states in the nanocrystallites. The presence of single peak further signifies the purity of the nanocrystallites. The line width of the emission band is significantly lower and blue shifted in comparison with the previous reports [36a] indicating a regularity in the size of nanocrystallites that show emission peak at 460 nm. The grey spectrum in Figure 4.12 corresponds to the PL spectrum obtained from the aqueous PbS nanocrystallites excited at 280 nm. The spectrum shows a sharp emission peak with the maximum intensity around 460 nm as observed from the spectrum obtained by excitatation at 330 nm (black spectrum in Figure 4.12). This emission spectrum clearly shows two separate emission maxima indicating the presence of nanocrystallites with two different sizes. The low intensity region of the spectrum with the maximum intensity centered at 360 nm corresponds to the smaller nanocrystallites. On the other hand the high intensity component of the spectrum corresponds to the bigger nanocrystallites. As observed with ZnS nanocrystallites, the intensity of the PL decreases with increasing the excitation energy, indicating that the line width of spectrum increases at higher energy of the absorption edge. This can be due to the simultaneous excitation of all nanocrystallites present in the solution giving rise to a homogeneous profile of luminescence. The peak position in both the PL spectra is almost independent of the excitation energy suggesting that the origin of the luminescence lies in PbS nanocrystallites.

4.2.4.4 X-ray diffraction (XRD) analysis

Figure 4.13 represents the XRD analysis performed on the drop cast film of aqueous PbS nanocrystallites on a glass substrate. The XRD spectrum consists of a number of Bragg reflections, most of which originate from PbS nanocrystallites. The XRD pattern was indexed on the basis of a mixed phase of lead sulfide consisting of FCC galena and cubic PbS. Almost half of the peaks could be indexed on the basis of cubic PbS, while other half belonged to galena (marked as "*" in the Figure 4.13A). The XRD pattern shows broadening of peaks indicating the small size of PbS nanocrystallites. The broadening of peaks is further evident in Figure 4.13B, that shows the magnified view of the XRD spectrum in the 2 θ region of 29 to 32 degrees, which clearly indicates the peak broadening. The XRD peaks corresponding to (200) and (420) lattice planes are broadened considerably. The crystallite size of PbS calculated by Debye – Scherrer formula is found to be ~ 7 nm, which is larger in comparison to TEM analysis. The broadening of XRD peak corresponding to (200) is considered for calculation of crystallite size by Debye – Scherrer formula, as it represents the most intense Bragg reflection arising from the PbS nanocrystallites.

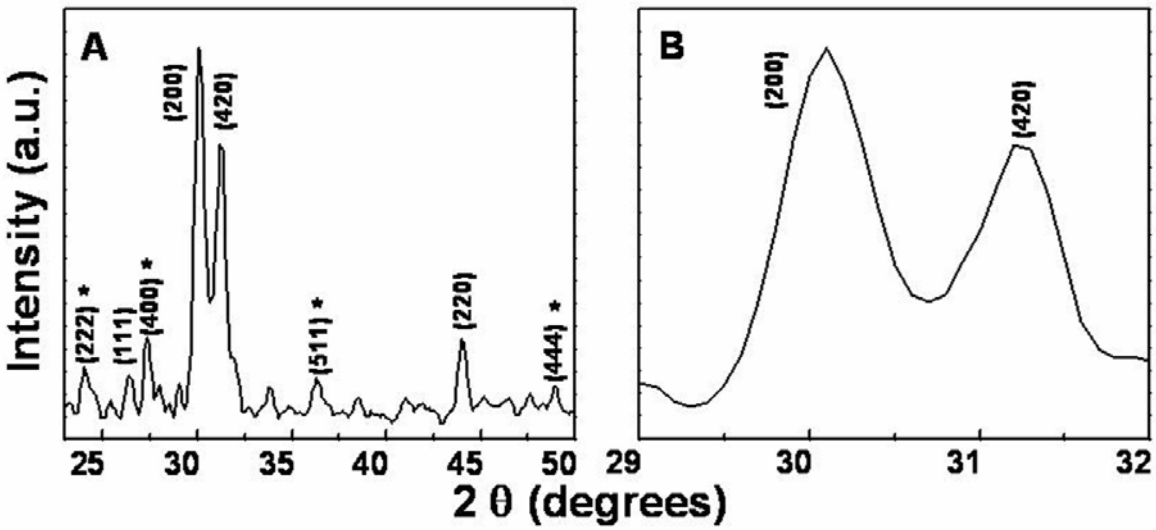

Figure 4.13 *(A) XRD pattern obtained from the solution cast film of PbS nanocrystallites. Bragg reflections arising from the film are indexed with the respective crystal planes. Symbol "*" indicates the XRD peaks corresponding to the galena phase of PbS. (B) Magnified view of the XRD pattern in the region of (200) and (420) reflections indicating the peak broadening due to the very small size of PbS nanoparticles.*

The XRD pattern obtained from aqueous biogenic PbS is in agreement with the HRTEM analysis indicating the highly crystalline nature of the nanoparticles. The respective crystal planes with their corresponding *d* values (in Å) are as follows; for cubic PbS: 3.38 (111), 2.96 (200), 2.63 (420), 2.09 (220), for galena marked as "*": 1.71 (222), 1.48 (400), 1.14 (411), 0.85 (444) [39].

4.2.5 Biomolecular mechanism of metal sulfide nanoparticle formation by *P.aeruginosa*

Biological synthesis of group II – VII sulfide nanoparticles semiconductors have been described previously using different microorganisms like yeast, fungi and bacteria. Though previous reports successfully describe the synthesis of CdS or PbS nanoparticles, the biological mechanism that lead to the formation of metal sulfide nanoparticles is unclear. It has been postulated that the yeast cells upon exposure to Cd or Pb ions synthesize metal chelating peptide to nullify the stress generated by metal ions. On addition of the metal ions, a metal ion – γ glutamyl complex is initially formed and this is accompanied by an increase in the intracellular sulfide levels. Later Cd or Pb ions complex with sulfide to form CdS or PbS nanocrystals, which accumulate in vacuoles present inside the yeast cells. Bacteria like *Klebsiella planticola* and *K. pneumoniae* have been shown to synthesize CdS nanoparticles in high quantity under anaerobic conditions [22-23]. An enzyme thiosulfate reductase produced by *K. planticola* has been shown to be responsible for the synthesis of CdS nanoparticles, while cysteine desulfydrase secreted by *Klebsiella pneumoniae* converts cysteine into H_2S, which in turn reacts with Cd^+ ions to form CdS. Cysteine desulfydrase gene has been successfully cloned and overexpressed in *E. coli* for the synthesis of CdS nanoparticles. However, synthesis of CdS was observed only after 48 h of the bacterial growth.

In this chapter we have described biological synthesis of semiconductor sulfide nanoparticles like CdS, ZnS and PbS using the bacterium *P.aeruginosa*. Unlike previous reports, synthesis of metal sulfide nanoparticles proceeds by reduction of the respective metal sulfate salts indicating that exogenous sulfur is utilized for the synthesis of CdS, ZnS and PbS nanocrystallites. This observation led to the hypothesis that bacterial sulfate reductases are responsible for the synthesis of sulfide nanocrystallites. In microorganisms, sulfate reductases are broadly categorized as the dissimilatory sulfate reductases (DSR) and assimilatory sulfate reductases (ASR). DSR are responsible for the anaerobic respiration in sulfate reducing bacteria [20], while ASR are responsible for the metabolism of sulfur containing amino acids like methionine and cysteine in aerobic bacteria. Sulfate ions are taken inside the bacterial cell by the action of sulfate permease. Once inside cell, the sulfate ions are acted upon by APS sufurylase, which converts inorganic sulfate into adenosine phosphosulfate (APS). APS is further phosphorylated in 3′ phosphoadenosine 5′ phosphosulfate (PAPS) and this reaction is catalysed by APS kinase. PAPS is reduced to respective sulfite in the next step by the action of PAPS reductase, which generally called as sulfate reductase [40]. This step is followed by the action of sulfite reductase (SIR), converting sulfites into sulfide. The metal sulfides formed in the last step are effluxed in the surrounding medium by CZR transporter. The sulfate reduction pathway leading to synthesis of nanocrystalline semiconductor metal sulfides is illustrated in the following flow chart, which explains the uptake, reduction and efflux of metal sulfate ions by *P. aeruginosa.*

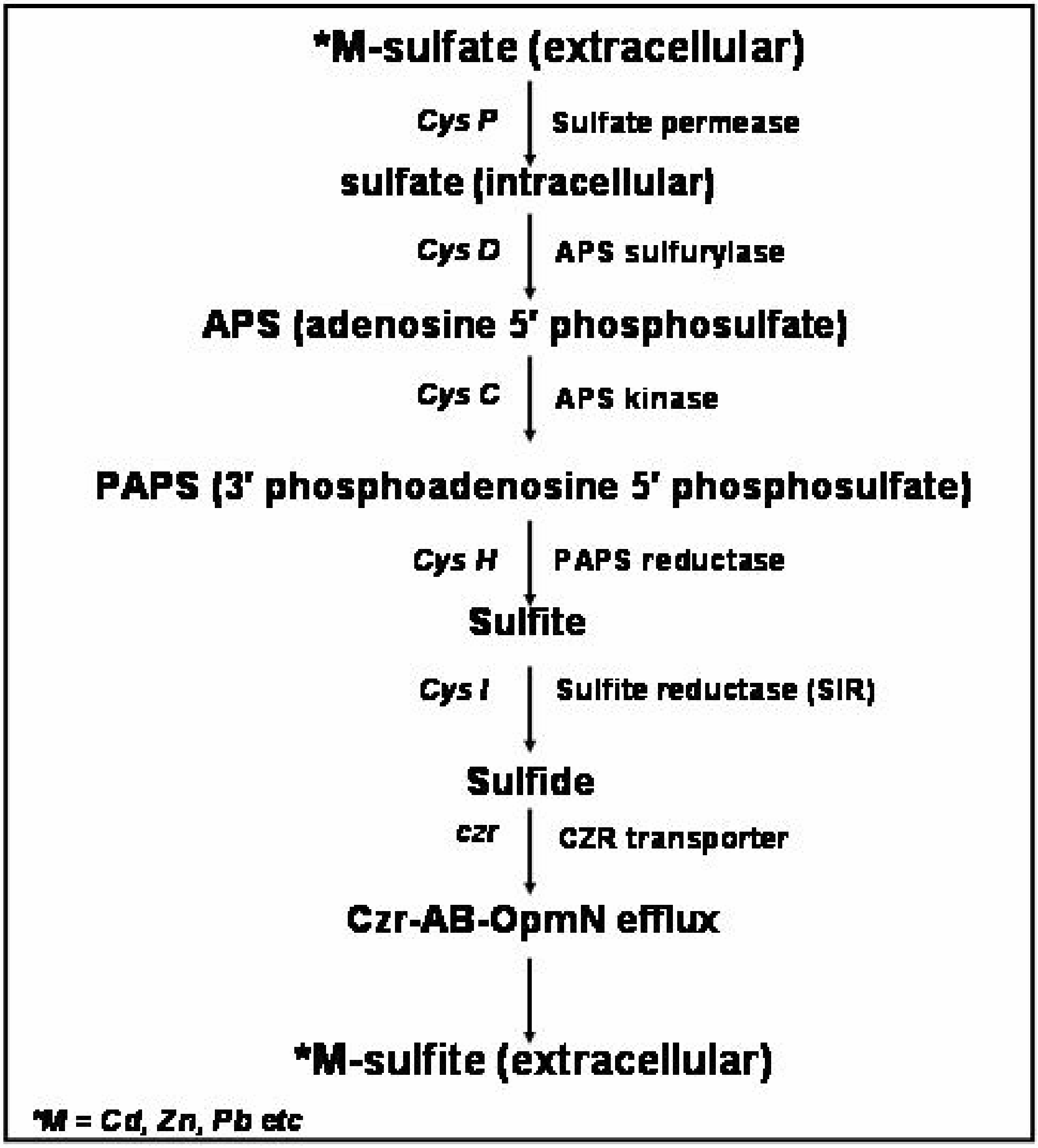

The actual reduction of inorganic sulfate is a two step reaction. The first step is catalyzed by PAPS reductase in which, sulfate ions are reduced to sulfite ions. In the second step sulfite ions are converted into sulfide by the action of SIR. Therefore, keeping in mind the central role of these enzymes in sulfate reduction by assimilatory sulfate reduction pathway, genes encoding PAPS reductase (*cys H*) and SIR (*cys I*) in *P.aeruginosa* are identified, isolated and amplified using PCR (polymerase chain reaction). The amplified individual *cys*H and *cys*I genes could be successfully cloned and overexpressed in *E.coli* BL 21 AI™.

4.2.5.1 PCR amplification, sequencing and cloning of *cysH* and *cysI* genes and their overexpression in recombinant *E.coli* BL 21 AI

Figure 4.14 shows PCR analysis performed on *P.aeruginosa* genomic DNA for the amplification of *cysH* and *cysI* genes using sequence specific degenerative primers.

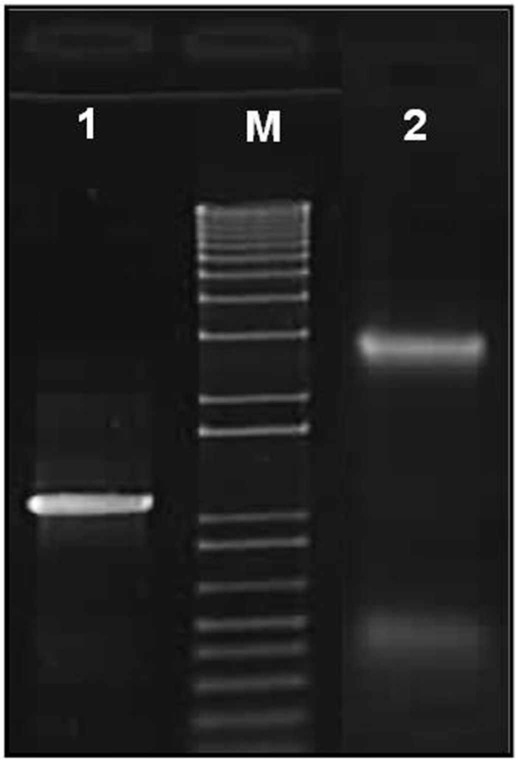

Figure 4.14 Agarose gel electrophoresis image of cysH and cysI genes after PCR amplification using gene specific primers. Lane 1, 2 and M corresponds to amplified genes cysH, cysI and standard DNA size molecular wight marker respectively.

The presence of two distinct bands at 0.9 kb and 1.2 kb on 0.8 % agarose gel indicates that gene specific primers are highly specific for *cysH* and *cysI* genes encoding enzymes PAPS reductase and SIR respectively. The molecular size of amplified DNA fragments is calculated to be 0.9 kb and 1.2 kb respectively, which show perfect match with the reported value of *cysH* and *cysI* genes. This result indicates the presence of functional *cysH* and *cysI* genes encoding two proteins, PAPS reductase and SIR, which catalyzes sulfate reduction in *P.aeruginosa*. Lane 1 in Figure 4.14 corresponds to PCR amplified cysH gene fragment with molecular size 0.9 kb, while lane 2 in Figure 4.14 represents PCR amplified *cysI* gene fragment measuring molecular size of 1.2 kb. Lane M in Figure 4.14 is a standard molecular weight DNA marker. Further, 0.9 kb and 1.2 kb gene fragments were sequenced by eluting DNA from agarose gel on automated DNA sequencer. The DNA sequences obtained were analyzed on BLAST program of NCBI server. GenBank database revealed that the amino acid sequences encoded by *cysH* and *cysI* gene fragment are most similar to that encoded by *cysH* and *cysI* homologes [GenBank accession no. CP 000 438 and AE 004091] indicating that amplified DNA fragments indeed belong to *cysH* and *cysI* genes.

To further illustrate the role of *cysH* and *cysI* genes in the formation of metal sulfide nanocrystallites such as CdS, ZnS and PbS, *cys H* and *cysI* genes were cloned and overexpressed separately as heterologous proteins in *E.coli* BL21 AI™ [33]. Initially two genes were separately cloned in plasmid vector pDONR^{TM}221 known as entry vector. This was followed by LR recombination reaction between entry vectors and destination vector pDEST™17 which was engineered in *E.coli* BL 21 AI™ cells by transformation. These transformed *E.coli* BL 21 AI™ cells were induced by L-arabinose in the presence of 100 μg/μl ampicillin. Overexpression of two proteins, PAPS reductase and SIR was analyzed on 10% sodium dodecyl sulfate-polyacrylamide gel electrophoresis and the gels were visualized by staining with Coomassie blue R 250. Gateway® technology for cloning and overexpression of the gene has a limitation over the size of gene fragment that can be successfully overexpressed in *E. coli* BL 21 AI™ cells as a functional protein [33]. Usually proteins with molecular weight more than 20 kDa cannot be overexpressed as a functional protein because *E.coli* BL 21 AI™ senses it as non-functional by an unknown way. Therefore, the resulting overexpressed protein may not be folded in the appropriate conformation, which is destined for inclusion bodies as a non-functional protein. However, in spite of high molecular weights, PAPS reductase and SIR could be overexpressed functionally in *E.coli* BL 21 AI™ cells. A fraction of both proteins was found to be synthesized extracellularly as indicated by SDS-PAGE anlysis of extracellular proteins. Activity of PAPS and SIR was analyzed by synthesis of metal sulfide nanocrystallites by recombinant *E.coli* BL 21 AI™ cells harboring cysH and cysI genes from *P.aeruginosa* as discussed in the following section. Figure 4.15 shows SDS-PAGE electropherograms of intracellular and extracellular proteins synthesized by *E.coli* BL 21 AI™ cells. Overexpression of PAPS reductase and SIR is evident by the analysis of intracellular and extracellular proteins on 10% SDS-polyacrylamide gel.

Figure 4.15A shows the electropherograms of intracellular proteins synthesized by *E.coli* BL 21 AI™ cells during the incubation of 4 h in LB medium at 37 °C.

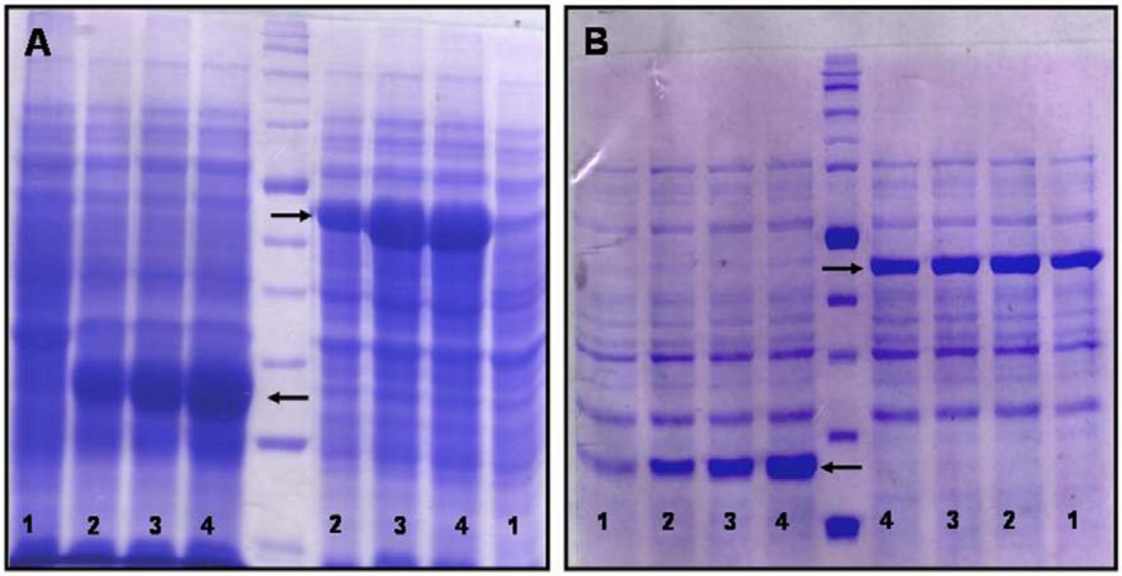

Figure 4.15 *(A) SDS-polyacrylamide gel electropherogram showing the intracellular protein profile obtained from E.coli BL 21 AI™ cells. Lanes 2 to 4correspond to the intracellular-protein profile of E.coli BL 21 AI™ cells after 2, 3 and 4 h of induction respectively, while lane 1 corresponds to the protein profile obtained from uninduced cells. PAPS reductase and SIR are indicated by arrow facing to the left and right of the image. (B) SDS-PAGE electropherogram image of extracellular proteins synthesized by E.coli BL 21 AI™ cells during 4 h of induction. Lane 1 to 4 corresponds to protein profile obtained after 1, 2, 3 and 4 h of induction respectively. PAPS reductase and SIR are indicated by arrow facing to the left and right of the image. Central lane in both images corresponds to standard protein molecular weight marker with molecular weights (kDa) 212, 158, 116, 97.2, 66.4, 56.6, 42.7, 34.6, 27, 20 from top to bottom respectively.*

Time dependent analysis of intracellular protein profile clearly indicates the synthesis of two proteins with molecular weights of 30 kDa and 65 kDa in an increasing amount during the incubation period of 4 h after induction (lane 2 to 4, Figure 4.15A).On the other hand, it is clearly observed that PAPS reductase and SIR are indistinguishable from other intracellular proteins synthesized by uninduced *E.coli* BL21 AI™ cells (lane1, Figure 4.15). This result is obvious to consider the overexpression of PAPS reductase and SIR as intracellular proteins in recombinant *E.coli* BL21 AI™ cells. Also both overexpressed proteins remain functional after 4 h of induction.

Figure 4.15B shows the electropherograms of extracellular proteins synthesized by *E.coli* BL 21 AI™ cells during the incubation of 4 h in LB medium at 37 °C. Even, extracellular protein profile of recombinant *E.coli* BL 21 AI™ cells show similar trend observed with intracellular protein analysis. It is clearly observed that PAPS reductase and SIR with molecular weights of 30 kDa and 65 kDa are overexpressed with increasing incubation period upto 4 h of induction. Lane 1 to 4 in Figure 4.15B corresponds to the extracellular protein profile obtained from *E.coli* BL 21 AI™ cells after 1, 2, 3 and 4 h of induction respectively. It is clear that the amount of PAPS reductase and SIR increases in extracellular medium with time. Electropherogram also indicates that both proteins are stable even after 4 h of induction when secreted outside the cells in culture medium.

Figure 4.15 clearly shows the overexpression of PAPS reductase and SIR by recombinant *E.coli* BL 21 AI™ cells. Non transformed *E.coli* BL 21 AI™ cells do not show presence of any detectable proteins with molecular weights of 30 kDa and 65 kDa, indicating that presence of these proteins could be realized only after transformation with plasmid harboring *cysH* and *cys I* genes encoding PAPS reductase and SIR respectively.

4.2.5.2 Biosynthesis of CdS, ZnS and PbS using recombinant *E.coli* BL 21 AI™

The previous section describes PCR amplification, cloning and overexpression of PAPS reducatse and SIR in *E.coli* BL 21 AI™ cells. Owing to the central role of PAPS reductase and SIR during sulfate reduction it has been hypothesized that metal sulfides are synthesized from metal sulfate by the sequential action of PAPS reductase and SIR. To analyze the functionality of PAPS reductase and SIR, growing recombinant *E.coli* BL 21 AI™ cells were exposed with 10^{-3} M $CdSO_4$, $ZnSO_4$ and $PbSO_4$ for 12h and the culture supernatant was analysed by TEM, UV-vis spectroscopy and photoluminescence spectroscopy for the presence of CdS, ZnS and PbS respectively. Since *cysH* and *cysI* could not be engineered in single plasmid owing to their large size, two different construct are used for transformation of *E.coli* BL 21 AI™ cells separately. For the synthesis of metal sulfides, different set of recombinant *E.coli* BL 21 AI™ cells separately growing and harboring *cysH* and *cysI* genes were mixed in equal numbers prior to addition of respective metal sulfates.

Figure 4.16 shows respective TEM, UV-vis spectroscopic, and PL spectroscopic analysis performed on CdS, ZnS and PbS nanocrystallites synthesized using equal population of recombinant *E.coli* BL 21 AI™ cells harboring *cysH* and *cysI* genes from *P.aeruginosa.* Figure 4.16A1 shows TEM image of CdS nanocrystals synthesized using recombinant *E.coli* BL 21 AI™ cells after exposure to 10^{-3}M $CdSO_4$. Large population of nanoparticles with average size of ~ 2 nm has been observed, which is smaller in comparison with CdS nanoparticles synthesized using *P. aeruginosa*.

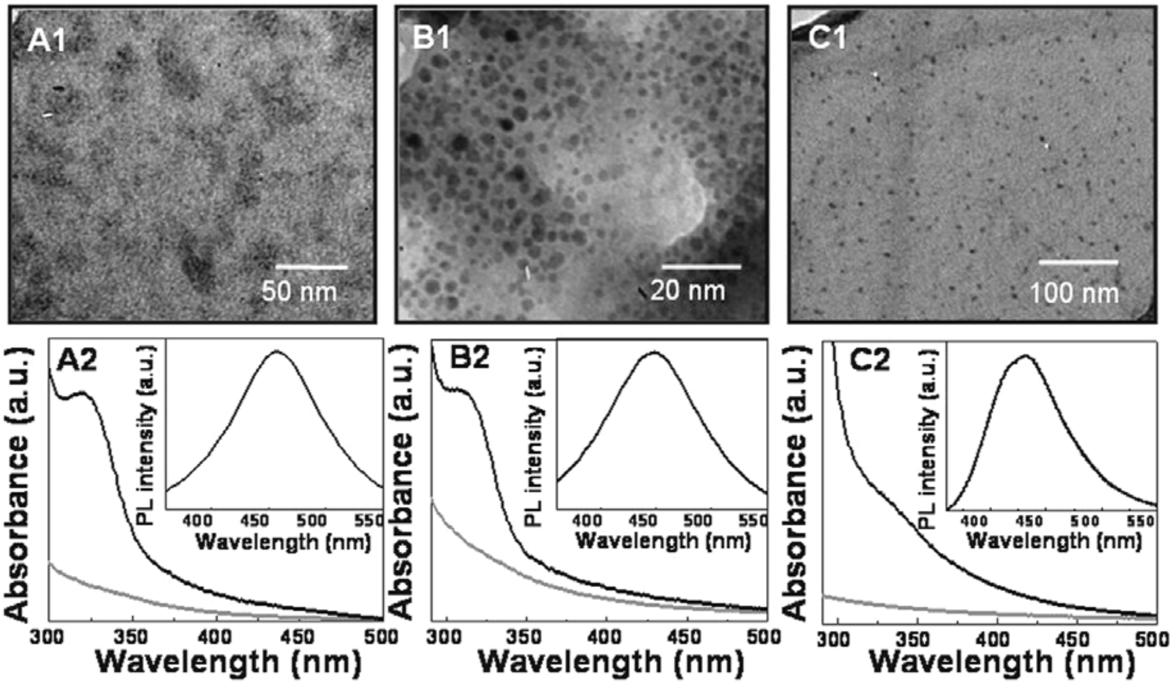

Figure 4.16 *TEM, UV-vis and PL spectroscopic analysis of CdS, ZnS and PbS nanoparticles synthesized using recombinant E.coli BL 21 AI™ cells. Images A1, B1 and C1 are TEM micrographs obtained from CdS, ZnS and PbS nanoparticles respectively. A2, B2 and C2 correspond to respective UV-vis analysis of aqueous solutions of cdS, ZnS and PbS nanoparticles. Insets in A2, B2 and C2 are PL spectra obtained from the aqueous solution of CdS, ZnS and PbS nanoparticles respectively.*

Corresponding UV-vis spectrum of aqueous solution of CdS nanocrystallites has been shown in Figure 4.16A2. Black curve in Figure 4.16A2 represents UV-vis absorption spectrum of the reaction mixture of 10^{-3}M $CdSO_4$ and recombinant *E.coli* BL 21 AI™ cells. Wild type *E.coli* BL 21 AI™ cells without pDEST™17 plasmid harboring *cysH* and *cysI* genes do not show formation of CdS nanoparticles as indicated by grey curve in Figure 4.16A2. The spectrum shows a well defined absorption peak with absorption maxima centered at 315 nm with large blue shift in comparison with bulk CdS, which can be ascribed to the size quantization effect in CdS nanocrystallites. Inset in Figure 4.16A2 represents the PL spectrum corresponding to the aqueous solution of CdS nanocrystallites synthesized using recombinant *E.coli* BL 21 AI™ cells after exciting at 300 nm and shows a well defined emission spectrum with intensity maxima centered at 460 nm.

Figure 4.16B1 shows the representative TEM image of ZnS nanocrystallites synthesized using recombinant *E.coli* BL 21 AI™ cells. Nanoparticles with the average size between 2-5 nm have been observed indicating the size distribution among nanoparticles. This feature is reflected in the UV-vis spectrum of ZnS nanoparticles, which shows a shoulder peak around 309 nm (Figure 4.16B2, black curve) instead of a sharp peak. Wild type *E.coli* BL 21 AI™ cells without engineered cysH and cysI genes do not show the formation of ZnS nanoparticles (Figure, 4.16B2, grey curve). Inset in Figure 4.16B2 represents the PL spectrum obtained by exciting the aqueous solution of ZnS nanoparticles at 300 nm after 12 h of reaction between 10^{-3}M $ZnSO_4$ and recombinant *E.coli* BL 21 AI™ cells and shows a sharp emission peak at 445 nm.

Figure 4.16C1 represents a TEM image of PbS nanoparticles synthesized using recombinant *E.coli* BL 21 AI™ cells and shows nanoparticles with average diameter of 5 nm. The corresponding UV-vis spectrum obtained from PbS nanoparticles shows clear absorption hump at 330 nm (Figure 4.16 C2, black curve), which is not observed in the UV-vis spectrum obtained from reaction between wild type *E.coli* BL 21 AI™ cells and precursor salt (Figure 4.16C2, grey curve). Inset in Figure 4.16C2 shows PL spectrum obtained by exciting the aqueous solution of PbS nanoparticles at 325 nm, which shows well defined emission peak with intensity maxima centered at 430 nm.

4.2.6 Discussion

This part of the chapter describes biological synthesis of metal sulfide semiconductor quantum dots using the bacteria *P. aeruginosa.* Biogenic nanocrystalline CdS, ZnS and PbS exhibited size quantization effect as indicated by their optical properties. Synthesis of all metal sulfide semiconductor nanocrystallites occurred under aerobic conditions and was found to be extracellular. Time dependent UV-vis spectroscopic analysis of the reaction indicated that metal sulfide nanoparticles are synthesized within 28 h of reaction. The average size of CdS, ZnS and PbS nanocrystallites was observed between 2-7 nm. The molecular mechanism of biological metal sulfite formation by P. aeruginosa revealed that sulfate reduction is a two step reaction catalyzed by two enzymes PAPS reductase and SIR of assimilatory sulfate reduction pathway. Two genes, *cysH* and *cysI* encoding PAPS reductase and SIR respectively have been identified, cloned and overexpressed in *E.coli* BL 21 AI™ cells.

Further recombinant *E.coli* BL 21 AI™ cells were used for the synthesis of cdS, ZnS and PbS. Wild type *E.coli* BL 21 AI™ cells without *cysH* and *cysI* gene inserts were unable to synthesize CdS, ZnS or PbS nanoparticles indicating the necessity of PAPS reductase and SIR during the biological synthesis of metal sulfide nanocrystallites.

4.3 Part II: Biosynthesis of iron sulfide and silver sulfide nanoparticles using *Actinobacter* spp.

This part of the chapter describes biosynthesis of magnetic iron sulfide e.g. greigite and silver sulfide nanoparticles using *Actinobacter spp*. Additionally preliminary biological mechanism for biosynthesis of iron sulfide and silver sulfide nanoparticles operational in *Actinobacter spp*. has been discussed.

4.3.1 Experimental details

The Gram positive bacterium Actinobacter spp. was isolated and identified as described in chapter 3. For the cultivation of bacteria in 100 ml batch, bacterial seed culture was grown overnight in small volume (~2 ml) of Luria broth (LB) medium. This seed culture was then inoculated in 100 ml of LB medium without NaCl in 500 ml Erlenmeyer flask for bacterial propagation. For the biosynthesis of iron sulfide nanoparticles, the bacterial cells were freshly grown in 100 ml of LB medium (without NaCl) in 500 ml Erlenmeyer flask and incubated on the rotary shaker (200 rpm) at 37° C for ~ 48 h until the stationary phase is attained. Next, filter sterilized aqueous solution of ferric citrate and ferrous sulfate was added to the bacterial culture at the final concentration of 2:1 M ratio.

Silver sulfide nanoparticles were synthesized by adding the filter sterilized 10^{-3} M aqueous solution of Ag_2SO_4 to the bacterial culture in separate flasks. Both the flasks were incubated on the rotary shaker (200 rpm) at 37 °C for 48 to 72 h. The bacterial culture supernatants containing iron sulfide and silver sulfide nanoparticles were isolated by separating the bacterial biomass by centrifugation at 5000 rpm. The culture supernatant containing iron sulfide and silver sulfide nanoparticles were characterized by TEM, XRD, FTIR, UV-vis spectroscopy, TGA, Photoluminescence analysis and magnetic measurements etc. Magnetization as a function of the field at different temperatures was recorded by varying the applied field between -50 KOe to 50 KOe.

Temperature dependent magnetization of iron sulfide nanoparticles was studied in the ZFC (Zero-field-cooled) and FC (field cooled) modes for as-synthesized as well as calcined nanoparticles. Extracellular protein profile of the bacterial culture supernatant was checked for the induction of new protein/s upon metal salt addition. To check the induction of new protein/s, extracellular protein profile of *Actinobacter spp*. culture supernatant was analyzed in the presence and the absence of metal salts. Proteins were analyzed by denaturing polyacrylamide gel electrophoresis (SDS-PAGE) as well as native polyacrylamide gel electrophoresis on 12% gels (12% T and 2.7% C).

For analysis of the proteins bound to the surface of the nanoparticles, iron sulfide and silver sulfide nanoparticles were separated from the culture supernatant. First, bacterial biomass was removed by centrifugation at 5000 rpm (2560 *X g*) and the culture supernatant containing nanoparticles was collected. This culture supernatant was again subjected to centrifugation at 20000 rpm (20579 *X g*) for 30 minutes. After centrifugation the supernatant was discarded and the black pellet of iron sulfide and silver sulfide each were washed thrice with 50mM sodium phosphate buffer (pH 7.4) before dissolving in 100 μl of the same buffer. Proteins were separated from the nanoparticles by treatment with 8M urea and 1% SDS. The solutions were then heated at 60 °C for 10 minutes and then centrifuged at 20,000 rpm for 30 minutes. The supernatant was analyzed on SDS-PAGE for the presence of proteins as described above. To study the association of PAPS (phosphoadenosyl phosphosulfate) reductase in the reduction of sulfate to sulfide, biosynthesis of iron sulfide and silver sulfide by *Actinobacter spp*. was carried in the presence of 100 μM of chromium ions as chromium ions are known to inhibit PAPS reductase activity. The reaction was carried out for around four days. For the isolation and sequencing of the sulfate reductase genes from *Actinobacter spp*., genomic DNA was isolated from *Actinobacter* spp. by standard phenol/chloroform extraction method as described previously. One of the genes (PAPS reductase) for sulfate reduction pathway was amplified with paps-F (5’ – GTT CTG CGT GAC CTC CTC CAT – 3’) and paps-R (5’–GTC CTC GCC CTC CAG CAC AC– 3’) for the amplification of sulphate reductase (PAPS reductase). The primers were designed from the available sequences of cysH (PAPS reductase gene) in *Sterpromyces avermitilis* MA-4680 genome (NC 003155). The PCR conditions used were an initial denaturation at 94 °C for two minutes, followed by

35 cycles of denaturation at 94 °C for one minute, annealing at 60 °C for one minute and extension at 72 °C for 30 seconds and final extension at 72 °C for 10 minutes. From the amplified PCR product bands with desirable sizes were excised from the gel by QIAquick gel extraction kit according to manufacturer's instructions (Qiagen). The gel eluted PCR products were then sequenced from both the directions using same set of primers on automated DNA analyzer 3730 of Applied Biosystem BigDye terminator chemistry. The sequences so obtained were analyzed at the NCBI server using different BLAST programs.

4.3.2 Biosynthesis of magnetic iron sulfide nanoparticles

4.3.2.1 TEM analysis

Figure 4.17 shows the TEM analysis of iron sulfide nanoparticles synthesized by reaction between iron salts and *Actinobacter spp*. A number of quasi–spherical nanoparticles of iron sulfides are uniformly distributed on the grid area.

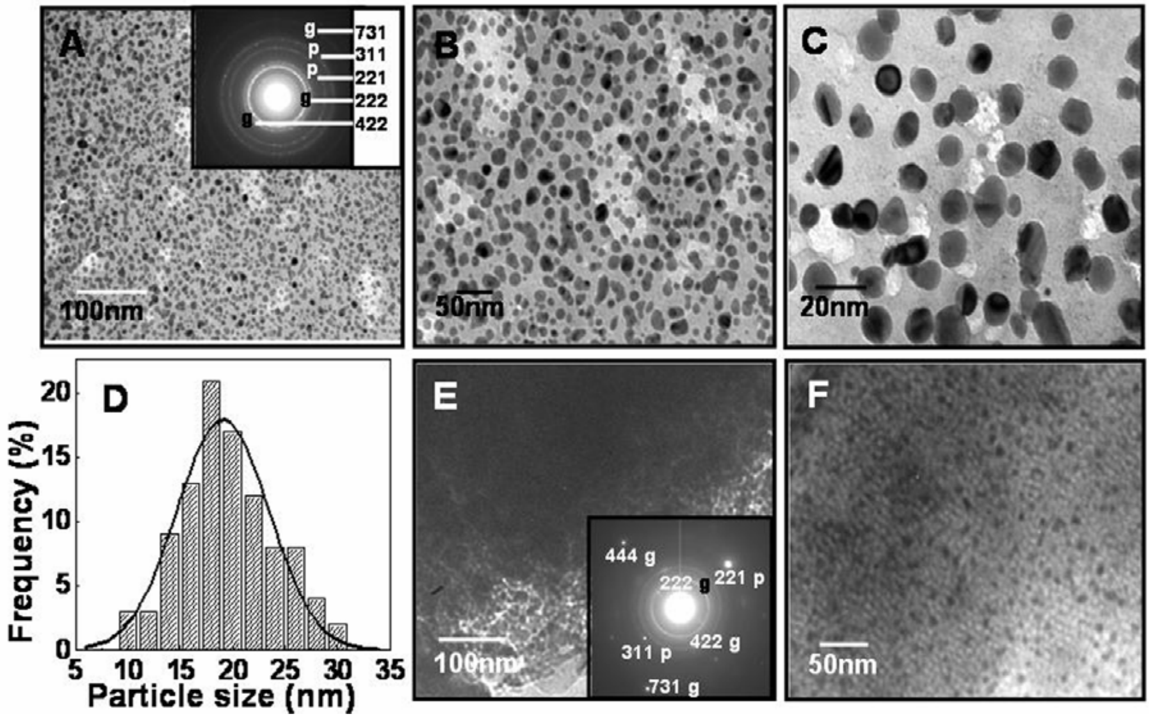

Figure 4.17 *TEM images of as-prepared iron sulfide nanoparticles synthesized by Actinobacter spp. iron salts reaction mixture after 48 h of reaction (A to E). The inset in A shows SAED pattern of as-synthesized iron sulfide nanoparticles. Letters P and G represent pyrite and greigite phase of iron sulfide. (D) Particles size distribution analysis of as-synthesized iron sulfide nanoparticles. (E – F) TEM images of as-synthesized iron sulfide nanoparticles after calcination at 300° C for 2 h. Inset in E shows SAED pattern of the calcined iron sulfide nanoparticles.*

Images A to E in Figure 4.17 corresponds to the as – synthesized iron sulfide nanoparticles after reaction of 48 h. Nearly monodisperse, well separated nanoparticles are clearly observed with the average diameter of 19 nm as indicated by the particle size distribution analysis (Figure 4.17D). Higher magnification TEM images of as-synthesized nanoparticles showed the presence of twin boundaries within nanoparticles (Figure 4.17C). SAED analysis performed on as – synthesized iron sulfide nanoparticles shows a well defined electron diffraction pattern (inset, Figure 4.17A). The diffraction pattern was indexed on the basis of mixed phases of iron sulfide, i.e. greigite (Fe_3S_4) and pyrite (FeS_2). Most of the diffraction rings (indicated by subscript g in diffraction pattern, inset in Figure 4.14A) were analyzed on the basis of greigite (Fe_3S_4) phase of iron sulfide while two rings (indicated by subscript p) show excellent match with pyrite (FeS_2) [41]. TEM Images E and F in Figure 4.14 correspond to iron sulfide nanoparticles after calcination at 300 °C for 2 h. The average size of iron sulfide nanoparticles remains unaltered after heat treatment, though some degree of aggregation is observed among the nanoparticles. This is probably due to the fact that some of the organic matter is retained even after the calcination at 300 °C (see TGA data for the detailed discussion) that prevents the nanoparticles from getting aggregated.

SAED pattern observed from calcined iron sulfide nanoparticles as well could be indexed on the basis of the mixed phases of iron sulfide namely greigite and pyrite (inset in Figure 4.14E greigite-g, pyrite p).

4.3.2.2 FTIR and Thermogravimetric (TG) analysis

Figure 4.18A illustrates the FTIR spectroscopic analysis performed on the as – synthesized, purified iron sulfide nanoparticles after 48 h of reaction between *Actinobacter spp*. and iron salts. FTIR analysis shows the presence of characteristic Fe-S bond vibrations [42]. The broad peak in the region between 620 cm^{-1} and 850 cm^{-1} is assigned to Fe-S bending vibrations while the small sharp band at 1160 cm^{-1} could be ascribed to the stretching of Fe-S bonds. These Fe-S bonds are accompanied with the presence of amide I and II vibration bands, which appear at 1660 and 1540 cm^{-1} respectively, indicating the presence of proteins along with the nanoparticles (Figure. 4.18A). The nanoparticles are probably stabilized by capping of the proteins secreted by *Actinobacter spp*.

TGA was performed on as–synthesized iron sulfide nanoparticles to calculate the amount of bio-organic molecules present with iron sulfide nanoparticles. TGA carried out on as-prepared sample of iron sulfide shows a weight loss in two major regions (Figure 4.18B). The first region is centered between 100° C to 500 °C showing a gradual weight loss this can be assigned to the evaporation of the water molecules present in the sample and decomposition of protein molecules.

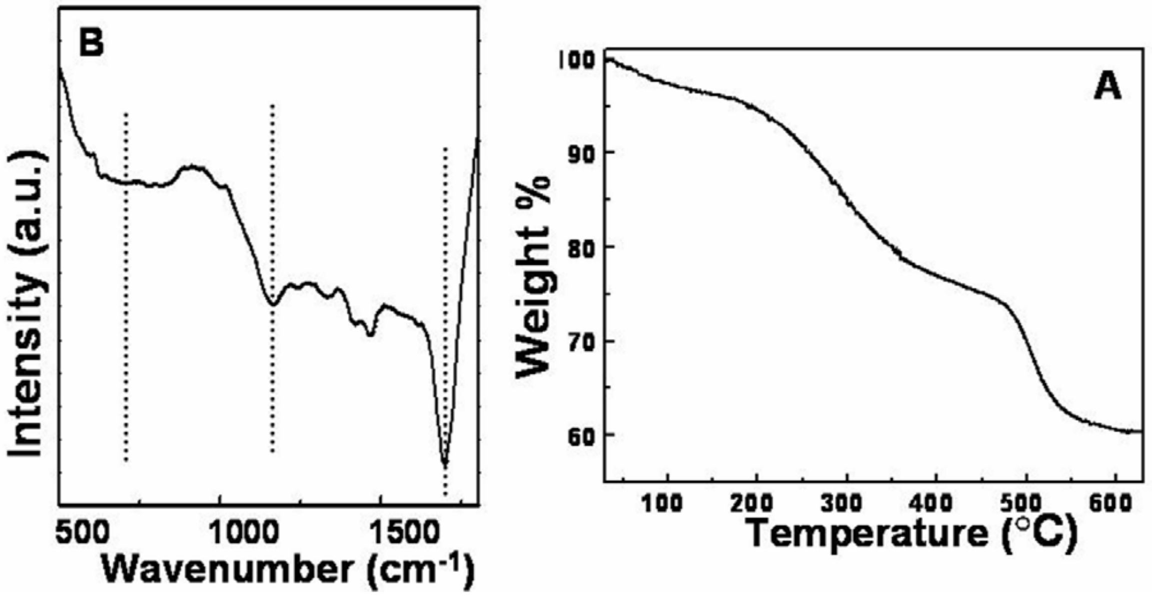

Figure 4.18 *(A) The FTIR spectroscopic analysis performed on the purified iron sulfide nanoparticles synthesized after 48 h of reaction. Dotted lines indicate Fe-S vibrational bands along with amide bond vibrations respectively. (B) TGA analysis performed on as – synthesized iron sulfide nanoparticles.*

A sharp weight loss is observed after around 450 °C, which is probably due to the rapid degradation of organic matter present in the sample. The gross weight loss observed by TGA is calculated to be about 64 %.

4.3.2.3 X-ray diffraction analysis

Figure 4.19 represents the XRD pattern obtained from the solution cast film of as – synthesized and calcined (300 °C, 2h)iron sulfide nanoparticles on the glass substrate. A number of strong Bragg reflections originating from the solution cast films are observed. The diffraction pattern obtained from as – synthesized and calcined iron sulfide nanoparticles was indexed on the basis of the mixed phase structure of iron sulfide. Most of the reflections were indexed on the basis of greigite (Fe_3S_4) phase of iron sulfide, which are indicated as "Δ" in the Figure 4.19. Rest of the reflections were assigned to pyrite (FeS_2) phase of iron sulfide and indicated as "○" in Figure 4.19. The curve 1 (gray curve) in Figure 4.19 corresponds to the as – synthesized iron sulfide nanoparticles, while curve 2 (black curve) in Figure 4.19 represents the diffraction pattern obtained from iron sulfide nanoparticles after calcination at 300 °C for 2 h. Both curves are almost identical when superimposed with very little observable variation.

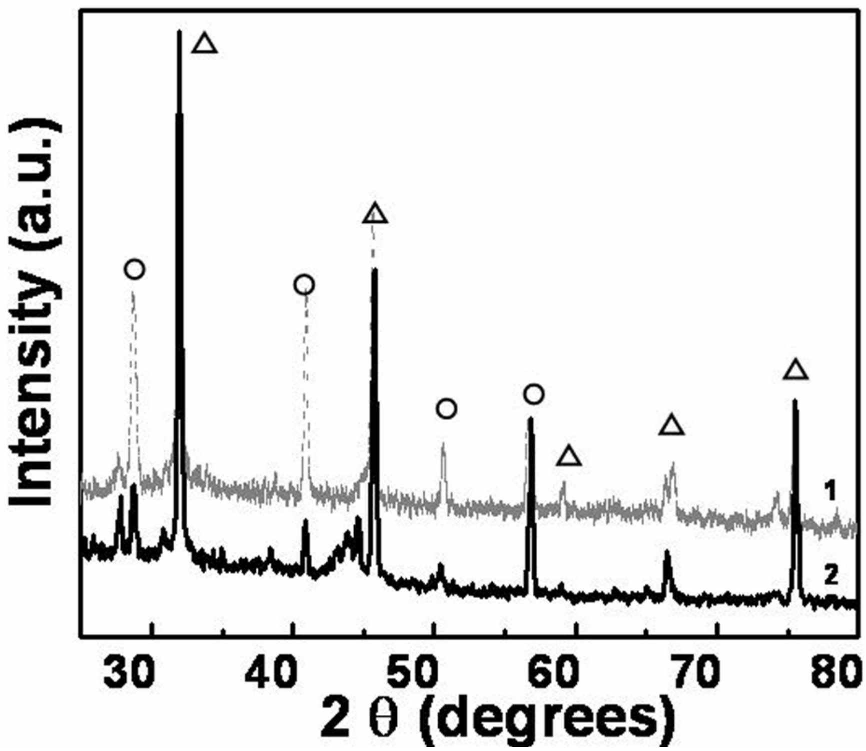

Figure 4.19 *The XRD pattern obtained from iron sulfide nanoparticles synthesized by the reaction between iron salts and Actinobacter spp. after 48 h of reaction. Curve 1 (grey curve) represents XRD pattern of as – synthesized iron sulfide nanoparticles, while curve 2 (black curve) indicates the XRD pattern of iron sulfide nanoparticles after calcination at 300° C for 2 h.*

This observation indicates that calcination treatment does not alter the indigenous crystal structure of as – synthesized iron sulfide nanoparticles. However, enhancement in the crystallinity of individual domains of the nanoparticles can not be ruled out. On the basis of X-ray diffraction analysis it can be deduced that the iron sulfide synthesized by *Actinobacter spp.* gives $Fe_{x-1}S_x$ kind of crystal structure. The respective *d* values for the corresponding *hkl* planes are as follows: for greigite (marked as Δ): 2.86 (222), 2.09 (422), 1.59 (620), 1.47 (444), 1.43 (731) and for pyrite (marked as ○): 3.12 (111), 2.21 (221), 1.75 (221), 1.60 (311) [41].

4.3.2.4 Magnetic measurements

Magnetic measurements were performed on dried iron sulfide nanoparticles before and after calcination. Magnetization as a function of the field at different temperatures was recorded by varying the applied magnetic field between -50 KOe to 50 kOe. Temperature dependent magnetization of magnetite nanoparticles is studied by ZFC (Zero-field-cooled) and FC (field cooled) modes for as prepared as well as calcined nanoparticles. Figure 4.20A shows the magnetization curves (M-H curves) obtained from as synthesized powdered iron sulfide nanoparticles at 5 K, 20 K, 150 K and 250 K, respectively.

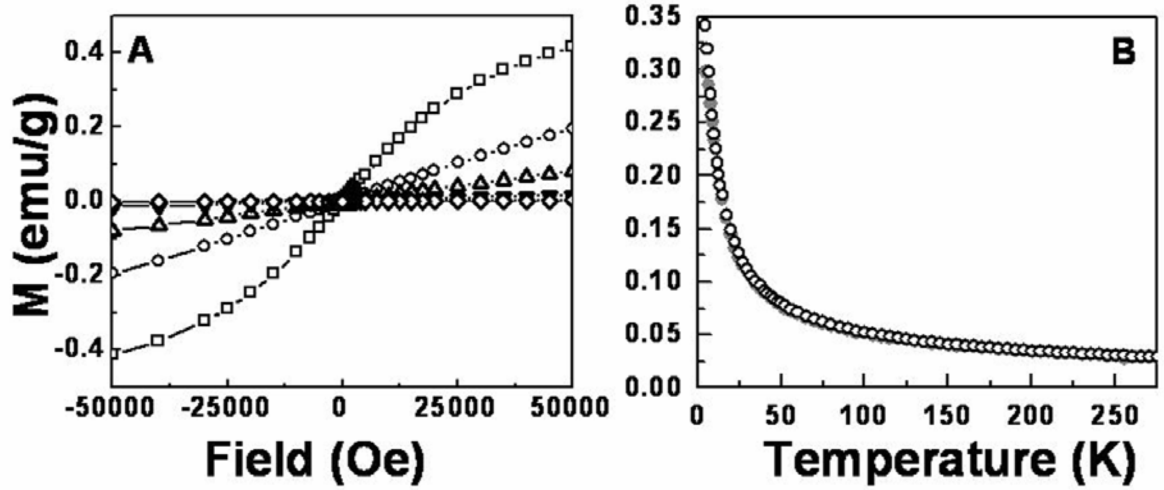

Figure 4.20 *(A) M – H curve obtained from as – synthesized iron sulfide nanoparticles at various temperatures. Different experimental temperatures are displayed by different symbols. (□- 5 K, ○- 20 K, Δ- 50 K, ∇- 150 K and ◊- 250 K). (B) FC and ZFC curves obtained from as – synthesized iron sulfide nanoparticles at the extern alapplied magnetic field of 1000 Oe.*

Magnetization studies carried out on as synthesized iron sulfide nanoparticles show weak magnetic response at higher temperature (above 50 K) and the induced magnetization in the nanoparticles is negligible indicating the paramagnetic behavior (Figure 4.20A, curves corresponding to 150 K and 250 K in). However, as the temperature is lowered, a gradual increase in the induced magnetization value was observed. Iron sulfide nanoparticles show superparamagnetism at lower temperatures (Figure 4.20A, curves corresponding to 20 K and 5 K) and the opening of a hysteresis loop was not observed even at the applied field of 50 kOe. Figure 4.20B shows the magnetization as the function of temperature studied by field cooled (FC) and Zero field cooled (ZFC) curves obtained from as synthesized iron sulfide nanoparticles. ZFC and

FC curves almost superimpose with each other indicating the absence of blocking phenomena [43].

Figure 4.21 shows the magnetization studies performed on iron sulfide nanoparticles after the calcination at 300 °C for 2 h. Magnetization curves obtained from calcined iron sulfide nanoparticles at various temperatures are shown in Figure 4.21A. As observed with as – synthesized iron sulfide nanoparticles, the calcined nanoparticles also exhibited weak magnetic response at higher temperatures and tend to be paramagnetic (at 150 K and 250 K). However at lower temperatures enhanced magnetization signal is observed in the nanoparticles.

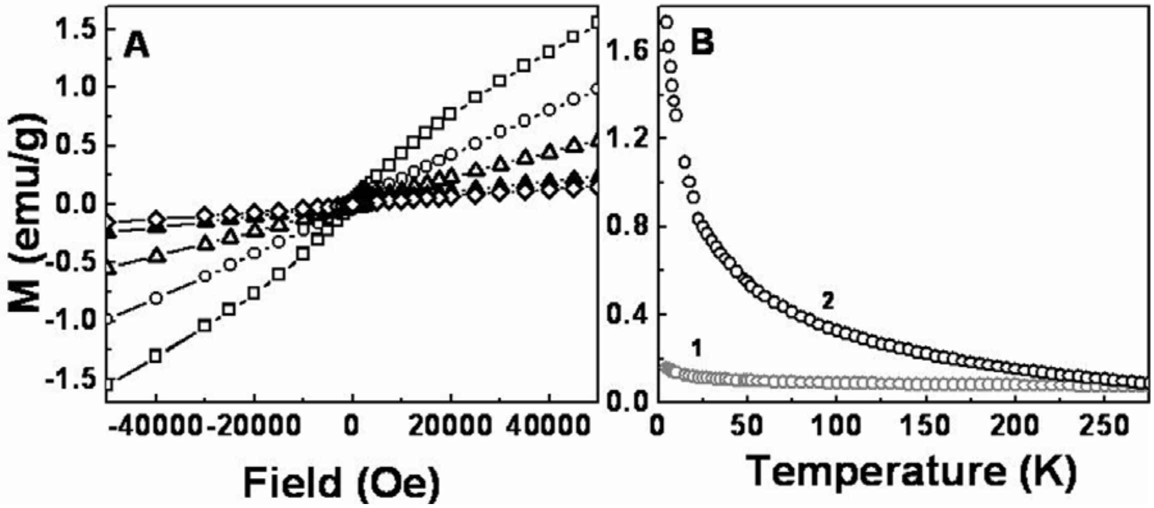

Figure 4.21 *(A) M-H curves obtained from iron sulfide nanoparticles after calcination at 300 °C for 2 h at various temperatures. Different experimental temperatures are shown with various symbols as 5 K-□, 20 K-○, 50 K,-Δ, 150 K-▲, 250 K- ◊. (B) FC and ZFC curves obtained from calcined iron sulfide nanoparticles at the external applied magnetic field of 1000 Oe.*

Iron sulfide nanoparticles after calcination shows superparamagnetic behavior as indicated by increasing induced magnetization at the applied magnetic filed as high as 60 KOe. The increase in the magnetization signal of the calcined sample is attributed to the removal of diamagnetic bio-organic molecules with the proteins from the surface of nanoparticles. This result is quite consistent with TGA studies, which indicated that bio-organic molecules are present in considerable amount along with maghaemite nanoparticles. The value for maximum magnetization per unit mass (σ_s) under given experimental conditions for iron sulfide nanoparticles synthesized by *Actinobacter* spp. is found to be around 3.8 emu/g while the coercivity was calculated to be ~ 120 Oe at 5 k.

The low magnetization and Coercivity value obtained for iron sulfide nanoparticles are due to the small size of nanoparticles and presence of non-magnetic phases of iron sulfide like pyrite that reduces the overall magnetization value.

Figure 4.21B shows temperature dependence of magnetization of calcined iron sulfide nanoparticles studied by ZFC and FC curves. ZFC and FC curves show clear divergence at around 225 indicating that the blocking temperature of iron sulfide nanoparticles can be around 200 K. This result is consistent with the magnetization curves above 150 K where nanoparticles show almost paramagnetic behavior.

4.3.3 Biosynthesis of silver sulfide nanoparticles (Ag_2S)

4.3.3.1 TEM analysis

Figure 4.22 shows the TEM analysis carried out on the solution cast film of Ag_2S nanoparticles synthesized using *Actinobacter* spp. 24 h after reaction. Image A and B shows the low magnification TEM images of Ag_2S nanoparticles and clearly reveal the nanoparticles of apparently two different sizes. The bigger nanoparticles 10 to 20 nm in diameter are also observed in all the images and seem to be embedded in a kind of bio – organic matrix. The bigger nanoparticles are highly irregular in shape and are observed to be surrounded by a dense population of smaller sized nanoparticles. The smaller

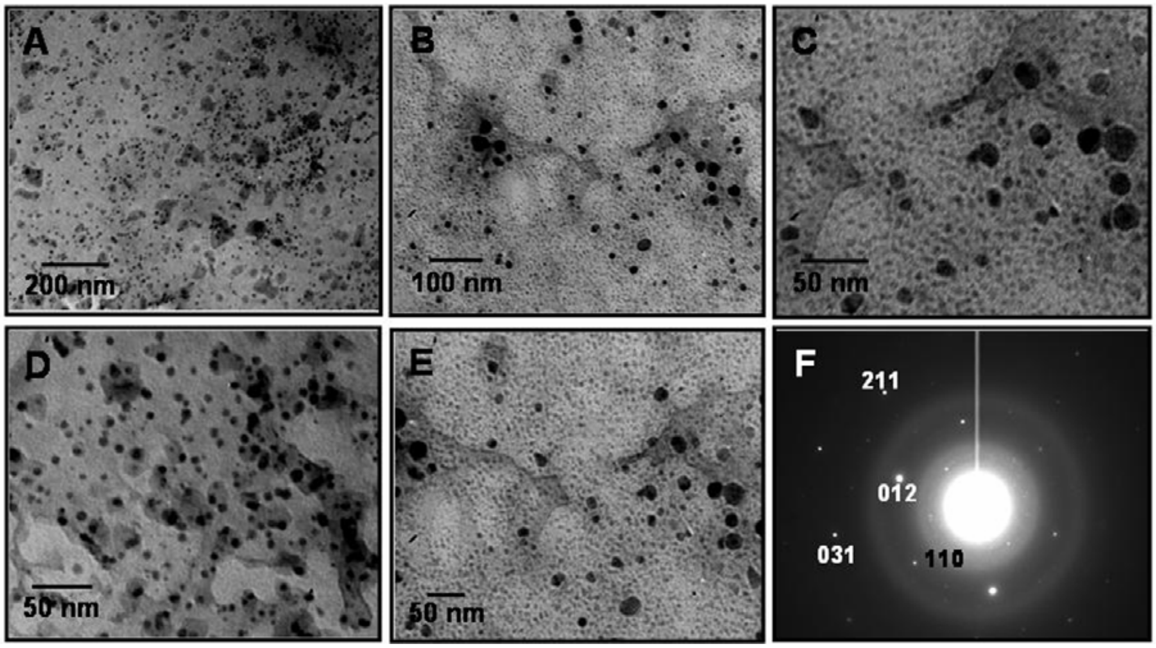

Figure 4.22 TEM images of as – synthesized Ag_2S nanoparticles 24 h of the reaction between silver sulfate and Actinobacter spp (A to E). Image F shows the SAED pattern obtained from Ag_2S nanoparticles with the respective lattice planes.

nanoparticles are spherical in the shape, 3 to 5 nm in diameter and seem to be distributed in a regular order. However, it is very difficult to predict about the arrangement and the exact shape of the smaller nanoparticles with the existing TEM machine used for analysis. Ag_2S nanoparticles synthesized by *Actinobacter* spp. are highly crystalline as indicated by the well defined SAED pattern. Image F in Figure 4.22 shows SAED pattern obtained from as – synthesized Ag_2S nanoparticles and the diffraction spots were indexed on the basis of hexagonal structure of α-Ag_2S [44].

4.3.3.2 UV-vis spectroscopic and PL analysis

Ag_2S is a direct band gap semiconductor with a band gap energy value of ~1 eV and shows a featureless absorption in infrared region of the electromagnetic spectrum [45]. The optical properties of Ag_2S nanoparticles are highly size and shape dependent. Figure 4.23 depicts the optical properties of Ag2S nanoparticles synthesized using *Actinobacter* spp. A time dependant UV-vis absorption spectrum of Ag_2S nanoparticles is shown in Figure 4.23A and indicates the progress of reaction. At the initial stage, after 6 h of reaction the UV-vis spectrum does not show any sharp feature, and rather shows a monotonous increase in the absorption at lower wavelength at around 390 nm (curve 1 in Figure 4.23A). After about 12 h of reaction a broad absorption onset is observed in the region of 380 nm to 440 nm with the absorption maxima centered at 400 nm (curve 2 in Figure 4.23A). The appearance of this weak shoulder peak in the UV-vis spectrum corresponds to the exitonic transitions in the Ag_2S nanoparticles [46]. As the progress of reaction continues the shoulder peak around 380 nm increases with intensity and becomes narrower (curve 3 in Figure 4.23A). Further evolution of the reaction brings the sharper features in the UV-vis spectrum and after 24 of reaction a well defined shoulder peak is observed with absorption maxima centered at ~ 390 nm (curve 4, Figure 4.23A). A large blue shift in the absorption spectra of Ag_2S nanoparticles synthesized using *Actinobacter* spp. is observed in comparison to the optical band edge of bulk Ag_2S. This large change in the absorption of Ag_2S is due to the change in the electronic properties that occurs when the diameter of the particles approaches the excitonic diameter of Ag_2S. As the size of Ag_2S particles decreases, a widening of the forbidden band occurs resulting in a blue shift in the absorption spectrum. The formation of Ag_2S nanoparticles is highly dependent on the presence of exogenous sulfate ions in the reaction medium. Sliver sulfide nanoparticles are only synthesized when the bacterium was reacted with silver sulfate.

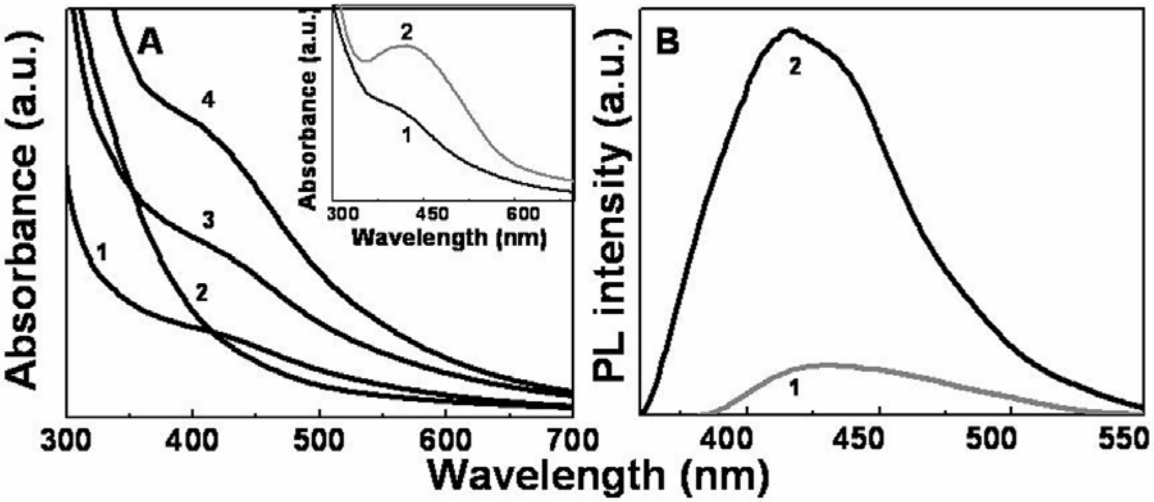

Figure 4.23*(A) UV-vis spectra obtained from Ag_2S nanoparticles after different time intervals of reaction between Actinobacter spp. and silver sulfate. Curves 1 to 4 are obtained after 6, 12, 18 and 24 h of reaction. The inset in A shows that Ag_2S nanoparticles are synthesized only in the presence of exogenous sulfate ions. Curve 1 in black represents UV-vis spectrum obtained by reaction of the bacterium with 1mM Ag_2SO_4 while curve 2 in grey shows the formation of Ag nanoparticles when reacted with 1 mM $AgNO_3$. (B) PL spectra of Ag_2S nanoparticles obtained by exciting the aqueous solution of the nanoparticles at 400 nm (curve 1 in grey) and 350 nm (curve 2 in black).*

When the same reaction was carried out in the presence of 1 mM $AgNO_3$ formation of silver nanoparticles are observed surprisingly instead of silver sulfide. Inset in Figure 4.20A shows the UV-vis spectra obtained from the reaction mixture between *Actinobacter* spp. and different silver salts. The curve 1 in black represents UV-vis spectrum obtained from the reaction between *Actinobacter* spp. and 1mM Ag_2SO_4, while curve 2 in grey shows the formation of Ag nanoparticles by the reaction between *Actinobacter* spp. and 1 mM $AgNO_3$. A sharp peak at 420 nm in the curve 2 is due to the surface plasmon resonance band, which arises due to the oscillation of the surface electrons, while the absorption onset at ~ 390 nm is due to the excitonic transitions in Ag_2S nanoparticles.

This result indicates that Ag_2S nanoparticles are synthesized only in the presence of exogenous sulfide ions, which are provided by silver sulfate. Figure 4.20B shows the room temperature PL spectra obtained from as – synthesized Ag_2S nanoparticles after 24 h of reaction exhibiting the luminescent nature of biogenic Ag_2S nanoparticles. PL spectra were obtained by exciting the aqueous solution of the nanoparticles at 350 nm and 400 nm respectively. Ag_2S nanoparticles exhibit size dependent luminescent properties and PL spectrum shifts towards lower wavelengths as the size of nanoparticles is decreased. Curve 1 (grey curve) in Figure 4.23 B represents the PL spectrum obtained by exciting Ag_2S nanoparticles at 400 nm, which shows a sharp emission band with emission maxima centered at 440 nm. This emission of Ag_2S nanoparticles falls in the blue- green region of the visible wavelength of the electromagnetic spectrum. Curve 2 (black curve) in Figure 4.23 B shows the emission spectrum obtained by exciting Ag_2S nanoparticles at 350 nm. A sharp emission peak with the maximum intensity centered at 450 nm is observed. The peak position in both the PL spectra is almost independent of the excitation energy suggesting that Ag_2S are solely responsible for the observed luminescence. However, there is a large difference in the emission intensities, which could be assigned to the simultaneous excitation of all Ag_2S nanoparticles present in the solution.

4.3.3.3 X-ray diffraction (XRD) analysis

The crystalline nature of silver sulfide nanoparticles can be analyzed by the X-ray diffraction studies. Figure 4.24 illustrates the X-ray diffraction pattern (XRD) obtained by as–synthesized silver sulfide nanoparticles.

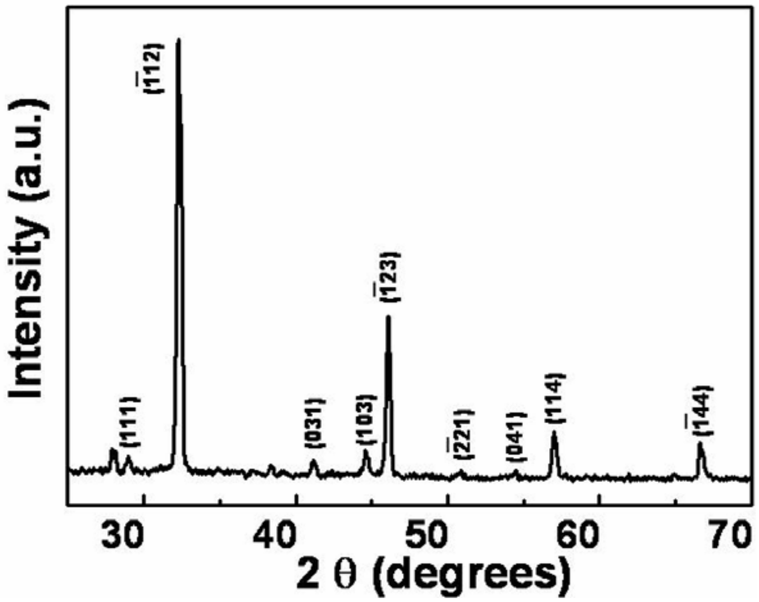

Figure 4.24 *The XRD pattern of Ag_2S nanoparticles synthesized by reaction between silver sulfate and Actinobacter spp. The XRD pattern was indexed on the basis of α- Ag_2S. The Bragg reflections arising from the nanoparticles film are indexed with the respective crystal planes.*

A large number of intense Bragg reflections are observed originating from the solution cast film sample of Ag_2S nanoparticles on the glass substrates. The XRD pattern obtained from Ag_2S nanoparticles confirm their highly crystalline nature. All intense peaks originating from the nanoparticles film can be indexed with the monoclinic α – Ag_2S phase of silver sulfide [43]. The XRD pattern obtained from silver sulfide nanoparticles well corroborates with the SAED analysis performed on silver sulfide nanoparticles. The respective *d* values obtained for the corresponding *hkl* planes are as follows: 3.08 (111), 2.83 (-112), 2.21 (031), 2.04 (103), 1.96 (-123), 1.79 (-221), 1.69 (041), 1.61 (114), 1.40 (-144) [44].

4.3.4 Biochemical insight into metal sulfide formation by *Actinobacte*r spp.

Actinobacter spp. can synthesize iron sulfide and silver sulfide nanoparticles when reacted with the respective iron and silver salts containing sulfate ions. However, the synthesis of iron sulfide and silver sulfide are highly specific to the exogenous sulfate ion source and in the absence of exogenous sulfate ions synthesis of respective metal sulfide nanoparticles does not occur. In the absence of sulfate ion source *Actinobacter* spp. synthesizes iron oxide nanoparticles as described in the previous chapter, while the same bacterium capitulate metallic silver nanoparticles in the absence of sulfate ions. This results indicate that a highly specific and sulfate dependent biological mechanism is responsible for the biosynthesis of iron sulfide and silver sulfide nanoparticles. We believe that the presence of exogenous sulfate ions trigger the formation of sulfate reductases in *Actinobacter* spp. As indicated in the preceding section of this chapter, the sulfate reductases involved in the formation of iron sulfide and silver sulfide nanoparticles are most likely to be a component of assimilatory sulfate reduction pathway, since *Actinobacter* spp. is a highly aerobic bacterium and also the formation of metal sulfate nanoparticles occurs in total aerobic conditions.

Figure 4.25 A shows the image of the agarose gel electrophoresis pattern of DNA fragment corresponding to the gene encoding PAPS (3′ phosphoadenosine 5′ phosphosulfate) reductase in *Actinobacter* spp. after PCR amplification. A sharp and intense single band of the gene fragment at 0.9 kb is observed on 1% agarose gel after

PCR amplification with specific primers designed from *Sterpromyces avermitilis* MA-4680 genome (NC 003155).

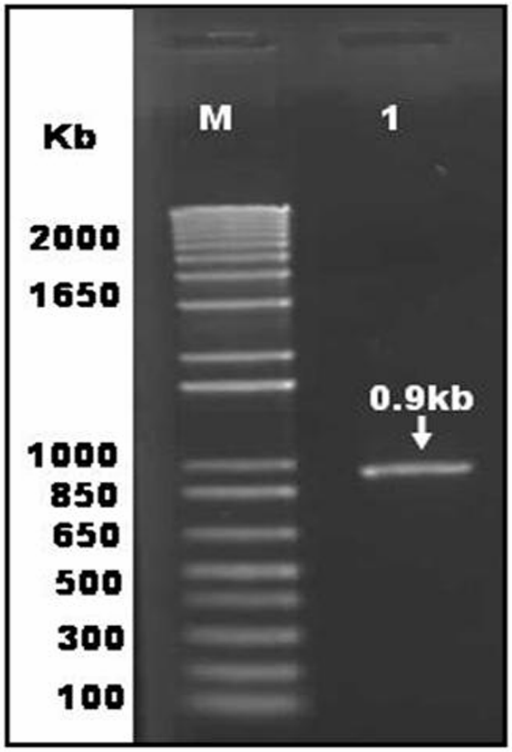

5'
CCAGGCACGCCCCGATCCTCGACAAACCCCGG
CAAAAGCCCGACACTCAAACGCAGGCACAGCA
GCCCGTTCCGGCGGCGCACGTAAATTGGCCGT
CCACGCCCGCGGCGACGGGCCTAAAAGGGCG
GGGGCCGGTCCGGCAGCGTGCGTAAAAGGGG
CCCCGCGCCCCAGGGCTCGCCGCGAAGCGGCC
AAGCCGGGGCGCGGGGAATAGCACGCAGAGG
ACCGGGCCCCACCCGACCATAGACGCACCAAG
ACAAAAGGTCCCCCCAGCTGAAGCCGGGGGGA
CCTTTCGTGGTACTACCGGGTGTTACTGCTCGA
CGACGAGGAGCAGGTCACCGCCCTGCACCTGC
TCCACCGCGGAGATGGCGAGGCGGGACACCTT
GCCGCCCACCGGCGTCGTGATGGAGGCTTCCA
TCTTCATGGCTTCGATGGTGGCTACCGTGTCGC
CGGCGTTCACCGTGTCTCCGGCCTTCACTGTGA
CGGTGACGGCACCGGCGAACGGCGCGGCGAC
CTGGCCGGGCTGGGCGGGGTCGGCCTTCTCGG
CAGCCTTGACGTTGCTGACCACGGAACGGTCG
CGGACCACCACGGGCCGGGACTGTCCGTTGAG
TGTGCACATGACGGTCCGCATGCCTTTTTCGTC
GGGCTCGGATACAGCCTCCAGCGAGGCGATCA
GGCGCACGCCGCGTTCCAGCTGGATCTCGTGTT
CGGCTCCGCGCTGGAAGCCG 3'

Figure 4.25 *Agarose gel electrophoresis pattern of putative PAPS reductase gene fragment amplified by PCR reaction. Lane 1 represents a single DNA band of 0.9 kb while lane M represents the DNA molecular weight marker with the respective molecular weight. Gene Sequence of the putative PAPS reductase gene fragment from Actinobacter spp.*

The gene fragment with 0.9 kb size could be assigned to a gene encoding for the enzyme PAPS reductase based on molecular weight as studied before (NCBI GenBank accession no. NC 003155).PAPS reductasae is a first enzyme in the sulfate reduction that converts sulfate into sulfite. When this 0.9 kb gene fragment was sequenced and analyzed on BLAST server no significant match in NCBI database was obtained. However, a domain of 102 bases showed the similarity with putative reductase gene from *S. avermitilis* in TBLASTX program at NCBI. Further, the role of PAPS reductase in the formation of iron and silver sulfide was analyzed by reacting the iron and silver salts in the presence of chromate ions, which are known to inhibit sulfate reduction pathway [47]. When sulfate salts of iron and silver were reacted with *Actinobacter* spp. in the presence of 100 μM chromate ions the formation of iron sulfide or silver sulfide nanoparticles was not observed even after eight days of reaction. Chromate ions were not found to inhibit the bacterial growth, since *Actinobacter* spp. could grow normally with the chromate ion concentration used in this experiment (100 μM). This result together with the PCR amplification and sequencing of PAPS reductase gene fragment shows the presence and active role of PAPS reductase in sulfate reduction and the formation of iron sulfide and silver sulfide nanoparticles via sulfate reduction pathway. Presence of metal salts in excess amounts (usually more than μM concentration) generally induces the synthesis of new proteins in bacterial cells to nullify the toxic effect exerted by metal salts.

When the culture supernatant of *Actinobacter* spp. grown in the presence and absence of iron salts was assayed by SDS-PAGE, two proteins are found to be induced in the presence of iron salts. Figure 4.26A shows the comparative SDS-PAGE analysis of the extracellular protein profile of *Actinobacter* spp. grown in the presence and absence of iron salt.

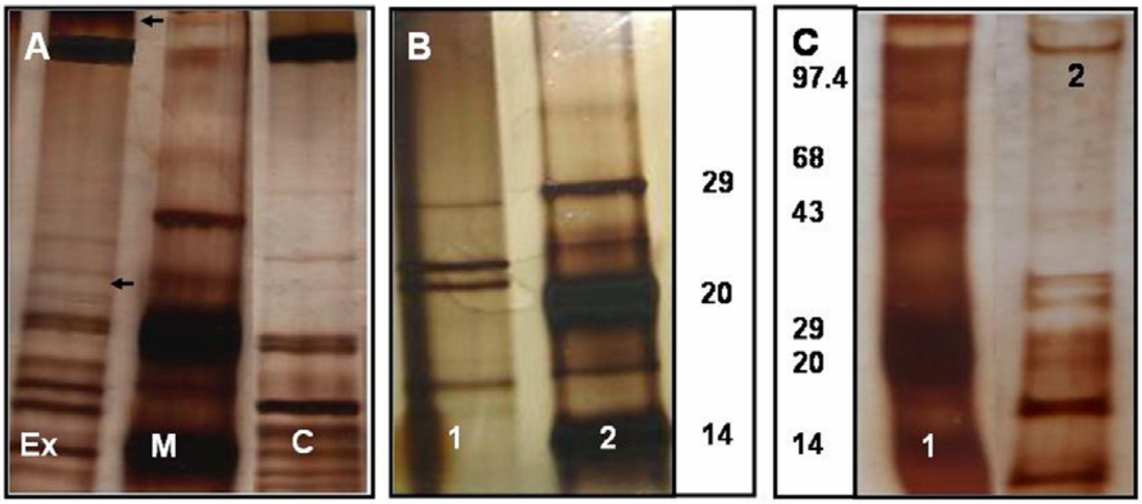

Figure 4.26 *(A) SDS-PAGE analysis of the extracellular protein profile of Actinobacter spp. obtained by growing the bacterium in the presence (lane Ex) and the absence (lane C) of iron salts. Presence of the two extra bands in lane Ex corresponds to the induction of new proteins with the molecular weight of 55 KDa and 120 kDa respectively, which are absent in the lane C. Lane M corresponds to the standard protein molecular weight marker. (B) SDS-PAGE analysis of the proteins bound to the surface of iron sulfide nanoparticles (lane 1). Lane 2 corresponds to the standard protein molecular weight marker with the respective molecular weight in kDa. (C) SDS-PAGE analysis of the proteins bound to the surface of Ag_2S nanoparticles (lane 2). Lane 1 shows the standard protein molecular weight marker with the respective molecular weight in kDa.*

The lane Ex in Figure 4.26A corresponds to the extracellular protein profile of *Actinobacter* spp. grown in the presence of iron salts while the lane C in Figure 4.26A corresponds to the extracellular protein profile of *Actinobacter* spp. grown in the absence of iron salts. Induction of the two new proteins with molecular weights of 120 kDa and 55 kDa are observed after the addition of iron salt to *Actinobacter* spp (shown by arrows in lane Ex) culture medium. Lane M in Figure 4.26A corresponds to the molecular weight marker (the respective molecular weights in kDa from top to bottom are as follows: 97.4, 68, 43, 29 and 20). The proteins present on the surface of iron sulfide nanoparticles were also analyzed by SDS-PAGE. Figure 4.26B shows SDS-PAGE analysis of the proteins present on the surface of iron sulfide nanoparticles. SDS-PAGE analysis of the surface bound proteins reveal the presence of five different surface bound proteins with the respective molecular weights of 15, 16, 20, 23 and 27 kDa (lane 1 in Figure 4.26B). Lane 2 in Figure 4.26B indicates the standard molecular weight marker with the respective molecular weights. The association of these proteins with the nanoparticles surface indicates that they can be responsible for the stabilization of maghaemite nanoparticles. However, the exact function of these proteins is yet to be understood completely at this stage of time.

Figure 4.26C shows SDS-PAGE analysis of the proteins isolated from the surface of Ag_2S nanoparticles. The presence of five different proteins was observed on 12% resolving gel with the respective molecular weights of 97, 32, 30, 16 and 12 kDa. Lane 1 in Figure 4.26C represents the standard molecular weight marker, while lane 2 in Figure 4.26 shows the well separated capping proteins isolated from the surface of Ag_2S nanoparticles. These proteins could be silver binding proteins which bind to silver ions to nullify the toxic effects exerted by silver ions. However, some of these proteins can act as capping agents, which binds and stabilize Ag_2S nanoparticles. One of these proteins with a molecular weight of 16 kDa is also found to be associated with the surface of iron sulfide nanoparticles. Presence of this protein on the surface of iron sulfide as well as silver sulfide nanoparticles indicate that it, could have an affinity for sulfide moiety present in both, iron sulfide and silver sulfide nanoparticles.

4.3.5 Discussion

This section of the chapter explains the biological synthesis of iron sulfide has silver sulfide nanoparticles using *Actinobacter* spp. Iron sulfide nanoparticles are composed of the mixture of greigite (Fe_3S_4) and pyrite (FeS_2) as indicated by XRD analysis. Magnetic measurements revealed the superparamagnetic nature of iron sulfide nanoparticles at low temperature. Biogenic silver sulfide nanoparticles exhibited quantum confinement within the nanoparticles. *Actinobacter* spp. exhibited high specificity towards iron and silver salts, since sulfide nanoparticles are synthesized only in the presence of respective sulfate salts of iron and silver i.e. $FeSO_4$ and Ag_2SO_4. In the absence of exogenous sulfate salts synthesis of iron sulfide and silver sulfide was not observed. Biochemical insight into metal sulfide formation by *Actinobacter* spp. indicated that sulfide formation proceeds via the sulfate reduction pathway. Presence of the gene for PAPS reductase has been conclusively shown to be present in *Actinobacter* spp. by PCR amplification and DNA sequencing of the gene. Presence of chromate ions inhibited the formation of iron sulfide and silver sulfide nanoparticles further indicating that the synthesis of iron sulfide or silver sulfide occurs via sulfate reduction pathway. Extracellular protein profile of *Actinobacter* spp. grown in the presence and absence of iron salts indicated the formation of two new proteins with the molecular weights of 120 kDa and 55 kDa, which are probably synthesized in response to the iron salt stress. Five different proteins are found to be associated with the surface of iron sulfide nanoparticles with the respective molecular weights of 15, 16, 20, 23 and 27 kDa. Analysis of proteins associated with the surface of silver sulfide nanoparticles also showed the presence of five different proteins with the respective molecular weights of 97, 32, 30, 16 and 12 kDa.

4.4 Conclusions

This chapter describes the biological synthesis of metal sulfide nanoparticles using bacteria. Nanocrystalline semiconductor sulfides such as CdS, ZnS and PbS were synthesized using a Gram negative aerobic bacterium *Pseudomonas aeruginosa*. All the semiconductor sulfide nanocrystallites were in quantum size regime and exhibited the phenomenon of quantum confinement. All the biogenic sulfide nanocrystallites showed excellent optical properties that are comparable to the semiconductor sulfide nanocrystallites synthesized by chemical means. In comparison with the earlier reports on the biosynthesis of CdS, ZnS and PbS, the formation of semiconductor sulfide nanoparticles was rapid using *P.aeruginosa*. The biosynthesis of semiconductor metal sulfide occurs by the assimilatory sulfate reduction pathway operating in *P.aeruginosa* cells. Two genes encoding the two enzymes namely PAPS reductase and SIR reductase responsible for the reduction of sulfate have been identified, cloned and overexpressed in *E. coli* cells. All the semiconductor sulfide nanocrystallites synthesized by overexpressed sulfate reductase genes show excellent optical properties with the size quantization effect. Another part of this chapter describes the biological synthesis of iron sulfide and silver sulfide nanoparticles using a Gram positive aerobic bacterium *Actinobacter* spp. Biogenic iron sulfide nanoparticle was found to consist of mixed phases, greigite (Fe_3S_4) and pyrite (FeS_2). Iron sulfide nanoparticles exhibited superparamagnetic behavior at low temperature with overall weak magnetic response. Silver sulfide nanoparticles synthesized by *Actinobacter* spp. show of monoclinic α- Ag_2S crystal structure. The large blue shift in the absorption and emission spectra obtained from silver sulfide nanoparticles were observed indicating the phenomenon of quantum confinement. Biochemical insight of metal sulfide nanoparticles by *Actinobacter* spp. indicated that sulfate reductases are responsible for the formation of respective sulfide nanoparticles. These metal sulfide nanoparticles were found to be stabilized by different capping proteins, which are present on the surface of sulfide nanoparticles.

4.5 References

[1] (a) Brown, K. R., Lidar, D. A., Whaley, K., B. *Phys Rev A* **2002**, *65*, 101103. (b) Alivisatos, P. A. *Science* **1996**, *271*, 933.

[2] (a) Alivisatos, P. A. *et al*. *Nature* **1996**, *382*, 609. (b) Klostranec, J. M., Chan, C. W. *Adv. Mater*. **2006**, *18*, 1953.

[3] (a) Duan, X., *et al*. *Nature* **2003**, *425*, 274. (b) Liu, Y. K., *et al*. *Appl. Phys. Lett*. **2004**, *85*, 3241. (c) Zhang, J. Jiang, F., Zhang, L. *J. Phys. Chem. B* **2004**, *108*, 7002. (d) Bruss, L. E. *Appl. Phys. A*. **1991**, *53*, 465. (e) Duan, X. F., Huang, Y., Agarwal, R., Lieber, C. M. *Nature* **2003**, *421*, 241.

[4] Yanagida, S. *et al*, *Bull. Chem. Soc. Jpn*. **1995,** *681*, 811.

[5] Magafas, L., Anagnostopoulos, A. N., Antomopoulos, J. G. *Phys*. *Stat*. *Sol*. **1989**, *111*, K175.

[6] Cao, G. Nanostructures and Nanomaterials: Synthesis, Properties and Applications. 2004, Imperial College Press, London.

[7] (a) Mitchell, J. W. *J. Imaging Sci. Technol.* **1998**, *42*, 215. (b) Motte, L., Pileni, M. P. *J. Phys. Chem. B* **1998**, *102*, 4104.

[8] Roucoux, A., Schulz, J., Patin, H. *Chem. Rev*., **2002**, *102*, 3757.

[9] (a) Hu, J., Li, L.-S., Yang ,W., Manna, L., Wang, L.-W., Alivisatos, A. P. *Science*, **2001**, *292*, 2060. (b) Peng, X., *et al*. *Nature*, **2000**, *404*, 59.

[10] (a) Bonneau, P. R., Jarris Jr. R. R., Kaner, R. B. *Nature*, **1991**, *349*, 510. (b) Ferrer, I. J., Caballero, F., Delas, H. C., Sarchez, C., *Solid state Comm*. **1994**, *89*, 349.

[11] (a) Quan, X. F., *et al*. *Mater. Sci. Engg. B* **1999**, *64*, 170. (b) Jeong, Y. U., Manthiram, A. *Inorg. Chem.* **2001,** *40,* 73.

[12] Roberts, A. P. *Earth Planet. Sci. Lett*. **1995**, *134*, 227.

[13] (a) El-Sayed, M. A. *Acc. Chem. Res.* **2004,** 37, 326 (b) Kumar, S., Thomas, N. *Small*, **2006**, *2*, 316.

[14] Mann, S. *Biomineralization: Principles and Concepts in Bioinorganic Materials Chemistry* **2001**, Oxford University Press, Oxford.

[15] (a) Dameron, C. T., *et al*. *Nature*, **1989**, *338*, 596. (b) Williams, P., Keshavartz-Moore, E., Dunnill, P., *Enz. Microb. Technol*. **1996**, *19*,208.

[16] Kowshik, M. *et al*, *Biotechnol. Bioengg*. **2002**, *78*, 583.

[17] Kowshik, M., Vogel, W., Urban, J., Kulkarni, S. K., Paknikar, K. M. *Adv. Mater.* **2002**, *14*, 815.

[18] Reese, N. R., Winge, D. R. *J. Biol. Chem.* **1988**, *263*, 12832.

[19] Ahmad A., *et al. J. Am. Chem. Soc.* **2002**, *124*, 12108.

[20] Lovley, D. R. *Ann. Rev. Microbiol.* **1993**, *47*, 263.

[21] Labrenz, M., *et al. Science*, **2000,** *290*, 174.

[22] Sharma, P. K., Balkwill, D. L., Frankel, A., Vairavamurthy, M. A., *Appl. Environ. Microbiol.* **2000**, *66*, 3083.

[23] Holmes, J. D. *et al*, *Microbiol.* **1997**, *143*, 2521.

[24] Sweeney, R. Y., *et al. Chem. Biol.* **2004**, *11*, 1553.

[25] (a) Bae, W. O., Abdullah, R., Henderson, D. V., Mehra, R. K. *Bichem. Biophys. Res. Commun.* **1997**, *237*, 16. (b) Bae, W., Mehra, R. K. J. *Inorg. Biochem*. **1998**, *69*, 33. (c) Bae, W. O., Abdullah, R., Mehra, R. K. *Chemosphere* **1998**, *37*, 363.

[26] Yu, W. W., Wang, Y. A., Peng, X.,G. *Chem. Mater*. **2003**, *15*, 4300.

[27] (a) Shenton, W., Douglas, T., Young, M., Stubbs, G., Mann, S. *Adv. Mater*. **1999**, *11,* 253. (b) Mao, C. B., *et al. Proc. Natl. Acad. Sci.* USA. **2003**, *100*, 6946.

[28] (a) Flynn, C. E., *et al. J. Mater. Chem.* 2003, 13, 2414. (d) Mao, C. B., *et al. Science*, **2004**, *303*, 213.

[29] Shenton, W., Dietmar, P., Sleytr, U. B., Mann, S. *Nature*, **1997**, *389*, 585.

[30] Klaus, T., Joerger, R., Olsson, E., Granqvist, C. G. *Proc. Nat. Acad. Sci.* **1999**, *96*, 3611.

[31] (a) Farina, M. D., Esquivel, M. S., Lins de Barros, H. G. P. *Nature*, **1990**, *343*, 256. (b) Mann, S., Sparks, N. H. C., Frankel, R. B., Bazylinski, D. A., Jannasch, F. W. *Nature*, **1990**, *343*, 258.

[32] (a) Marius, M. S., James, P. A. B., Bahaj, A. J., Smallman D. J., *J. Mag. Mag. Mater.*, **2005**, *293*, 567. (b) Watson, J. H. P., Ellwood, D. C., Soper, A. K., Charnock, J. *J. Mag. Mag.Mater.*, **2003**, *203*, 69. (c) Bazylinski, D. A., Frankel, R. B., Garratt-Reed, A. J., Mann, S. *Iron Biominerals (eds Frankel, R. B. and Blackmore, R. P.)*, **2000**, *239*, Plennum Press, New York.

[33] Gateway® Technology instruction manual http://www.invitrogen.com/content.cfm

[34] The XRD pattern was indexed with reference to wurtzite and cubic phase of CdS

from *JCPDS – International Center for Diffraction Data PCPDFWIN* version 1.30, 41-1049.

[35] Alivisatos, A. P. *J. Phys. Chem.* **1996**, *100*, 13226

[36] (a) Henglein, A. *Chem. Rev*. **1989**, *89*, 1861. (b) Weller, S., *et al.* Chem. Phys. Lett. 1986, 124, 557. (c) Lippens, P. E., Lannoo, M. *Phys. Rev. B* **1989**, *39*, 10935.

[37]. Nanda, J., Kuruvilla, A., Sarma, D. D. *Phys. Rev. B* **1999**, *59*, 7473.

[38] The XRD pattern was indexed with reference to wurtzite and sphalerite phases of ZnS from *JCPDS – International Center for Diffraction Data PCPDFWIN* version 1.30, 10-0434 and 05-0566 respectively.

[39] The XRD pattern was indexed with reference to the cubic and galena phase of PbS from *JCPDS – International Center for Diffraction Data PCPDFWIN* version 1.30, 05-0592 and 03-0614 respectively.

[40] Bick, J. A., Dennis, J. J., Zilstra, G. J., Nowack, J., Leustrk, T. *Appl. Environ Microbiol.* **2000**, *182*, 135.

[41] The XRD pattern was indexed with reference to the crystal structure of iron sulfide from *JCPDS – International Center for Diffraction Data PCPDFWIN* version 1.30, 16-0713 for greigite (Fe_3S_4) and 42-1340 for pyrite (FeS_2).

[42] Rath, R. K., Subramanian, S., Pradeep, T. *J. Colloid. Interface Sci.* **2000**, *229*, 82.

[43] Ivanov, S. A. O.; Kuznetsoba, O. B. *Phys. Rev. E*, **2001**, *64*, 41405.

[44] The XRD pattern was indexed with reference to α- Ag_2S phaseof silver sulfide from *JCPDS – International Center for Diffraction Data PCPDFWIN* version 1.30, 14-0072.

[45] (a) Pileni, M. P., Motte, L., Billoudet, F., Mahrt, J., Willig, F. *Mater. Lett* **1997**, *31*, 255. (b) Schaaff, T. G., Rodinone, A. J. *J. Phys. Chem. B* **2003**, *107*, 10416.

[46] (a) Mote, L., Billoudet, F., Pileni, M. P. *J. Phys. Chem.* 1995, 99, 16425. (b) Brelle, M. C., Zang, J. Z., Nguyen, N., Mehra, R. K. *J. Phys. Chem. A* 1999, 103, 10194.

[47] Smith, W. L., Gadd, G. M. *J. Appl. Microbiol.* **2000**, *88*, 983.

Chapter V

Bacterial Synthesis of Anisotropic Metal Nanoparticles

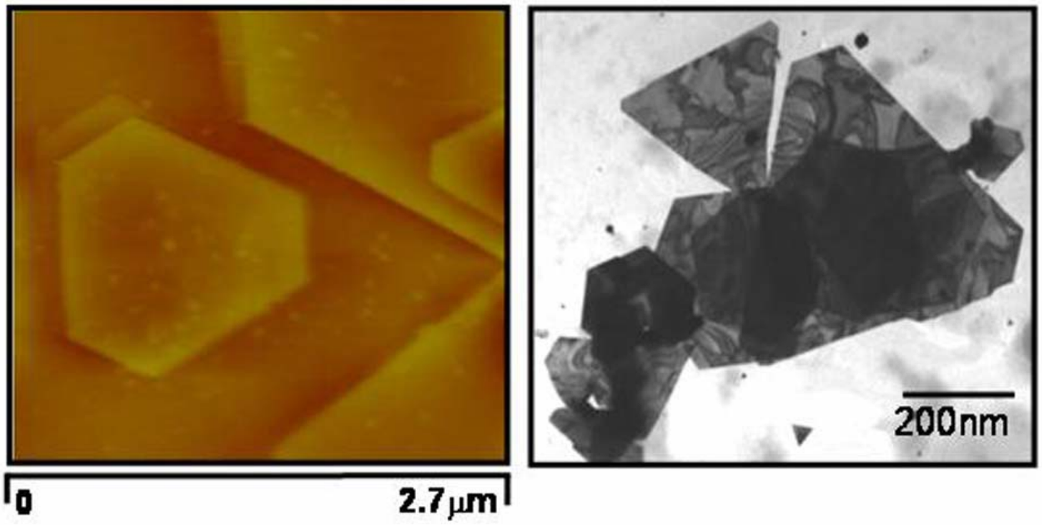

This chapter describes the biological synthesis of anisotropic metal nanoparticles using the bacterium *Actinobacter* spp. The biogenic gold nanoparticles thus synthesized show triangular and hexagonal morphology with edge lengths between 0.05 μm to 2 μm. The surface topography of triangular gold particles indicated that they are ~ 9 nm thick. These flat particles show a strong absorption in the near infra-red (NIR) region of the electromagnetic spectrum. Individual nanotriangles were found to be single crystals highly oriented in the (111) crystallographic direction. Biochemical analysis of the process revealed that the reduction of gold ions is mediated by the bacterial cytochrome oxidase. Capping proteins associated with the surface of the triangular particles act as a shape directing agent along the bacterial cell wall. *Actinobacter* spp. exerts high specificity towards gold ions while fabricating triangular and hexagonal gold particles. Silver nanoparticles synthesized using *Actinobacter* spp. also result in flat, plate–like structures. Biological reduction of silver ions is possibly mediated by silver binding proteins that bind and stabilize silver nanoparticles.

Part of the work presented in this chapter has been communicated in the following journals: (1) Bharde, A. A., Sastry M. Nature nanotechnol.(2007). (2) Bharde A. A., Sastry M. Small (2007).

5.1 Introduction

Nanotechnology is a steadily evolving branch of science which constitutes the development of synthesis protocols for nanomaterials over a range of chemical compositions, sizes and certain shapes. Much of the interest in this direction is fuelled by the unusual physical and chemical properties exhibited by nanomaterials, which are quite different from their bulk counterparts [1]. Progress in the synthesis methods for metallic nanoparticles is of substantial interest due to their remarkable optoelectronic properties [2]. Most of the research carried in this direction enjoys the success of chemical protocols developed in due time.

Due to their optoelectronic properties, metal nanoparticles with different size and shapes find potential applications in catalysis [3], biosensing [4], and optics [5]. Gold and silver nanoparticles are studied in great detail in this regard. In anticipation of such unique properties and potential applications various shapes such as nanorods/nanowires [6], nanoplates [7], nanocubes [8], nanodumbbells [9], nanodiscs [10], nanotapes/nanobelts [11] nanotetrapods/arrows [12] and numerous other shapes [13] have been synthesized successfully by various chemical or physical methods. Out of myriad shapes of nanoparticles that have been synthesized until now, history of the synthesis of anisotropic gold nanoparticles goes back to 1951, when gold nanotriangles were synthesized via citrate reduction method by Turkevich *et al* [14].

Though chemical methods continue to be investigated for the shape and size controlled synthesis of metal nanoparticles, they can be hazardous to the environment due to the use of toxic chemicals. Research over the past few years has demonstrated that utilization of biological organisms has been emerging as a novel method for the synthesis noble metal nanoparticles, which can be preferred over the existing chemical and physical methods. Synthesis of metallic nanoparticles has been shown to occur in many biological systems such as bacteria, fungi and plants or plant extracts. Bacteria from different habitats and nutritional modes have been employed for the synthesis of gold and silver nanoparticles either intracellularly or extracellularly. Beveridge and coworkers have demonstrated the deposition of gold nanoparticles inside the bacterial cells [15]. Reduction of Ag^+ ions and subsequent formation of silver nanoparticles within the periplasmic space of the bacterium *Pseudomonas stutzeri* AG 259 was shown by Klause-

Joerger and coworkers [16]. Impregnating of silver nanoparticles has been shown to occur intracellularly or on the surface of *E.coli* in a controlled manner [17].

Reductive precipitation of gold nanoparticles has been demonstrated in dissimilatory iron reducing bacteria and archaea [18]. Recently it has been shown that Au and Pt nanoparticles can be synthesized by a cyanobacterial species *Plectonema borianum* [19]. Similarly, Pradeep *et al* have synthesized silver, gold and their alloy nanoparticles using a *Lactobacillus* strain commonly found in buttermilk [20]. Equivalent to chemical synthesis, the formation of gold nanoparticles with uniform size has been shown to occur extracellularly by *Thermomonospora* sp. [21]. Accelerated synthesis of palladium nanoparticles has been demonstrated with the sulfate reducing bacterium *Desulfovibrio desulfuricans* NCIMB-8703 [22].

Reports from this laboratory have recently demonstrated the synthesis of gold and silver nanoparticles by exploring eukaryotic organisms like fungi as living nanofactories. The acidophilic fungus *Verticillium sp*. was shown to synthesize gold nanoparticles by intracellular reduction of gold chloride [23]. This fungus also synthesized silver nanoparticles that were subsequently immobilized in the mycelial matrix. Exposure of the fungus *Fusarium oxysporum* to gold and silver ions was also found to result in the synthesis of gold and silver nanoparticles respectively [24]. However, contrary to *Verticillium* sp. metal nanoparticles synthesized by *F. oxysporum* were deposited extracellularly in the surrounding. Furthermore, extracellular biosynthesis of bimetallic gold and silver alloy nanoparticles was demonstrated using the fungus *F. oxysporum* [25].

While microorganisms continue to be explored for the biosynthesis of nanoparticles, use of plants or plant extracts has emerged as a novel alternative to micro-organisms based biological synthesis of metallic nanoparticles. Similar to microorganisms, plants have also been used for remediation of heavy metal ions from contaminated soil and water [26]. Jose-Yakaman and coworkers have shown that live alfalfa plants when supplied with Au^{3+} ions, reduce them to metallic Au and absorb them resulting in the internal formation of gold nanoparticles [27]. Jose-Yacaman's group has also extended this approach to demonstrate the synthesis and assembly of silver nanoparticles within alfalfa shoots by supplying the plants with Ag^{+} ions [28]. Alternative to existing methods, a novel plant extract based method for the synthesis of metallic nanoparticles has been designed from this laboratory. Aqueous extracts from plants like geranium (*Pelargonium graveolens*), and neem (*Azadirachta Indica*) have been used for the synthesis of gold, silver and gold-silver bimetallic nanoparticles [29]. Recently, it has been demonstrated that plant extracts can also be used for the shape directed synthesis of prism shaped gold nanoparticles [30].

Though, ample work has been done on the biological synthesis of metallic nanoparticles, biological methods are still not competent with chemical methodologies which offer size and shape control during the synthesis of nanoparticles. Nevertheless there are few reports that describe the shape controlled biological synthesis of gold nanoparticles [30]. Biological methods for size and shape controlled synthesis of metal nanoparticles still remains an unexplored and underexploited alternative due to the lack of the information on the biomolecular mechanism responsible for the process of nanoparticles formation, where biomolecules that lead to the formation of anisotropic structures have remained unidentified yet.

In this chapter, one–step synthesis of gold and silver nanoparticles has been described using the bacterium *Actinobacter spp.* Further, the biological mechanism underlying the process of synthesis of metal nanoparticles has been discussed. Although there are plenty of reports describing the biological synthesis of gold nanoparticles, none of them have so far discussed about the biomolecules responsible for the reduction of gold ions leading to the formation of gold nanoparticles. Lovley *et al* have postulated the presence of an enzyme Au (III) reductase in anaerobic Fe (III) reducing bacteria [18]. Beveridge and coworker have predicted the possibility of the involvement of mannuronic and guluronic acids present in exopolymeric substances from *Pseudomonas aeruginosa* biofilms during the bioreduction of gold [31]. In yet another study, Beveridge and coworkers have demonstrated extra and intracellular precipitation of colloidal gold by *Bacillus subtilis*. In this report it was proposed that gold ions were first stabilized by the bacteria as soluble organo-gold complexes within the cell structure with subsequent precipitation of colloidal form only when a critical gold concentration was reached [32]. Recently, synthesis of triangular gold colloids has been observed in cyanobacterial species *Plectonema boryanum* UTEX 485. However, the biosynthesis process was very slow requiring long incubation period of more than 30 days. Also, the yield of triangular particles was very poor and the biochemical mechanism of nanoparticles formation have not been described [19].

Previously unaddressed questions in the biological synthesis of metal nanoparticles, such as identification of biological reducing agents and shape controlling agents have been discussed in this chapter. Though plant extract based methods can compete with existing chemical methods for the synthesis of gold nanoparticles, they are not explored in detail from the biological mechanism point of view. *Actinobacter* spp. was chosen for this work since it was capable of reducing both gold and silver ions, subsequently converting them in elemental form yielding anisotropic nanostructures.

Outline of the present work:

This chapter demonstrates the biological synthesis of flat triangular gold particles and plate–like silver nanoparticles using the bacterium *Actinobacter spp*. when exposed to gold and silver ions respectively. The first part of this chapter describes the synthesis of flat triangular and hexagonal gold nanoparticles by *Actinobacter* spp. Here, the biochemical processes responsible for the reduction of gold ions during the bacterial metabolism have been discussed. Further the role of the bacterial cell surface i. e. cell wall components in the nucleation and growth of triangular gold nanoparticles has been demonstrated. The second part of the chapter describes synthesis of silver nanoparticles by the bacterium *Actinobacter* spp. Though, the synthesis of gold and silver nanoparticles was demonstrated using different bacteria and fungi, control over morphology of gold or silver nanoparticles could not be achieved till now using micro-organisms as a means of silver and gold nanoparticles synthesis. Further, the method described in this chapter could be advantageous over existing biological processes since, it offers shape directed synthesis of gold nanoparticles with an insight into the biochemical mechanism responsible for the synthesis of gold and silver nanoparticles.

5.2 Biosynthesis of flat triangular gold nanoparticles using *Actinobacter* spp.

5.2.1 Experimental details

Actinobacter spp. was revived from mother culture and grown in nutrient medium as described in previous chapters. Briefly, *Actinobacter* spp. was grown overnight in 2 ml preinoculum at 37 °C. Then, preinoculum was used as a seed culture for propagation of the bacterium in 100 ml of LB in 500 ml Erlenmeyer flask. The flask was incubated at 37 °C on shaker (200 rpm) for 48 h. After 48 h of incubation, the bacterium enters into the stationary phase of growth cycle. At this stage the bacterial biomass was separated from the culture medium (LB) by centrifugation at 5,000 rpm (2560 X *g*). The supernatant containing spent medium was decanted and pellet constituting of bacterial biomass was washed twice with sterilized saline (0.85% NaCl) followed by deionised water to remove the media components associated with the biomass.

For the synthesis of gold nanotriangles, 0.5 g of bacterial biomass was suspended in 100 ml aqueous solution of autoclaved 10^{-3} M $HAuCl_4$ in 500 ml Erlenmeyer flask. The reaction was carried out for the period of 24 h. Bacterioform gold nanoparticles were then isolated from the reaction medium by centrifugation at 3,000 rpm. The supernatant containing gold nanoparticles was then characterized by Transmission electron microscopy (TEM), Scanning electron microscopy (SEM), UV-vis- NIR spectroscopy, Energy dispersive X-ray analysis (EDX), Atomic force microscopy (AFM) and X-ray diffraction (XRD).

To illustrate the role of cytochrome oxidase in reduction of gold ions, cytochrome oxidase activity assay was done in the presence of cytochrome oxidase inhibitors. In a typical experiment, bacterial cells were reacted with gold ions as discussed above, in the presence of 0.02 % of sodium azide (Na_3N), which is a known inhibitor of cytochrome oxidase enzyme. To further illustrate the role of cytochrome oxidase in the reduction of gold ions, 1 μg/ml of purified, commercial cytochrome oxidase (Sigma chemicals) was reacted with 10 ml of 10^{-3} M $HAuCl_4$. Additionally, the same reaction was carried out in the presence of Na_3N and 1-Aminobenzotriazole (ABT), a specific, non toxic inhibitor of cytochrome oxidase. The role of bacterial cell wall components in shape directed synthesis of gold nanotriangles was demonstrated by hydrolyzing the cell wall of bacteria by reacting bacterial cells with lysozyme. *Actinobacter* spp. was incubated for 3 h with 0.5 mg/ml of lysozyme (sigma chemicals) in 10mM sodium phosphate buffer (pH 7.2). Bacterial spheroplasts (bacterial cells devoid of cell wall) so obtained were again treated with gold ions for the reduction and subsequent formation of nanoparticles.

Further, bacterial cell wall components were isolated by centrifugation from lysozyme treated bacterial cells. First, bacterial spheroplasts were separated by centrifugation at 10,000 rpm (9279 X *g*) for 10 minutes. The supernatant containing disrupted cell wall components were again centrifuged at 20,000 rpm (37118 X *g*) for 60 minutes and the pellet containing cell wall components were stored at -20 °C for further experiments. Additionally, formation of gold nanoparticles was carried out in 0.01% of Tween 80, which is a non ionic detergent used for cell membrane disruption or to increase cell membrane fluidity and permeability. This experiment was performed to demonstrate the role of bacterial cell wall in shape directed synthesis of gold nanoparticles. Analysis of proteins, bound on the surface of gold nanotriangles was performed by polyacrylamide gel electrophoresis under denaturing conditions (SDS-PAGE). Briefly, gold nanotriangles were separated from bacteria by centrifugation at 3,000 rpm for five minutes and the resulting pellet of gold nanotriangles was washed thoroughly with deionised water before redissolving in minimum volume of deionised water. Next, the solution of nanotriangles was sonicated for a brief period, followed by heating at 60 °C for five minutes. The resulting solution of gold nanotriangles was then centrifuged at 20,000 rpm (37118 X *g*) for 15 minutes. The supernatant was collected and stored at -20 °C for further experiments. For protein analysis, 20 μl of supernatant was loaded on 12 % gel (12 % T and 2.7 % C). Protein bands were visualized by silver staining procedure.

To analyze the role of surface bound proteins in shape control of the nanoparticles, protein solution was reacted with 10^{-3} M $HAuCl_4$ in the presence and absence of cytochrome oxidase (sigma chemicals). The reaction was carried out for 6 h at 37 °C under agitation. To elucidate the ionic specificity exhibited by the bacterium towards the synthesis of gold nanotriangles, the bacterium was reacted separately with Au^+ ions and $HAuCl_4$ (Au^{3+}). In this case, the reaction was carried out for the period of about 72 h on a shaker. Gold nanoparticles synthesized by reaction between *Actinobacter spp*. and Au^+ are characterized by TEM and UV-vis spectroscopy. To illustrate the specificity of the surface bound proteins towards Au^{3+} ions in comparison with Au^+ ions, they were reacted with Au^+ ions in the presence of cytochrome oxidase. Control experiments were performed to check the credibility of shape directed biosynthesis of gold nanotriangles in which, 100 ml of 10^{-3} M $HAuCl_4$ and AuCl was incubated in the absence of bacterial biomass under the conditions described above.

5.2.2. Electron microscopic analysis

Figure 5.1 shows representative TEM images of bacterially reduced gold ion solution after 24 h of the reaction. Fairly large number of triangular and hexagonal nanoparticles is observed in all images shown in the Figure 5.1. More than 50 % of total population of gold nanoparticles is either triangular or hexagonal in shape. This population of gold nanotriangles is quite significant in comparison with earlier reports [33]. The triangular particles have edge length between 0.05 μm to 2 μm and often show truncated vertices similar to that observed for silver and gold nanotriangles previously reported [34].

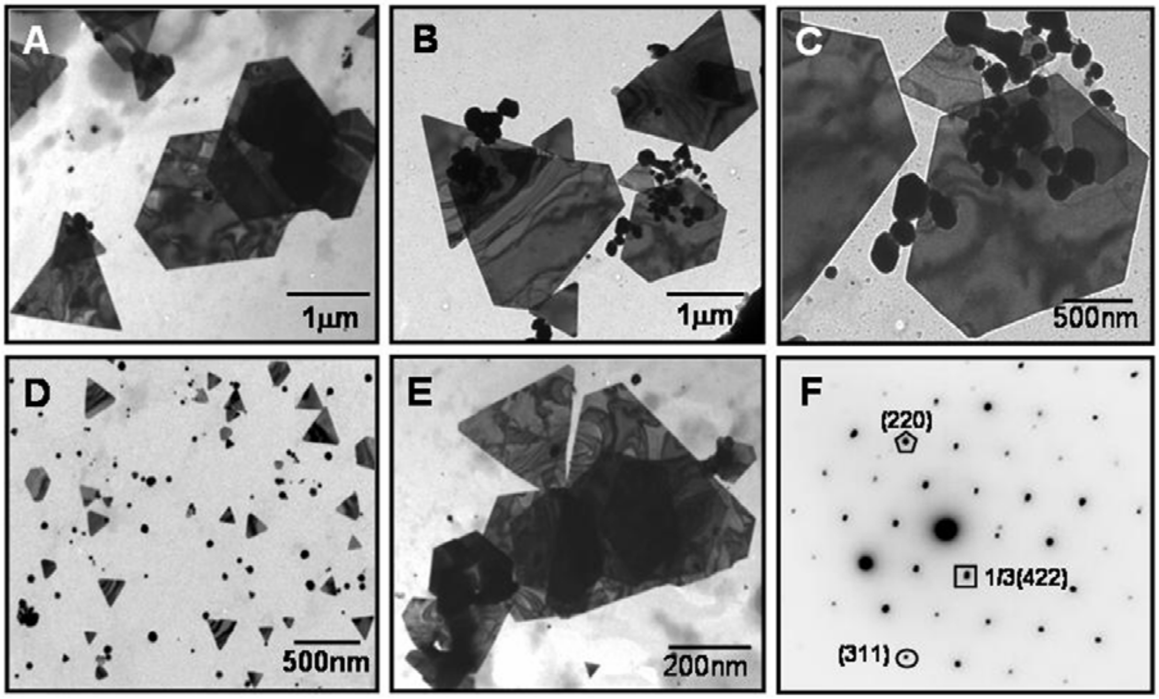

***Figure 5.1** Representative Transmission electron microscopic images (A-D) of gold nanotriangles synthesized by the reaction between gold ions and Actinobacter spp. after 24 h of incubation. (E) Purified nanotriangles after centrifugation and redispersion in water. (F) SAED pattern obtained from a single triangular nanoparticle showing the representative lattice planes.*

The contrast and mosaic pattern observed on the surface of triangular and hexagonal nanoparticles (Figure 5.1B, C and E) can be attributed to stresses in the particles arising due to buckling of the extremely thin nanosheets. The total population of flat gold nanoparticles could be enhanced by repetitive centrifugation (3000 rpm), washing and redispersion. Figure 5.1E shows a representative TEM image of such purified gold nanotriangles. The selected area diffraction (SAED) pattern obtained from a single triangular particle clearly indicates that it is single crystalline (Figure 5.1F). The hexagonal nature of the diffraction spots is a clear indication that the triangular gold nanoprisms are highly (111) oriented with the top normal to the electron beam. Diffraction spots could be indexed on the basis of face centered cubic structure of gold [35]. The presence of the forbidden reflection (1/3{422}) indicates that the gold triangle could have faults along (111) direction of the crystal [36].

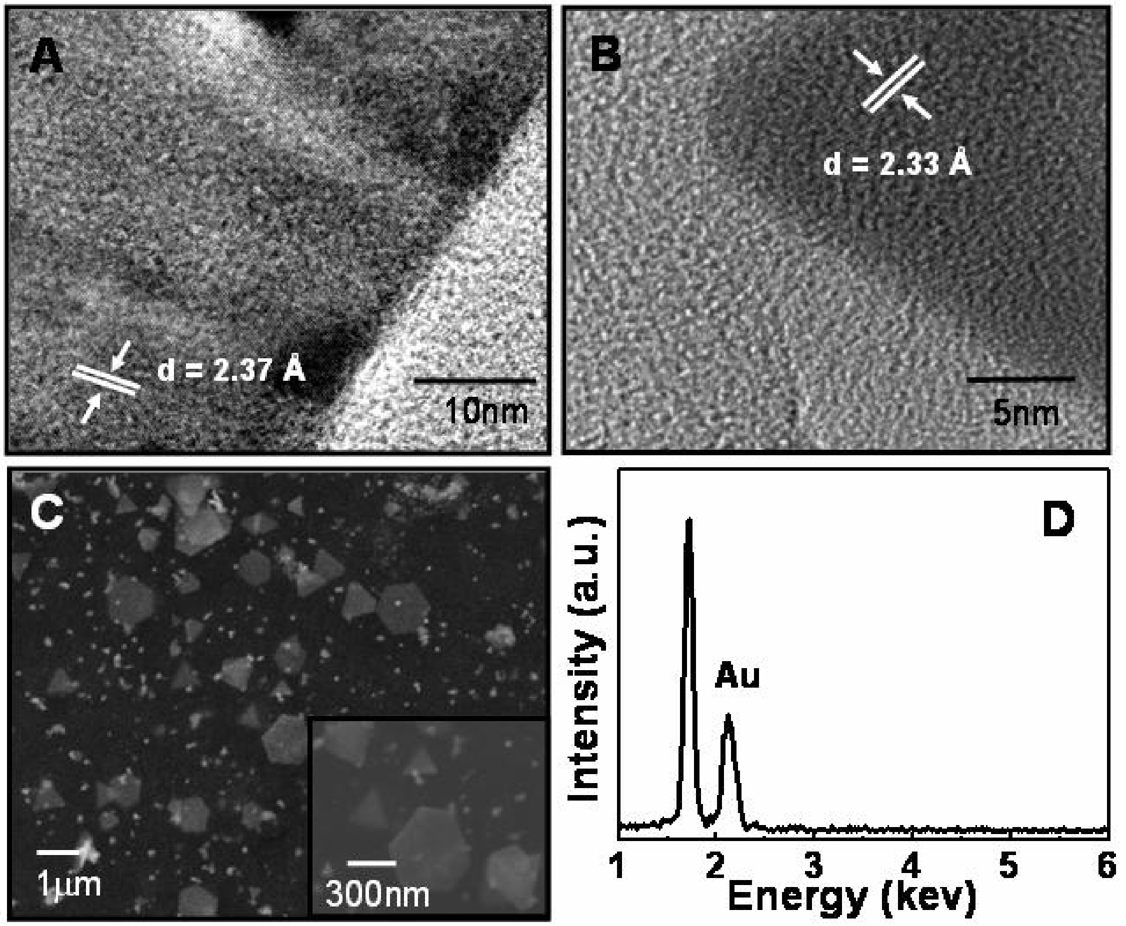

Figure 5.2 *HRTEM analysis of a triangular (A) and hexagonal (B) gold nanoparticle. Orientation of the particles in (111) crystal plane is clearly observed. The lattice spacing of 2.33 Å is a clear indication of the growth of these nanoparticles in (111) direction. SEM images of triangular and hexagonal gold nanoparticles (C). The inset in (C) shows SEM image after purification of triangular and hexagonal particles. (D) EDAX analysis of bacterially synthesized gold particles, indicating the presence of strong gold signal.*

Figure 5.2 shows the high resolution TEM (HRTEM) and SEM images of the triangular and hexagonal gold nanoparticle. HRTEM images were recorded from the edges of triangular (image A, Figure 5.2) and hexagonal (image A, Figure 5.2) gold particles respectively. Though the lattice planes could be imaged at particular instances, in general the lattices were quite unstable under the incident electron beam of the microscope and could not be recorded properly resulting in images with poor contrast and clarity. The lattice spacings obtained from the captured images were c.a. 2.37 Å and 2.33 Å for hexagonal and triangular gold particle respectively (Figure 5.2A & B). These lattice spacings could not be indexed on the basis of any of the reported lattice planes for gold. However, it is nearer to the standard value of 2.355 Å for FCC gold (111) lattice plane. Since these flat gold particles are observed to be oriented in (111) direction it may imply that the observed triangular or hexagonal particles are not lying perpendicular to the incident electron beam but could be tilted slightly while imaging. SEM images of bacterially synthesized gold nanoparticles (Figure 5.2C) indicate the presence of flat triangular and hexagonal particles. A large number of triangular and hexagonal nanoparticles were observed indicating their high population. With the nanoparticles, proteinacious organic mater from bacterial origin is also visible in the image, which could not be removed even after repetitive centrifugation and washing (inset Figure 5.2C). As observed in TEM, triangular and hexagonal nanoparticles varied in edge length between 0.2 μm to 2 μm. EDAX analysis (Figure 5.2 D) of the solution cast film of gold nanotriangles on Si (111) surface show strong Au signal arising from gold nanoparticles, along with silicon signal originating from the substrate on which sample was prepared.

5.2.3 Atomic force microscopy (AFM) measurements

Figure 5.3 shows the AFM images of the triangular and hexagonal gold particles. Images were obtained from solution casted film of gold particles on Si (111) surface in tapping mode. Figure 5.3A shows AFM image of a well separated triangular gold particle with the edge length of ~ 500 nm. Three dimensional image of this triangular gold particle indicates that it is buckled inwards from the edges. This could be due to the stresses in the particles that might arise because of extreme thin nature of the particles. Along with triangular gold particle, stack of large triangular and hexagonal particles is also observed in image A. Figure 5.3 B and C shows topographical images of large triangular and well separated hexagonal gold particle. The respective surface topographic plots obtained from a triangular and hexagonal particles shown in the image B and C are presented in image E and F, Figure 5.3 and indicate that the triangular and hexagonal gold particles have a thickness of 9 nm and 18 nm respectively.

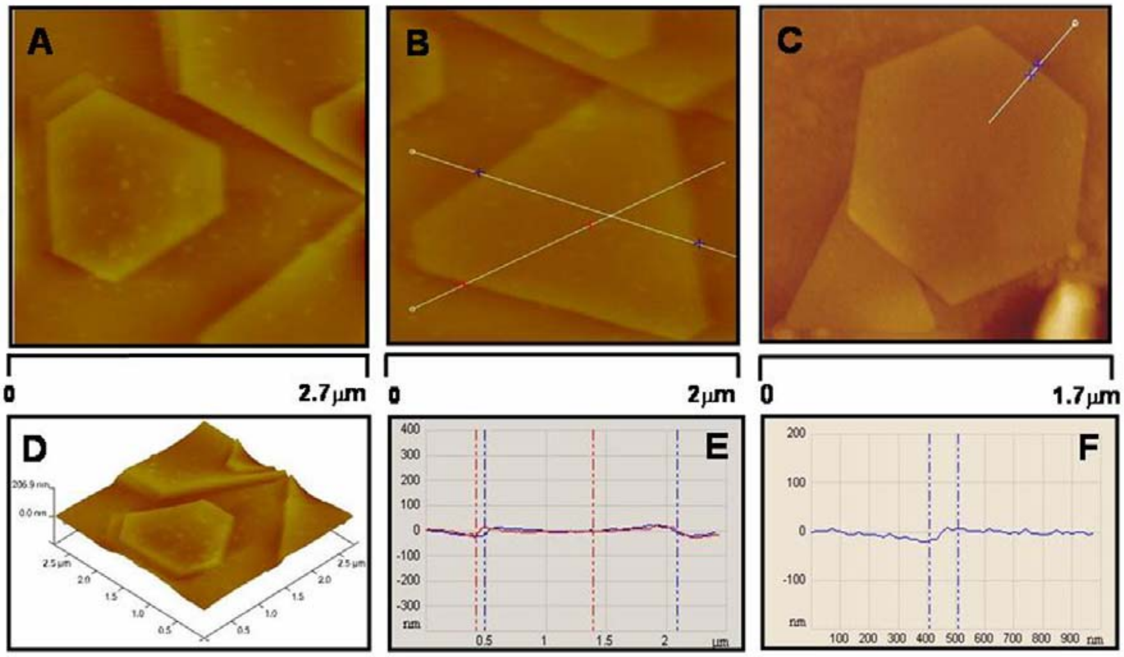

Figure 5.3 *AFM images of triangular (A-B) and hexagonal (C) gold particles. (D) 3- D image of a triangular gold particle, shown in image A indicates that the particle tend to buckle from its edges giving it concave appearance. Graph in (E) and (F) indicates line profile (topographical height) of triangular and hexagonal gold particles shown in image B and C respectively.*

AFM analysis performed on the number of triangular and hexagonal gold particles show that their thickness varied from 9 nm to 24nm. Presence of the proteinacious matrix is observed on the surface of triangular and hexagonal gold nanoparticles similar to SEM images, indicating that they are strongly associated with the nanoparticles surface.

5.2.4 UV-vis-NIR spectroscopic analysis

On visual inspection, it is observed that by mixing aqueous 10^{-3} M $HAuCl_4$ with *Actinobacter* spp. biomass, the originally yellow colour of the solution turned to yellowish brown that gradually faded and turned into brick red indicating the formation of gold particles. The UV-vis spectrum of triangular and hexagonal gold particles synthesized by *Actinobacter* spp. at 37 °C is shown in Figure 5.4 A. UV-vis analysis of bacterially synthesized gold nanoparticles indicated the presence of a surface plasmon resonance band at 540 nm after 3h of reaction (curve 1, Figure 5.4A). The surface plasmon resonance band recorded after 3 h of reaction shows weak absorbance at 540 nm, which gradually red shifts to 580 nm and increases in intensity with time (curves 2-5, Figure 5.4A). As reaction proceeds, this SPR band is accompanied by an increase in absorption in the near infrared region (NIR) of the electromagnetic spectrum (curves 2-5, Figure 5.4A).

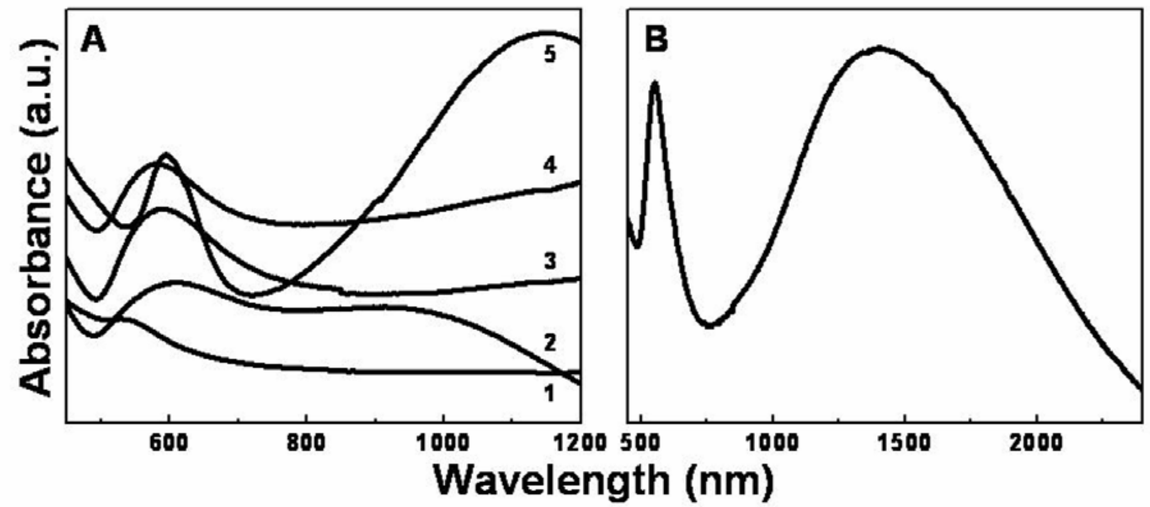

Figure 5.4 *(A) UV-vis spectra recorded as a function of time of reaction between Actinobacter spp. and aqueous gold (III) ions; curves 1 to 5 correspond to spectra recorded after 3, 6, 12, 18 and 24h of reaction. (B) UV-vis-NIR spectrum corresponding to solution cast film of gold nanotriangles on quartz substrate showing the absorption in near infrared region.*

The absorption band observed at 580 nm is due to the transverse component of the SPR band originating from the out-of-plane plasmon vibrations in the triangular and hexagonal gold particles. Thus UV-vis spectra show two SPR bands corresponding to transverse and longitudinal axis of the nanoparticle [2d]. These time-dependent features observed in the UV-vis spectra shown in Figure 5.4 A are characteristic of either formation of spherical gold nanoparticles that aggregate with time [37], formation of anisotropic particles whose aspect ratio increases with time [38, 2d] or a combination of both processes. From the TEM images of *Actinobacter* reduced gold nanoparticles, where large percentage of triangular gold particles were observed with hardly any signs of aggregated particles, it can be concluded that the large NIR absorption observed in the corresponding UV-vis-NIR spectra is clearly due to the highly anisotropic nature of gold nanoparticles.

After 24 h of the reaction, all the gold (III) ions are reduced to triangular and hexagonal gold particles (curve 5, Figure 5.4A). The corresponding UV-vis spectrum indicates that, transverse SPR band at lower region does not increase in intensity in comparison with the spectra corresponding to 12 and 18 h. However, the longitudinal component of UV-vis spectra corresponding to 24 h shows enhanced absorption most probably suggesting the presence of large number of anisotropic nanoparticles in the solution (curves 3-5, Figure 5.4A).

Figure 5.4B shows the UV-vis-NIR spectrum corresponding to the solution casted film of triangular gold particles on a quartz substrate. This spectrum clearly shows a large absorption in NIR region with maxima centered at 1500 nm. The observed large red shift in the spectrum recorded after 24 h of reaction could be due to the change in dielectric environment of gold triangle on forming a dry film from an aqueous solution phase [39].

5.2.5 X-ray diffraction analysis

Figure 5.5 shows the XRD pattern recorded from biogenic gold nanoparticles obtained 24 h after reaction.

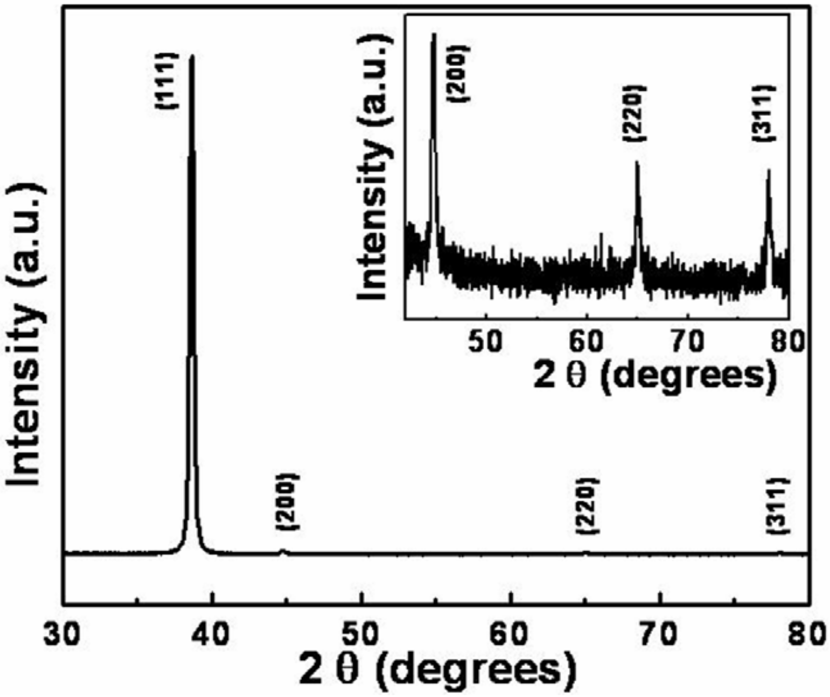

Figure 5.5 *X-ray diffraction analysis of gold nanoparticles synthesized using Actinobacter spp. by reduction of gold (III) ions. The intense Bragg reflection arising from gold particles indicates that they are highly oriented in the direction of (111) lattice planes. Inset in figure shows the weak intensity of Bragg reflections arising from other sets of lattice plane respectively. All the Bragg reflections could be indexed on the basis of FCC gold.*

The XRD pattern recorded from the solution caste film of *Actinobacter* spp. reduced gold nanoparticles on a glass substrate shows a very intense Bragg reflection at 38.6 degree. This reflection corresponds to (111) crystal lattice of gold. However, with this very intense Bragg reflection other extremely weak reflections arising at 44.8, 64.8 and 78.1

degrees are also observed (the inset in Figure 5.5). These reflections could be indexed to (200), (220) and (311) set of lattice planes for FCC gold. The intense Bragg reflection corresponding to (111) set of lattice planes and negligible intensities of Bragg reflection arising from other corresponding lattice planes indicates that the gold particles synthesized by *Actinobacter* spp. are highly oriented in (111) direction. This observation is well supported by the conclusions drawn from TEM and SAED analysis. The corresponding *d* values for the respective crystal planes are as follows: 2.37 (111), 2.04 (200), 1.45 (220), 1.25 (311) [35].

5.2.6 FTIR spectroscopy and agarose gel electrophoresis analysis

Figure 5.6A shows the FTIR spectrum recorded from purified, powdered triangular gold particles synthesized by the reduction of gold ions using *Actinobacter* spp. FTIR analysis was carried out to illustrate the association of proteins with gold particles.

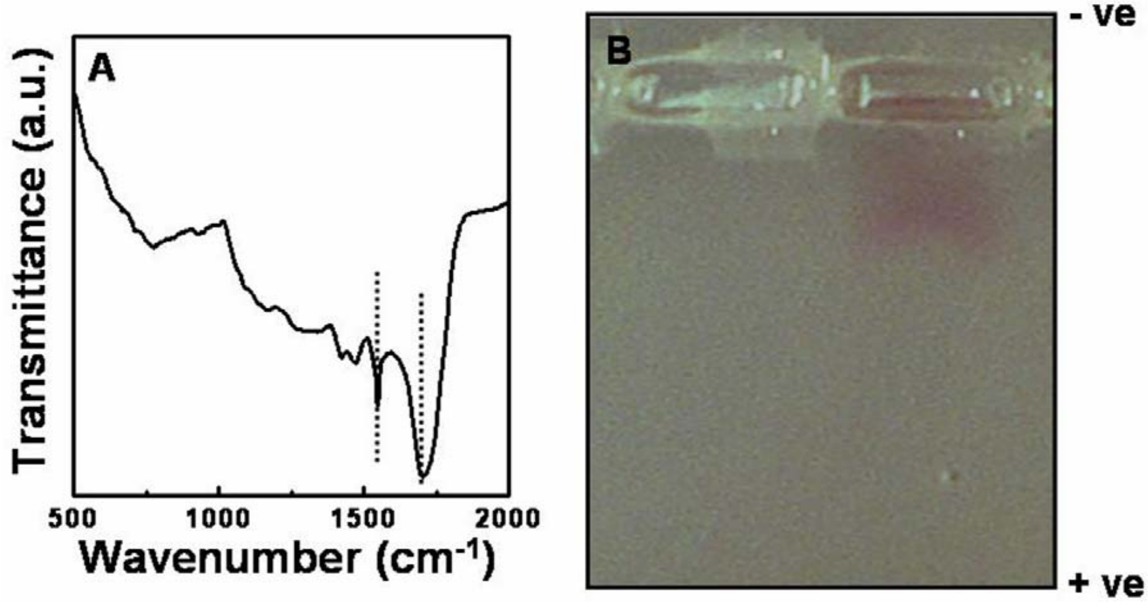

Figure 5.6 *(A) FTIR spectrum obtained from purified triangular gold particles indicating the presence of amide bond vibrations. Presence of amide I and amide II vibrational bands indicates that proteins are associated with the nanoparticles and are shown by dotted lines. (B) Agarose gel electrophoresis pattern of purified triangular gold particles in 0.8% agarose gel. Migration of nanoparticles towards anode indicates that they have negative charge on their surface.*

The spectral analysis does not indicate the presence of any intense peak in the fingerprint region of organic molecules. However, two sharp peaks are observed in the region, where amide bonds show absorption. The presence of sharp vibration band at 1650 cm $^{-1}$ and at 1540 cm $^{-1}$ can be attributed to amide II and amide I bands arising due to the peptide (amide) bonds present in proteins. Presence of amide vibration bands indicates the association of protein/s with gold nanoparticles that could be responsible for the stabilization of nanoparticles [24a].

Figure 5.6B shows the agarose gel electrophoresis pattern of triangular gold particles purified by repetitive centrifugation and washing. Migration of nanoparticles towards the anode indicates the negative charge present on the surface of nanoparticles. The charge on the surface of the nanoparticles could be a consequence of surface bound proteins or unreduced chloroaurate ions present on the surface of gold nanoparticles.

5.2.7 Specificity of gold ions in the formation of triangular and hexagonal gold particles

Formation of flat triangular and hexagonal gold particles was observed when aqueous Au^{3+} ions ($HAuCl_4$) were reacted with *Actinobacter* spp. To assess the role of ionic specificity of gold in the formation of triangular and hexagonal gold particles, *Actinobacter* spp. was reacted with Au^+ ions (AuCl) under the similar experimental conditions as described for the reaction between *Actinobacter* spp. and $HAuCl_4$. After mixing of Au^+ ions with *Actinobacter* spp. and subsequent incubation for 24 h, no change in the colour of reaction solution was observed visually. Subsequent incubation for another 48 h led to the formation of gold nanoparticles as indicated by deep purple colour of reaction mixture. The slower reduction of Au^+ ions and subsequent formation of gold nanoparticles could be attributed to the low solubility of Au^+ in water.

The TEM analysis of gold nanoparticles synthesized by reduction of Au^+ ions using *Actinobacter* spp. after 72 h of reaction is shown in Figure 5.7 A and B. Unlike the reaction between $HAuCl_4$ and *Actinobacter* spp. presence of triangular and hexagonal or any other kind of flat structure was not observed in this case. TEM images indicate the presence of aggregates of nanoparticles with irregular morphology and dimensions of 50 to 200 nm. (Figure 5.7A & B). SAED analysis obtained from gold nanoparticles shown in Figure 5.7 B indicated the presence of well-defined ring diffraction pattern that was indexed on the basis of FCC crystal structure of gold (Figure 5.7C). The UV-vis spectrum recorded from the aqueous solution of gold nanoparticles synthesized by reaction between Au^+ ions and *Actinobacter* spp. shows the presence of SPR band at 580 nm (Figure 5.7D). Red shift in the SPR band could be due to the small degree of aggregation associated with individual gold nanoparticles. As observed previously, the UV-vis spectrum does not show any additional SPR band.

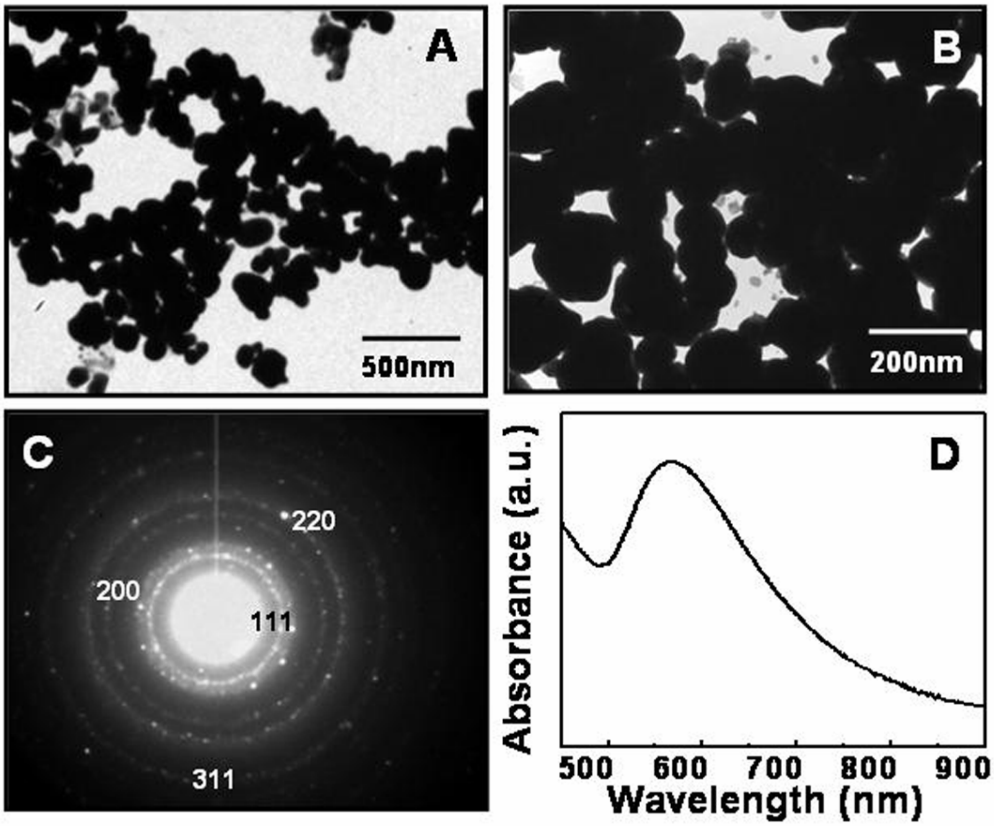

Figure 5.7 *TEM analysis of gold nanoparticles synthesized by reduction of Au$^+$ ions using Actinobacter spp. (A and B). Irregularly shaped aggregates of gold nanoparticles are observed. SAED pattern shows the crystalline nature of gold nanoparticles with respective crystal planes. (C). UV-vis spectrum obtained from gold nanoparticles shown in images A and B indicating the presence of SPR band at 580 nm (D).*

The TEM and UV-vis spectroscopic analysis indicated that the specificity of *Actinobacter spp*. towards precursor gold salt is the deciding factor for the synthesis of triangular and hexagonal gold particles. The reaction between Au^{3+} ions and *Actinobacter* spp. led to the formation of flat triangular and hexagonal gold nanoparticles, while reduction of Au$^+$ ions by the same bacterium could not result in the synthesis of anisotropic nanostructure of gold. This result indicates that, there is some degree of specificity in the selection of gold ions by *Actinobacter* spp. Reduction of Au^{3+} and Au$^+$ ions by *Actinobacter* spp. shows that gold ions are possibly reduced with the common reducing agent from the bacterial origin. However, there is a likelihood of the presence of the specific nucleation site on the bacterial surface or presence of some kind of protein/s that guide the formation of triangular or hexagonal gold nanoparticles. There is also a possibility of the presence of strong electrostatic interaction between bacterial surface and Au^{3+} ions against Au^{+} ions. Thus, the TEM and UV-vis analysis indicates that the formation of triangular and hexagonal gold nanoparticles is specific to the aqueous Au^{3+} ions.

5.2.8 Biochemical basis of gold ion reduction and the formation of triangular gold nanoparticles

Biosynthesis of inorganic nanostructures is relatively a new field of interest due to its enormous potential for materials synthesis. However, in biological synthesis of nanoparticles much remains to be understood in terms of biochemical mechanism that defines the biosynthetic process. Although, there are plenty of reports on biosynthesis of metallic nanoparticles like gold and silver, none of the report so far has explained the biochemical mechanism underlying the process. Beveridge and co-workers have suggested the presence of specific biomolecules on the surface of bacteria, which could be responsible for the precipitation and nucleation of colloidal gold [31, 32]. Also, Lovley and coworkers have indicated the presence of specific metal ion reductases in metal reducing bacteria [40]. It has been postulated that, the bacterial cell surface can be an ideal site for metal precipitation and nucleation, due to the electrostatic interaction between bacterial cell surface, which contain many charged molecules and metal ions. Based on the inherent metal-binding capacity of bacteria, Beveridge and Murray [41] proposed a two step mechanism for the development of metal colloids in association with the bacterial cells. The first step involves a stoichiometric interaction between metal ions in aqueous solution and the cell's reactive chemical groups. Once bound, in second step, these metals reduce activation energy barriers to nucleation by providing sites where strong surface chemical interactions can take place and more soluble components can be deposited [42]. In spite of these suggestions and hypotheses, no systematic attempt has been made till date to elucidate the mechanistic aspects of biological synthesis of metal nanoparticles at the biochemical level.

Biological synthesis of triangular gold particles by *Actinobacter* spp. seems to occur in at least three discrete steps. In the first step chloroaurate ions are reduced to metallic gold followed by nucleation at specific site on cell wall in the second step. In the last step various proteins lead the morphologically controlled growth of nanoparticles in the formation of flat structures. Since gold nanoparticles are synthesized extracellularly or in close association with the external bacterial cell surface, biological reducing agent is thought be present on the cell surface, either on the cell wall or in the cell membrane of bacteria. A number of experiments described below indicate that gold ion reduction is mediated by cytochrome oxidase, an integral enzyme of the bacterial electron transfer chain, which catalyses the transfer of electrons to oxygen. Further, the bacterial cell wall components appear to play an important role in the formation of triangular gold particles since they provide nucleation site for the precipitation of the reduced metal, while various proteins appears to regulate the morphology of reduced metallic gold particles.

5.2.8.1 Reduction of gold ions by cytochrome oxidase

Cytochrome oxidase is an integral part of all the electron transfer processes in which the molecular oxygen acts as a terminal electron acceptor. This enzyme is present in all aerobic organisms and shows enormous variation from species to species [43]. To determine the role of cytochrome oxidase in the reduction of gold ions by *Actinobacter* spp., reaction was carried out in the presence of cytochrome oxidase inhibitors.

The reaction between *Actinobacter* spp. and gold ions is carried out in a similar way as described earlier for the synthesis of gold nanoparticles; except that the reaction was carried out in the presence of 0.02% sodium azide (Na_3N). Visual observation shows no change in the originally yellow colour of the reaction medium indicating that gold ions are not reduced ever after 96 h of reaction. This observation suggests that cytochrome oxidase could be involved in the transfer of electrons to gold ions and the process is inhibited by the presence of sodium azide. To further confer the reduction of gold ions by cytochrome oxidase, reduction of gold ions was carried out by commercial cytochrome oxidase (sigma chemicals). When chloroaurate ions were reacted with cytochrome oxidase under continuous mixing conditions, pale yellow colour of the reaction mixture changed to deep pink within 6 h of the incubation.

Representative TEM images obtained from the reaction mixture of cytochrome oxidase and chloroaurate ions shows the presence of dense population of spherical gold nanoparticles. The high magnification image of these nanoparticles shows the linear arrangement of nanoparticles and hence indicates a fair degree of ordering (Figure 5.8A).

Gold nanoparticles synthesized by cytochrome oxidase shows overall dimensions in between 5 to 10 nm (Figure 5.8A). SAED pattern obtained from these gold nanoparticles indicate the presence of well defined diffraction spots, which show excellent match with FCC structure of gold (Figure 5.8C). The UV-vis spectroscopic analysis of the aqueous solution of gold nanoparticles shows a sharp SPR band at 575 nm (Figure 5.8D).

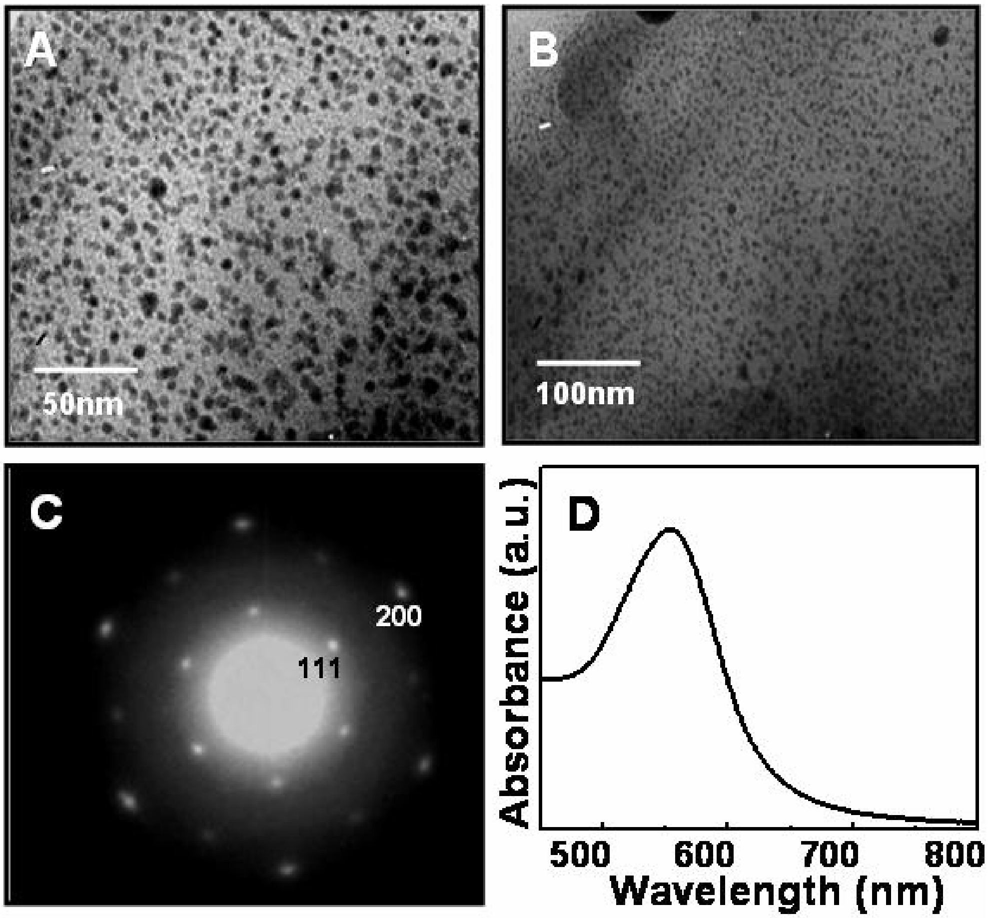

Figure 5.8 *Representative TEM images of gold nanoparticles synthesized by the reduction of chloroaurate ions using commercial cytochrome oxidase enzyme (A and B). SAED pattern of gold nanoparticles indicates their crystalline nature (C). (D) UV-vis spectrum of gold nanoparticles synthesized by cytochrome oxidase indicates the presence of SPR band at 575 nm.*

However, when the reduction of gold ions by commercial cytochrome oxidase was carried out in the presence of 0.02% Na_3N and 100 μg/ml of 1-Aminobenzotriazole (ABT), the formation of gold nanoparticles was not observed even after 72 h of reaction as indicated by the unaltered pale yellow colour of the reaction mixture.

5.2.8.2 Role of bacterial cell wall in the nucleation and controlled growth of nanoparticles

Experiments described above illustrate the role of cytochrome oxidase in the biological reduction of gold ions. Once reduced, smaller gold nanoparticles nucleate and further grow to result in the flat structures. Under the experimental conditions described here for extracellular synthesis of flat gold nanoparticles by *Actinobacter* spp. bacterial cell wall can act as an ideal nucleation center for the growth of flat gold particles. This could be either due to the electrostatic interaction between cell wall and chloroaurate ions or the presence of different functional groups that interact with chloroaurate ions. Following experimental results describe the role of *Actinobacter* cell wall in morphology controlled synthesis of gold nanoparticles. To determine the role of *Actinobacter* spp. cell

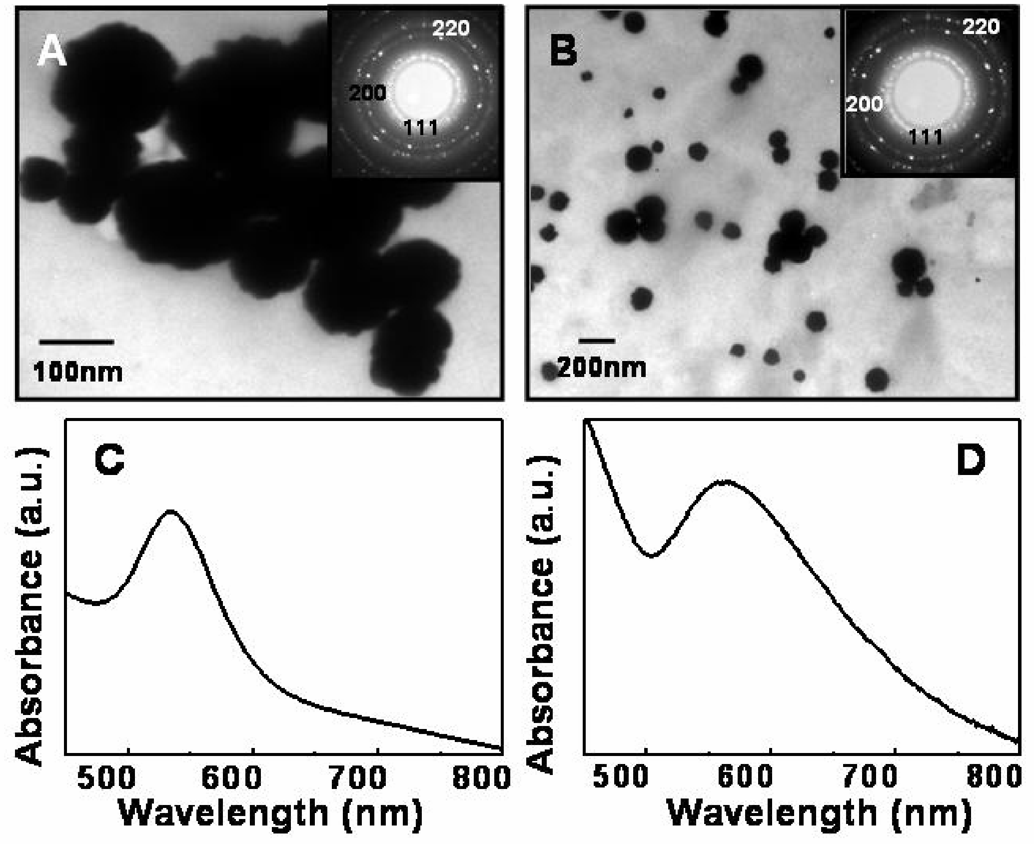

Figure 5.9 *TEM images of gold nanoparticles synthesized by Actinobacter spp. spheroplasts and Actinobacter spp. cells treated with Tween 80 (A & B). Insets in A & B are SAED pattern of gold nanoparticles with respective crystal planes,(B) Respective UV-vis spectrum of gold nanoparticles synthesized by Actinobacter spheroplasts (C) and cells treated with Tween 80 (D) showing the SPR band of gold nanoparticles.*

wall in the shape control of gold nanoparticles, the reduction of gold ions was carried out by bacterial cells treated with lysozyme in controlled manner (see experimental section for details). Lysozyme is an enzyme that hydrolyses the cell wall of almost all eubacterial species [44]. Treatment of this enzyme in a controlled manner with bacterial cells can hydrolyze bacterial cell wall without killing the bacterial cells. The resulting cells without or partial cell wall is called as spheroplasts. Formation of speroplasts is a routine practice in many cell biology and molecular biology experiments [45].

When *Actinobacter* spheroplasts were reacted with gold ions for 24 h, formation of gold nanoparticles was observed by the change in the colour of the reaction mixture from pale yellow to deep pink. Figure 5.9 shows the TEM analysis of the aqueous solution of gold ions reduced by *Actinobacter* spp spheroplasts. From TEM images, it was observed that gold nanoparticles tend to form aggregates of 50-150 nm (Figure 5.9A) which are irregularly shaped. SAED pattern obtained from these nanoparticles shows well defined diffraction rings, which correspond to FCC structure of gold (inset in Figure 5.9A). The UV-vis spectrum obtained from the solution of gold nanoparticles indicated the presence of intense SPR band at 550 nm (Figure 5.9C). In another experiment *Actinobacter* spp. was treated with non ionic surfactant Tween 80, which is known to disrupt cell wall of the bacteria and enhances the fluidity of the cell membrane. When *Actinobacter* spp. was reacted with gold ions in the presence of Tween 80, formation of gold nanoparticles occurs within 12 h of incubation as indicated by pink coloration of the reaction mixture. TEM analysis of this solution show the aggregates of gold nanoparticles 50-100 nm in size similar to gold nanoparticles observed in case of *Actinobacter* spp. spheroplasts (Figure 5.9A). However, unlike to *Actinobacter* spp. spheroplasts aggregates observed in this case are more uniform in shape. SAED pattern is consistent with FCC structure of gold (inset in Figure 5.9B). UV-vis spectrum obtained from the aqueous solution of these gold nanoparticles indicates the presence of SPR band at 560 nm (Figure 5.9D). The broad absorption indicates the presence of some degree of aggregation associated with gold nanoparticles.

Thus, TEM images, along with the UV-vis spectroscopic analysis do not show the presence of any flat triangular structure of gold particles as observed with intact *Actinobacter* spp. cells. This result indicates that, for the synthesis of flat gold particles bacterial cell was is essential. Further, in another set of experiments, gold ions were reacted with the cell wall components obtained by treatment of intact *Actinobacter* spp. cells with lysozyme in the presence of cytochrome oxidase. After about 3 h of the reaction, gold nanoparticles were synthesized as indicated by the deep purple colour of the reaction mixture. When the reaction mixture was further incubated for another 3 h, the colour of reaction mixture changed to brick red.

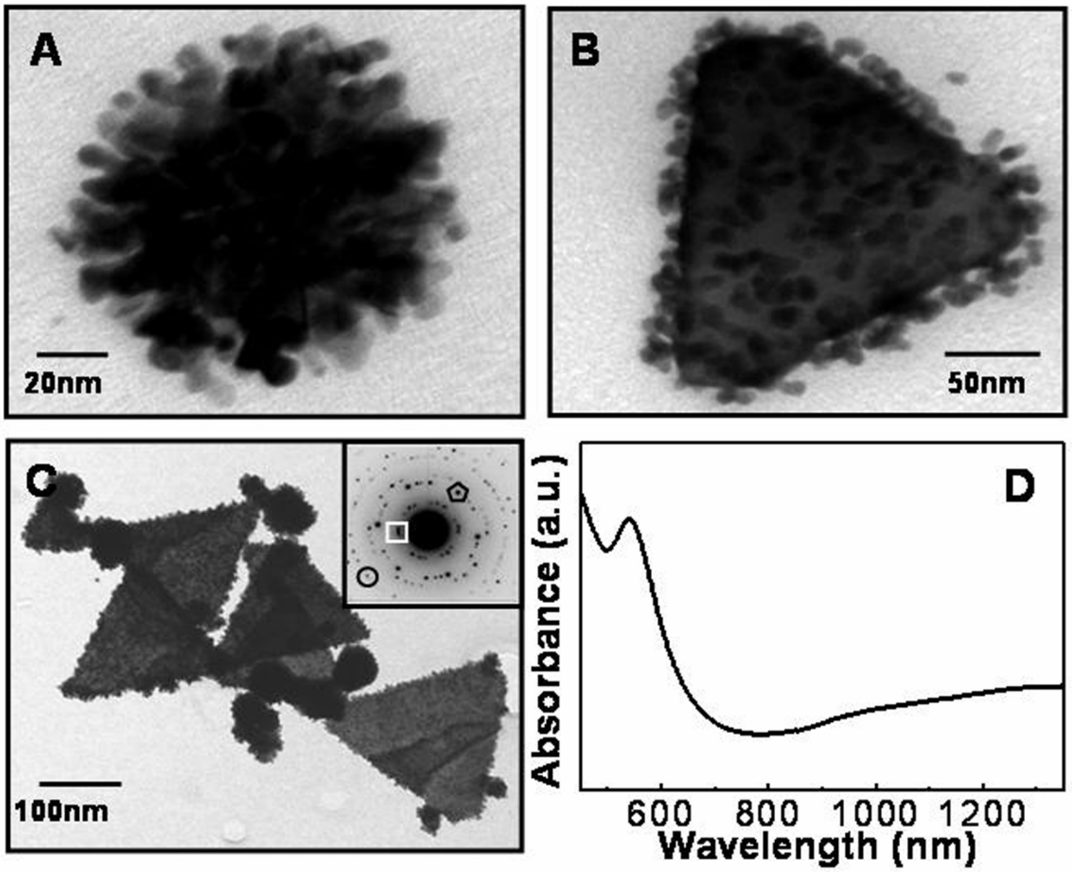

Figure 5.10 *TEM images of gold nanoparticles synthesized by the reaction between gold ions and cytochrome oxidase in the presence of cell wall components obtained after 3 (A) and 6 h (B & C). SAED pattern obtained from triangular particles shown in image C. The respective symbols corresponding to lattice planes are as follows - □ (111), Δ (200), ○ (220) (D) UV-vis-NIR spectrum recorded from aqueous solution of triangular gold particles shown in the TEM image.*

The TEM analysis of this reaction mixture after 3 h and 6 h of the incubation is shown in Figure 5.10 A, B and C respectively. At the initial stage of reaction (Figure 5.10A) spherical gold nanoparticles tend to aggregate on bacterial cell wall, where the growth of small particles eventually occurs leading to the formation of triangular gold particles (Figure 5.10B & C). SEAD pattern obtained from gold nanoparticles shown in TEM images is consistent with the FCC structure of gold (inset in Figure 5.10C). UV-vis spectroscopic analysis of the reaction mixture after 6 h of the incubation shows the presence of well defined SPR band at 560 nm. The SPR band at 560 nm is accompanied with absorption in the NIR region and is due to the longitudinal SPR absorption band (Figure 5.10D). The presence of longitudinal SPR band in UV-vis-NIR spectrum indicates the shape anisotropy in gold nanoparticles. The set of experiments described here indicate that the cell wall of *Actinobacter* spp. is essential for growth of the triangular gold particles. Experimental observations described here are consistent with the theories described in previous reports [41, 42]. Formation of the triangular gold particles by *Actinobacter* spp. is mediated by different reducing and shape directing agents present on bacterial cell surface.

5.2.8.3 Analysis of surface capping proteins

Capping proteins were isolated from the surface of triangular gold particles as discussed in the experimental section. Presence of proteins that stabilizes the triangular gold particles by binding to nanoparticles surface was analyzed by SDS-PAGE. Figure 5.11A shows the electrophoresis pattern of proteins present on the surface of the triangular gold particles under denaturing conditions. Protein analysis indicates the presence of three different well resolved bands on 12% polyacrylamide gels with the molecular weights of 95, 57 and 30 kDa respectively. Synthesis of gold nanoparticles was not observed when these proteins were reacted with gold ions indicating that they are not involved in the reduction of gold ions. However their association with the triangular gold particles suggests that they can be responsible for the stabilization and shape control of triangular gold particles. Formation of triangular gold particles was readily observed when the mixture of surface bound proteins was reacted with Au^{3+} ions in the presence of cytochrome oxidase and incubated for 6 h (Figure 5.11B). However, when the same reaction was carried out in the presence of Au^{+} ions, formation of triangular gold particles was not observed (Figure 5.12D). This observation indicates that the mixture of capping proteins capping proteins with the molecular weight of 95, 57 and 30 kDa might specifically interact with Au^{3+} ions leading to the formation of the triangular gold particles.

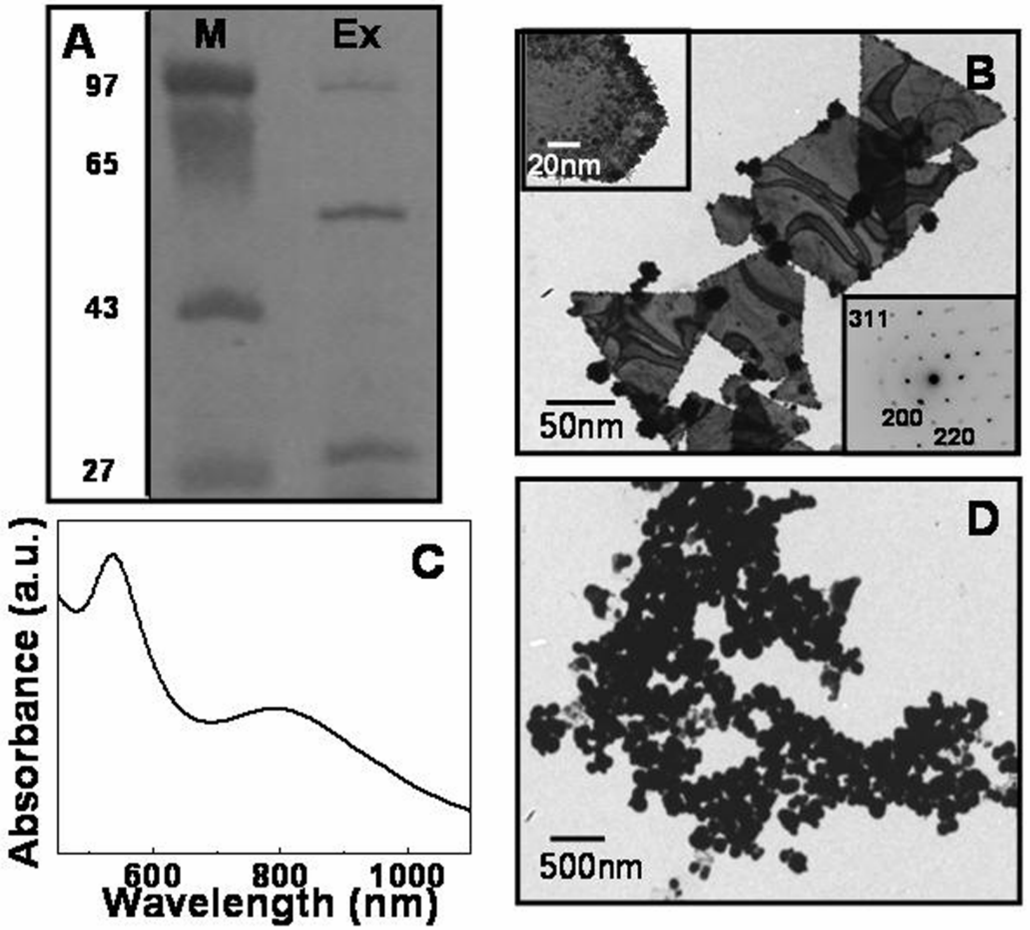

Figure 5.11 *(A) SDS-Page analysis of capping proteins isolated from the surface of triangular gold particles. Three different proteins (marked by arrows) with the molecular weight of 95, 57 and 30 kDa could be resolved on 12% gel (lane Ex in Figure 5.11A). Lane M shows the standard protein molecular weight marker (B) TEM image of gold nanoparticles synthesized by the reduction of* Au^{3+} *ions using cytochrome oxidase in the presence of capping proteins. The inset at upper left side in (B) shows the high magnification image of one of triangular gold particle while inset at lower right side in (B) is corresponding SAED pattern with crystal planes. (C) The UV-vis spectrum of triangular gold particles that correspond to image B. (D) The TEM image of gold nanoparticles obtained by reacting* Au^{+} *ions with cytochrome oxidase in the presence of capping proteins.*

SAED pattern obtained from on of the gold nanoparticles (inset, upper left corner in Figure 5.11B) synthesized by reaction between Au^{3+} ions and cytochrome oxidase in the presence of capping proteins confirms the crystalline nature of gold nanoparticles and the diffraction pattern was indexed on the basis of FCC structure of gold (inset lower right corner in Figure 5.1B). Higher magnification TEM image obtained from one of the hexagonal gold particles indicate that the flat particles are composed of very small particles that assemble in unknown way to form a large triangular or hexagonal particle.

The capping proteins could specifically interact with the Au^{3+} ions in the presence of reducing agent (cytochrome oxidase) possibly providing the site for the nucleation and growth of gold nanoparticles formed by the reduction of Au^{3+} ions. It is also likely that these three proteins associated with the surface of triangular gold particles are present on the cell wall of *Actinobacter* spp. Figure 5.12C shows the UV-vis spectrum obtained from the solution of gold nanoparticles synthesized by the reduction of Au^{3+} ions by cytochrome oxidase in the presence of capping proteins. UV-vis spectrum shows two distinct SPR band corresponding to transverse and longitudinal components. The transverse SPR band shows maximum absorption at 525 nm while the longitudinal SPR band shows maxima at 800 nm.

Thus, based on the various experimental analyses described here, it can be inferred that gold ions are nonspecifically reduced by bacterial cytochrome oxidase irrespective of charge or oxidation state of the precursor ions. However a high degree of ionic specificity is observed in the formation of triangular gold particles. Capping proteins isolated from the surface of triangular nanoparticles directs the formation of triangular gold particles in the presence of biogenic reducing agent (here cytochrome oxidase).

5.2.9 Discussion

This part of the chapter describes biological synthesis of extremely flat triangular and hexagonal gold particles and the biological mechanism responsible for their synthesis. The triangular and hexagonal gold particles synthesized by *Actinobacter* spp. were found to be 0.050 μm-2 μm in the edge length. Each triangular particle acts as a single crystal and is highly oriented in (111) direction as indicated by HRTEM and XRD analysis. AFM analysis indicated that the thickness of triangular and hexagonal gold particles varies in between 9 nm to 24 nm. UV-vis-NIR spectroscopic measurements performed on aqueous solution of the triangular gold particles indicated a strong absorption in the NIR region of the electromagnetic spectrum, which could be attributed to the anisotropic nature of gold nanoparticles. The UV-vis spectroscopic measurements as a function of time indicated that the formation of gold nanoparticles is completed in 24 h. *Actinobacter* spp. shows high specificity towards the synthesis of triangular gold particles with respect to the precursor gold ions. Synthesis of triangular gold particles is observed only when Au^{3+} ions were used as a precursor, while reaction between *Actinobacter* spp. and Au^{+} ions could not result in the formation of anisotropic structure. However, the formation of irregularly shaped aggregates of gold nanoparticles was observed with overall dimensions of 50-200 nm. The biochemical analysis of the reaction indicated that the bacterial cytochrome oxidase is responsible for biological reduction of gold ions. Three proteins with molecular weights of 95, 57 and 30 kDa respectively are found to be associated with the surface of triangular gold particles and are responsible for controlling the shape of gold nanoparticles. The bacterial cell wall also specifically directs the morphology control of gold nanoparticles indicating that capping proteins could be associated with cell wall. The capping proteins could very specifically interact with Au^{3+} leading the formation of triangular gold particles in the presence of cytochrome oxidase. However the possibility of involvement of other proteins and biological molecules in shape control of gold nanoparticles can not be ruled out at this moment and needs further experimentation.

5.3 Biosynthesis of silver nanoparticles by *Actinobacter* spp.

5.3.1 Experimental details

Actinobacter spp. was grown as described previously in section 5.2.1. In a typical experiment, *Actinobacter* spp. was grown in LB medium until the stationary phase of the growth cycle is attained (after 48 h of growth). Bacterial biomass was harvested from the growth medium by centrifugation at 5,000 rpm. About 0.5 g (wet weight) of the pellet containing bacterial cells was washed twice with autoclaved saline and then with deionised water before redispersing in 100 ml of 10^{-3} M aqueous silver nitrate ($AgNO_3$) solution in 500 ml Erlenmeyer flask. The reaction was carried out for 24 h on the shaker (150 rpm) at 37 °C. Bacterially synthesized silver nanoparticles were isolated from reaction mixture by centrifugation at 5000 rpm and characterized by TEM, UV-vis spectroscopy, XRD, and FTIR. Analysis of capping proteins present on the surface of silver nanoparticles was carried out on 12% polyacrylamide gel under denaturing conditions of SDS. Briefly, Silver nanoparticles were isolated from the solution by centrifugation at 10,000 rpm, redispersed in minimum quantity of deionised water containing 8 M urea. The resulting solution was heated for 5 minutes at 60 °C, cooled and centrifuged at 20,000 rpm for 15 minutes. The supernatant was collected and dialyzed extensively against deionised water and stored at -20 ^{O}C for further analysis.

5.3.2 TEM analysis

Figure 5.12 shows TEM images recorded from the drop coated films of silver nanoparticles synthesized by treating aqueous silver ions with *Actinobacter* spp. for 24 h. A large number of flat, plates – like particles were observed with the size range in between 50 to 200 nm. Though TEM images shows presence of flat structures with undefined morphology, some triangular and elongated nanoparticles with a length scale of 50 nm was also observed (Figure 5.12D& E).

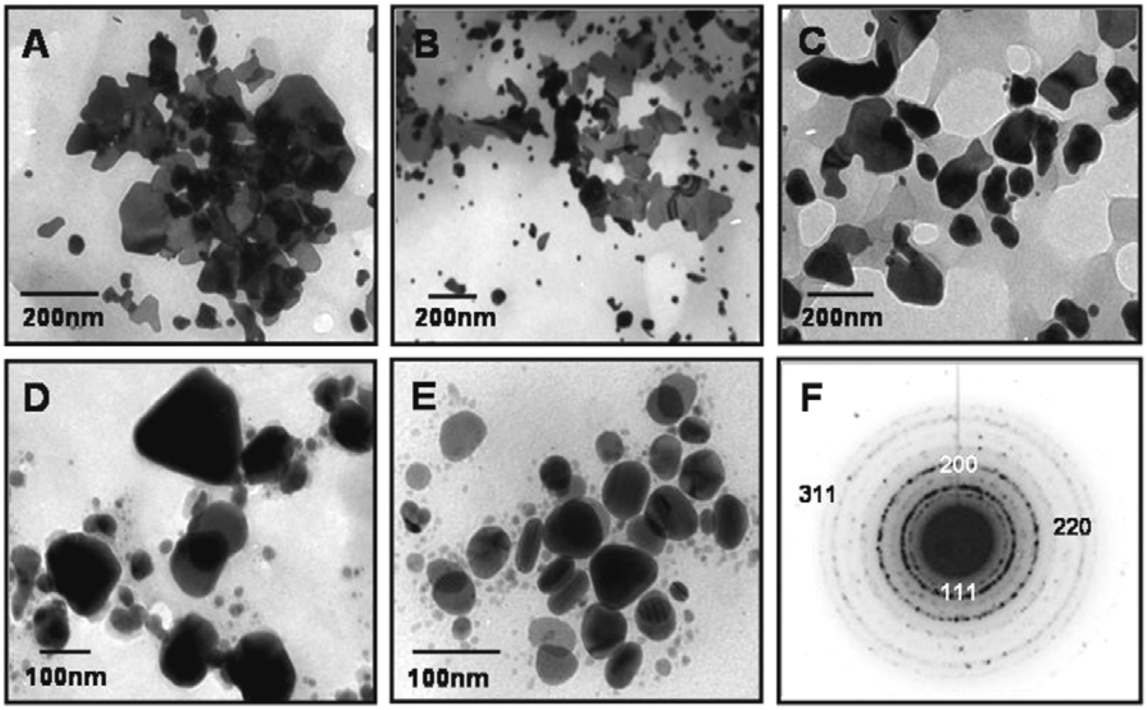

Figure 5.12 *(A – E) TEM images of silver nanoparticles synthesized by the reduction of silver ions using Actinobacter spp. A number of flat, plates – like nanoparticles with irregular morphology are observed along with some elongated and triangular particles (D and E). SAED pattern obtained from silver nanoparticles indicate the presence of strong diffraction rings corresponding to FCC structure of silver (F).*

From higher magnification TEM image it was observed that silver nanoparticles show twin boundaries (Figure 5.12E) indicating the presence of crystal defects in the nanoparticles. As observed with the triangular and hexagonal gold particles, some of flat silver nanoparticles also show contrast on their surface. The contrast observed on the surface of flat silver particles could be a result of stresses on the surface of extremely thin particles (Figure 5.12B). A high degree of aggregation is observed to be associated with the flat silver nanoparticles (Figure 5.12A&B). The nanoparticles seem to be entrapped in a kind of proteinacious matrix, indicating the association of proteins at the surface of silver nanoparticles. SAED pattern obtained from silver nanoparticles is presented in Figure 5.12 F, which indicates well-defined diffraction rings and the diffraction pattern could be indexed on the basis of FCC structure of silver [44].

5.3.3 UV-vis spectroscopic analysis

After the exposure of silver ions to *Actinobacter spp*. the colour of reaction medium changed to yellow during 12 h, which eventually became brown after 24 h of the reaction. The time dependant UV-vis spectra recorded from the aqueous silver nitrate-*Actinobacter* spp. reaction mixture is shown Figure 5.13A.

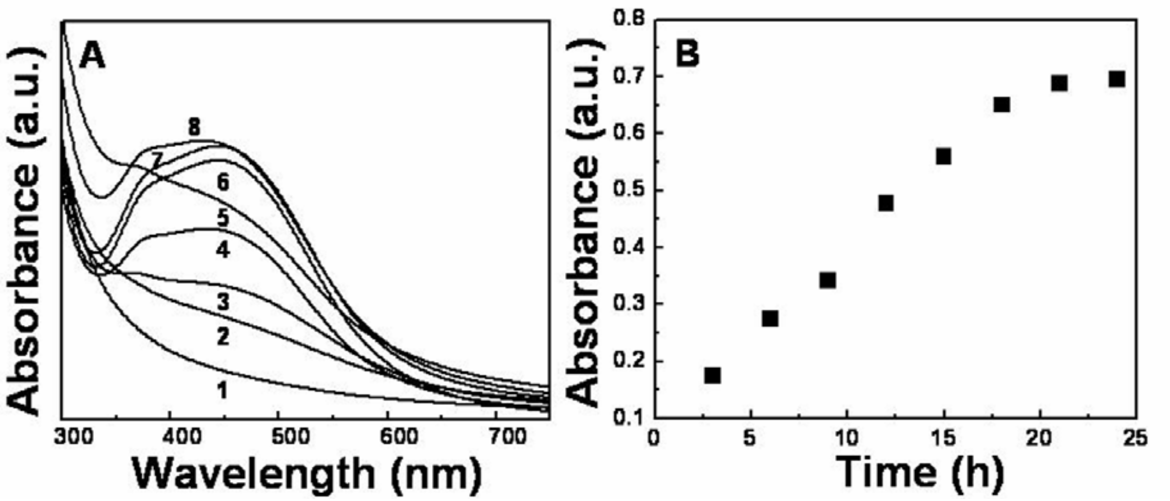

Figure 5.13 *(A) UV-vis spectroscopic measurements performed on silver nanoparticles as a function of time. The spectra were measured after 3, 6, 9, 12, 15, 18, 21 and 24 h of reaction respectively (curves 1-8 corresponding to 3, 6, 9, 12, 15, 18, 21 and 24 h respectively. (B) A plot showing the increase in the maximum absorbance of silver nanoparticles with time.*

The SPR band due to silver nanoparticles occurs at 440 nm after about 6 h of the reaction (curve 2, Figure 5.13A). The SPR band shows blue shift after 9 h of the reaction and is centered at 385 nm, which steadily increases in intensity with time (curve 3, Figure 5.13A). As reaction proceeds, this SPR band is accompanied with a strong absorption at 500 nm, which also gradually increases in the intensity with time (curve 4, Figure 5.13A). The appearance of such an asymmetric peak form could indicate the formation of some anisotropic structures or some degree of aggregation among the nanoparticles. This result is in well agreement with the TEM analysis (Figure 5.12). The peak at 385 nm corresponds to the transverse plasmon vibration in silver nanoparticles whereas peak at 500 nm is due to the excitation of the longitudinal plasmon vibrations of either anisotropic silver nanoparticles or aggregates of spherical silver nanoparticles. The reaction is completed in around 24 h and at this time all the silver ions are converted into nanoparticulate form (curve 8, Figure 5.13A). Figure 5.13B shows the plot of absorbance of silver nanoparticles at 500 nm (λ_{max}) vs reaction time. It can be inferred that the reduction of silver ion initiates after 3 h of the reaction and completes after 24 h of the reaction. In the previous reports on biosynthesis of silver nanoparticle using bacteria [16, 20] and fungi [23, 24]; the time required for completion of the reaction was found to be around 120 h, which is considerably longer than that reported in the present study.

5.3.4 X-ray diffraction analysis

Figure 5.14 shows the XRD pattern recorded from solution cast film of *Actinobacter* sp. reduced silver nanoparticles on the glass substrate.

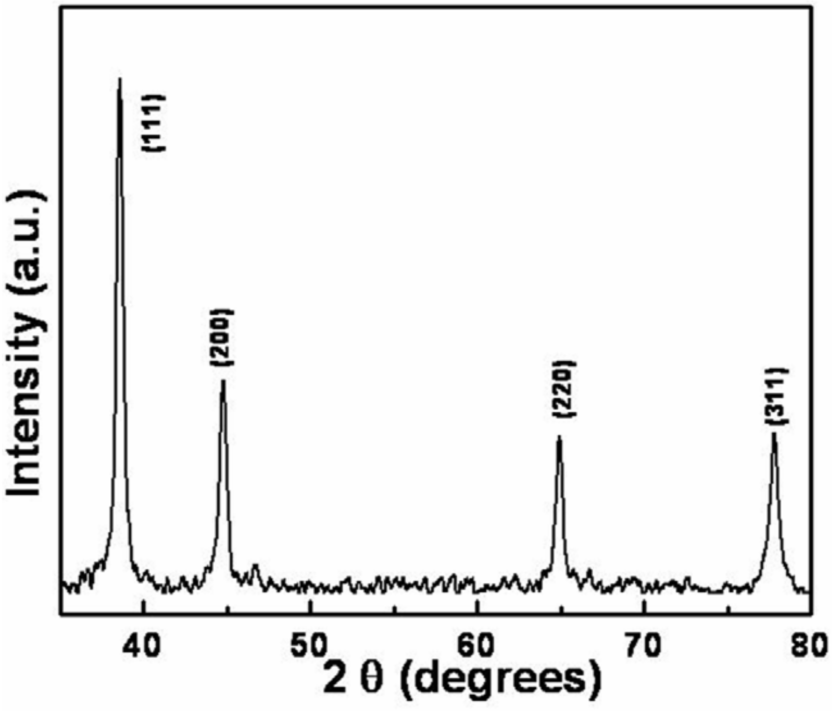

Figure 5.14 *The XRD pattern recorded from solution cast film of silver nanoparticles. The strong Bragg reflections show excellent match with FCC structure of silver. The broadening of XRD peaks suggests small size of the nanoparticles.*

A number of intense Bragg reflections are observed originating from the film of silver nanoparticles. The Bragg reflections were indexed on the basis of FCC structure of silver and corresponds to (111), (200), (220) and (311) set of lattice planes [44]. The broadening of the XRD peaks corresponding to the lattice planes of silver indicates the smaller size of nanoparticles as compared with bulk. The corresponding *d* values for the respective crystal planes are as follows: 2.37 (111), 2.047 (200), 1.44 (220), 1.24 (311) [44].

5.3.5 FTIR and agarose gel electrophoresis analysis

Figure 5.15A illustrates the FTIR spectrum recorded from the purified, silver nanoparticles synthesized by the reaction between aqueous silver ions and *Actinobacter* spp. FTIR analysis was carried out to verify the association of proteins with silver nanoparticles. As discussed for gold particles (section 5.2.7), the spectrum do not show any prominent peak in the region of 500 cm^{-1} to 1200 cm^{-1}, where most of the small organic molecules absorb. However, two sharp peaks at 1560 cm^{-1} and 1650 cm^{-1} corresponding to amide I and II bands respectively are observed indicating the association of proteins with silver nanoparticles [23-25].

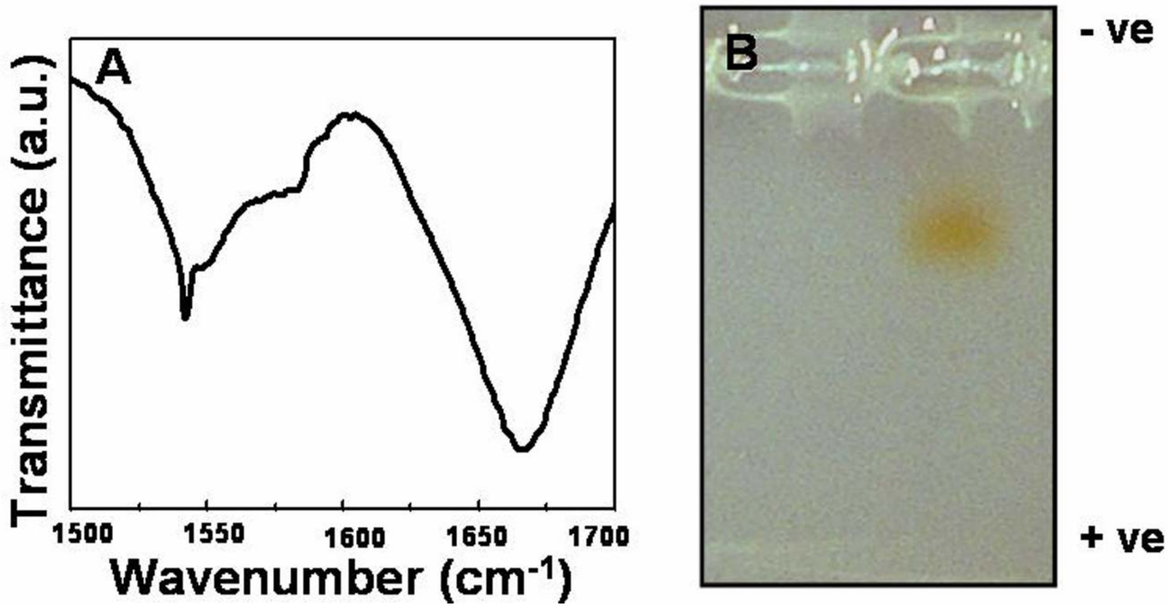

Figure 15 *(A) FTIR spectrum recorded from purified silver nanoparticles showing amide vibration bands. This indicates the association of protein molecules on the surface of nanoparticles. (B) Agarose gel electrophoresis pattern of the purified silver nanoparticles indicating the negative charge present on the surface of nanoparticles.*

Figure 5.15B shows the agarose gel electrophoresis pattern of silver nanoparticles purified by repetitive centrifugation and washing. Like gold nanoparticles synthesized by

Actinobacter spp., silver nanoparticles also migrate toward the anode under applied electric field indicating the presence of negative charge on the surface of nanoparticles. The presence of negative surface charge on silver nanoparticles indicates the possibility of electrostatic interaction between silver ion and silver binding proteins, which bind to the positively charged silver ions.

5.3.6 Analysis of surface capping proteins

FTIR spectrum obtained from the purified and powdered silver nanoparticles shows an association of proteins on the surface of silver nanoparticles. The nanoparticles are stabilized due to the capping of proteins on the surface of nanoparticles. The capping proteins were isolated from the surface of silver nanoparticles as discussed in experimental section (5.3.1). Figure 5.16A shows the polyacrylamide gel electrophoresis profile of the surface bound proteins. SDS-PAGE analysis of the surface bound proteins shows the presence of three different proteins when resolved on 12% gel with the molecular weights of 64, 52 and 29 kDa (lane Ex, Figure 5.16A).

Some of the bacterial species are known to synthesize silver binding proteins as a defense mechanism to nullify the toxic effect of silver ions. Silver binding proteins bind to the ionic silver and stabilize them [45]. However, binding of silver ions with these proteins may not result in the reduction of silver ions and the formation of silver nanoparticles [46]. It is highly possible that one of the silver binding proteins observed here could be involved in the reduction of silver ions, while others facilitate the formation and stabilization of silver nanoparticles.

The formation of silver nanoparticles was readily observed when the capping proteins isolated from purified silver nanoparticles were reacted with silver ions. Figure 5.16B shows the UV-vis spectrum recorded from reaction solution containing silver ions and the capping proteins. A prominent peak observed at 440 nm indicates the SPR band originating from silver nanoparticles. This observation clearly demonstrates the formation of silver nanoparticles. A small red shift in the peak position of the SPR band of silver nanoparticles indicates some degree of aggregation among the nanoparticles. The representative TEM image of silver nanoparticles synthesized using capping proteins is shown in Figure 5.16C. Aggregated nanostructures with the dimensions of 30-200 nm and irregular morphology are observed. This observation is consistent with the UV-vis analysis (Figure 5.16B). The inset in Figure 5.16C shows SAED pattern obtained from silver nanoparticles indicating the crystalline nature of nanoparticles.

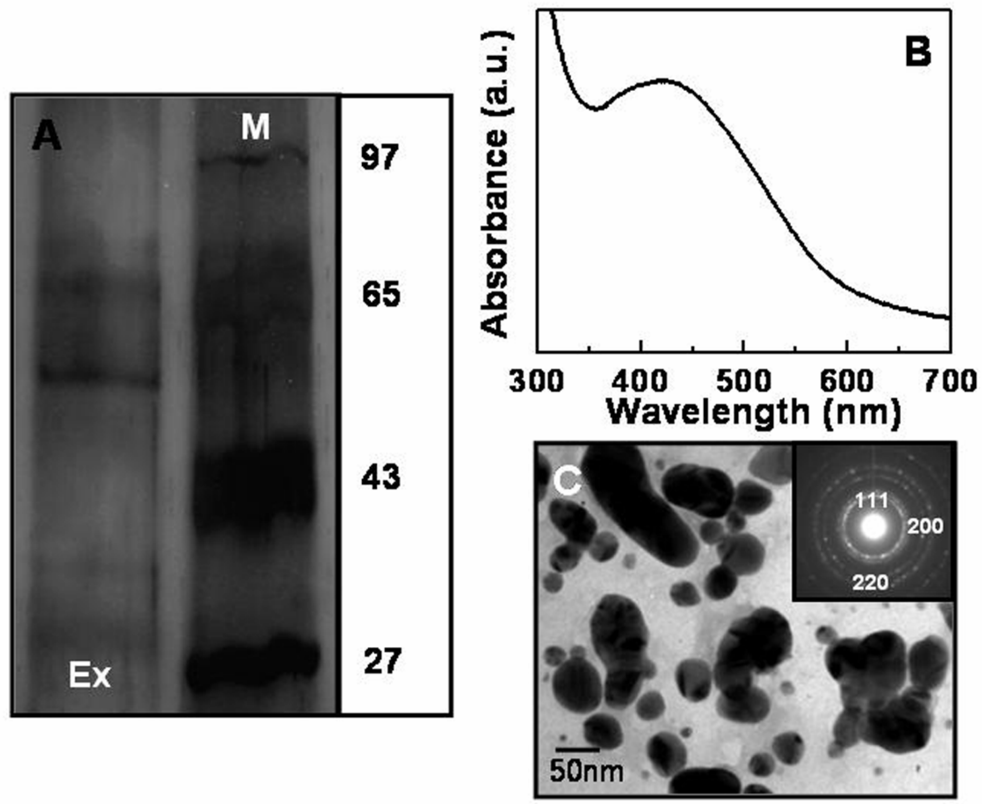

Figure 5.16 *(A) SDS-PAGE analysis of the capping proteins associated with the surface of silver nanoparticles. Three different proteins with the molecular weights of 64, 52 and 29 kDa could be resolved on 12% gel (lane Ex). Lane M shows the standard protein molecular weight markers with the respective molecular weights. (B) The UV-vis spectrum recorded from the aqueous solution containing silver ions and the capping proteins isolated from silver nanoparticles. (C) The TEM image recorded from silver nanoparticles synthesized by reaction between silver ions and the capping proteins. The inset shows SAED pattern of silver nanoparticles along with the lattice planes.*

The UV-vis spectroscopic analysis together with TEM measurements clearly indicates that the capping proteins associated with the surface of silver nanoparticles are responsible for the synthesis and stabilization of silver nanoparticles. One of the capping proteins could be responsible for the reduction of silver ions, while other two proteins could be involved in the stabilization of silver nanoparticles. However, the association of other bacterial proteins in the formation of silver nanoparticles can not be ruled out.

5.3.7 Discussion

This section of the chapter illustrates biosynthesis of flat silver nanoparticles using *Actinobacter* spp. The reaction between silver ions and *Actinobacter* spp. resulted in the formation of flat silver nanoparticles with dimension of 50-200 nm. TEM analysis also indicated the presence of twin boundaries in silver nanoparticles. The UV-vis spectroscopic analysis of *Actinobacter* spp. reduced silver nanoparticles showed two SPR bands corresponding to the anisotropic nature of nanoparticles. UV-vis spectrum recorded from the reaction mixture containing silver ions and *Actinobacter* spp. as a function of time indicated that the reaction is completed in 24 h. The XRD analysis showed that the silver nanoparticles are highly crystalline with well defined Bragg reflections. FTIR analysis illustrated the presence of protein molecules on the surface of silver nanoparticles indicating that the nanoparticles could be stabilized by surface bound proteins.

Analysis of capping proteins showed the presence of three different proteins with the molecular weights of 64, 52 and 29 kDa on polyacrylamide gel under denaturing conditions. Silver nanoparticles are readily synthesized by reaction between silver ions and the capping proteins isolated from purified silver nanoparticles. The UV-vis spectrum recorded from silver nanoparticles synthesized by the reduction of silver ions using capping proteins demonstrated the intense SPR band at 440 nm. TEM analysis of these nanoparticles showed a number of aggregated nanoparticles with irregular morphology and size range in between 30 – 200 nm.

5.4 Conclusions

In this chapter biosynthesis of anisotropic gold and silver nanoparticles has been demonstrated using the bacterium *Actinobacter spp*. Though, biological synthesis of flat gold particles has been described previously using plant extracts, there are no such reports on microbial synthesis of anisotropic gold nanoparticles to the best of our knowledge. Also we describe here the detailed biological mechanism responsible for the synthesis of triangular gold particles. Precise biochemical basis of metal nanoparticle synthesis has not been described previously. Extremely flat, triangular and hexagonal particles of gold are synthesized by the reaction between Au^{3+} ions and *Actinobacter* spp. As shown by various microscopic analyses, the edge length of triangular gold particles vary between 0.05 μm to 2 μm, while the thickness of triangular particles was found to be in the range of 9 to 24 nm. Biogenic triangular and hexagonal gold particles show very strong absorption in the NIR region of the electromagnetic spectrum. *Actinobacter* spp. synthesizes triangular and hexagonal gold particles only when Au^{3+} ions were used as a precursor, though the bacterium could reduce both Au^{3+} and Au^{+} ions. This indicates the presence of highly Au^{3+} specific shape directing biological agent in *Actinobacter* spp. Synthesis of triangular gold particles by *Actinobacter* spp. occurs in two steps. In the first step bacterial cytochrome oxidase reduces gold ions, which are subsequently assembled by the action of proteins present on the cell wall of *Actinobacter* spp. The bacterial cell wall components also selectively bind to Au^{3+} ions and guide the assembly of triangular gold particles indicating that the capping proteins are probably present on the cell wall of *Actinobacter* spp. However, other specific functional groups present on the cell wall could also be involved in the triangular assembly of gold particles. The exposure of silver ions to *Actinobacter* spp. results in the formation of flat – plate like silver nanoparticles with irregular morphology. These silver nanoparticles are found to be 50-200 nm in dimensions. Similar to silver binding proteins reported in other bacteria, *Actinobacter* spp. synthesizes various proteins that reduce silver ions converting them into silver nanoparticles.

Though the biosynthetic method described here could result in the formation of anisotropic gold and silver nanoparticles; it is quite primitive to compete with the existing chemical methods due to the slow reduction rate of gold and silver ions. Proteins synthesized by *Actinobacter* spp. have the ability to reduce metal ions and specifically interact with reduced metal. The detailed investigation of metal reducing and metal binding ability of these proteins could be worth following as it would help in tailoring the morphology of metal nanoparticles. Such efforts could render biosynthesis of metal nanoparticles competitive with the existing chemical methods.

5.5 References

[1] Henglein, A. *J. Phys. Chem.* **1993**, *97*, 8457.

[2] (a) Link, S., El-Sayed, M. A. *Annu. Rev. Phy. Chem*. **2003**, *54*, 331. (b) Peng, X. G., *et al. Nature*, **2000**, *404*, 159. (c) Narayanan, R., El-Sayed, M. A. *Nano Lett*. **2004**, 4, 1343. (d) Burda, C., Chen, X., Narayanan, R., El-Sayed, M. A. *Chem. Rev.* **2005**, 105, 1025.

[3] Moreno-Manas, M., Pleixats, R. *Acc. Chem. Res*. **2003**, *36*, 638.

[4] (a) Mirkin, C. A., Letsinger, R. L., Mucic, R. C., Storhoff, J. J. *Nature* **1996**, *382*, 607. (b) Han, M., Gao, X., Su, J. Z., Nie, S. *Nature Biotechnol.* **2001**, *19*, 631.

[5] Kamat, P. V. *J. Phys. Chem. B*. **2002**, *106*, 7729.

[6] (a) Hutchinson, T. O., Liu, Y.-P., Kiely, C., Kiely, C. J., Brust, M. *Adv. Mater.* **2001**, *13*, 800. (b) Busbee, B. D., Obare, S. O., Murphy, C. J. *Adv. Mater.* **2003**, *15*, 414. (d) Jana, N., Gearheart, L., Murphy, C. *J. Chem. Mater.* **2001**, *13*, 2313.

[7] Sun, X., Dong, S., Wang, E. *Angew. Chem. Int. Ed.* **2004**, *43*, 6360.

[8] (a) Sun, Y., Xia, Y. *Science* **2002**, *298*, 2176. (b) Xiong, Y., *et al. Nano Lett.* **2005**, *5*, 1237.

[9] Huang, C. C., Yang, Z., Chang, H.-T. *Langmuir* **2004**, *20*, 6089.

[10] (a) Hao, E., Kelly, K. L., Hupp, J. T., Schatz, G. C. *J. Am. Chem. Soc.* **2002**, *124*, 15182. (b) Puntes, V. F., Zanchet, D., Erdonmez, C. K., Alivisatos, A. P. *J. Am. Chem. Soc.;* **2002**, *124*, 12874.

[11] Sun, Y., Mayers, B., Xia, Y. *Nano. Lett.* **2003**, *3*, 675.

[12] (a) Manna, L., Scher, E. C., Alivisatos, A. P. *J. Am. Chem. Soc.* **2000**, *122*, 12700. (b) Chen, S., Wang, Z. L., Ballato, J., Foulger, S. H., Carroll, D. L. *J. Am. Chem. Soc.* **2003**, *125*, 16186.

[13] (a) Sau, T. K., Murphy, C. J. *J. Am. Chem. Soc.* **2004**, *126*, 8648. b) Hu, J., *et al. J. Am. Chem. Soc.* **2004**, *126*, 470.

[14] Turkevich, J., Stevenson, P. C., Hiller, J. *Discussions Faraday, Soc.*, **1951**, *11*, 55.

[15] (a) Southam, G., Beveridge, T. J. *Geochim .Cosmochim. Acta* **1996**, *60*, 4369. (b) Beveridge, T. J., Murray, R. G. E. *J. Bacteriol.* **1980**, *141*, 876. (c) Fortin, D., Beveridge, T. J. in *Biomineralization. From Biology to Biotechnology and Medical Applications* (Ed. E. Baeuerien), Wiley-VCH, Weinheim **2000**, *7*.

[16] (a) Klaus, T., Joerger, R., Olsson, E., Granqvist, C. G. *Proc. Nat. Acad. Sci.* **1999**, *96*, 3611. (b) Klaus, T., Joerger, R., Olsson, E., Granqvist, C. G. *Trends Biotech.* **2001**, *19*, 15. (c) Joerger, R., Klaus, T., Granqvist, C. G. *Adv.Mater.* **2000**, *12,* 407.

[17] Efrima, S., Bronk, B. V. *J. Phys. Chem. B* **1998**, *102*, 5947.

[18] Kashifi, K., Torr, J. M., Nevin, K. P., Lovley, D. R. *Appl Environ MIcrobiol* **2001**, *67*, 3275.

[19] (a) Lengke, M. F., Fleet, M. E., Southam, G. *Langmuir*, **2006**, 22, 2780. (b) Lengke, M. F., Fleet, M. E., Southam, G. *Langmuir* **2006**, 22, 7318.

[20] Nair, B., Pradeep, T. *Crystal Growth & Design*, **2002**, *2*, 293.

[21] Ahmad, A., Senapati, S., Khan, M. I., Kumar, R.,Sastry, M. *Langmuir* **2003**, *19*, 3550.

[22] Yong, P., Rowson, N. A., Far, J., P. G., Harris, R., Macaskie, L. E. *Biotechnol Bioeng*, **2002**, *80*, 369.

[23] (a) Mukherjee, P. *et al Angew. Chem. Int. Ed*. **2001**, *40*, 3585. (b) Mukherjee, P. *et al Nano Lett.* **2001***, 1,* 515.

[24] (a) Mukherjee, P., *et al. Chem Bio Chem,* **2002***, 3,* 461. (b) Ahmad, A. *et al Coll. Surf. B.* **2003***, 28,* 313.

[25] Senapati, S., Ahmad, A., Khan, M. I., Sastry, M., Kumar, R. *Small*, **2005**, *1*, 517.

[26] Gardea-Torresdey, J. L., Peralta-Videa, J. R., de la Rosa, G., Parsons, J. G. *Coord. Chem. Rev.* **2005**, *249*, 1797.

[27] Gardea-Torresdey, *et al*. *Nano Lett.* **2002**, *2*, 397.

[28] Gardea-Torresdey, *et al*. *Langmuir* **2003,** *19*, 1357.

[29] (a) Shankar, S. S., Ahmad, A., Pasricha, R., Sastry, M. *J. Mater. Chem.* **2003**, *13*, 1822. (b) Shankar, S. S., Ahmad, A., Sastry, M. *Biotechnol. Prog.*, **2003**, *19*, 1627. (c) Shankar, S. S., Rai, A., Ahmad, A., Sastry, M. *Applied Nanoscience* **2004**, *1*, 69. (d) Shankar, S. S., Rai, A., Ahmad, A., Sastry, M. *J. Colloid Interface Sci.* **2004**, *275*, 496.

[30] (a) Shiv Shankar, S., *et al*. *Nat. Mater.* **2004**, *3*, 482. (b) Chandran, S. P., Chaudhari, M., Pasricha, R., Ahmad, A., Sastry, M. *Biotechnol Prog.* 2005, 22, 577. (c) Liu, B., Xie, J., Lee, J. Y., Ting, Y. P., Chen, J. P. *J. Phys. Chem. B* **2005**, *109*, 15256.

[31] Kartikeyan, S., Beveridge, T. J. *Environmental Microbiol*. **2002**, *4*, 667.

[32] Southam, G., Beveridge, T. J. *Geochim Cosmochim Acta*, **1994**, *58*, 4527.

[33] (a) Milligan, W. O., Morriss, R. H. *J. Am. Chem. Soc.* **1964**, *86*, 3461. (b) Chiang, Y. S., Turkevich, J. *J. Colloid Sci* **1963**, *18*, 772.

[34] (a) Chen, S., Carroll, D., L. *Nano.Lett.* **2002**, *2*, 1003. (b) Jin, R. *et al*. *Science*, **2001**, *294*, 1901. (c) Jin, R. *et al Nature* **2003***, 425,* 487. (d) Sarma, T. K., Chattopadhyay, A. *Langmuir* **2004**, *20*, 3520. (e) Métraux, G. S., Mirkin C. A. *Adv. Mater.* **2005**, *17*, 412. (f) Malikova, N., Pastoriza-Santos, I., Schierhorn, M., Kotov, N. A., Liz-Marzan, L. M. *Langmuir*, **2002**, *18*, 3694.

[35] The XRD pattern was indexed with reference to FCC gold structure from *JCPDS-International Center for Diffraction Data PCPDFWIN* version 1.30, 04-0784.

[36] Germain, V., Li, J., Ingert, D., Wang, Z. L., Pileni, M. P. *J. Phys. Chem. B* **2003**, *107*, 8717.

[37] Mirkin, C. A., Letsinger, R. L., Mucic, R. C., Storhoff, J. J. *Nature* **1996**, *382*, 607.

[38] Hao, E., Kelly, K. L., Hupp, J. T., Schatz, G. C. *J. Am.Chem. Soc.* **2002**, *124*, 15182.

[39] Mulvany, P. *Langmuir* **1996**, *12*, 788.

[40] Lovley, D. R. *Annu. Rev. Microbiol*. **1993**, *47*, 263.

[41] (a) Beveridge, T. J., Murray, R. G. E. *J. Bacteriol*, **1976**, *127*, 1502.

[42] Mann, S. *Nature*, **1988**, *332*, 119.

[43] (a) Meunier, B., de Vissar, S. P., Shaik, S. *Chem Rev*. **2004**, *104,* 3947.

[44] Chipman, P. M., Sharon, N. *Science*, **1969**, *165*, 454.

[45] Adamich, M., Hemmingsen, B. *Protoplast and spheroplast production* 1980, Cambidge University press.

[44] The XRD pattern was indexed with reference to FCC silver structure from *JCPDS-International Center for Diffraction Data PCPDFWIN* version 1.30, 04-0783.

[45] (a) Gupta, A, Matsui, K., Lo, J. F., Silver, S. *Nat. Med*. **1999**, 5, 183. (b) Gupta, A., Silver, S. *Nat. Biotechnol*. **1998**, *16*,886.

[46] Lie, X. Z., Nikaido, H., Williams, K. E. *J. Bacteriol*. **1997**, *79*, 6127.

Chapter VI

Biological synthesis of anisotropic metal nanoparticles using bacterial metabolites

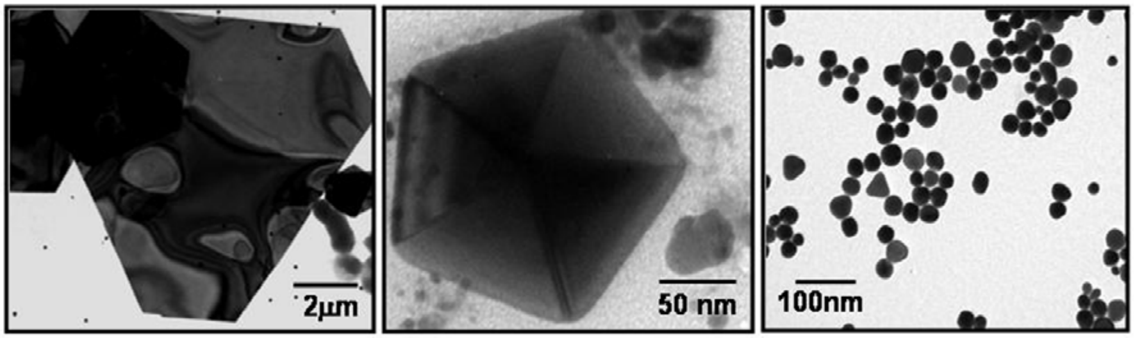

This chapter describes biological synthesis of anisotropic gold and silver nanoparticles using bacterial metabolites. A number of primary or secondary metabolites like siderophores, pigments and enzymes were explored for the shape directed synthesis of gold and silver nanoparticles. The ferric ion chelating siderophore–pyoverdin from the bacterium *Pseudomonas aeruginosa* was shown to be capable of synthesizing triangular gold nanoparticles. The edge length of the triangular gold particles could be controlled by varying the concentration of siderophore. Pyocyanin, a blue–green pigment produced by *Pseudomonas aeruginosa* was capable of synthesizing nearly uniform sized gold nanoparticles and wire-like silver nanoparticles. This chapter also illustrates the accelerated synthesis of small triangular gold nanoparticles employing protease enzyme synthesized by *Actinobacte*r spp. in the presence of bovine serum albumin (BSA).

Part of the work presented in this chapter has been communicated in the following journals:
(1) Bharde, A. A., M. Sastry, *Small*. 2007
(2) Bharde, A. A., Kulkarni, A., Rao, M., Prabhune, A., Sastry M. *J. Mater. Chem*. 2007

6.1 Introduction

Development of new synthetic protocols for the synthesis of metallic nanoparticles with different size and shapes constitutes an ever-growing field of nanoscience. Among various metallic nanoparticles, noble metal nanoparticles show exciting optical properties such as wavelength selective plasmon absorption resonances, conductivity and catalysis [1]. These properties of noble metal nanoparticles depend on their size and shape which can be exploited for numerous applications ranging from catalysis [2] to biosensing [3] to optics [4]. Hence, it is highly desirable to produce gold and silver nanoparticles with different morphology and size in high yield. A large volume of work on the synthesis of gold and silver nanoparticles with myriad shapes is based primarily on the chemical synthesis methodologies developed until now [5].

Research in the past few years has demonstrated that biological synthesis of inorganic materials can be equally important due to the environmental hazards caused by chemical synthesis methods. Many biological systems exert exquisite control over formation of the metal nanoclusters through of concerted mechanisms. The means of nanocluster formation involves bioaccumulation [6], reduction and mineralization processes [7]. Recent work in this field has inclined towards biological methods owing to their environmental friendly and economically viable nature [8].

So far, biological synthesis of gold and silver nanoparticles has relied on the systematic use of micro-organisms like bacteria [9] and fungi [10] or plants/plant extracts [11]. Several studies have demonstrated that proteins isolated from biological organisms can be used as enzymes or templates for material synthesis in vitro. This includes silica and silicones synthesis by silicateins [12], silaffins [13] and silica precipitating peptides [14], calcium carbonate by specialized biological macromolecules [15], cadmium sulfide by glutathione and phytochelatins [16] etc. Though these reports show formation of inorganic materials, similar protocols for the synthesis of metallic nanoparticles have not been explored extensively. Nevertheless, there are a few reports on biomimetic synthesis of metallic nanoparticles. Small peptide molecules, called as dodecapeptides derived by phage display library have been implemented for the synthesis of gold nanoparticles [17]. A small peptide isolated from a combinatorial phage display peptide library associated with silver binding and reduction has been used to synthesize silver nanoparticles with a variety of crystal morphologies [18].

This chapter illustrates the biological synthesis of gold and silver nanoparticles using bacterial metabolites, which are intermediates or products of metabolism. Metabolites like a ferric ion chelating compound siderophore and pigment from *Pseudomonas aeruginosa* have been used to synthesize anisotropic gold and silver nanoparticles. Furthermore, the accelerated synthesis of small triangular gold nanoparticles by protein hydrolyzing enzyme protease from *Actinobacter* spp. has been illustrated.

Pseudomonas aeruginosa is a gram negative aerobic bacterium known to synthesize a number of primary and secondary metabolites with physiological significance. Under the limiting conditions of ferric ion, *P. aeruginosa* produces two types of siderophores, pyochelin and pyoverdin [19]. Pyochelin is a salicylic acid derivative [20], while pyoverdin is a small linear octapeptide bound to 2,3-diamino-6,7 dihydroxyquinoline [21]. The structure of pyoverdin is as follows:

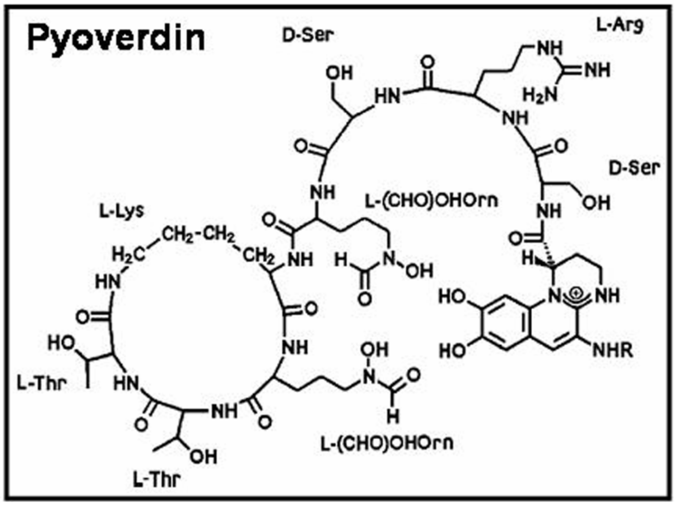

Chemical structure of the siderophore pyoverdin synthesized by the bacterium P.aeruginosa used in the present work.

Pyochelin and pyoverdin show strong fluorescence when exposed to UV light [22]. Though the primery function of siderophores synthesized by *P.aeruginosa* is iron acquisition under iron limiting conditions, many physiological implications for these molecules are reported. Pyochelin and pyoverdin can act as an excellent biocontrol agent in plant growth promoting pseudomonads [23]. The biosynthesis of these siderophores is governed by the genes *pchDCBA* and *pchEF*, which are clustered in the chromosome of *P.aeruginosa* [19].

Pseudomonas aeruginosa is also known to synthesize a blue-green coloured pigment called pyocyanin. Structurally, pyocyanin is 1-hydroxymethyl-5-methyl phenazyne, synthesized in the late logarithmic or stationary phase of the bacterial life cycle [24]. Pyocyanin exerts a strong antimicrobial action against the closely related species of pseudomonas [25] and also has cytotoxic effects against mammalian cells [26]. In addition, pyocyanin acts as a redox shuttle and can undergo a reversible two electron reduction to form a colorless product leucopyocyanin, which in turn, is readily oxidized by molecular oxygen [27]. Further, pyocyanin is speculated to play a role in bacterial energy metabolism under non-optimal growth conditions [27]. Biosynthesis of pyocyanin, an offshoot of shikimic acid pathway, is controlled by the enzymes involved in the synthesis of phenazine [28]. Phenazine biosynthesis is governed by an operon consisting of seven genes in *P. aeruginosa* that encodes seven enzymes generally named as Phz A–G [28]. The structure of pyocyanin synthesized by *P. aeruginosa* is as follows:

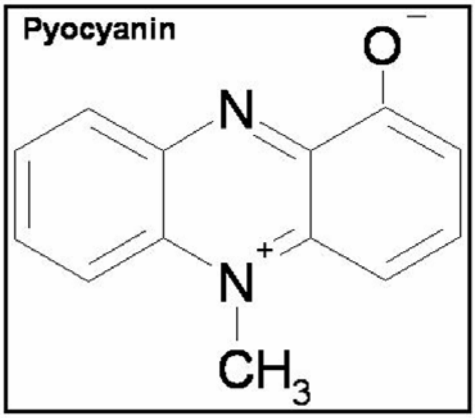

Chemical structure of pyocyanin molecule synthesized by the bacterium P. aeruginosa.

Many micro-organisms extracellularly synthesize protein hydrolyzing enzymes known as proteases. Proteases are divided into the four subclasses; cysteine, serine, aspartic and metallo-proteases depending on the amino acid residues present in their active sites [29]. Aspartic protease contains aspartic acid in their active site triad and show structural and functional variation from species to species. Proteases are essential for the growth and metabolism of all living cells, hence they are considered as primary metabolites. There are few reports on the interaction of protease and gold nanoparticles

[30]. Recently, enzymatic catalysis has been used for the synthesis of nanoparticles [31]. However, in this case, nanoparticles were not synthesized by the direct action of enzymes.

In pursuing new "green chemistry" methods for the synthesis of metallic nanoparticles, the use of bacterial primary and secondary metabolites like siderophores, enzymes and pigments respectively have been demonstrated in this chapter. Numerous metabolites are at the center of redox or electron transfer reactions occurring inside the cell fulfilling various physiological demands. Many biological molecules have their redox potential lower than ionic gold and silver and hence can be used for the synthesis of metallic nanoparticles. Use of bacterial metabolites as a reducing and shape directing agent for the synthesis of anisotropic gold and silver nanoparticles can be considered as an important development in the steadily evolving biological synthesis methods. Biological synthesis methods described here are rapid and are comparable with existing chemical synthesis methods.

Outline of the present work:

The current chapter describes biological synthesis of the anisotropic gold and silver nanoparticles using a siderophore and pigment from Gram negative bacterium *P. aeruginosa*, which was isolated from Arabian sea, Goa, India. Siderophores show higher affinity towards Au^{3+} ions and rapidly reduces them to Au^0, eventually resulting in the formation of the triangular gold particles. It is also capable of reducting Ag^+ ions and results in the subsequent synthesis of silver nanoparticles. However, the rate of silver ion reduction was found to be lower indicating the lower affinity of the siderophore molecules towards silver ions in comparison with gold ions. On the other hand, reduction of Ag^+ ions with pyocyanin, a pigment from *P. aeruginosa* is very rapid and the synthesis of silver nanoparticles could be observed in 60 minutes resulting in ribbon like structures. Pyocyanin could also synthesize gold nanoparticles with a narrow size distribution. However, the synthesis of gold nanoparticles was slower in comparison with silver nanoparticles. The last part of this chapter describes the accelerated synthesis of small gold nanoparticles by induction of the enzyme protease in *Actinobacter* spp. The presence of atmospheric oxygen seems to be a crucial factor in controlling the rate of nanoparticle synthesis.

6.2 Biological synthesis of gold and silver nanoparticles by the siderophore pyoverdin

This part of the chapter describes biological synthesis of gold and silver nanoparticles from gold and silver ions using pyoverdin as a reducing agent.

6.2.1 Experimental details

The siderophore pyoverdin was isolated from *P. aeruginosa* by a previously described method [32]. Briefly, bacterial seed culture was grown in LB medium for a period of 12 h. This seed culture was then inoculated in 100 ml of King's B medium in a 500 ml Erlenmeyer flask for the induction of siderophore formation. The flask was incubated on the shaker (150 rpm) for 48 h at 37 °C. Next, the siderophore was isolated from the aqueous medium by solvent extraction described as follow. The supernatant containing siderophore was collected by centrifugation at 7000 rpm (5533 X *g*) and the pellet containing the bacterial cells was discarded. The supernatant was acidified with concentrated hydrochloric acid until pH of the solution became 2. The acidified supernatant was mixed with ethyl acetate in 1:1 ratio and incubated overnight. The organic layer was separated from the aqueous layer. The organic layer of ethyl acetate was evaporated and the dried and the powdered residue containing siderophore was dissolved in a small volume of methanol. Thin layer chromatography (TLC) was performed to assess the production and purity of pyoverdin by applying to Silicagel 60F254 TLC plate (Merck). The plate was developed using chloroform-acetic acid-ethanol (90:5:2.5 vol/vol/vol) solvent system and then visualized under UV light ($\lambda \sim 305$ nm). For the synthesis of gold and silver nanoparticles, 10^{-3} M of aqueous $HAuCl_4$ and 10^{-3} M $AgNO_3$ was reacted with 0.05%, 0.1% and 0.2% of pyoverdin in the final reaction volume of 10 ml respectively. Gold and silver nanoparticles were characterized by TEM, AFM, UV-vis-NIR spectroscopy, and FTIR spectroscopy.

6.2.2 Isolation and purification of Pyoverdin

Synthesis of siderophore by *P. aeruginosa* is induced by the iron limiting conditions, which are generally developed in the stationary phase of bacterial growth due to the depletion of nutrients in the growth medium. Growth of *P.aeruginosa* in King's B medium promotes the synthesis of pyoverdin and suppresses the synthesis of pyochelin [33]. Pyoverdin was secreted extracellularly in the surrounding medium as indicated by the yellow–green colour of the medium. Bacterial cell-free supernatant when acidified with concentrated HCl became pale brown in the colour due to the presence of pyoverdin. The acidified supernatant was mixed with ethyl acetate and kept overnight. The organic layer showed a brown colour due to the presence of pyoverdin, which was later isolated by evaporation of ethyl acetate.

The presence of pyoverdin is indicated by the UV spectroscopic analysis, where pyoverdin shows a strong absorption at 402 nm. Purity of the pyoverdin is checked by TLC analysis. The TLC plate is irradiated with UV light (λ ~ 305 nm) and shows the presence of a single spot, which exhibits blue–green fluorescence. Figure 6.1A shows a photograph of TLC plate after irradiation with UV light showing the presence of a single spot. The R_f values calculated for pyoverdin is found to be 0.4. Pyoverdin forms a highly stable brown coloured complex with ferric iron under acidic conditions [32]. Figure 6.1B shows a photograph of the TLC plate after spreading with 0.1 M $FeCl_3$ in 0.1 M HCl indicating the brown colour due to the formation of complex with ferric ions.

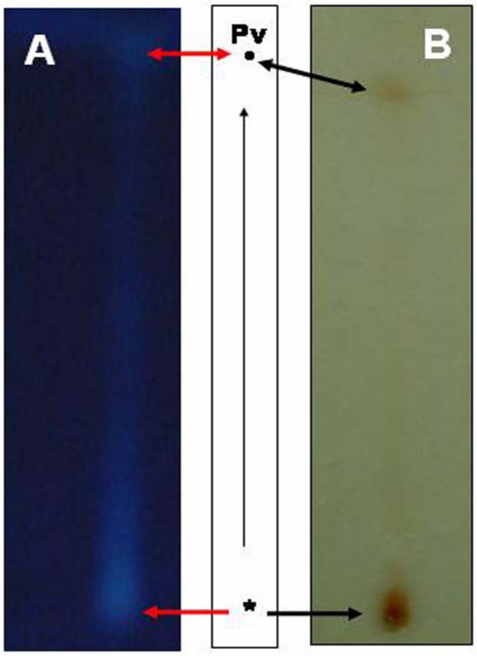

Figure 6.1 *(A) Photograph of TLC plate showing the migration of pyoverdin in chloroform: acetic acid: ethanol solvent system. A single spot of pyocyanin showing bluish green fluorescence in UV-light (λ~305 nm) was observed. "*" indicates the origin, at which pyoverdin was spotted, while "•" indicates the final position of the spot attained by migration in the solvent system as mentioned in the text. (B) Photograph of TLC plate after reaction with 0.1 M* $FeCl_3$ *in 0.1 M HCl.*

6.2.3 Synthesis of anisotropic gold particles by Pyoverdin

6.2.3.1 TEM analysis

Representative TEM images of pyoverdin reduced gold ions solution show a number of nanoparticles with the triangular and hexagonal morphology. The edge length of the triangular and hexagonal particles varied between 0.2 μm to 5 μm depending on the concentration of pyoverdin used for reduction of chloroaurate ions. It was observed that the edge length of triangular and hexagonal nanoparticles synthesized using pyoverdin depends on the concentration of pyoverdin used for the reduction of gold ions. At lower concentration of pyoverdin i.e. 0.05 % (V/V), large, flat triangular and hexagonal particles are formed with the edge lengths up to ~ 6 μm (Figure 6.2A). The size range for gold particles varied between 3 to 5 μm. On the other hand, at a concentration of 0.1 % (V/V) of pyoverdin, the edge length of triangular and hexagonal particles varied between 0.5 μm to 3 μm (Figure 6.2 B&C).

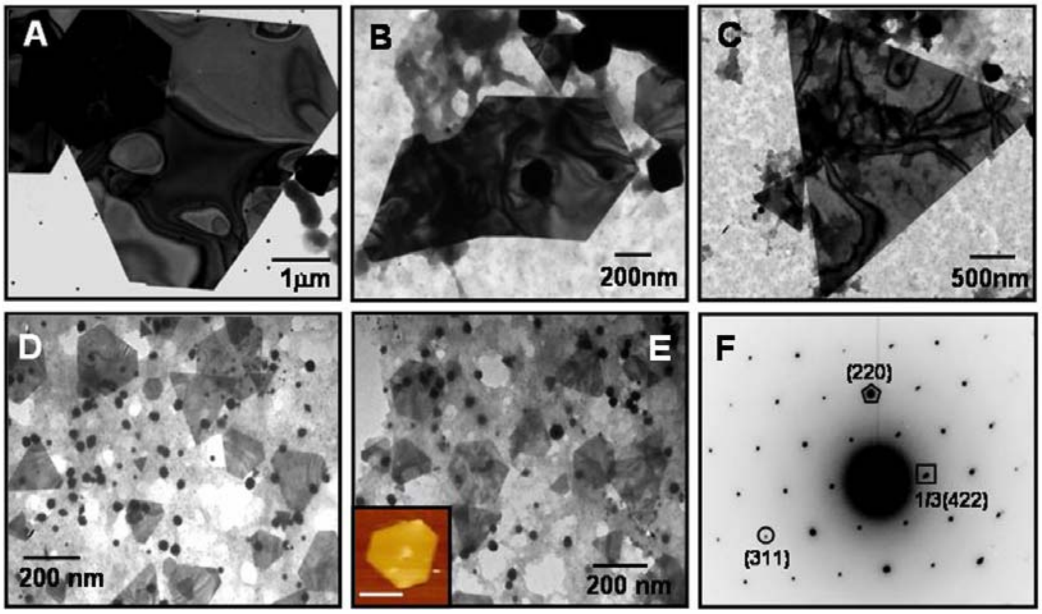

Figure 6.2 *Representative TEM images of gold nanoparticles synthesized by reaction between* $HAuCl_4$ *and pyoverdin. The edge length of triangular particle increases with the decreasing concentration of pyoverdin. Triangular and hexagonal gold particles of edge length between 100 nm to 5 μm are synthesized using 0.05 % (A), 0.1 % (B & C) and 0.2 % (D & E) concentrations of pyoverdin. The inset in (E) shows the AFM image of one of the triangular gold particles synthesized using 0.2 % pyoverdin. The scale bar in AFM image is 250 nm. (F) SAED pattern obtained from a single triangular gold particle along with the lattice planes.*

Triangular and hexagonal gold particles with nearly uniform edge length of 200 nm to 250 nm are synthesized at 0.2 % (V/V) concentration of pyoverdin. However, a number of small spherical particles are also observed along with triangular and hexagonal particles at this concentration of pyoverdin (Figure 6.2 D & E). AFM analysis carried out on one of the triangular gold particle synthesized using 0.2 % pyoverdin indicates that the thickness of the triangular gold particle is ~ 25 nm (inset in image E, Figure 6.2). The selected area diffraction pattern obtained from one of the triangular particle indicates that each particle is a single crystal and the diffraction pattern was indexed on the basis of FCC structure of gold. The corresponding *d* values for the respective crystal planes are as follows: 2.04 (200), 1.45 (220), 1.25 (311) [34].

6.2.3.2 UV-vis-NIR spectroscopic analysis

After the addition of pyoverdin to 10^{-3} M $HAuCl_4$, the originally yellow colour of the reaction medium gradually changed to a dark brown within 4 h of reaction, indicating the formation of gold nanoparticles. Figure 6.3A shows UV-vis spectra of gold nanoparticles synthesized using 0.05 % and 0.1 % solution of pyoverdin respectively. A strong absorption band at 580 nm is observed due to the formation of gold nanoparticles by 0.05 % and 0.1 % of pyoverdin respectively (curves 1 and 2, Figure 6.3A). The absorption band shows a red shift in comparison with the surface plasmon resonance of spherical gold nanoparticles, which is normally centered at 520 nm. Further, the absorption band at 580 nm corresponding to gold particles synthesized using 0.05 % of pyoverdin shows broadening (curve 1 in Figure 6.3A), due to the aggregation of small spherical particles. The SPR band at 580 nm is accompanied by gradually increasing absorption in the near infra-red (NIR) region of the electromagnetic spectrum. The absorption in the NIR region is due to the in-plane collective electronic oscillation indicating the anisotropic nature of gold particles [35]. The absorption observed in the NIR region is higher in intensity for gold particles synthesized using 0.1 % of pyoverdin in comparison with gold particles synthesized using 0.05 % of pyoverdin (Figure 6.3, curves 1 and 2). The rise in intensity of the absorption in the NIR region could be due to increasing population of anisotropic gold particles. Figure 6.3B shows UV-vis spectra as a function of time of reaction between aqueous solution of gold ions and 0.2 % of pyoverdin. The surface plasmon resonance band recorded after 1 h of reaction shows a weak absorption at 560 nm (curve 1, Figure 6.3B), which gradually red shifts and increases in intensity after 4 h (curve 4, Figure 6.3B).

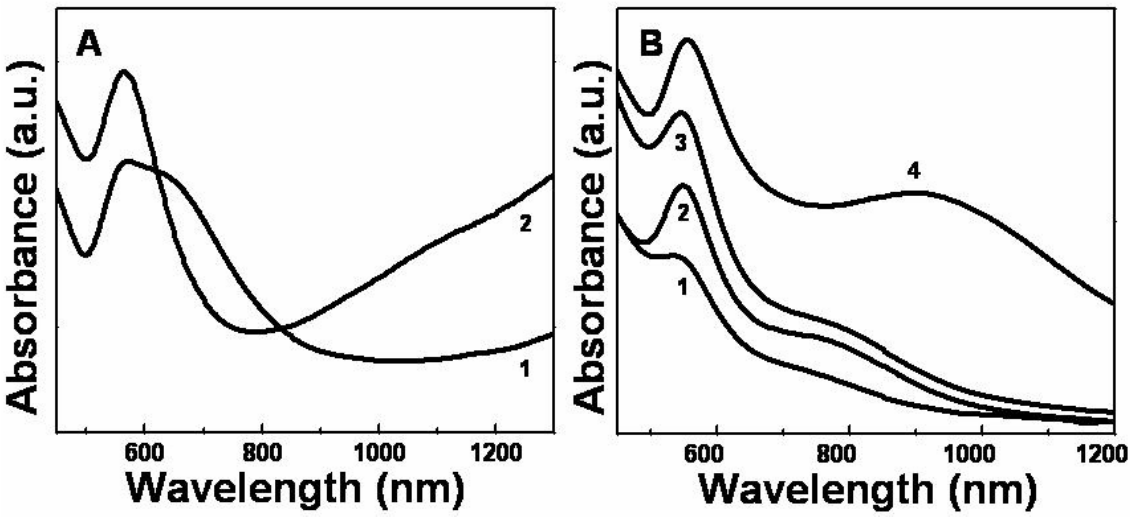

Figure 6.3 *(A) UV-vis-NIR spectra of gold nanoparticles synthesized by reaction between gold ions and 0.05 % (curve 1) and 0.1 % (curve 2) of pyoverdin. (B) UV-vis-NIR spectra recorded as a function of time of reaction between 0.2 % of pyoverdin and aqueous gold ions. Curves 1 to 4 correspond to the progress of reaction after 1, 2, 3 and 4 h respectively.*

As observed with gold particles synthesized by 0.05 % and 0.1 % of pyoverdin (curves 1 & 2, Figure 6.3A), the SPR band at 560 nm is accompanied by an absorption at 850 nm (curve 4, Figure 6.3B). However, the intensity of the observed in plane SPR band at 850 nm is lower than that of out of plane SPR band at 560 nm probably indicating that the population of anisotropic gold particles is less than that of spherical gold nanoparticles (curve 4, Figure 6.3B) [36].

6.2.3.3 FTIR spectroscopic analysis

FTIR measurements were carried out to identify the binding of gold nanoparticles with various functional groups present in pyoverdin. The mechanism of reduction of chloroaurate ions by pyoverdin can also be studied by FTIR spectroscopic analysis carried out on pyoverdin before and after the reaction with chloroaurate ions. As mentioned earlier, chemically pyoverdin is a octapeptide bound to dihydroxyquinoline [21]. Figure 6.4 shows the FTIR spectra of purified pyoverdin molecules (curve 1) and pyoverdin–chloroaurate ions reaction mixture (curve 2) after the synthesis of gold nanoparticles. The different vibrational frequencies shown in the FTIR spectra are given in the Table 6.1. A prominent absorption band at 1144 cm^{-1} in the spectrum corresponding to pyoverdin originates due to the stretching vibrations of C–N bonds (curve 1, Figure 6.4A), which are not observed in the spectrum corresponding to pyoverdin – chloroaurate ion reaction mixture after the formation of gold nanoparticles (curve 2, Figure 6.4A). The complete disappearance of a small vibrational band at 1544 cm^{-1}, assigned to amide II (N–H) stretching vibrations from curve 2, which corresponds to the reduction of chloroauric acid indicates that it could be involved in the formation of gold nanoparticles (curve 2, Figure 6.4A). This observation is consistent with the disappearance of the C–N bond absorption and supports the idea that amide or amine groups could be responsible for the reduction of chloroaurate ions or the interaction with gold nanoparticles.

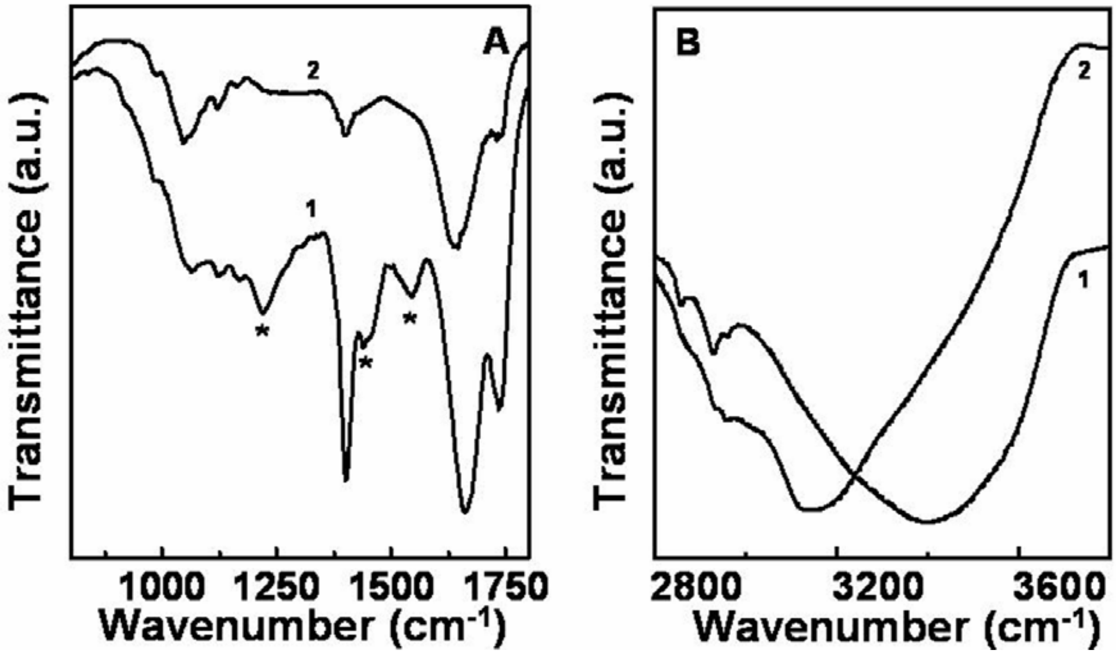

Figure 6.4 *(A) FTIR spectra obtained from pyoverdin in powdered KBr before (curve 1) and after reaction with chloroauric acid (curve 2). Symbol "*" indicates vibrational bands that could be involved in the reduction of chloroauric acid and binding to the surface of gold nanoparticles. (B) Enlarged view of the same spectra in the amine and hydroxyl groups vibrational regions.*

The presence of a weak absorption band centered at 1438 cm^{-1} in curve 1 could be assigned to the CH_2 group stretching vibrations that is not observed in the spectrum equivalent to pyoverdin–chloroaurate ion reaction mixture (curve 2 Figure 6.4A). The strong absorption at 1663 cm^{-1} due to amide I (C=O) vibrational band in pyoverdin (curve 1, Figure 6.4A) is shifted towards lower wavenumber at 1642 cm^{-1} (curve 2, Figure 6.4A) after reaction with chloroauric acid. This observation further suggests that amine or amide groups play an important role in the formation of gold nanoparticles. A broad and strong absorption band at 3140 cm^{-1} could be assigned either to the stretching vibrations of amine or hydroxyl groups present in pyoverdin as shown in the curve 1 and 2 in Figure 6.4B. Amine and hydroxyl groups have overlapping absorption (3200–3600 cm^{-1}) in the FTIR spectrum and therefore it is very difficult to assign the bond vibrations in this region to a particular functional group. The absorption band at 3140 cm^{-1} observed in the curve 1 in Figure 6.4B, which corresponds to pyoverdin before reaction with chloroaurate ions is considerably shifted to 3400 cm^{-1} after reaction with chloroaurate ions and the formation of gold nanoparticles (curve 2, Figure 6.4B).

Table 6.1 *Vibration frequency assignment for the peaks observed in the FTIR spectra of pyoverdin before and after reaction with chloroaurate ions represented by the curves 1 and 2 in Figure 6.3, respectively* [36].

Vibration modes	Pyoverdin (cm^{-1})	Pyoverdin treated with chloroaurate ions (cm^{-1})
C – O (ν)	1067	1048
C – N (ν)	1144	1142
C – O (ν)	1221	– –
CH_3 (δ)	1402	1400
O – C – H (δ), CH_2 (δ)	1438	– –
N – H (δ) of amide group	1545	– –
C = O (ν) of amide group	1663	1641
C = O (ν) of aldehyde and ketone	1735	1730
C – H	2929	2930
N – H (ν) of amine group or O – H (ν)	3140	3400
(δ) bending vibrations, (ν) stretching vibration		

This shift could be because of the interaction of amine groups with the surface of gold nanoparticles. However, it is very difficult to draw such a conclusion at this stage due to the overlapping absorption of amine and hydroxyl group in the FTIR spectrum. Nevertheless, the disappearance or shift in amide stretching vibrations strongly suggests that this group of pyoverdin is possibly responsible for the synthesis of gold nanoparticles and their stabilization. Thus the FTIR analysis reveals considerable changes in the vibrational frequencies of different functional groups present in pyoverdin after reacting with aqueous chloroaurate ions. However, due to the complex structure of pyoverdin it is not possible to precisely monitor the exact functional group that donates the electrons and reduces gold ions by FTIR spectroscopy.

6.2.4 Biological synthesis of silver nanoparticles by Pyoverdin

6.2.4.1 TEM analysis

Figure 6.5 shows TEM images of silver nanoparticles synthesized by reaction between 10^{-3} M $AgNO_3$ and 0.1% pyoverdin after 6 h of reaction. A large number of silver nanoparticles are observed to be distributed throughout the grid surface (images A & B in Figure 6.5).

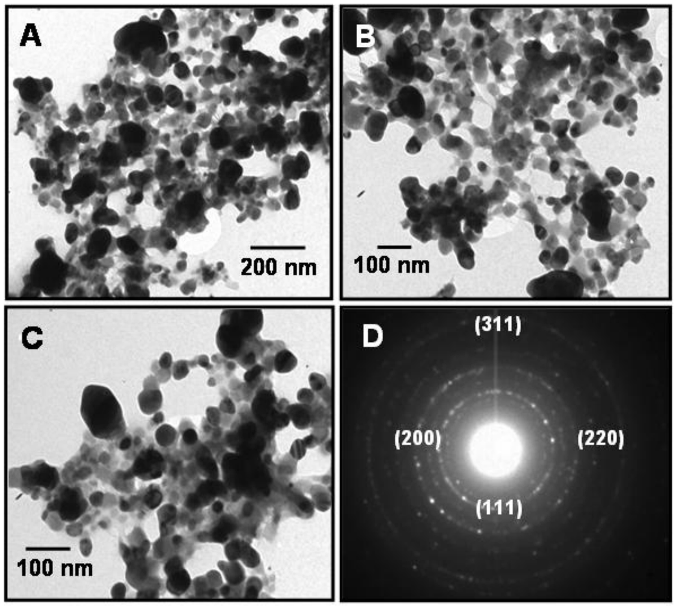

Figure 6.5 *TEM images of silver nanoparticles synthesized by reaction between 0.1% pyoverdin and 10^{-3} M $AgNO_3$ solution after incubation for 6 h. (A-C). SAED pattern obtained from silver nanoparticles indicates their crystalline nature and the diffraction pattern was indexed on the basis of FCC structure of silver (D).*

The nanoparticles are irregular in shape with a broad particle size distribution. The overall size of silver nanoparticles appears to be in between 50 to 100 nm. The nanoparticles are not regularly separated and tend to form the aggregated structures. The nanoparticles are observed to be embedded in a continuous matrix consisting of the organic siderophore molecules as indicated by the lighter contrast at the periphery of silver nanoparticles (image C, Figure 6.5). Therefore, the overall structure appears as an interconnected network with high degree of irregularity. SAED analysis obtained from silver nanoparticles shows well defined diffraction rings indicating the crystalline nature of silver nanoparticles (image D, Figure 6.5). The diffraction pattern was readily indexed on the basis of FCC structure of silver. The corresponding *d* values for the respective crystal planes are as follows: 2.372 (111), 2.05 (200), 1.44 (220), 1.24 (311) [34].

6.2.4.2 UV-vis spectroscopic analysis

Figure 6.6A illustrates the UV-vis spectroscopic analysis of silver nanoparticles formation using 0.1% of pyoverdin solution as a function of time of reaction. Following the addition of 0.1% pyoverdin to 10^{-3} M $AgNO_3$ and subsequent incubation for 2 h**,** a weak absorption hump at 430 nm was observed (curve 1, Figure 6.6A). This absorption arises due to the surface plasmon resonance of silver nanoparticles, which is responsible for the bright yellow colour of the solution of silver nanoparticle. The absorption at 430 nm gradually increases in intensity with time (curve 2 and 3 in Figure 6.6A)

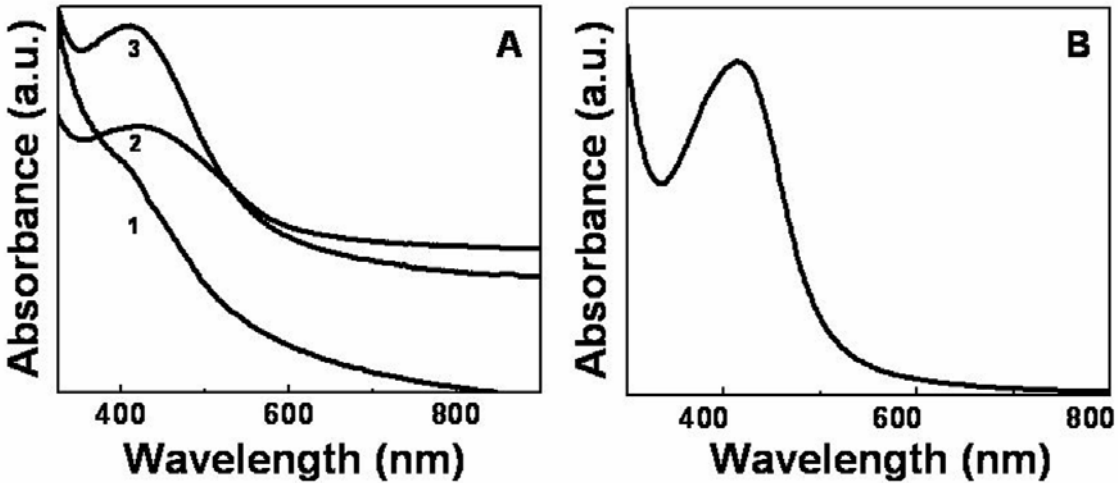

Figure 6.6 *(A) UV-vis spectroscopic analysis of silver nanoparticle synthesis by 0.1% pyoverdin as a function of time of reaction. Curve 1– 3 corresponds to pyoverdin – silver ions reaction mixture after 2, 4 and 6 h. (B) UV-vis spectrum recorded after 6 h of reaction from the solution of silver nanoparticles synthesized using 0.2% pyoverdin.*

After 6 h of the reaction no appreciable rise in the absorption intensity at 430 nm was observed indicating that the reaction is completed. Figure 6.6B shows the UV-vis spectrum obtained from the aqueous solution of silver nanoparticles synthesized using

0.2% pyoverdin. The SPR band of silver nanoparticles is centered at 430 nm as observed with the solution of silver nanoparticles synthesized using 0.1% pyoverdin. However the SPR band is prominent and sharper in comparison with silver nanoparticles synthesized using 0.1% pyoverdin (curve 3, Figure 6.6A).

6.2.4.3 FTIR spectroscopic analysis

Biological synthesis of silver nanoparticles can also be easily monitored by FTIR spectroscopic analysis as demonstrated in the case of gold particles. FTIR analysis was carried out on pyoverdin in powdered KBr before and after reaction with silver ions. FTIR analysis also enables following the interaction of pyoverdin molecules with the surface of silver nanoparticles, as indicated by the change in the positions of vibrational bands arising due to the various functional groups present in pyoverdin.

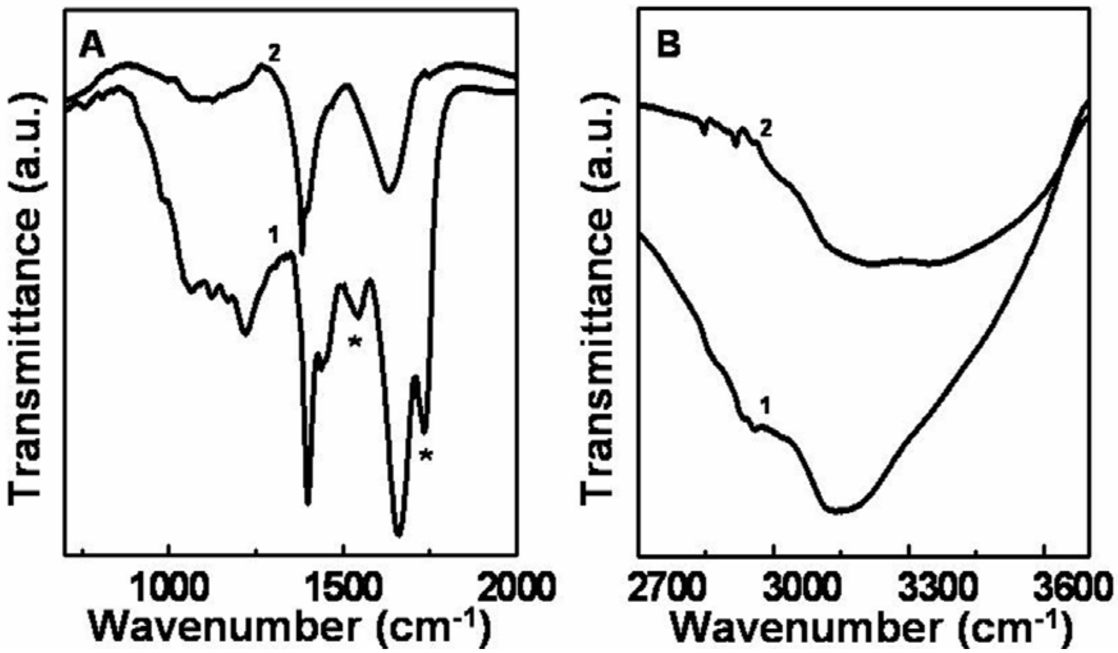

Figure 6.7 *(A) FTIR spectra of pyoverdin molecules before (curve 1) and after reaction with silver ions. Symbol "*" indicates the vibrational bands which are not observed after reaction with silver ions. (B) Enlarged view of the same spectra in amine and hydroxyl bonds vibration region.*

Figure 6.7 shows the FTIR spectra obtained from pyoverdin molecules before and after reaction with silver ions. Considerable variation is observed in the vibrational bands in the FTIR spectra of pyoverdin molecules before and after reaction with silver ions. Two distinct bands in the 1540 to 1670 cm^{-1} are assigned to vibrations of amide I and II bands that originates from the amide bonds present in the structure of pyoverdin. As observed earlier with gold particles, a prominent peak at 1663 cm^{-1} due to the amide I vibrational band in pyoverdin (curve 1, Figure 6.7A) is shifted towards lower wavenumbers to 1633 cm^{-1} (curve 2, Figure 6.7A) after reaction with 10^{-3} M $AgNO_3$, which is reduced to metallic silver. The amide II vibrational band at 1544 cm^{-1} observed from the FTIR spectrum obtained from unreacted pyoverdin molecules (curve2, Figure 6.7A). This indicates that –NH– group of peptide bond, which is responsible for amide II vibrations bands mat be involved in the reduction of silver ions. The shift in the amide I band vibration after reaction with silver ions could be due to the binding of –CO– group of pyoverdin on the surface of silver nanoparticles. The disappearance of the amide II vibrational band along with the shift in the amide I vibrational band indicates strong interaction between pyoverdin and silver ions.

6.2.5 Discussion

This part of the chapter describes the biological synthesis of gold and silver nanoparticles by the siderophore – pyoverdin isolated from *P.aeruginosa*. It is observed that flat triangular gold particles with edge length between 0.2 μm to 6 μm can be synthesized using pyoverdin as a reducing agent. The edge length of triangular and hexagonal gold particles was strongly dependent on the concentration of pyoverdin used for the reduction of gold ions. At lower concentration of pyoverdin (0.05%), triangular and hexagonal gold particles with edge length between 3 μm to 6 μm were predominantly formed. When 0.1% pyoverdin was used for the reduction of gold ions, triangular particles with the edge length in between 0.5 μm – 2 μm are synthesized. At higher concentration of pyoverdin, the formation of triangular gold particles with nearly uniform edge length of 200 nm to 250 nm were readily observed. The FTIR spectroscopic analysis performed on pyoverdin before and after reaction with gold ions indicated that amine groups of pyoverdin are likely to be involved in the formation of gold nanoparticles. FTIR analysis also indicated the possibility of some interaction between the surface of gold nanoparticles and pyoverdin molecules. Silver nanoparticles were also synthesized using pyoverdin as a reducing agent. However, no anisotropy in silver nanoparticles is observed as compared to gold. A large number of silver nanoparticles with irregular morphology were observed with dimension of 20 to 100 nm. In contrast to gold nanoparticles, no change in the size and shape of silver nanoparticles was observed when the concentration of pyoverdin was varied. FTIR analysis of pyoverdin molecules before and after reaction with silver ions indicated that carbonyl and amide groups are likely to be involved in either formation of silver nanoparticles or binding on the surface of silver nanoparticles.

6.3 Biological synthesis of gold and silver nanoparticles by the pigment – pyocyanin

6.3.1 Experimental details

Bacteria from the genus *Pseudomonas* are known to synthesize a number of different pigments, which give characteristic appearance to the bacterial colony [32]. *P. aeruginosa* synthesizes a blue – green pigment pyocyanin during the stationary phase of growth. Pyocyanin was isolated from *P.aeruginosa* using a broth culture as described previously [38]. Freshly inoculated bacterial culture was grown overnight in 2 ml of LB medium, which was further used as a seed culture for bacterial propagation in 100 ml LB in a 500 ml Erlenmeyer flask. The flask was incubated at 30 °C on the rotary shaker (200 rpm) and incubated for 72 h until the medium showed a dark green colour. The bacterial biomass was then separated from the rest of the medium by centrifugation at 7000 rpm. The colored supernatant was isolated in another sterilized conical flask and the pH of the supernatant was adjusted to 2 with concentrated hydrochloric acid (HCl). This acidified supernatant was repeatedly treated with the equal volume of chloroform until all the blue – green colored part was transferred to the chloroform phase. The chloroform layer was then subjected to alternative extractions with acidified and neutral water layers to allow the separation of red, acid form, and blue – green forms of pyocyanin. After five such conversions the pyocyanin was crystallized by evaporation of chloroform, washed with the deionised water and dried to a powder. Pyocyanin was solubilized in deionised water before use for the synthesis of gold and silver nanoparticles. Thin layer chromatography (TLC) was performed to assess the formation and purity of pyocyanin by applying the extracted pyocyanin to Silicagel 60F254 TLC plates (Merck). The plate was developed using chloroform-acetic acid-methanol (90:5:2.5 vol/vol/vol) solvent system and visualized under UV light (λ 305 nm) for detection of fluorescence signal. Gold and silver nanoparticles were synthesized by reacting 10^{-3} M of $HAuCl_4$ and $AgNO_3$ respectively with 0.1% of purified pyocyanin in the final reaction volume of 10 ml. Gold and silver nanoparticles so obtained were characterized by TEM, UV-vis-NIR spectroscopy, X-ray diffraction, and FTIR spectroscopy.

6.3.2 Isolation and purification of pyocyanin

After growth of *P.aeruginosa* in LB medium for 48 h, the colour of the growth medium became dark and blue–green as observed visually. When the cell free supernatant was repetitively extracted with equal volume of chloroform, pyocyanin was transferred to the chloroform phase as indicated by the blue–green coloration of the organic layer. After evaporation of the chloroform layer, pyocyanin was dissolved in deionised water.

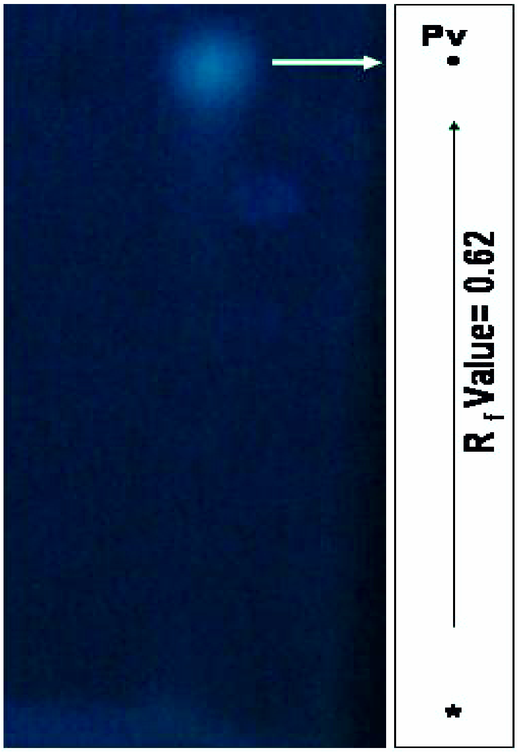

Figure 6.8 *A photograph of TLC plate showing the migration of pyocyanin in chloroform: acetic acid: ethanol solvent system. A single spot of pyocyanin showing bluish green fluorescence in the UV-light (λ 305 nm) was observed. "*" indicates the origin, at which pyocyanin sample is spotted, while "•" indicates the final position of the spot after migration in the solvent system mentioned above.*

Presence of pyocyanin was indicated by UV spectroscopic analysis, where a strong absorption at 360 nm was observed. Purity of the pyocyanin was checked by TLC analysis. Figure 6.8 shows a picture of TLC plate after irradiation with UV light that shows the presence of a single spot. The TLC plate irradiated with the UV light (λ 305 nm) showed the presence of single spot, which emitted bluish – green fluorescence. The R_f value calculated for pyocyanin was found to be 0.62 [38].

6.3.3 Biological synthesis of gold nanoparticles by Pyocyanin

6.3.3.1 TEM analysis

Representative TEM images of gold nanoparticles obtained from the reaction of 0.1% pyocyanin with 10^{-3} M aqueous chloroauric acid solution at different magnifications are shown in Figure 6.9. A highly dense population of gold nanoparticles was obtained after 7 h of reaction. At low magnification (image A & B, Figure 6.9) large population of spherical gold nanoparticles can be observed. Uniformity in the size of gold nanoparticles with a narrow size distribution is a significant achievement of the biological synthesis method described here.

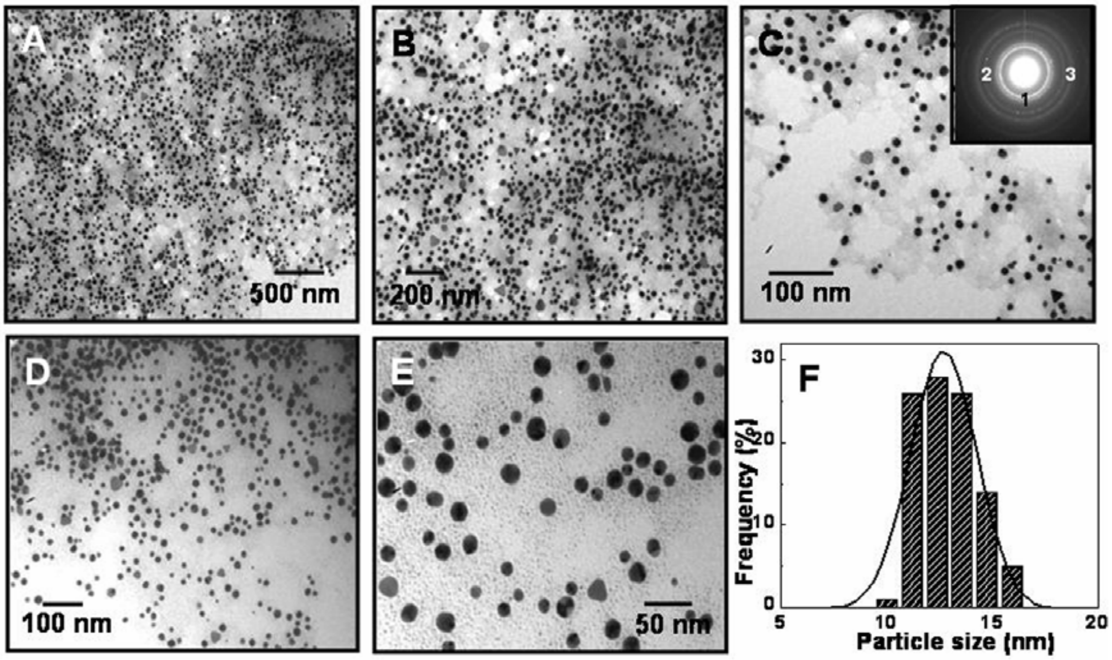

Figure 6.9 *Representative TEM images of gold nanoparticles obtained by the reaction between 0.1% pyocyanin and aqueous chloroaurate ions at different magnifications (A-E). The inset in E shows SAED pattern obtained from gold nanoparticles. Rings 1, 2 and 3 correspond to (111), (200) and (220) set of lattice planes respectively. (F) A histogram of particle size distribution in gold nanoparticles synthesized using pyocyanin.*

The high magnification image (image E, Figure 6.9) obtained from gold nanoparticles also shows a small number of triangular particles with edge length of ~15 nm. Particle size distribution analysis performed on 100 particles in different micrographs indicated that the average diameter of gold nanoparticle was centered at 12.7 nm with a standard deviation of 1.57 nm (image F, Figure 6.9). SAED analysis indicates the crystalline nature of gold nanoparticles and the diffraction pattern was indexed on the basis of FCC structure of gold (inset in image C, Figure 6.9). The corresponding *d* values for the respective crystal planes are as follows: 2.36 (111), 2.06 (200), 1.44 (220) [34].

6.3.3.2 UV-vis spectroscopic analysis

Reduction of gold ions and the formation of gold nanoparticles by pyocyanin can be easily followed by UV-vis spectroscopy. Figure 6.10 shows UV-vis spectroscopic analysis performed on gold nanoparticles synthesized using 0.1% pyocyanin as a reducing agent. UV-vis spectroscopic analysis of chloroaurate ion reduction indicates that reaction is completed in six hours.

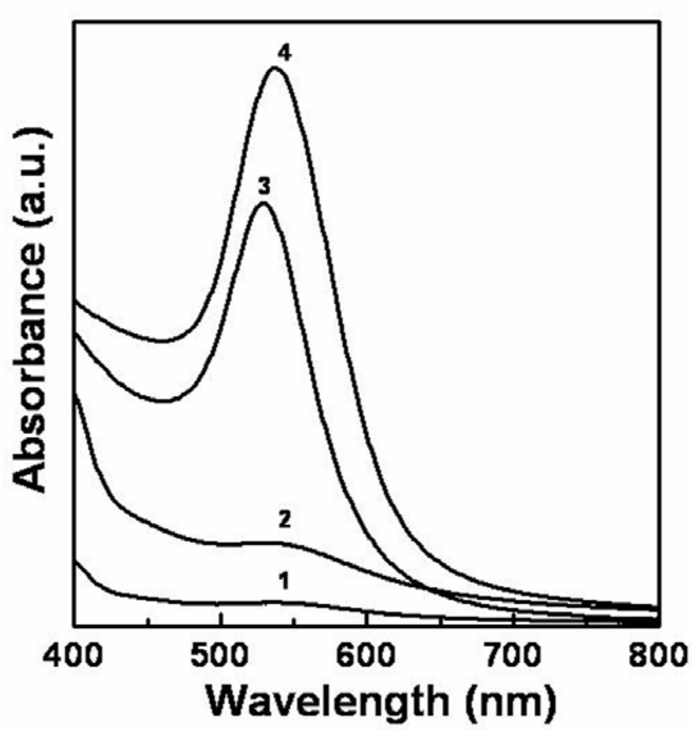

Figure 6.10 *UV-vis spectroscopic analysis of the formation of gold nanoparticles using pyocyanin. Gradual rise in the absorption at 540 nm shows that the number of gold nanoparticles increases with time. Curves 1-4 indicate the progress of the reaction after 1, 2, 4 and 6 h respectively.*

It is observed that the formation of gold nanoparticles begins after 1 h of reaction between 0.1% pyocyanin and aqueous chloroaurate ions as indicated by a weak absorption at 545 nm, which is due to the surface plasmon resonance of gold nanoparticles (curve 1, Figure 6.10). As the reaction progresses, the population of gold nanoparticles increases steadily. During the 4 h of reaction large number of gold nanoparticles is accumulated in the solution as indicated by the sharp and intense SPR band (curve 3, Figure 6.10). This is indicated by the sharp rise in the SPR absorption band, which is stabilized after 6 h, where no further increase in SPR absorption band intensity is observed (curve 4, Figure 6.10). A sharp SPR peak after complete reduction of chloroaurate ions may be due to the narrow size distribution of gold nanoparticles.

6.3.3.3 FTIR analysis

FTIR analysis of pyocyanin before and after the reduction of chloroaurate ions was done in KBr powder and the spectra are shown in Figure 6.11. The FTIR analysis shows a number of vibrational bonds, which corresponds to the various functional groups present in pyocyanin molecules (curve 1, Figure 6.11A and B).

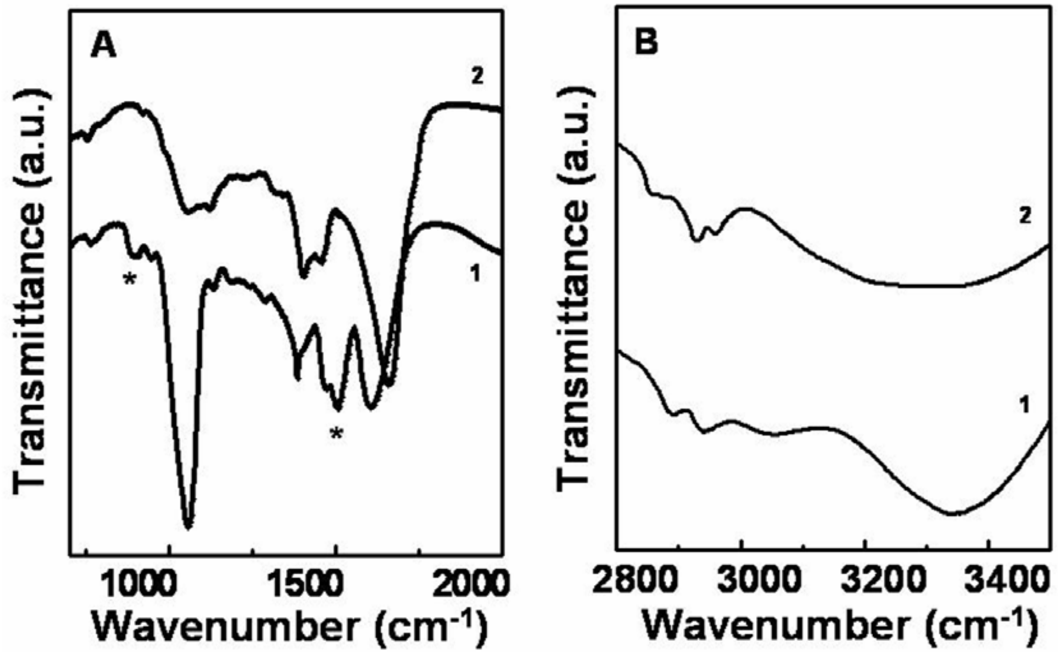

Figure 6.11 (A) *FTIR spectra obtained from pyocyanin before (curve 1) and after reaction with aqueous chloroaurate ions (curve 2). Symbol "*" indicates the vibrational bands that are absent from curve 2, which corresponds to the FTIR spectrum of gold nanoparticles obtained by reaction of pyocyanin and chloroauric acid. (B) Enlarged view of the same spectra in amine and hydroxyl groups absorption region.*

All the major vibrational bands corresponding to the respective functional groups are listed in Table 2. A substantial variation is observed in the 1500 cm^{-1} to 1700 cm^{-1} region of the spectrum after reaction with chloroauric acid (curve 2, Figure 6.11A). A region of the spectrum in between 1450 cm^{-1} to 1650 cm^{-1} corresponds to the stretching vibration bands of C = C of aromatic rings. The disappearance of a sharp absorption band at 1509 cm^{-1} from the spectrum corresponding to pyocyanin treated with chloroaurate ions (curve 2, Figure 6.11A) could be due to the loss of the aromatic character of pyocyanin ring structure. Also, a prominent absorption band at 1603 cm^{-1} is shifted at 1657 cm^{-1} indicating the possibility of alteration in the aromatic character of pyocyanin after reacting with chloroaurate ions (curve 2, Figure 6.11A).

Table 6.2 *Vibration frequency assignment for the peaks observed in the FTIR spectra of pyocyanin before and after reaction with chloroaurate ions represented by the curves 1 and 2 in Figure 6.10 respectively* [37].

Vibration modes	Pyocyanin (cm^{-1})	Pyocyanin treated with chloroaurate ions (cm^{-1})
C – H of aromatic ring	896	– –
C – O (ν)	1056	1060
C – O (ν)	1120	1132
CH_3 (δ)	1387	1400
O – C – H (δ), CH_2 (δ)	1458	1470
C = C of aromatic ring	1508	– –
C = C of aromatic ring	1603	1657
CH_3 (ν)	2895	2930
C – H	3058	– –
O – H	3344	3345
(δ) bending vibrations, (ν) stretching vibration		

Out of plane C–H bond vibration of the aromatic ring present in pyocyanin was not observed in the spectrum of pyocyanin after reaction with chloroauric acid (curve 2, Figure 6.11A). This observation also indicates that the aromaticity from pyocyanin ring structure could be altered after reaction with chloroaurate ions. The ring nitrogen of pyocyanin can donate one electron and get oxidized. This feature is observed in the FTIR spectrum, where 3058 cm^{-1} absorption band disappears from the spectrum corresponding to pyocyanin after the reaction with chloroauric acid (Curve 2, Figure 6.11B). Thus from FTIR spectrum it can be concluded that the pyocyanin can be also involved in the binding on the surface of gold nanoparticles.

6.3.4 Biological synthesis of silver nanoparticles using Pyocyanin

Pyocyanin can also mediate the extracellular electron transfer reaction during the metabolism of *P.aeruginosa* and thus is capable of reduction of many metal ions. Anisotropic silver nanoparticles were obtained after reduction of silver ions with pyocyanin. We have developed here a new protocol for biological synthesis of silver nanoparticles.

6.3.4.1 TEM analysis

Pyocyanin shows greater affinity towards silver ions, as the mixing of pyocyanin with the solution of silver ions readily results in their reduction and the formation of silver nanoparticles. Figure 6.12 shows representative TEM images of pyocyanin reduced silver ion solution after 30 min of the reaction. Large number of nanoparticles with different morphologies like wires, triangles, pentagons, hexagons and spindles are observed after reaction of 0.1 % pyocyanin and the aqueous solution of 10^{-3} M $AgNO_3$. The wire-like structures with high aspect ratio are predominantly present on the grid surface (image A-E, Figure 6.12). The wire-like structures are found to be continuous and with interconnecting junctions. The thickness of silver nanowire is found to be around 30 nm, while length is up to 3 μm. Silver nanoparticles appears to be aggregated at the junction point from where the nanowires branch out.

Along with the wire-like structures, triangular and pentagonal silver nanoparticles with edge length of 100 nm to 300 nm are observed. However, the overall population of these structures was less in comparison with the wires. Insets in C and F shows the representative images of such triangular and pentagonal silver nanoparticle present along with the wire-like structures. The triangular and pentagonal structures show multiple twinning. A high magnification image of one of such pentagon clearly shows multiple twin boundaries in five-fold symmetry (Inset in Figure 6.12B). Reduction of silver ions by pyocyanin also results in the formation of spindle shaped silver nanoparticles, which are 100 nm to 200 nm long (image F, Figure 6.12). Inset in image E shows the SAED pattern obtained from silver nanoparticles, which indicates the crystalline nature of silver nanoparticles.

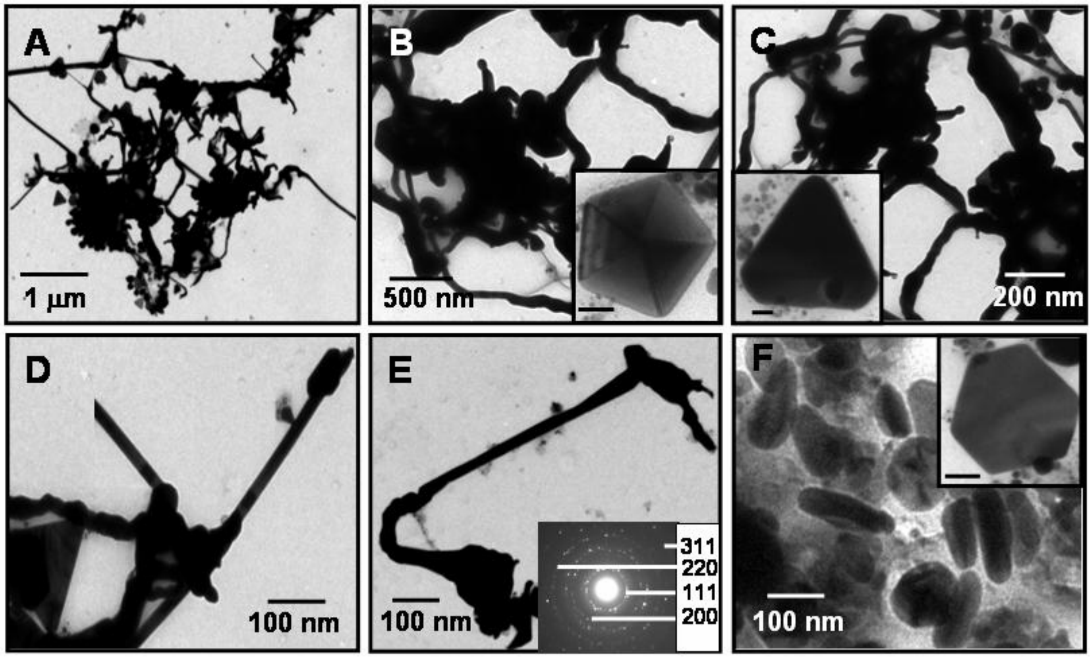

Figure 6.12 *(A–F) Representative TEM images of silver nanoparticles obtained by reaction between silver ions and pyocyanin. Various anisotropic structures like wires, triangles and pentagons were observed. Insets in B, C and F show a pentagon, triangle and hexagon nanoparticles respectively. The scale bar for the images in the inset is 50 nm. The inset in E shows the SAED pattern obtained from silver nanoparticles shown in the main images.*

The diffraction pattern is in good agreement with the FCC structure of silver. Respective *d* values for the corresponding crystal planes are as follows: 2.374 (111), 2.05 (200), 1.44 (220), 1.24 (311) [34]

6.3.4.2 UV-vis spectroscopic analysis

When silver ions were reacted with pyocyanin, the originally colorless reaction medium changed to yellow after 10 min of incubation at 37 °C, which eventually became yellowish brown after 30 min and finally dark brown after 60 min of reaction. Time dependent UV-vis spectra recorded from the aqueous silver nitrate-pyocyanin reaction mixture are shown in Figure 6.13. The reaction between pyocyanin and silver ions is considerably faster and was complete within 1 h in comparison with the reduction of gold ions by pyoverdin as discussed earlier. The faster reduction of silver ions could be due to the greater affinity of pyocyanin molecules toward silver ions. A characteristic absorption at 440 nm is observed after 15 minutes of the reaction as observed from the curve 1 in

Figure 6.13. This absorption in the region of 420-440 nm is due to the surface plasmon resonance (SPR) of silver nanoparticles.

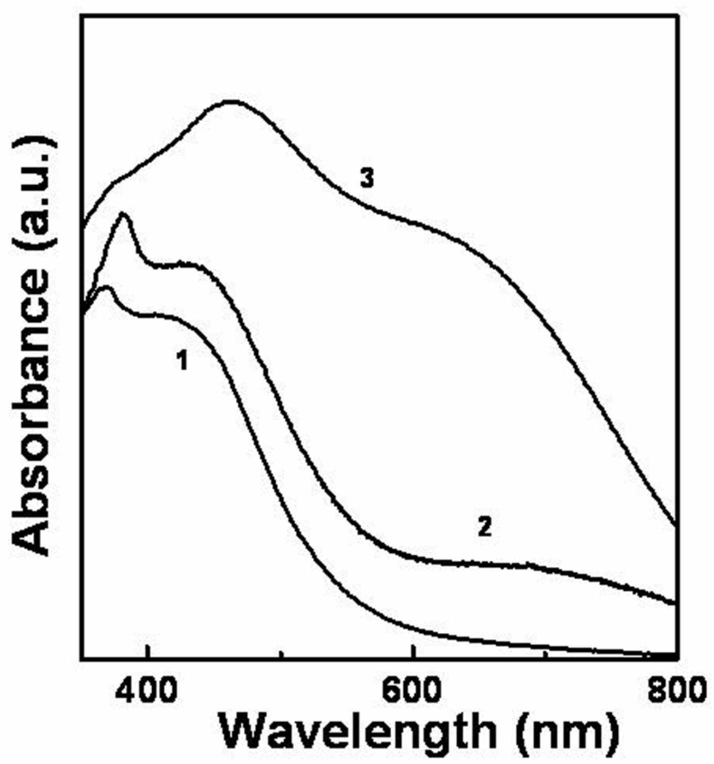

Figure 6.13 *UV-vis spectra recorded from silver nanoparticles synthesized by reaction between pyocyanin and silver ions. The UV-vis spectra were recorded as a function of time, which indicate rise in the SPR absorption intensity. The occurrence of longitudinal SPR absorption band indicates the presence of anisotropic silver nanoparticles. Curves 1 to 3 indicate the progress of reaction after 15, 30 and 60 minutes.*

The SPR absorption at around 440 nm is accompanied by a small sharp absorption band at 390 nm after 15 min of the reaction, which further shifts to 395 nm after 30 min of reaction (curve 2, Figure 6.13). However, this absorption band is not observed after 60 min of reaction (curve 3, Figure 6.13). The SPR band at 440 nm shows gradual increase in the intensity with time. After 60 min of reaction, the SPR absorption band at 440 nm red shifts with the absorption maxima centered at 475 nm (curve 3, Figure 6.13). The shift in the SPR absorption band at 440 nm indicates some degree of aggregation in silver nanoparticles. TEM images obtained from the reaction mixture after 60 min of reaction indeed showed the aggregation in silver nanoparticles (images A-C, Figure 6.12). After 30 min of reaction the SPR band at 440 nm is accompanied with a weak absorption at 680 nm (curve 2, Figure 6.13). This absorption band shows increase in intensity after 60 min of reaction and can be either due to aggregation of nanoparticles or presence of anisotropic nanoparticles or a combination of both [5] (curve 3, Figure 6.13). UV-vis spectroscopic analysis is in good agreement with the TEM analysis, which indicated the presence of aggregated silver nanoparticles as well as anisotropic structures like wires, triangles, and spindles. The SPR band at 440 nm can be assigned to the transverse component of silver nanoparticles and occurs due to the out of plane collective electronic oscillations, while the SPR band at 680 nm corresponds to the longitudinal component and originates due to the in-plane electronic oscillations [39]. No further increase was observed in intensity of the SPR absorption band after 60 min of the reaction indicating that all silver ions have been converted into silver nanoparticles (curve 3, Figure 6.13).

6.3.4.3 FTIR analysis

The reduction of silver ions and the formation of silver nanoparticles can be analyzed by FTIR spectroscopy. FTIR analysis carried out on pyocyanin before and after reaction with silver ions indicates a number of vibrational bands characteristic of the functional groups present in the structure of pyocyanin (Figure 6.14). Curve 1 in Figure 6.14 corresponds to the spectrum obtained from pure pyocyanin molecules while curve 2 in Figure 6.14 indicates the spectrum of pyocyanin – $AgNO_3$ reaction mixture after the reduction of silver ions and formation of silver nanoparticles. Most of the features in curve 2 of Figure 6.14 are similar to the FTIR spectrum obtained from pyocyanin – chloroaurate ion reaction mixture.

Considerable variation is observed in the 1500 cm^{-1} to 1700 cm^{-1} region of the spectrum after reaction with silver ions (curve 2, Figure 6.14A). Loss of a sharp absorption band at 1509 cm^{-1} initially present in curve 1 of Figure 6.14A could be due to the loss of aromatic character of pyocyanin ring structure. Further, the wide absorption band at 605 cm^{-1}, which corresponds to C = C bond vibrations in aromatic ring is found to be reduced in the intensity (curve 2, Figure 6.14A). A sharp absorption band at 1032 cm^{-1} in pyocyanin molecule corresponds to the C–O bond stretching vibrations (curve 1, Figure 6.14A). After reaction with silver ions, this absorption band shows shift towards higher wavenumber with the loss in intensity (curve 2, Figure 6.14A). This observation indicates that pyocyanin molecules may be involved in the capping of the surface of silver nanoparticles.

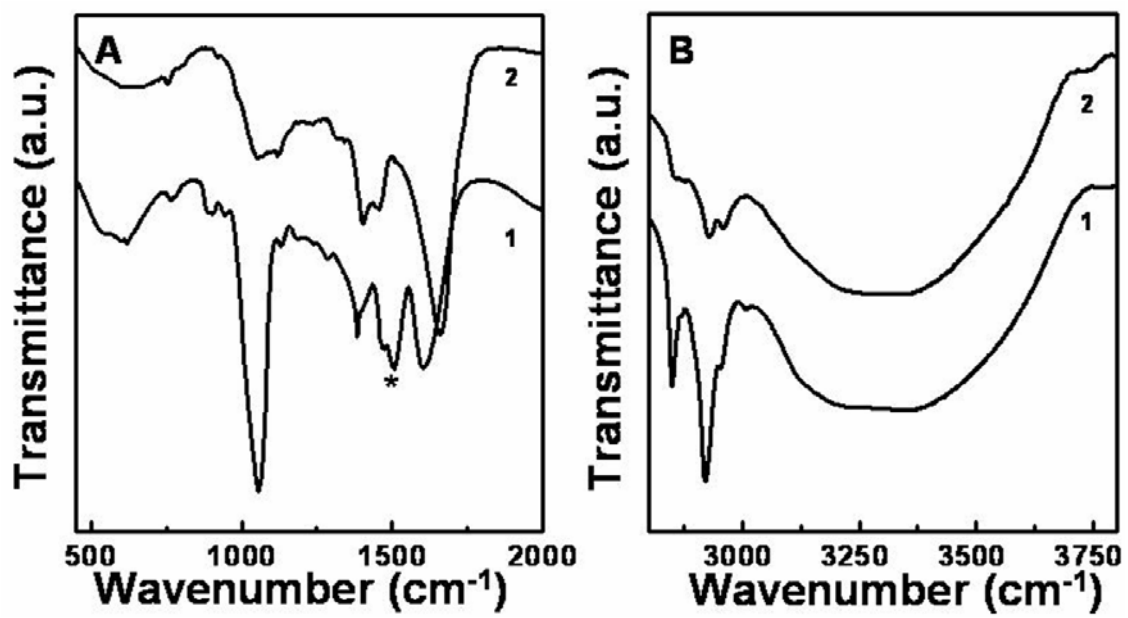

Figure 6.14 *(A) FTIR spectra obtained from the purified pyocyanin (curve 1) and pyocyanin-silver ion reaction mixture after the reduction of silver ions and the formation of silver nanoparticles (curve 2). Symbol "*" indicates the vibrational bands not observed in the curve 2. (B) Enlarged view of the same spectra in the 2900 cm*$^{-1}$ *to 3800 cm*$^{-1}$*.*

A sharp absorption band in the region 2850 cm^{-1} to 2970 cm^{-1} corresponds to the asymmetric and symmetric stretching vibrations arising due to the C–H bond in CH_3 group and the aromatic ring of pyocyanin (Figure 6.14B). In pyocyanin – silver ion reaction mixture the CH_3 band vibrations appear as a weak shoulder (curve 2, Figure 6.14B). Figure 6.14B shows the enlarged view of the same spectra and corresponds to the amine and hydroxyl group vibrations in pyocyanin molecule (curve 1, Figure 6.14B). Not much change in the amide and hydroxyl vibrational bands are observed after the reaction of pyocyanin molecules with silver ions (curve 2, Figure 6.14B).

6.3.5 Discussion

In this section of the chapter, synthesis of gold and silver nanoparticles using the pigment molecule, pyocyanin, from *P.aeruginosa* has been described. Pyocyanin is considered as a secondary metabolite since it is synthesized in the stationary phase of the bacterial growth. Gold nanoparticles with nearly uniform size were obtained by the reaction between an aqueous solution of chloroaurate ions and pyocyanin. The mean diameter of gold nanoparticles was found to be 12.7 nm with a standard deviation of 1.6

nm. Pyocyanin was also capable of synthesizing silver nanoparticles when reacted with silver ions. A number of anisotropic nanoparticles such as wires, triangles, pentagons and spindles were obtained after 60 min of the reaction between silver ions and pyocyanin. The edge length of triangular, pentagonal and spindle-like silver nanoparticles was observed to be around 100 to 300 nm. Nanowires of silver were measured to be 30 nm in diameter and were up to 3 μm in length. UV-vis spectroscopic analysis performed on silver nanoparticles further showed the characteristic feature of anisotropic structures. The FTIR spectroscopic analysis performed on the pyocyanin–chloroaurate ions and pyocyanin–silver ions indicated that pyocyanin can interact with gold and silver nanoparticles.

6.4 Bacterial enzyme mediated biosynthesis of gold nanoparticles

This section of the chapter illustrates the bacterial enzyme as a mean to synthesize gold nanoparticles. It has been conclusively shown that presence of protein hydrolyzing enzyme-protease accelerates the rate of gold nanoparticle biosynthesis by *Actinobacter spp*. Also, the oxygen deficiency in the experimental conditions is shown to have a drastic effect on the morphology of gold nanoparticles. Presence of the protein Bovine serum albumin (BSA) triggers the induction of protein hydrolyzing enzyme protease which can accelerate the synthesis of gold nanoparticles.

6.4.1 Experimental details

The biosynthesis of gold nanoparticles was carried out at 37 °C under aerobic as well as anaerobic conditions using *Actinobacter* spp. In all the experiments bovine serum albumin (BSA) was added to the reaction mixture leading to final concentration of 3 mg/ml. Soil bacterium *Actinobacter Spp.* was grown and cultured as follows. The seed culture was inoculated in 100 ml of LB medium. The flask was incubated at 37 °C for 48 h on a shaker (150 rpm). For the synthesis of gold nanoparticles at 37 °C, 0.5 g of the bacterial biomass was harvested from the culture medium by centrifugation at 5000 rpm and inoculated in 500 ml Erlenmeyer flask containing 100 ml of autoclaved aqueous solution of 10^{-3} M $HAuCl_4$. Filter sterilized BSA (Bovine serum albumin) was added to the above solution leading to the final concentration of 3 mg/ml as an inducer of the enzyme protease. The flask was then kept on a shaker (150 rpm) at 37 °C and reaction was carried out for 12 h. Biologically reduced gold nanoparticles were collected from the reaction mixture under sterile conditions by centrifugation at 5000 rpm and used for characterization. Aliquots were taken at different time intervals from the reaction medium to monitor the progress of the reaction. For the reduction of $HAuCl_4$ under anaerobic conditions, the bacterial biomass was harvested and processed as described above. The bacterial biomass was placed in a surface sterilized rectangular glass container containing 100 ml of autoclaved 10^{-3} M $HAuCl_4$ and filter sterilized BSA (3mg/ml). Bioreduction of $HAuCl_4$ was carried out under anaerobic conditions generated by passing nitrogen gas at fixed flow rate (5 psi). The reaction was carried out for 4 h and aliquots containing gold nanoparticles were periodically removed for characterization. Bioreduction of $HAuCl_4$ was monitored by recording the UV-vis spectra as a function of time of reaction.

To establish the role of enzyme protease in the synthesis of gold nanoparticles, 100 μg of commercial fungal protease (source- *Aspergilus saitoi*, sigma chemicals) was reacted with 10^{-3} M $HAuCl_4$ in glycine – HCl buffer (0.05 M, pH 3.0). Final volume of the reaction mixture was kept 10 ml and the reaction was carried out for the period of 8 h at 37 °C. The bacterial reaction supernatant was analyzed for protease activity. In all the experiments the reaction mixture containing the bacterial biomass, BSA and $HAuCl_4$ were subjected to the centrifugation at 5000 rpm. In all the experiments, where the presence of protease activity was expected from the culture supernatant, protease assay was performed using hemoglobin as a substrate. The standard reaction mixture contained 1ml of 5 % (w/v) hemoglobin in glycine – HCl buffer (0.05 M, pH 3.0) and 200 µl of the supernatant containing enzyme. After the incubation at 37 °C for 30 minutes, 1 ml of 1.7 mM perchloric acid (PCA) was added to terminate the reaction. Then the mixture was left undisturbed for 30 minutes at room temperature. The undigested material was removed by filtration (Whatman number 1). Proteolytic activity was measured as the increase in the absorbance at 280 nm of PCA soluble fraction. The appropriate blanks were made by adding PCA before the enzyme. One unit of proteolytic activity was defined as the amount of enzyme required to increase the absorbance by 0.001 under the conditions previously described [40]. To verify the presence of aspartic protease in solution, pepstatin was used as a standard inhibitor at 2 μM concentration from a concentrated stock of 1 mg/ml. To elucidate the role of protease in the synthesis of gold nanoparticles, *Actinobacter spp*. was grown in minimal medium. 10 ml of culture supernatant of the minimal medium containing protease was mixed with 10^{-3} M $HAuCl_4$ in the absence and presence of the protease inhibitor pepstatin at a final concentration of 2 μM. The reaction was carried out for 8 h. Different control experiments were performed to show the role of protease enzyme in the synthesis and shape control of gold nanoparticles. In the first control experiment, bacterial reduction of $HAuCl_4$ was carried out in absence of BSA under aerobic as well as anaerobic conditions as discussed above. In another control experiment, the aqueous $HAuCl_4$ was mixed with BSA in the absence of *Actinobacter* spp. and incubated under the aerobic and anaerobic conditions with similar reaction conditions.

6.4.2 TEM analysis

Figure 6.15 shows TEM images obtained from gold nanoparticles reduced using *Actinobacter* spp. in the presence of BSA under the aerobic and anaerobic conditions. TEM images of gold nanoparticles synthesized under aerobic conditions show mixed population of flat nanoparticles with irregular morphology along with the few triangular particles (images A & B, Figure 6.15). A fair degree of aggregation is also observed within the nanoparticles. The edge length of the triangular particles varied between 250 – 500 nm. Insets in image A and B shows the representative TEM images of triangular and hexagonal gold particles that appear with the aggregated spherical gold nanoparticles. SAED pattern obtained from one of the triangular gold particles is shown in image C. SAED pattern indicates that each gold nanotriangle is a single crystal and the diffraction spots are in good agreement with the FCC structure of gold.

A considerable variation occurs in the morphology of gold nanoparticles when synthesized under anaerobic conditions. Images D, E and F in Figure 6.15 correspond to the TEM micrographs of gold nanoparticles synthesized under anaerobic conditions. Nearly uniform size spherical gold nanoparticles of 10 nm diameter are observed. Further, almost half the population of gold nanoparticles shows triangular morphology. The gold nanotriangles observed here are small with edge lengths measuring 30 – 50 nm. The vertices of the triangles are not truncated or sharp, but instead appear blunt unlike in previous studies [11]. Inset in F shows linear arrangement of triangular and spherical nanoparticles. Inset in image E shows the SAED pattern obtained from gold nanoparticles shown in image E. The SAED pattern indicates the crystalline nature of gold nanoparticles and the diffraction pattern is in well agreement with the FCC structure of gold.

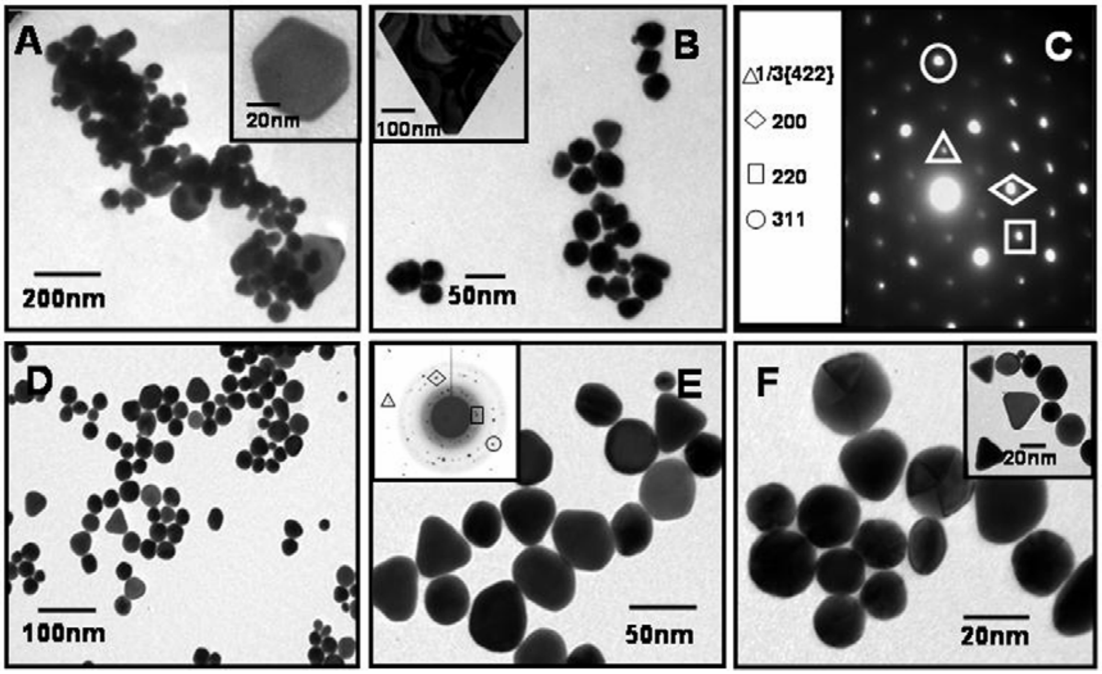

Figure 6.15 *TEM images of gold nanoparticles obtained by the reaction between aqueous chloroaurate ions and Actinobacter spp. under aerobic conditions (A and B). The SAED pattern obtained from gold nanoparticles shown in A and B indicates that the flat gold particles are single crystalline (C). TEM images of gold nanoparticles synthesized under anaerobic conditions (D to F). The inset in E shows SAED pattern of gold nanoparticles synthesized under anaerobic conditions. Crystal planes are shown with different symbols as follows- □ (111), ◊ (200), ○ (220) and Δ (311) while inset in F shows the presence of small triangular gold nanoparticles.*

The corresponding *d* spacing for the respective crystal planes are as follows: 2.357 (111), 2.063 (200), 1.442 (220) and 1.23 (311) [34]. From TEM images it is clear that presence or absence of atmospheric oxygen drastically alters the morphology of gold nanoparticles synthesized in presence of BSA.

6.4.3 UV-vis spectroscopic analysis

Figure 6.16 shows the UV-vis spectroscopic analysis of gold nanoparticles synthesized using *Actinobacter* spp. in presence of aerobic and anaerobic conditions. Figure 6.16A corresponds to the time dependent UV–vis spectroscopic analysis indicating the progress of the synthesis of gold nanoparticles under aerobic conditions. The SPR band originating from gold nanoparticles appears at 550 nm after 3 h of reaction (curve 1, Figure 6.16A) and gradually increases in intensity with time. No additional absorption band corresponding to anisotropy in the shape of nanoparticles is observed and this may be due to very small population of triangular particles present in the solution. At the initial stage of reaction, SPR shows broad absorption band (curve 1 and 2, Figure 6.16A), which became sharper with the progress of reaction (curve 3–5, Figure 6.16A).

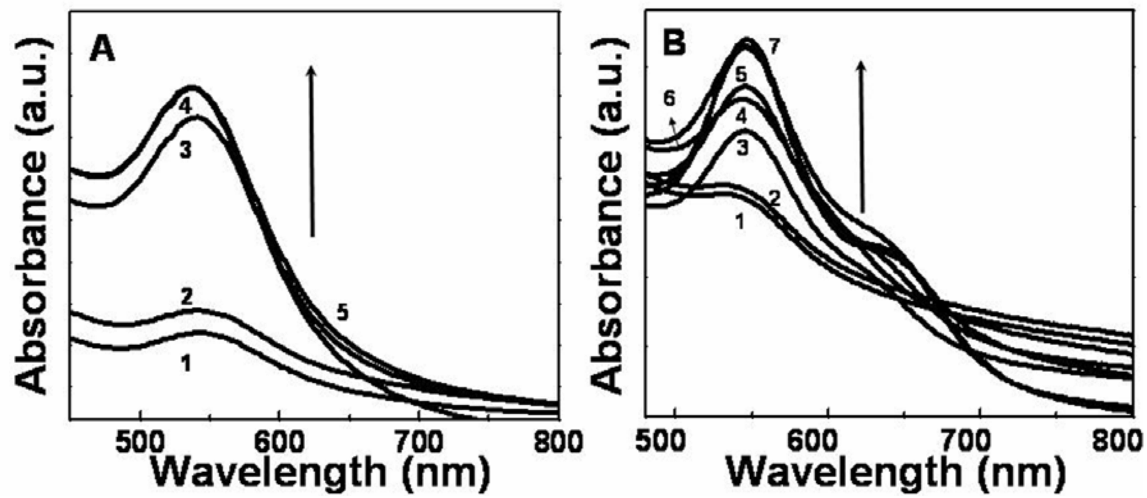

Figure 6.16 *UV-vis spectroscopic analysis of the formation of gold nanoparticles using Actinobacter spp. in the presence of BSA under (A) aerobic and (B) anaerobic conditions. Number 1 to 5 in (A) correspond to the UV-vis spectra recorded after 3, 6, 9, 12 and 15 h of the reaction under aerobic conditions, while number 1 to 7 in (B) correspond to the UV-vis spectra recorded after 0.5, 1, 1.5, 2, 2.5, 3, 3.5 h of the reaction under anaerobic conditions.*

The reaction is completed after 12 h as indicated by the saturation of SPR absorption band, which do not rise in intensity after 12 h (curve 5 corresponding to 15 h, Figure 6.16A). Figure 6.16B shows the UV-vis spectroscopic analysis of gold nanoparticle synthesis under anaerobic conditions as a function of time. Under anaerobic conditions, the formation of gold nanoparticles is faster as compared to the aerobic conditions. The SPR absorption band due to the formation of gold nanoparticles appears at 550 nm at the initial stages of the reaction (Curve 1 and 2, Figure 6.16B). Complete reduction of the aqueous chloroaurate ions occurs in 3 h and no further increase in the intensity of SPR band occurs (Curve 6 and 7, corresponding to 3 and 3.5 h, Figure 6.16B). A weak absorption band with intensity maxima cantered at 650 nm is developed after 1 h of reaction. This absorption band also increases in intensity with time and corresponds to the longitudinal SPR absorption. This additional plasmon band can be attributed to the in-plane plasmon resonance of the triangular gold nanoparticles. These time-dependent features are characteristic of formation of gold nanoparticles that aggregate with time or formation of anisotropic particles whose aspect ratio increases with time, or a combination of both processes [4]. This observation is in agreement with the TEM images which showed the presence of number of small triangular and hexagonal gold nanoparticles.

6.4.4 Induction of protease from Actinobacter spp. and its role in the accelerated synthesis of gold nanoparticles

The presence of biological molecules like proteins in the growth medium is known to induce hydrolytic enzymes proteases that hydrolyze proteins/peptides extracellularly [29]. Keeping this fact in mind, we hypothesize here that extracellular protease secreted by the bacterium *Actinobacter* spp. could be involved in the synthesis of gold nanoparticles. To check this hypothesis we carried out various experiments where the enzyme activity was assayed for protein hydrolysis. When chloroaurate ions were reduced by *Actinobacter* spp. in the presence of BSA under aerobic as well as anaerobic conditions, it was found that the reaction supernatant containing gold nanoparticles indeed had intrinsic proteolytic activity.

In another experiment, *Actinobacter* spp. was grown in M9 minimal medium containing BSA (3 mg/ml) as a sole source of nitrogen for the cellular growth and metabolism. The bacterial cells are usually grown in minimal medium in the presence of inducer for induction of desired hydrolytic enzymes. The culture supernatant was then assayed for the protease activity after 12 hrs of incubation using hemoglobin as a substrate, which is one of the standard assay substrate for protease [40]. This culture supernatant when reacted with 10^{-3} M $HAuCl_4$ and incubated for about 8 h was found to yield gold nanoparticles readily as shown by the TEM analysis. Images A and B in Figure 6.17 correspond to the TEM analysis of gold nanoparticles synthesized by the culture supernatant of *Actinobacter* spp. grown in M9 medium supplemented with BSA. Spherical gold nanoparticles of ~ 10 nm diameter are observed along with the triangular nanoparticles with edge lengths around 20 nm (image B, Figure 6.17). The UV-vis spectroscopic analysis performed on gold nanoparticles synthesized by the culture supernatant of *Actinobacter* spp. grown in M9 medium and supplemented with BSA shows characteristic SPR absorption band at 540 nm (curve 2, Figure 6.17C).

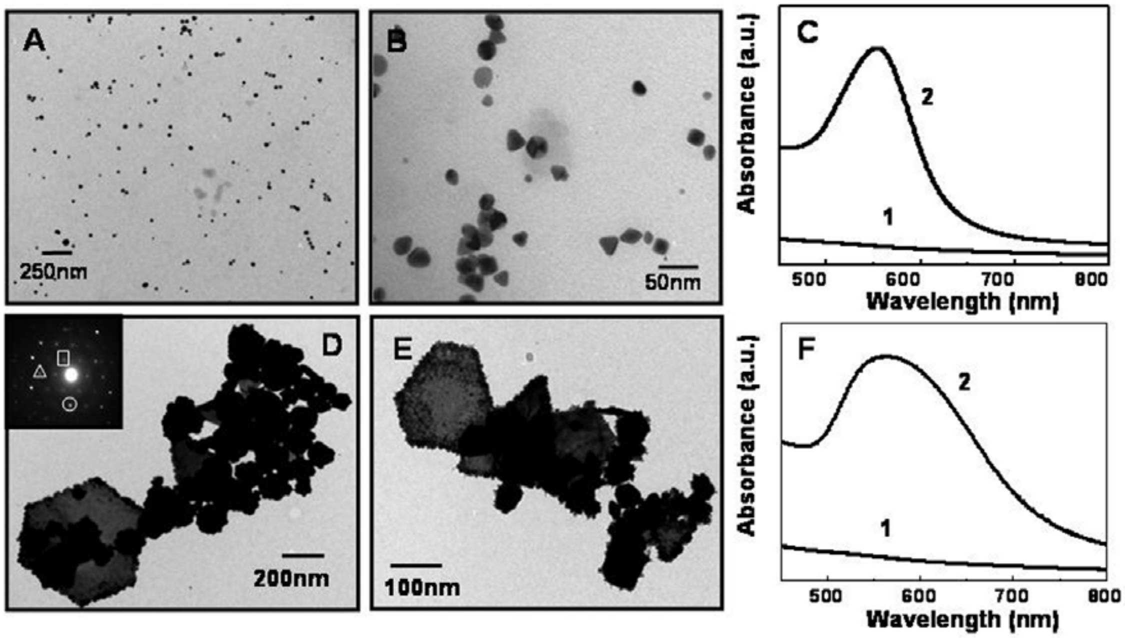

Figure 6.17 *TEM images of gold nanoparticles synthesized using crude protease enzyme secreted by Actinobacter spp. in M9 medium supplemented with BSA (A and B). (C) UV-vis spectrum obtained from gold nanoparticles synthesized by crude protease (curve 2). Synthesis of gold nanoparticles was not observed when crude protease was reacted with chloroaurate ions (curve 1) in the presence of protease inhibitor pepstatin. Images D and E shows gold nanoparticles synthesized by commercial protease. Curve 2 in the graph F corresponds to the UV-vis spectrum obtained from gold nanoparticles shown image D and E, while curve 1 represent UV-vis spectrum of commercial protease – chloroaurate ions reaction mixture in the presence of pepstatin.*

However no proteolytic activity was detected from the culture supernatant obtained from the growth medium of *Actinobacter* spp. when grown in M9 medium without supplemented BSA. The synthesis of gold nanoparticles was not observed at all when this supernatant was reacted with chloroaurate ions. This result indicates that the enzyme protease synthesized in the presence of BSA is responsible for the biological synthesis of gold nanoparticles. The role of protease as a reducing agent in the formation of gold nanoparticles can be illustrated by using the protease inhibitor, which is known to block the biological activity of the enzyme. Protease inhibitor binds to the active site or substrate binding site of protease and renders them inactive. Protease activity was not detected from the culture supernatant of M9 medium, in the presence of pepstatin. Further, the synthesis of gold nanoparticles was not observed when the pepstatin mixed culture supernatant was reacted with chloroauric acid as indicated by the UV-vis analysis of this solution, which do not show the SPR absorption band originating from gold nanoparticles (Curve 1, Figure 6.17C).

To further elucidate the role of protease in the synthesis of gold nanoparticles, commercial protease from the fungus *A. saitoi* (Sigma chemicals) was mixed with 10^{-3} M $HAuCl_4$ in the presence of glycine – HCl buffer (0.05 M, pH 3.0). After incubation of about 8 h the colour of solution turned pink from original pale yellow indicating the formation of gold nanoparticles. Images D and E from Figure 6.17 correspond to the TEM analysis of gold nanoparticles synthesized using commercial protease and aggregated gold nanoparticles along with triangular and hexagonal particles are observed. Most of the grid area was covered by aggregates of gold nanoparticles measuring 50 to 200 nm in size and it was difficult to observe the size of individual nanoparticles. The edge length of the triangular and hexagonal gold particles is measured to be around 200 nm. SAED pattern arising from these particles showed single crystalline hexagonal diffraction pattern that could be indexed on the basis of FCC structure of gold (inset in Figure 17D). UV-vis spectroscopic analysis performed on the solution of gold nanoparticles reveals the presence of the SPR absorption band at 580 nm (curve 2 in Figure 6.17F). The SPR absorption band shows broad curve with a small red shift as SPR band originating from spherical gold nanoparticles is usually centered on 520 nm. The observed red shift could be due to the aggregation of individual nanoparticles or the presence of anisotropic nanoparticles. This observation is in well agreement with the TEM analysis (Images D and F in Figure 6. 17), which shows the presence of aggregated nanoparticles together with triangular and hexagonal particles. Curve 1 in Figure 6.17F corresponds to the UV-vis analysis of reaction mixture containing the aqueous chloroaurate ions and commercial protease in the presence of protease inhibitor pepstatin. Even in this case the formation of gold nanoparticles was not observed at all as indicated by the absence of SPR absorption band in the range of 520-560 nm (Curve 1 in Figure 6.17F).

In yet another experiment chloroaurate ion were reacted with BSA under aerobic and anaerobic conditions in the absence of *Actinobacter* spp. Synthesis of gold nanoparticles was not observed even after seven days of reaction, indicating that the reduction of aqueous chloroaurate ions was mediated by *Actinobacter* spp. Experiments carried out using M9 minimal medium supplemented with BSA suggest that protease enzyme was induced in the presence of BSA, which mediates the reduction of aqueous chloroaurate ions and the formation of gold nanoparticles. Also the use of protease inhibitor-pepstatin confirmed that the synthesis of gold nanoparticles is mediated by protease. Thus, from the experimental results it can be inferred that the synthesis of gold nanoparticles by *Actinobacter* spp. in the presence of BSA is resulted due to the bacterial protease.

6.4.5 Discussion

This part of the chapter describes biological synthesis of gold nanoparticles under experimental conditions that favored the induction of proteolytic enzyme protease from *Actinobacter* spp. The presence of protease was found to be responsible for reduction of aqueous chloroaurate ions and the formation of gold nanoparticles. Also the synthesis of gold nanoparticles was accelerated in the presence of BSA. The size and shape of gold nanoparticles was affected due to the presence or absence of molecular oxygen in the reaction medium. Gold nanoparticles with irregular morphology were found to be synthesized in the presence of aerobic conditions along with few triangles and hexagons with the edge length measuring 250–500 nm. Under anaerobic conditions, gold nanoparticles with nearly uniform spherical morphology with 10 nm diameter are observed. A fairly good population of small triangular nanoparticles with edge length around 20 nm is observed together with spherical nanoparticles. Protease activity was detected from solutions of gold nanoparticles synthesized by *Actinobacter* spp. in the presence of BSA under aerobic as well as aerobic conditions as indicated by enzyme assays. The presence of protease inhibitor in reaction mixture inhibited the protease activity and the formation of gold nanoparticles. This observation indicates that the active site of protease enzyme may be involved in reduction of chloroaurate ions. Reaction of chloroaurate ions with commercial and purified protease also resulted in the synthesis of gold nanoparticles. The nanoparticles formed aggregates of 50 to 200 nm along with the triangular and hexagonal particles with ~ 200 nm edge length. Further the formation of gold nanoparticles was inhibited when commercial protease was reacted with the aqueous chloroaurate ions in the presence of pepstatin, as observed earlier.

6.5 Conclusions

This chapter describes new biological methods for the synthesis of gold and silver nanoparticles. Primary and secondary metabolites like siderophore – pyoverdin and a fluorescent blue – green pigment, pyocyanin, from the bacterium *P. aeruginosa* are used for biological synthesis of gold and silver nanoparticles. Also, protease enzyme mediated biosynthesis of gold nanoparticles using *Actinobacter* spp. has been demonstrated. The control over morphology and size of gold and silver nanoparticles can be achieved by various biological synthesis methods described here. Triangular gold nanoparticles with tunable edge lengths can be synthesized by varying the concentration of pyoverdin used for the synthesis of gold nanoparticles. Reduction of chloroaurate ions and silver ions by pyoverdin resulted in uniform spheroid of gold nanoparticles and wire-like silver nanostructures. Protease mediated reduction of chloroaurate ions by *Actinobacter* spp. resulted in the small triangular gold nanoparticles and nearly uniform spherical gold nanoparticles. The possibility of achieving shape control of metallic nanoparticles at a level equal to chemical routes by purely green chemistry approach makes biological synthesis protocols promising for the future development. The biological procedures for the synthesis of metallic nanoparticles described in this chapter can be important in this regard.

6.6 References

[1] (a) Mulvaney, P. *Langmuir*, **1996**, *12*, 188. (b) Edelstein, A. S., Cammarata, R. C. Nanoparticles: Synthesis, Properties and Applications, 1996, Bristol: Inst. Phys.

[2] Aiken, J. D. III, Finke, R. G. *J. Mol. Catal. A* 1**999**, *145*, 1.

[3] (a) Mirkin, C. A., Letsinger, R. L., Mucic, R. C., Storhoff, J. J. *Nature* **1996**, *382*, 607. (b) Rosi, N. L., Mirkin, C. A. *Chem. Rev* **2005**, *105*, 1547.

[4] Kamat, P. V. *J. Phys. Chem. B*. **2002**, *106*, 7729.

[5] Burda, C., Chen, X., Narayanan, R., El-Sayed, M. A. *Chem. Rev.* **2005**, 105, 1025.

[6] (a) Gardea-Torresdey, J. L., Peralta-Videa, J. R., de la Rosa, G., Parsons, J. G. *Coord. Chem. Rev.* **2005**, *249*, 1797. (b) Anderson, C. W. N., Brooks, R. R., Stewart, R. B., Simcock, R. *Nature*, **1998**, *395*, 553.

[7] Mann, S., Frankel, R. B. *Biomineralization: Chemical and Biochemical perspectives*, **1989**, 349, VCH publishers, New York.

[8] Sastry, M., Ahmad, A., Khan, M. I., Kumar, R., *Nanobiotechnology*, (eds. Niemeyer, C., M., Mirkin, C., A.) **2004**, 126, Wiley-VCH, Weinheim.

[9] (a) Southam, G., Beveridge, T. J. *Geochim .Cosmochim. Acta* **1996**, *60*, 4369. (b) Lengke, M. F., Fleet, M. E., Southam, G. *Langmuir*, **2006**, 22, 2780. (c) Klaus, T., Joerger, R., Olsson, E., Granqvist, C. G. *Proc. Nat. Acad. Sci.* **1999**, *96*, 3611.

[10] (a) Mukherjee, P., *et al. Angew. Chem. Int. Ed*. **2001**, *40*, 3585. (b) Mukherjee, P., *et al.Nano Lett.* **2001***, 1,* 515. (c) Mukherjee, P., *et al. Chem Bio Chem,* **2002***, 3,* 461. (d) Ahmad, A., *et al. Coll. Surf. B.* **2003***, 28,* 313.

[11] (a) Shankar, S. S., Ahmad, A., Pasricha, R., Sastry, M. *J. Mater. Chem.* **2003**, *13*, 1822. (b) Shiv Shankar, S., *et al*. *Nat. Mater.* **2004**, *3*, 482. (c) Liu, B., Xie, J., Lee, J. Y., Ting, Y. P., Chen, J. P. *J. Phys. Chem. B* **2005**, *109*, 15256.

[12] Cha, J. N., *et al*. *Proc. Natl. Acad. Sci. USA* **1999**, 96,361.

[13] Krogger, N., Deutzmann, R., Sumper, M. *Science* **1999**, *296*, 1129.

[14] Naik, R. R., Brot, L. L., Clarson, S. J., Stone, M. O. *J. Nanosci. Nanotechnol* **2002**, *2*, 95.

[15] Aizenberg, J., Lambert, G., Addadi, L., Weiner, S. *Adv. Mat* **1996**, *8*, 222.

[16] Bae, W., Mehra, R., K. *J. Inorg. Biochem* **1998**, *69*, 33.

[17] Slocik, J. M., Stone, M. O., Naik, R. R. *Small* **2005**, *1*, 1048.

[18] Naik, R. R. *et al*, *Nat. Mater* **2002**, *1*, 169.

[19] Chrosa, J. H., Walsh, C. T. *Microbiol. Mol Biol. Rev* **2002**, *66*, 223.

[20] Cox, C. D., Rinehart, K. L., Moore, M. L., Cook, J. C. *Proc. Natl. Acad. Sci. USA* **1981**, *78*, 4256.

[21] Wendenbaum, S., Demange, P., Dell, A., Meyer, J. M., Abdallah, M. A. *Tetrahedon Lett* **1983**, *24*, 4877.

[22] (a) Ankenbauer, R. G., Cox, C. D. *J. Bacteriol* **1988**, *170*, 5364. (b) Cox, C. D., Graham, R. *J. Bacteriol* **1979**, *137*, 357.

[23] (a) Becker, J. O., Cook, R. J. *Phytopathology* 1988, 78, 778. (b) Buysens, S., Heungens, K., Poppe, J., Hofte, M. *Appl. Environ. Microbiol* **1996**, *62*, 865.

[24] Frank, L. H., DeMoss, R. D. *J. Bacteriol* **1959**, *77*,776.

[25] Hassan, H. M., Fridovich, I. *J. Bacteriol* **1980**, *141*, 156.

[26] Britigan, B. E., *et al*, *J. Clin. Invest* **1992**, *90*, 2187.

[27] Hernandez, M. E., Newman, D. K. *Cell. Mol. Life Sci* **2001**, *58*, 1562.

[28] Mavrodi, D. V. *et al*, *J. Bacteriol* **2001**, 183, 6454.

[29] Rao, M. B., Tanksale, A. M., Ghatge, M. S., Deshpande, V. V. *Microbiol. Mol Biol. Rev* **1998**, *62*, 597.

[30] Phadtare, S., *et al Biotechnol. Prog.* **2002**, *18*, 700.

[31] Willner, I., Baron, R., Willner, B. *Adv. Mater* **2006**, *18*, 1109.

[32] Buysens, S., Heungens, K., Poppe, J., Hofte, M. *Appl. Environ. Microbiol*. **1996**, 62, 865.

[33] King, E. O., Wards, M. K., Raney, D. E. *J. Lab. Med.* **1954**, *44*, 301.

[34] The XRD pattern was indexed with reference to FCC gold and silver structure from *JCPDS – International Center for Diffraction Data PCPDFWIN* version 1.30, 04-0784 for gold and 04-0783 for silver.

[35] (a) Hao, E., Kelly, K. L., Hupp, J. T., Schatz, G. C. *J. Am.Chem. Soc.* **2002**, *124*, 15182. (b) Germain, V., Li, J., Ingert, D., Wang, Z. L., Pileni, M. P. *J. Phys. Chem. B* **2003**, *107*, 8717. (c) Burda, C., Chen, X., Narayanan, R., El-Sayed, M., A. *Chem. Rev.* **2005**, 105, 1025.

[36] Chandran, S. P., Chaudhari, M., Pasricha, R., Ahmad, A., Sastry, M. *Biotechnol. Prog.* **2006**, *22*, 577.

[37] (a) Silverstein, R. M., Bassler, G. C., Morril, T. C. Spectrometric identification of organic compounds, 1981, John Wiley & Sons, New York. (b) Pavia, D., Lampman, G., Kriz, G. Pavia : *Introduction to spectroscopy*, 3rd Ed. **2001**, 13, Harcourt college Publishers, Philadelphia.

[38] Cox,C., D. *Infect. Immun*. **1986**, *52*, 263.

[39] Wiley, B., Sun, Y., Mayers, B., Xia, Y. *Chem. Eur .J*. **2005**, *11*, 454.

[40] Barett, A. J. *Methods Enzymol*. **1995**, *248*, 183.

Chapter VII

Conclusions

This chapter contains concluding remarks on the salient features about the work described in this thesis and the scope for the future potential developments in this field.

7.1 Summary of the research work

Development of new synthetic protocols for nanomaterials over a range of composition, sizes and shapes constitutes a steadily evolving branch of nanotechnology. Chemical methodologies for the synthesis of inorganic nanoparticles are most popular and extensively practiced. However, use of caustic chemicals and ecologically hazardous non-polar organic solvents may cause environmental damage due to their excessive use. Therefore it has become necessary to device alternate, environmental friendly, “green chemistry” based methods for the synthesis of nanoparticles. In the present thesis an attempt has been made to design biological methods for the synthesis of simple metallic to more complex sulfide and oxide nanoparticles using micro-organisms. Naturally occurring biomineralization of exotic inorganic structures by living organisms has led the foundation of our study where we have used microbes for deliberate or induced synthesis of nanoparticles. This thesis describes biosynthesis of metal oxides, metal sulfides and metal nanoparticles using bacteria and fungi. Further, biochemical mechanism underlying the biosynthesis of oxides, sulfides and metal nanoparticles has been described. Magnetic iron oxide nanoparticles such as magnetite and maghaemite have been synthesized using the bacterium *Actinobacter* spp. isolated from our lab from aqueous mixture of ferri/ferrocyanide. *Actinobacter* spp. seems to be precursor dependent for the synthesis of magnetite and maghaemite. In the presence of anionic iron salts, *Actinobacter* spp. synthesized magnetite, whereas exposure of ferric ions resulted in the formation of maghaemite nanoparticles by the same bacterium. Different proteins induced in the presence of different iron salts indicated that there may exist distinctly separate pathways leading to synthesis of magnetite and maghaemite nanoparticles. Bacteriogenic magnetite and maghaemite nanoparticles exhibit excellent superparamagnetism, which is expected in nanosize dimensions. This thesis also describes biosynthesis of magnetite nanoparticles using two fungi *F. oxysporum* and *Verticillium* sp.

Semiconductor quantum dot nanocrystallites of metal sulfide such as CdS, ZnS and PbS have been synthesized using bacterial species *Pseudomonas aeruginosa*. All biogenic sulfide quantum dots were highly stable and exhibited excellent optical properties. Two genes coding for sulfate reductase enzymes has been identified from

P.aeruginosa, which were subsequently sequenced, cloned and overexpressed in *E. coli* cells. Moreover, recombinant *E. coli* cells harboring sulfate reductase genes were shown to be capable of synthesizing CdS, ZnS and PbS nanocrystallites. This indicate that our hypothesis that exogenous inorganic sulfates can be reduced even in aerobic bacteria by assimilatory sulfate reduction pathway.

Metal nanoparticles, especially gold and silver are very useful due to their optical properties in many technological applications. The optical properties of these nanoparticles depend on the size and shape. Therefore, investigation of ecologically innovative methods for the synthesis of metallic nanoparticles with different size and shapes would be ever lasting demand of nanotechnology. In such attempt, in current thesis we have described the biosynthesis of triangular and hexagonal gold nanoparticles, using *Actinobacter* spp. In addition synthesis of plate like, flat silver nanoparticles were synthesized using the same bacterium. Moreover, we have investigated the biological mechanism of the synthesis of metal nanoparticles along with the basis of shape control. Further, to investigate newer biological synthesis methods, we have successfully demonstrated the use of bacterial metabolites for the synthesis of metal nanoparticles. Metabolites such as siderophores, bacterial pigments and enzymes have been employed for the shape and size directed synthesis of gold and silver nanoparticles. Triangular gold nanoparticles with controllable edge length were synthesized using the siderophore-pyoverdin isolated from *P. aeruginosa*. Similarly, the pigment-pyocaynin isolated from *P.aeruginosa* resulted in the synthesis of monodisperse gold and wire-like silver nanoparticles. We have also demonstrated that an enzyme-protease from *Actinobacter* spp. can mediate the synthesis of monodisperse and triangular gold nanoparticles.

Nanoparticles as diverse as simple metals to metal sulfides to metal oxides can be synthesized using various biological methods described in this thesis. Therefore, the work described in the current thesis can lead towards the solution to fulfill demands of newer ecological, green chemistry based methods for the synthesis of inorganic nanoparticles.

7.2 Scope for future work

Synthesis of magnetic iron oxides and iron sulfide nanoparticles using *Actinobacter* spp. is an important result as the same bacterium could result in the formation of different iron oxides or iron sulfide nanoparticles depending on iron precursor used. Therefore it would be interesting to investigate the metabolic pathways operational in *Actinobacter* spp. that lead to the formation of nanoparticles of iron minerals. Further it would be useful to study in detail the magnetic properties of iron minerals synthesized using *Actinobacter* spp. since the association of proteins with nanoparticles may alter the magnetic properties. Similarly, it would be interesting to investigate the detailed optical properties of semiconductor metal sulfide quantum dots synthesized using *P.aeruginosa* and *Actinobacter* spp. Investigation of temperature dependent photoluminescent properties, quantum yield and stability of biogenic quantum dots would be important in comparison with chemical methodologies practiced for the synthesis of similar quantum dots. Moreover, it would be significant to characterize proteins present on the surface of metal sulfide nanoparticles, which may help in understanding the size confinement in quantum dots.

Size and shape controlled synthesis of metal nanoparticles using biological method is yet another aspect of the research work presented in this thesis. It can be interesting and important to study the interaction of biomolecules, such as proteins, siderophores or pigments with the metal ions and metallic nanoparticles they synthesize so that the control over crystal phases leading to the growth of anisotropic structure could be understood. Detailed analysis of metal ions and biomolecular interaction would help in designing new strategies for the synthesis of metal nanoparticles with different shapes.

Biological methods for the synthesis of inorganic nanoparticles described here are in the preliminary stage and needed to be optimized so as to be comparable with existing chemical methodologies. Effect of various experimental parameters such as, incubation temperature, aerobic or anaerobic conditions, use of alternate precursor salt, presence of certain metabolic constituents in the reaction medium etc. would give valuable information with which properties of nanoparticles e.g. shape, size, monodispersity could be controlled.

Appendix I

Microbiological Media

1) Luria Broth

Tryptone	1 %
Yeast extract	0.5 %
NaCl	0.5 %
D/W	100 ml
pH	7.2

2) MGYP

Maltose	0.5 %
Glucose	1 %
Yeast extract	0.3 %
Peptone	0.5
D/W	100 ml

3) King's B medium

Peptone	2 %
K_2HPO_4	0.15 %
$MgSO_4.7H_2O$	0.15 %
D/W	100 ml
pH	7.2

4) Medium for overexpression of *cys H* and *cys I* genes

Tryptone	1 %
Yeast extract	0.5 %
NaCl	0.5 %
Ampicillin	100 mg/ml
L-Arabinose	0.2 %
D/W	100 ml
pH	7.2

5) M 9 Minimal medium

Na_2HPO_4	0.6 g
KH_2PO_4	0.3 g
NaCl	0.25 g
NH_4Cl	0.1 g
$MgSO_4.7H_2O$	100 mM
Glucose	2 g
D/W	100 ml

Appendix II

List of Publications / Papers communicated

---

1) Biological synthesis of stable vaterite crystals by the reaction of calcium ions with germinating chickpea seeds

   D. Rautaray, A. Sanyal, **A. Bharde**, A. Ahmad and M. Sastry *Cryst.Growth & Des*. **2005**, *5*, 399.

2) Fungus-mediated biosynthesis of silica and titania nanoparticles

   V. Bansal, D. Rautaray, **A. Bharde**, K. Ahire, A. Ahmad and Murali Sastry *J.Mater.Chem.* **2005**, *15*, 2583.

3) Bacterial aerobic synthesis of nanocrystalline magnetite

   A. Bharde, A. Wani, Y. Shouche, P. A. Joy, B. L. V. Prasad, M. Sastry *J. Am. Chem. Soc* **2005,** *127*, 9326.

4) Fungus mediated synthesis of magnetite nanoparticles

   A. Bharde, D. Rautray, I. Sarkar, M. Seikh, M. Sanyal, A. Ahmad, M. Sastry *small*, **2006**, *2*, 135.

5) Bacterial enzyme mediated biosynthesis of gold nanoparticles

   A. Bharde, A. Kulkarni, M. Rao, A. Prabhune, M. Sastry *J. Mater. Chem*. **2007** (under revision)

6) Bacteria mediated precursor dependent biosynthesis of nanocrystalline maghaemite (γ-Fe_2O_3) and greigite (Fe_3S_4)

   A. Bharde, R. Parekh, M. Baidakova, T. EnoKi, B. L. V. Prasad, S. Ogale, M. Sastry *Nat. Mater.* **2007**, (communicated).

7) Precursor dependent biosynthesis of silver and silver sulfide nanoparticles using *Actinobacter spp*.

   A. Bharde, A. Prabhune, M. Sastry *Small* **2007**, (communicated).

8) Biological fabrication of semiconductor sulfide quantum dots : Nanomaterial synthesis through metabolic engineering.

   A. Bharde, R. Parekh, U. Roy, Y. Shouche, M. Sastry *Nature Biotechnol.* **2007** (communicated)

8) Synthesis of anisotropic gold and silver nanoparticles using bacterial metabolites- A novel biological approach for nanoparticle synthesis
   A. Bharde, M. Sastry, *Small*. 2007 (communicated).

9) Bacterial synthesis of gold nanoprisms and an insight into the biochemical mechanism
   Bharde, A. A., Sastry M. *Nat. nanotechnol.* **2007** (communicated)

10) Bacterial synthesis of semiconductor PbS nanocrystallite quantum dots.
    A. Bharde, A. Prabhune, M. Sastry (manuscript under preparation)

11) Magnetic properties of bacterially synthesized magnetite, maghaemite and iron sulfide nanoparticles under aerobic conditions
    A. Bharde, B. L. V. Prasad, B. Hannoyer, S. Ogale, M. Sastry (manuscript under preparation)